



# UNIVERSITÀ DEGLI STUDI DI TRIESTE

---

DIPARTIMENTO DI FISICA

XXXV CICLO DEL DOTTORATO IN FISICA

## Control of collective phenomena in complex materials through cavity electrodynamics

Settore scientifico disciplinare: FIS/03

Dottorando:  
**Giacomo Jarc**

Coordinatore:  
**Prof. Francesco Longo**

Supervisore:  
**Prof. Daniele Fausti**

---

ANNO ACCADEMICO 2021-2022



# ABSTRACT

---

The hybridization between light and matter within optical cavities has emerged as a promising avenue for controlling macroscopic functionalities in quantum material in both the weak and strong coupling regimes. In recent years, optical resonators have been shown to dramatically modify the path and rate of chemical reactions as well as the energy exchange and the electronic transport in semiconductors. Confining light fields in cavities provides therefore a novel approach towards the control of the ground state of quantum materials, establishing a connection between the manipulation through external static stimuli (like electric or magnetic fields) and the generation of non equilibrium light-driven phases.

In the present thesis we focus on the experimental possibility of exploiting the light-matter interaction in cavity-confined systems to dress collective excitations in complex materials and eventually gain control over their cooperative properties. For this purpose we developed a unique set-up to study the strong and weak coupling regimes between low energy excitations in correlated solid-state materials and tunable cavity modes. This has been realized in a Terahertz Fabry-Pérot resonator whose unique strength lies in its capability of tuning its fundamental mode in a cryogenic environment. The high versatility of the set-up makes it ideally suited to study a wide range of low energy modes in quantum materials and to subsequently investigate how their coupling with the extended cavity field may affect their collective dynamics.

We firstly study the strong coupling of vibrational excitations in  $\text{CuGeO}_3$ , a benchmark dielectric material exhibiting a strong phononic resonance in the Terahertz spectral range. Motivated by the possibility of reaching the strong and weak coupling limit in the designed resonators, we study the effect of cavity electrostatics on the metal-to-insulator transition in the Charge Density Wave (CDW) material  $1\text{T-TaS}_2$ . We observe a large modification of the linear response when  $1\text{T-TaS}_2$  is embedded within low energy Terahertz cavities. Importantly, the cavity electrostatics enables a reversible control of the metal-to-insulator phase transition, where a switch between the conductive and dielectric phases can be obtained by both tuning the cavity frequency and its alignment. Guided by the possibility offered by the cavity environment of controlling materials dissipations, we study how charge dissipations across the metal-to-insulator transition in  $1\text{T-TaS}_2$  influence the cavity response. We reveal that the free charges responsible of the conductive behaviour can couple to cavity modes and modify their dissipative dynamics. The presence of free charges in the system can induce a vibrational weak coupling regime when the cavity mode is hybridized with the phonons of the insulating CDW phase. Finally, motivated by the strong connection between electronic excitations in cuprates and their high-temperature superconducting response, we explore the possibility of hybridizing the charge transfer transition in YBCO in tailored cavity heterostructures.

Our findings show how cavity electrostatics can play a role in the intricate equilibrium physics of complex materials, possibly providing a new tool to control and engineer their static cooperative properties.



# CONTENTS

---

1	INTRODUCTION .....	1
2	LIGHT-MATTER COUPLING IN CAVITY-CONFINED SYSTEMS	5
2.1	Fabry-Pérot optical resonators.....	5
2.1.1	Properties of the cavity modes.....	6
2.2	Light-matter hybridization: a quantum picture.....	10
2.2.1	Coupled oscillator model.....	10
2.3	Role of dissipations on the coupling strength.....	15
2.3.1	Strong-to-weak coupling transition.....	16
2.4	Modelling linear response of light-matter hybrids.....	19
2.4.1	A classical approach: the Transfer-matrix formalism.....	19
2.4.2	A quantum approach: the Input-Output formalism.....	25
3	EXPERIMENTAL APPARATUS: TUNABLE CRYOGENIC TERAHERTZ CAVITY .....	31
3.1	Cryogenic cavity assembly.....	31
3.1.1	Semi-reflecting mirrors fabrication.....	33
3.1.2	Sample's mounting.....	33
3.2	Terahertz time-domain spectroscopy.....	34
3.2.1	The Terahertz domain.....	34
3.2.2	Terahertz generation and detection.....	34
3.2.3	Terahertz time-domain spectrometer.....	37
3.2.4	Determining THz optical properties.....	39
3.3	Characterization of the bare terahertz cavity.....	41
3.3.1	Empty cavity characterization at low temperature.....	41
3.3.2	Thermal evolution of the cavity resonance.....	43
4	VIBRATIONAL STRONG COUPLING IN $\text{CuGeO}_3$ .....	47
4.1	THz spectroscopy of $\text{CuGeO}_3$ normal phase.....	47
4.2	Phonon strong coupling evidences at 80 K.....	49
4.2.1	Resonant cavity measurements.....	49
4.2.2	Tunable cavity measurements: mapping polariton dispersion.....	52
4.3	Modelling phonon strong coupling in $\text{CuGeO}_3$ .....	53
4.3.1	Estimation of the components of the polariton wave-functions.....	53
4.3.2	Transfer-matrix simulations.....	57
4.3.3	Evolution of the polaritons linewidth.....	59
4.3.4	Dependence of the coupling on the quality factor.....	60
4.4	Temperature evolution of the vibro-polariton modes.....	62
4.5	Conclusions.....	66
5	CAVITY CONTROL OF THE METAL-TO-INSULATOR TRANSITION IN $1\text{T-TaS}_2$ .....	67
5.1	Motivation.....	67

5.2	Terahertz spectroscopy of 1T-TaS <sub>2</sub> across the charge ordering transition .....	69
5.3	Cavity-driven renormalization of the phase transition .....	74
5.3.1	Cavity alignment dependence .....	75
5.3.2	Cavity frequency dependence .....	79
5.4	Discussion .....	81
5.5	Measure protocols and data analysis .....	88
5.5.1	Characterization of the sub-THz empty cavities .....	88
5.5.2	Characterization of the sample thermalization time .....	89
5.5.3	Determination of the critical temperature .....	90
5.6	Theoretical models .....	91
5.6.1	Free energy picture .....	91
5.6.2	Control of dissipations through cavity electrodynamics .....	96
5.7	Methods .....	99
5.7.1	Measurement of the temperature within the cavity .....	99
5.7.2	Finite element simulations of incoherent thermal heating .....	100
5.8	Tests for the cavity-induced origin of the phase transition control .....	102
5.8.1	Does the sample affect the temperature difference between the cold finger and the cavity center? .....	103
5.8.2	Does the temperature of the cavity mirrors affect the sample temperature? .....	105
5.8.3	Does the cavity alignment modify the sample temperature? .....	112
5.8.4	Does the external radiation influence the sample temperature? .....	115
5.8.5	Does the THz thermal load affect the observed transition temperature? .....	116
5.9	Conclusions .....	118
6	<b>STRONG COUPLING SIGNATURES ACROSS 1T-TaS<sub>2</sub> METAL-TO-INSULATOR TRANSITION .....</b>	<b>119</b>
6.1	Coupling with the Drude excitation .....	120
6.1.1	Cavity dissipations across the charge ordering transition .....	120
6.1.2	Dependence of the coupling on the symmetry of the cavity mode .....	124
6.1.3	Transfer-matrix simulations across the phase transition .....	128
6.1.4	Dependence of the coupling on the cavity frequency .....	132
6.2	Multimode vibrational strong coupling in the C-CDW phase .....	134
6.2.1	Measurements .....	134
6.2.2	Multi-polariton mixing: the quantum model .....	138
6.2.3	Lifetimes properties of the multimode polaritons .....	141
6.3	Temperature-dependent coupling regimes .....	143
6.3.1	Evolution of the polaritons spitting .....	145
6.3.2	Signatures of vibrational weak coupling regime .....	146
6.4	Conclusions .....	149
7	<b>ELECTRONIC COUPLING: CHARGE TRANSFER HYBRIDIZATION IN SUPERCONDUCTING YBCO .....</b>	<b>151</b>
7.1	Motivation .....	151
7.2	Design of the YBCO-based cavity heterostructures .....	152

7.3	Three pulse optical measurements .....	155
7.3.1	Characterization of the non-linear response of the superconducting phase .....	155
7.3.2	Effect of the cavity of the superconducting optical response ...	158
7.4	Methods .....	161
7.4.1	Experimental set-up .....	161
7.4.2	Detailed analysis of the optical measurements .....	163
7.4.3	Fluence-dependence of the non-linear signal .....	164
7.5	Conclusions .....	165
8	CONCLUSIONS .....	167
	BIBLIOGRAPHY .....	169



# INTRODUCTION

---

Light-matter interaction is a key process in modern physics, providing the means to probe and actively manipulate material functionalities. This possibility has offered major breakthroughs in the field of complex materials.

Complex materials display several competing orders, originating from the delicate and intricate interplay between their degrees of freedom, such as electrons, lattice, spins etc. This delicate interplay makes complex materials highly susceptible to even small external stimuli that can induce giant collective responses and eventually modify their macroscopic properties.

A common way to exploit light-matter interaction to engineer collective properties in complex materials is represented by out-of-equilibrium optical methods [1, 2]. With these techniques materials are driven out of the thermodynamical equilibrium through non-thermal pathways by strong ultrafast laser pulses. In these out-of-equilibrium states the materials are characterized by the response of the excited quasi-particles, giving rise to new functionalities [3–10].

The light-driven control of complex materials can be also seen from a different perspective, where classical driving fields are replaced by extended photonic modes realized within **optical cavities**. This approach has been extensively explored in atomic and molecular physics, while its extension to correlated quantum materials is emerging only in the last years [11]. The experimental possibility of exploiting cavity electrodynamics to dress collective excitations in complex materials and eventually control their cooperative properties is the core of the present thesis.

The possibility of tailoring light-matter interaction in cavity confined systems is rooted in the pioneering experiments of Purcell [12], who firstly discovered that the atomic emission could be modified when atoms are placed in a resonant optical cavity. This was the first demonstration of the more general principle that material properties can be controlled by engineering their electromagnetic environment. In other words, properties that were thought to be intrinsic to matter turned out to be properties of the matter dressed by its reshaped electromagnetic environment.

Even though remarkable effects on the radiative properties of atoms or molecules could be observed by placing them within a poor metallic resonator [13–16], the most dramatic modification of their bare properties is expected to happen when the light-matter strength within the cavity volume overcomes any possible relaxation rate. In this limit, called *strong coupling regime*, the light-matter interaction overcomes the dissipative processes occurring in the uncoupled systems, and the wave-functions of the material excitations and the photon inside the cavity are coherently mixed. This mixing results in the formation of hybrid light-matter states dubbed polaritons [17, 18]. The core feature that has raised much interest in light-matter hybrids in the strong coupling limit is the fact that the coupled polaritonic states can be regarded as highly delocalized quantum states. This delocalization arises from the fact that if many emitters are placed within the optical mode volume, their simultaneous interaction with a common cavity mode induces quantum correlations among the spatially separated emitters. For this

reason, while the hybridization between light and matter was originally comprehended and realized in isolated atomic and molecular systems [13–16, 19–21], it has more recently been extensively studied in organic and inorganic semiconductors excitons [22–24], phonons [25–31], or magnons [32]. Exploiting the strong coupling limit is emerging as a promising tool to control material functionalities in different physical-chemical settings. In particular, it has been recently shown that vibrational strong coupling can affect chemical reactivity [33–35], conductivity [36], molecular structure [37] and charge and energy transfer [38–41].

These evidences have led to the suggestion that also condensed-matter platforms and their embedding in cavities should be further explored with the aim of modifying their cooperative properties. The main advantages of exploiting cavity electrodynamics to control collective properties in complex materials are:

- In an optical cavity the light-matter interaction can be strongly enhanced due to the resonant condition. This implies that even the hybridization with the vacuum cavity field is enough to trigger major changes in the material properties [42], thus leading to an effective control of the matter’s ground state. This is a major advantage over light-driving techniques, where heating effects are almost unavoidable and the recovery times are generally limited to much longer times which are determined by slower relaxation processes, ruled by the thermodynamic characteristic of the sample.
- The cavity environment provides the unique means to control the dissipations in quantum materials. This mechanism is fairly general and can be applicable also in the weak coupling regime, where dissipations dominate over the coherent energy exchange between light and matter.
- The cavity mode can be seen as an artificial or external bosonic mode with tunable energy, to which charges can couple. In this scenario the cavity plays a role similar to that of other natural bosonic modes (phonons and magnons) and can introduce additional scattering channels, which mediate the long-range interactions among the charges.

The perspective of employing light-matter coupling in optical cavities to control the properties of solid-state materials has recently stimulated a wealth of theoretical proposals. Among them we mention: enhanced superconductivity through cavity-mediated electron pairing [43–48], cavity control of the competing order between charge density wave and superconducting phases [49], cavity control of excitons [50], enhanced ferroelectricity [51–54], and cavity control of magnetic order [55].

From the experimental point of view, it has been recently proved that vacuum cavity fields in the strong coupling regime can reshape material functionalities even without external illumination, i.e. in the cavity photo-ground state. It has been recently experimentally shown that the coupling with cavity vacuum modes can change the magneto-transport in two dimensional materials [38], suppress the topological protection of the integer quantum Hall effect [56], or even modify the critical temperatures and the magnetic order in conventional and unconventional superconductors [57, 58].

Selecting the energy of the photon trapped inside the cavity is a crucial parameter in these experiments. Indeed, it sets the coupling energy scale and subsequently the energy scale of the targeted degree of freedom.

In this thesis we focus on the experimental possibility of using Terahertz and sub-Terahertz cavities to hybridize low energy excitations in quantum materials and eventually control their collective properties. For this aim we developed a unique set-up suitable to study the Terahertz optical properties of low energy degrees of freedom in crystalline samples coupled with a tunable optical cavity in cryogenic environment. The unique feature implemented in the set-up lies in its capability of tuning the cavity resonance at cryogenic temperatures, thus enabling to target different material excitations and study how the collective coupling with an optical cavity may affect the material's macroscopic properties.

The thesis is structured in the following way.

- In Chapter 2 we provide the general framework of light-matter coupling in the strong and weak coupling limit and show how dissipations can induce a transition between the two regimes. We will derive the full spectral response of the hybrid cavity in both a classical and quantum formalism, which will give us the theoretical connection with the experimental results presented in the thesis.
- Chapter 3 is dedicated to the description of the experimental set-up specifically developed in the *q4q* laboratory at Elettra Sincrotrone Trieste. This consists of a tunable cryogenic Terahertz (THz) cavity combined with a THz time-domain spectrometer for the characterization of the light-matter hybrids.
- Chapter 4 reports the experimental demonstration of the vibrational strong coupling at low temperatures in the benchmark material  $\text{CuGeO}_3$ . We will show how the strong coupling features of vibrational excitations are mapped in the THz domain and the thermal evolution of the emerging vibro-polariton resonances. The models presented in Chapter 2 will be exploited to justify the experimental results.
- Chapter 5 represents the core of the present thesis. We present here the first possible experimental evidence of the reversible cavity control of the metal-to-insulator transition in the correlated material  $1\text{T-TaS}_2$ . We will show that a large modification of the material's linear response can be obtained by embedding the material in THz and sub-THz Fabry-Pérot cavities. We will prove that the modification of the hybrid response is sensitive to the cavity frequency and alignment and present all the experimental tests performed to prove the cavity-induced origin of the observed behaviour.
- In Chapter 6 we study how charge dissipations across the model metal-to-insulator transition in  $1\text{T-TaS}_2$  affect the cavity electrodynamics. We will show that the lifetime of the cavity photons decreases going from the insulating to the metallic state when the cavity resonance lies in the low-frequency region dominated by the free carriers response. Conversely, when the cavity is tuned resonantly to the IR-active modes of the insulating state we reveal a multiple polariton mixing resulting from the cavity-mediated hybridization of the non-degenerated phonons of the dielectric phase. We will show that, due to a different dissipative response of the charges in the two phases, the splitting between the polaritons closes across the phase transition, reaching the weak coupling limit near the critical temperature.
- Lastly, in Chapter 7 we will explore the possibility of coupling the electronic charge transfer transition in the high-Tc superconductor YBCO to an optical cavity and exploit non-linear optical techniques to see how the electronic coupling may

affect the superconducting response. The results presented in this chapter are still very preliminary and complementary techniques will be needed to track the effect of the cavity on the superconducting behaviour.

# LIGHT-MATTER COUPLING IN CAVITY-CONFINED SYSTEMS

---

In quantum mechanics, the presence of a cavity surrounding a targeted emitter can be described as a coherent evolution with a photon repeatedly absorbed and re-emitted by the emitter itself. In this limit, the strength of the light-matter coupling, which in vacuum is limited by the fine structure constant  $\alpha \sim 1/137$  [17], is mainly determined by the oscillator strength of the targeted optical transition, which is fixed by the nature of the emitter, and by the cavity quality factor which can be tuned and set the lifetime of the trapped photons [18, 42]. If the cavity confinement is sufficiently high, i.e. in the strong coupling limit, the light-matter interaction can be enhanced at the point that the localized emitters can hybridize with the cavity field giving rise to hybrid delocalized states, dubbed polaritons [22, 23, 25, 59–61]. These hybrid states inherit both material's and light's features.

In this chapter we give the theoretical basis underlying the strong light-matter coupling in both non-dissipative and dissipative cavities and show how real systems dissipations skew the coherent strong coupling features. To simplify the discussion, we will focus on the case of co-planar Fabry-Pérot optical cavities, which are the ones employed in the experiments presented in the thesis. However, the main results derived in this chapter will remain valid for any kind of electromagnetic resonator [11, 62–64], provided that the light-matter coupling strength and the resonator losses remain in the same ratio.

After having outlined the main characteristics of a Fabry-Pérot resonator, we will describe the optical response of the hybrid resonator using a simple coupled oscillator quantum model [65, 66]. The abstraction of the hybrid cavity to coupled levels will enable us to gain insight on the nature of the new light-matter eigen-states, whereas its extension to more complex systems, where dissipative dynamics are included, will provide the full spectral response of the coupled cavity, giving a more realistic guideline to understand the experimental results. The spectral response of the cavity will be firstly derived in a classical framework (the *Transfer-matrix* method) and then extended to a fully quantum model (the *Input-Output* model). Importantly, we will show that the spectral response of the hybrid cavity predicted with the classical and quantum formalisms coincide in the linear regime, offering therefore a powerful tool to simulate the cavity spectra presented in this thesis.

## 2.1 FABRY-PÉROT OPTICAL RESONATORS

The schematic picture of a Fabry-Pérot cavity is represented by a slab of a material embedded between two mirrors. We will assume the mirrors to be partly transmitting with a reflectivity  $R_m$ . Let us consider a single mode optical field with wavelength  $\lambda$  entering the cavity from the left mirror. As the input field propagates through the cavity, it will acquire a phase component  $\phi_C$  which is determined by the cavity length  $L$  and

by the index of refraction  $n$  within the cavity volume. The total phase accumulated by the optical field over a round trip (Figure 2.1A) is:

$$\phi = 2\phi_M + 2\phi_C = 2\phi_M + 2\frac{2\pi nL}{\lambda}, \quad (2.1)$$

where we have indicated with  $\phi_M$  the phase shift due to the mirrors.

Given the boundary conditions set by the mirrors, the light will continue to cycle through the cavity volume, picking up this phase  $\phi$  at each round trip and interfering with itself. In order for the optical mode to be allowed within the cavity, the total phase  $\phi$  must be an integer multiple of  $2\pi$ . We will suppose that the phase shift induced by each mirror ( $\phi_M$ ) is exactly  $\pi$ . This is typically the case of broadband dielectric mirrors at the designed wavelength [67], and approximatively the case of the metallic mirrors of the Terahertz cavities employed in our studies. Under this assumption, we can therefore tune the cavity thickness to support a particular wavelength by selecting the distance between the two mirrors:

$$L = m\frac{\lambda}{2n} \quad m \in \mathbb{N}. \quad (2.2)$$

With each round-trip within the cavity, some light is transmitted through the second mirror with an advanced phase and an amplitude reduced relative to the previous cavity cycle due to the two reflections. After summing an infinite series of these transmissions and accounting for the interference effects, we can hence compute the full cavity transmission as a function of the phase shift per cycle [68]:

$$T(\phi) = \frac{1}{1 + 4\frac{R_m}{(1-R_m)^2} \sin^2\left(\frac{\phi}{2}\right)}. \quad (2.3)$$

The cavity interference induces therefore a strongly frequency-dependent transmission. At the frequencies  $\omega_m = \frac{2\pi cn}{\lambda_m}$ , where a cavity mode is allowed by the boundary conditions, the transmission through the cavity structure increases dramatically. We note that those frequencies  $\omega_m$  correspond to a total spectral phase accumulation of  $\phi = 2\pi m$  (Figure 2.1B).

The spacing between adjacent cavity modes  $\omega_m$  is called the Free-Spectral-Range (FSR) and entirely depends on the optical thickness of the cavity, i.e. on the tunable distance  $L$  between the cavity mirrors.

We stress that the constructive interference of light within the cavity greatly enhances the electric field amplitude of that cavity at particular positions, determined by the spatial symmetry of the standing modes. By placing materials with dipole-allowed transitions at the antinodes of the confined optical modes we can therefore think of coupling the material excitations more strongly to light than outside the resonator, i.e. in free space. This evidence is the core of light-matter coupling in cavity-confined systems, where a reshaping of the density of states of the vacuum optical mode can change the dissipative rates of the matter excitations (weak coupling regime) or even induce a light-matter hybridization (strong coupling regime). In particular, we expect the enhancement of the light-matter coupling to increase at higher spatial compressions of the cavity mode volume [42].

### 2.1.1 PROPERTIES OF THE CAVITY MODES

Once a cavity has been assembled, it is crucial to characterize the emergent Fabry-Pérot resonances in terms of their linewidths, which will subsequently set their lifetimes.

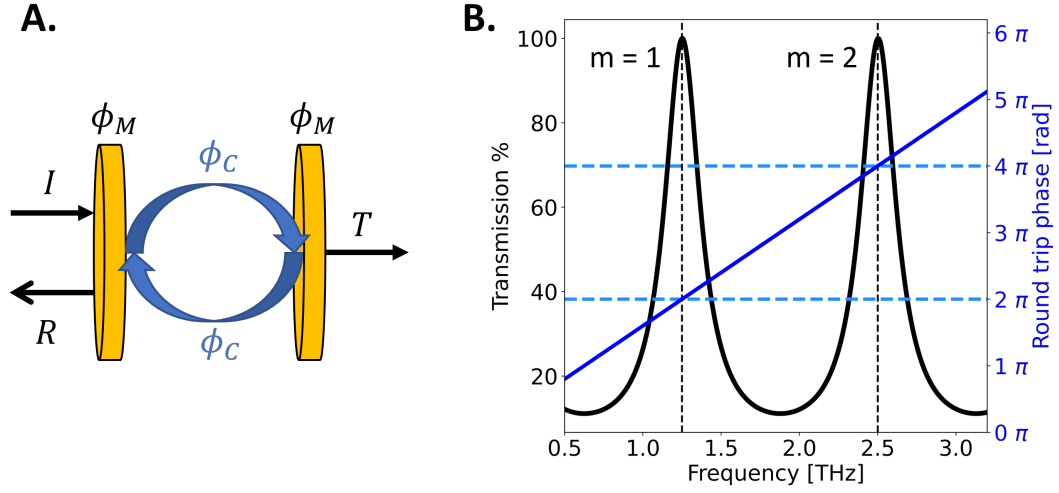


**Figure 2.1: Linear transmission of a Fabry-Pérot resonator.** **A.** Phase accumulation during round trip of light within a Fabry-Pérot planar cavity.  $\phi_M$  represents the phase accumulation due to the mirrors, while  $\phi_C$  accounts for the phase acquired within the cavity volume. **B.** Representative transmission of a Fabry-Pérot cavity ( $R_m = 0.8$ ). A resonant mode (vertical dashed lines) appears every times the round-trip phase accumulation (blue curve) matches an integer multiple of  $2\pi$  (horizontal dashed lines). The fundamental cavity mode ( $m = 1$ ) appears at a phase accumulation  $\phi = 2\pi$ , while the second order mode ( $m = 2$ ) in correspondence with  $\phi = 4\pi$ . In the present plot the fundamental mode is set at  $\omega_c = 1.25$  THz.

The cavity mode resonance can be well understood as a damped harmonic oscillator. Within this classical framework, the electric cavity field can oscillate with a certain resonant frequency and the amplitude of that oscillation decreases exponentially. We will show in the following that the damping is connected to the optical losses due to the finite mirrors transmission and extract the expression of the quality factor of the optical resonator. The latter is the used parameter to quantify the bare optical dissipations within the cavity volume.

#### 2.1.1.1 Quality factor

In an optical cavity, since the mirrors reflectivity is less than 1, the intensity of the confined cavity mode decays with time by photon escaping through the mirrors. These losses are characterized by a dimensionless parameter, the cavity quality factor  $Q$ , which is defined as the ratio between the energy stored inside the cavity and the energy dissipated per optical cycle [69]:

$$Q = \left| \omega_c \frac{U_c}{\frac{dU_c}{dt}} \right|. \quad (2.4)$$

In the previous expression  $\omega_c$  is the frequency of the cavity mode,  $U_c$  is the electromagnetic energy stored within the cavity volume and  $\frac{dU_c}{dt}$  is the energy loss rate, i.e. the dissipated optical power. As in the general case of damped oscillators, we expect the electromagnetic energy within the cavity to be dissipated exponentially as:

$$U_c(t) = U_0 e^{-\gamma_c t}, \quad (2.5)$$

where  $\gamma_c$  sets the lifetime of the  $m^{\text{th}}$  cavity mode. The dissipative dynamics of the optical power stored within the cavity volume hence reads:

$$P_d(t) = \left| \frac{dU_c(t)}{dt} \right| = \gamma_c U_c(t). \quad (2.6)$$

The previous equation allows to express the cavity quality factor as:

$$Q = \omega_c \frac{U_c(t)}{\gamma U_c(t)} = \frac{\omega_c}{\gamma_c}. \quad (2.7)$$

This definition is commonly used to experimentally determine  $Q$ , since it is enough to measure the cavity spectral response and extract from the Fourier spectrum the central frequency  $\omega_c$  and the linewidth of the cavity mode  $\gamma_c$ .

Considering the relationship between the electromagnetic energy  $U_c(t)$  and the electric field amplitude  $|\mathbf{E}(t)|^2$ , the electric field within the optical resonator can be expressed as:

$$\mathbf{E}(t) = \mathbf{E}_0 e^{-\frac{\omega_c}{2Q}t} e^{-i\omega_c t}, \quad (2.8)$$

where  $\mathbf{E}_0$  is the initial amplitude corresponding to  $U_0$ . The Fourier transform of Equation 2.8 gives the field and energy distribution of the cavity resonator in the frequency domain:

$$U_c(\omega) \propto |\mathbf{E}(\omega)|^2 \propto \frac{1}{(\omega - \omega_c)^2 + \left(\frac{\omega_c}{2Q}\right)^2}. \quad (2.9)$$

The cavity spectrum has therefore the form of a Lorentzian-like distribution. This is characterized by a central wavelength  $\omega_c$ , i.e. the targeted cavity mode<sup>1</sup>, and a Full Width Half Maximum (FWHM)  $\gamma_c = \frac{1}{2Q}$ . The latter sets the upper limit of the lifetime of the cavity photons<sup>2</sup> within the resonator volume.

Importantly, the cavity  $Q$ -factor can be related to the experimental design of the resonator, and in particular to the mirrors reflectivity  $R_m$  and to the mode order  $m$ . In the following we will explicitly show these connections.

In a schematic picture, the cavity confinement can be considered as a pulse of light bouncing back and forth between the mirrors. Every time the light bounces, photons will escape from the cavity with probability  $1 - R_M$ . This will correspond to a reduction of the stored optical energy  $U_{\text{fin}} = R_M U_{\text{in}}$ . In this picture, we can average the dissipated EM energy over the time light takes to complete half a round trip [69]. The energy lost in the cavity within half a round trip is:

$$\Delta U_{\text{trip}} = (1 - R_M) U_i, \quad (2.10)$$

corresponding to a time of flight:

$$\Delta t_{\text{trip}} = \frac{mn\lambda}{2c}. \quad (2.11)$$

The EM energy lost per oscillation can be expressed as the energy lost per half round trip times the ratio of oscillator to trip periods:

$$\Delta U_{\text{cycle}} = \Delta U_{\text{trip}} \frac{\Delta t_{\text{cycle}}}{\Delta t_{\text{trip}}} = \frac{2(1 - R_M)}{m} U_i. \quad (2.12)$$

<sup>1</sup> Note that for simplicity we have neglected the higher order harmonics of the cavity field.

<sup>2</sup> Here and in the following we will refer to the single particle optical mode inside the cavity as a cavity photon. This can be considered as a well defined particle with an energy and a lifetime.

Recalling now the definition of  $Q$  in Equation 2.7, we can express the quality factor of the Fabry-Pérot resonator as:

$$Q = \frac{m\pi}{2} \frac{1 + R_m}{1 - R_m}. \quad (2.13)$$

We highlight that the  $Q$  factor is directly determined by the cavity mode order  $m$  and by the mirror quality which, in this simplified classical picture, can be phenomenologically set through the mirrors reflectivity  $R_m$ . Comparing this expression to Equation 2.7, the inverse photon lifetime  $\gamma_c$  can be hence directly related to cavity design as:

$$\gamma_c = \frac{2\omega_m}{m\pi} \frac{1 - R_m}{1 + R_m}. \quad (2.14)$$

Therefore, all cavity photons have the same lifetime which is fixed by the cavity length and mirror quality. However, one can increase the lifetime of a desired wavelength by making the cavity longer, such that the targeted mode is a higher order. The trade-off typically made by making this choice is the reduction of the free spectral range of the resonator.

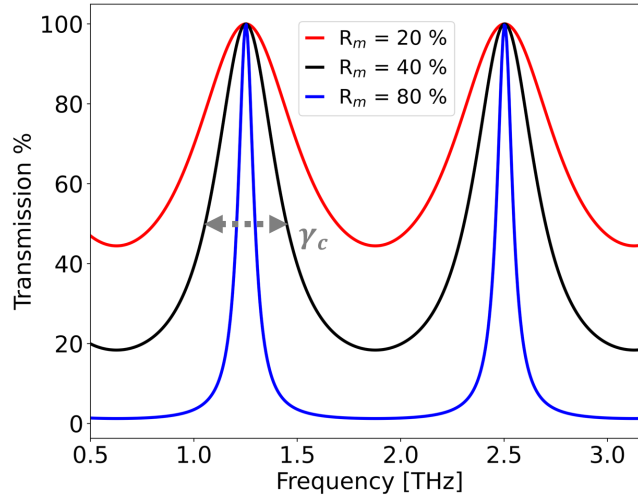


**Figure 2.2: Cavity transmission as a function of the mirrors reflectivity.** Transmission through a planar Fabry-Pérot cavity for different values of the mirrors reflectivity  $R_m$ . Changes in  $R_m$  are mapped in a modification of the linewidth of the cavity resonance  $\gamma_c$ , and hence of the quality factor of the resonator ( $Q$ ).

The  $Q$ -factor has two complementary physical interpretations, depending on the actual application of the Fabry-Pérot structure: (1) when working as a cavity to confine light, which is the main interest of this thesis, the  $Q$ -factor represents the lifetime of the confined field; (2) when working as an interferometer, the  $Q$ -factor represents the spectral resolution and is related to the interferometer finesse.

For an ideal absorption-less Fabry-Pérot cavity only the mirror losses contribute to reduce the value of the  $Q$  factor or, equivalently, to broaden the cavity modes. As an example, transmission spectra for different mirrors reflectivity  $R_m$  are shown in Figure 2.2. The linewidth of the cavity mode  $\gamma_c$  is reduced sharply with increasing mirror reflectivity, as a consequence of the longer decay time of the modal cavity field.

Conversely, in real systems, also light absorption inside the cavity volume, or incoherent light scattering due to imperfect interfaces contribute to the reduction of  $Q$ .

## 2.2 LIGHT-MATTER HYBRIDIZATION: A QUANTUM PICTURE

In the previous section we have described the optical features of Fabry-Pérot resonators and show how they can be exploited to reshape the EM environment, giving rise to frequency-localized optical modes with longer lifetimes. If we place a material within the cavity volume with a specific dipole-allowed transition resonant to the cavity mode, the boundary conditions will induce a coherent evolution of the trapped photon, which will be repeatedly absorbed and re-emitted by the material.

If the losses dominate over these coherent coupling between the cavity and the material mode, the dynamics is essentially incoherent and each material's emitter will interact independently with the cavity field. Nevertheless, even in this regime, named *weak coupling regime*, the reshaping of the EM density of states induced by the cavity manifests itself in the change of the excited states lifetimes of the material's emitters, as described by the Purcell effect [13–16].

Conversely, when the rate of the coherent energy exchange becomes comparable to the losses, the cavity-material system enters the *strong coupling regime*. In this limit, the recurrent exchange of excitation quanta between the cavity mode and the material's emitters leads to the formation of hybrid states, which inherit features of the both constituents parts [17, 18, 42, 70]. In this regime, the cavity field induces spatial correlation among the separated material's emitters forming collective delocalized states dubbed polaritons [22, 23, 25, 59–61].

We will present in the following the theoretical framework of strong-light matter coupling in cavity-confined systems. Starting from a coupled oscillator quantum model we will derive the polaritonic modes and discuss their hybrid features.

### 2.2.1 COUPLED OSCILLATOR MODEL

In order to see how the dynamics of the coherent energy exchange can emerge at a microscopic level, we resort to a quantum mechanical description of the light-matter coupled system. We will exploit a basic Hamiltonian approach, idealizing the material's excitations as an assembly of  $N$  two-level systems, and modelling the cavity field by a single quantized mode.

Let us start from the basic situation in which a single material's dipole with resonant frequency  $\omega_0$  interacts with the cavity mode. The interaction potential between the single dipole-allowed transition and the cavity field  $\mathbf{E}$  can be written as [71]:

$$U = -\boldsymbol{\mu} \cdot \mathbf{E}, \quad (2.15)$$

being the  $\boldsymbol{\mu}$  the dipolar strength.

Writing both the electric field and the transition dipole moment in a quantum representation, we can subsequently obtain the Hamiltonian description of the light-matter interaction within the cavity, known as Rabi model [72]:

$$\hat{H}_{\text{Rabi}} = \omega_c \hat{a}^\dagger \hat{a} + \omega_0 \hat{\sigma}_\sigma^\dagger + \hat{H}_{\text{int}}. \quad (2.16)$$

The interaction Hamiltonian, resulting from the quantization of the interaction potential  $\mathcal{U}$ , reads:

$$\hat{H}_{\text{int}} = g \left( \hat{\sigma} + \hat{\sigma}^\dagger \right) \left( \hat{a} + \hat{a}^\dagger \right). \quad (2.17)$$

In the previous Hamiltonians  $\hat{a}$  ( $\hat{a}^\dagger$ ) is the annihilation (creation) operator for the cavity photons of frequency  $\omega_c$ , and  $\hat{\sigma}$  ( $\hat{\sigma}^\dagger$ ) the lowering (raising) operator acting on the two-level dipolar system. The coupling strength  $g$  between cavity and dipole oscillators scales with the transition probability of the material's excitation (i.e. the dipolar strength) and with the spatial overlap between the dipole and the modal cavity field. The coupling constant  $g$  can be therefore generally expressed as:

$$g \propto |\boldsymbol{\mu}| \int_{\mathbb{R}^3} d\mathbf{r} u_{\text{cav}}(\mathbf{r}) u_{\text{dip}}(\mathbf{r}), \quad (2.18)$$

where  $u_{\text{cav}}(\mathbf{r})$  and  $u_{\text{dip}}(\mathbf{r})$  are the spatial-dependent wave-functions of the cavity and dipole modes.

The generalization to a large number of molecules is given by the Dicke model [65], which describes the interaction between a set of  $N$  two-level systems with a single-mode bosonic field, i.e. the single mode optical cavity. By working in the cavity ground state, i.e. by excluding the states with multiple photon excitations, the Dicke Hamiltonian reads:

$$\hat{H}_{\text{Dicke}} = \omega_c \hat{a}^\dagger \hat{a} + \sum_{i=1}^N \omega_0 \hat{\sigma}_i^\dagger \hat{\sigma}_i + g \sum_{i=1}^N \left( \hat{\sigma}_i + \hat{\sigma}_i^\dagger \right) \left( \hat{a} + \hat{a}^\dagger \right). \quad (2.19)$$

### 2.2.1.1 Tavis-Cummings Hamiltonian

A commonly used solution for the Dicke model is obtained under the rotating wave approximation [73] in which the fast oscillating terms corresponding to the multiple excited states ( $\hat{\sigma}^\dagger \hat{a}^\dagger$  and  $\hat{\sigma} \hat{a}$ ) are neglected. For near resonant light-matter interaction, those latter terms beat at high frequencies in the rotating frame and can be thus neglected as long as the coupling  $g$  remains small with respect to the cavity frequency  $\omega_c$ . On the contrary, if  $g$  approaches  $\omega_c$ , these multiple-excitations terms become relevant, leading to a new regime, named *ultrastrong coupling regime*, where phenomena like ground-state squeezing, band-gap opening, and dynamical Casimir effect can appear [64, 74–77].

This approximated Hamiltonian goes under the name of Tavis-Cummings model [66]:

$$\hat{H} = \omega_c \hat{a}^\dagger \hat{a} + \sum_{i=1}^N \omega_0 \hat{\sigma}_i^\dagger \hat{\sigma}_i + g \sum_{i=1}^N \left( \hat{\sigma}_i^\dagger \hat{a} + \hat{\sigma}_i \hat{a}^\dagger \right). \quad (2.20)$$

Importantly, since the Tavis-Cummings Hamiltonian conserves the total number of excitations (i.e. it commutes with the total number operator  $\hat{n} = \hat{a}^\dagger \hat{a} + \sum_{i=1}^N \hat{\sigma}_i^\dagger \hat{\sigma}_i$ ), its eigen-states are a linear superposition of states with the same number of excitations.

In the one-particle manifold, the eigen-states  $|\psi\rangle$  of the coupled Hamiltonian can be hence written as:

$$|\psi\rangle = \alpha|G, 1\rangle + \sum_{i=1}^N c_i|e_i, 0\rangle. \quad (2.21)$$

In the previous equation we have indicated with  $|G, 1\rangle$  the purely cavity eigen-state in which all the dipoles are in their ground state  $|G\rangle$  and there is one photon inside the cavity, and with  $\sum_{i=1}^N c_i|e_i, 0\rangle$  the purely matter state in which the cavity is in its ground state  $|0\rangle$  and each material's dipole is in its first excited state  $|e_i\rangle$  [61]. Additionally, we will suppose the coefficient  $c_i$  to be the same for all the material's excitations (i.e.  $\forall i = 1, \dots, N$ ). This hypothesis implies that the photon excitation is put to each of the  $N$  spatially separated dipoles with an equal probability.

In the one particle manifold the eigen-states of the light-matter system (Hamiltonian 2.21) are split into an upper and lower polariton branch whose energies as a function of the cavity frequency  $\omega_c$  are given by:

$$\begin{aligned} \omega_{LP} &= \frac{\omega_c + \omega_0}{2} - \sqrt{Ng^2 + \left(\frac{\omega_c - \omega_0}{2}\right)^2} \\ \omega_{UP} &= \frac{\omega_c + \omega_0}{2} + \sqrt{Ng^2 + \left(\frac{\omega_c - \omega_0}{2}\right)^2} \end{aligned} \quad (2.22)$$

and a set of  $N - 1$  dark states of material excitations at the energy  $\omega_0$  of the bare dipoles (Figure 2.3). The dark states are dipole-forbidden excitations generated through the strong light-matter coupling and hence invisible to linear spectroscopy<sup>3</sup>. We stress that the dark-states do not have the properties of the states of the uncoupled material, and notably, like the polaritonic states, they can acquire a delocalized character [78] that extends over the whole system.

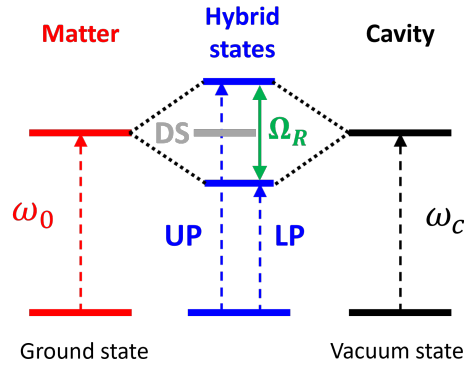


**Figure 2.3: Energy diagram of cavity-mediated light-matter strong coupling.** Strongly coupled material and optical transitions, leading to the formation of the hybrid dipole-allowed polaritonic states UP and LP separated in energy by the Rabi splitting  $\Omega_R$ , and the dipole-forbidden dark states (DS).

<sup>3</sup> This can be proved by calculating the average dipole operator  $\hat{\mu} = |\mu| \sum_{i=1}^N |G_i\rangle \langle e_i| + \text{h.c}$  on the dark states set and by verifying that it gives 0.

The energy of the lower (upper) polariton is smaller (larger) than the energy of the material's transition in free space and the energy splitting between the two polaritonic states in resonant condition (i.e.  $\omega_c = \omega_0$ ) is referred as Rabi frequency ( $\Omega_R$ ):

$$\Omega_R = 2\sqrt{N}g. \quad (2.23)$$

$\Omega_R$  can be therefore exploited to quantify the coupling strength between the cavity and the material oscillator. It is important to stress that the Rabi splitting  $\Omega_R$  scales with the squared root of the number of dipole-like oscillators ( $\sqrt{N}$ ). Therefore, for optically dense materials, such as the solid-state materials studied in this thesis, larger splitting can be achieved by tuning the thickness of the absorbing material within the cavity volume.

From a microscopical point of view, the Rabi splitting can be expressed as [18]:

$$\Omega_R = 2|\boldsymbol{\mu}| \sqrt{\frac{N\omega_c}{2\epsilon_0 V}} \times \sqrt{\langle \hat{n}_{\text{photon}} \rangle + 1}, \quad (2.24)$$

where  $V$  is the volume of the electromagnetic cavity mode, and  $\langle \hat{n}_{\text{photon}} \rangle$  is the number of photons involved in the coupling mechanism. From Equation 2.24 it is therefore clear that strong coupling can occur even with no photon driving, i.e. when the material's dipoles interact with the fluctuations of the confined vacuum EM field, for which  $\langle \hat{n}_{\text{photon}} \rangle = 0$ .

The Tavis-Cummings Hamiltonian (2.21) can be directly diagonalized in the single excitation manifold [79]. The diagonalization procedure yields 2 polariton eigen-states, which are a linear super-positions of optical and dipole excitations:

$$\begin{aligned} |\text{LP}\rangle &= X_0(\omega_c, \omega_0) \sum_{i=1}^N |e_i, 0\rangle + X_c(\omega_c, \omega_0) |G, 1\rangle \\ |\text{UP}\rangle &= X_c(\omega_c, \omega_0) \sum_{i=1}^N |e_i, 0\rangle - X_0(\omega_c, \omega_0) |G, 1\rangle, \end{aligned} \quad (2.25)$$

together with the  $N - 1$  dark states:

$$|\text{DS}\rangle = \sum_{i=1}^N c_i |e_i, 0\rangle. \quad (2.26)$$

The coefficients of the polaritonic wave-functions can be expressed as a function of the frequency of the cavity mode  $\omega_c$  as:

$$\begin{aligned} X_0(\omega_c, \omega_0) &= \frac{1}{\sqrt{1 + \left( \frac{\omega_{\text{LP}}(\omega_c, \omega_0) - \omega_0}{g} \right)^2}} \\ X_c(\omega_c, \omega_0) &= -\frac{1}{\sqrt{1 + \left( \frac{g}{\omega_{\text{LP}}(\omega_c, \omega_0) - \omega_0} \right)^2}}. \end{aligned} \quad (2.27)$$

The coefficients  $|X_0|^2$  and  $|X_c|^2$  of the hybrid wave-functions represent therefore the dipole and photon fractions of the polaritonic branches.

Figure 2.4A presents the calculated eigen-modes of the lower and upper polariton branches (Equation 2.22) as a function of the cavity frequency  $\omega_c$ , which is the tunable parameter in our experiments (Chapter 3). The polariton branches exhibit an anti-crossing feature as a function of the cavity detuning arising from the collective strong coupling [17–20, 22, 23, 33]. The frequency splitting between the two polariton resonances is minimum at resonance ( $\omega_c = \omega_0$ ) and corresponds to the collective Rabi splitting  $\Omega_R = 2g\sqrt{N}$ . The respective dipole and cavity fraction of the lower and upper polaritons are shown in Figure 2.4A, B respectively. We note that, as one polariton branch approaches the photonic dispersion, its cavity fraction  $|X_c|^2$  increases. Likewise, as it approaches the dipoles frequency  $\omega_0$ , its matter fraction  $|X_0|^2$  increases. Therefore, each polariton exhibits more matter-like or photon-like physical properties depending on the exact cavity detuning and the branch it populates. This feature will be extensively discussed in Chapter 6, where we will present the features of a multi-phonon mixing in the quantum material 1T-TaS<sub>2</sub>.

In general, the possibility of tuning the photon-dipole fraction offered by the cavity environment is crucial in the polaritonic field, in particular in processes like polariton Bose-condensation [80–82] or exciton-polariton lasing [83–86].

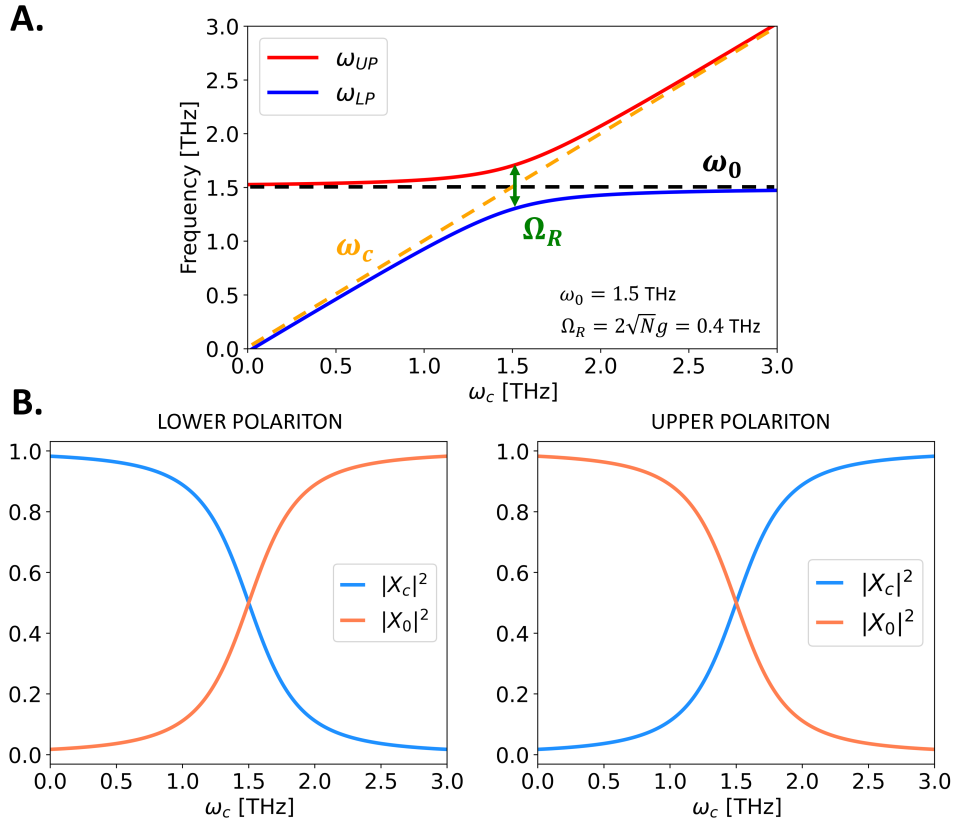


**Figure 2.4: Cavity-dependent properties of polariton modes predicted by the coupled oscillator quantum model.** **A.** Upper and lower polariton branches as a function of the cavity fundamental mode  $\omega_c$  calculated from the coupled oscillator model. The bare cavity and dipole dispersions are shown as dashed lines. **B.** Material (orange) and cavity (light blue) fractions of the lower and upper polariton branch as a function of the cavity detuning. The employed parameters are indicated in A.

## 2.3 ROLE OF DISSIPATIONS ON THE COUPLING STRENGTH

In the previous section we have highlighted the features of the hybrid polariton modes characteristic of the strong coupling regime. In this section we will introduce in a semi-classical way dissipations in the coupled system. In particular, we will show how the presence of dissipations can cause the coherent strong coupling dynamics to evolve into a dissipative-like dynamics characteristic of the weak coupling regime. We will discuss the boundary between strong and weak coupling and show how dissipations of the uncoupled systems can cause the anti-crossing between the hybrid states (Figure 2.4A) to collapse.

Based on Equation 2.22, we would always expect strong coupling between material's excitations and the cavity mode, regardless the value of the collective coupling constant  $g\sqrt{N}$ . However, we see experimentally that most systems require hard efforts to achieve strong coupling. Indeed, high quality mirrors are used in literature to enhance the cavity field within the mode volume and contain the cavity photon [32, 87–90], or highly absorptive materials, as the one studied in the present thesis, are employed. The reasons beyond these efforts lie in the role that dissipations play in the light-matter coupling. Indeed, only by coupling an infinite crystal with no incoherent scattering to an infinite coherent cavity mode we would expect strong coupling to occur at any coupling strength  $g\sqrt{N}$ . In real systems, dissipations of the uncoupled modes (cavity and material) would prevent the coherent energy exchange between the photonic and material degrees of freedom, and ultimately suppress the strong coupling regime when their rate overcomes the Rabi cycle  $1/\Omega_R$ .

Within the coupled oscillator quantum framework (Section 2.2.1), bare dissipations can be introduced through the semi-classical evolution of the uncoupled dipole ( $\sigma(t)$ ) and cavity fields ( $a(t)$ ) [60]:

$$\begin{cases} \partial_t \hat{a}(t) = -i\omega_c \hat{a}(t) + g\sqrt{N}\hat{\sigma}(t) - \gamma_c \hat{a}(t) \\ \partial_t \hat{\sigma}(t) = -i\omega_0 \hat{\sigma}(t) - g\sqrt{N}\hat{a}(t) - \gamma_m \hat{\sigma}(t) \end{cases} \quad (2.28)$$

In the previous coupled equations  $\gamma_c$  ( $\gamma_m$ ) indicates the linewidth of the bare cavity (dipole) mode, setting its lifetime in free space. We clarify that this approximation is semi-classical in the sense that with the fields definitions of Equation 2.28 the commutation relations  $[\hat{a}^\dagger, \hat{a}] = [\hat{\sigma}^\dagger, \hat{\sigma}] = 1$  is not satisfied. On the basis of this dissipative evolution we get indeed  $[\hat{a}^\dagger, \hat{a}] \sim e^{-2\gamma_c t}$  and  $[\hat{\sigma}^\dagger, \hat{\sigma}] \sim e^{-2\gamma_m t}$ , which converge to 1 for  $t \gg \frac{1}{\gamma_{c,m}}$ , i.e. for long-living uncoupled resonances.

Setting the initial conditions  $a(t=0) = a(0)$  and  $\sigma(t=0) = \sigma(0)$ , the solutions of the coupled field equations 2.28 read [60]:

$$\begin{aligned} a(t) = & \frac{(\omega_c - \widetilde{\omega}_{LP} - i\gamma_c) a(0) + i\sqrt{N}g\sigma(0)}{\widetilde{\omega}_{UP} - \widetilde{\omega}_{LP}} e^{-i\widetilde{\omega}_{UP}t} + \\ & + \frac{(-\omega_c + \widetilde{\omega}_{UP} + i\gamma_c) a(0) - i\sqrt{N}g\sigma(0)}{\widetilde{\omega}_{UP} - \widetilde{\omega}_{LP}} e^{-i\widetilde{\omega}_{LP}t}, \end{aligned} \quad (2.29)$$

$$\begin{aligned} \sigma(t) = & \frac{(\omega_0 - \widetilde{\omega}_{LP} - i\gamma_m) \sigma(0) - i\sqrt{N}ga(0)}{\widetilde{\omega}_{UP} - \widetilde{\omega}_{LP}} e^{-i\widetilde{\omega}_{UP}t} + \\ & + \frac{(-\omega_0 + \widetilde{\omega}_{UP} + i\gamma_m) \sigma(0) + i\sqrt{N}ga(0)}{\widetilde{\omega}_{UP} - \widetilde{\omega}_{LP}} e^{-i\widetilde{\omega}_{LP}t} \end{aligned} \quad (2.30)$$

In the previous equations the temporal evolution of the coupled fields is set by the complex frequencies  $\tilde{\omega}_{\text{LP}}$  and  $\tilde{\omega}_{\text{UP}}$ . The latter correspond to the eigen-modes of the dissipative-like Tavis-Cummings Hamiltonian:

$$\hat{H}_{\text{diss}} = (\omega_c - i\gamma_c) \hat{a}^\dagger \hat{a} + \sum_{i=1}^N (\omega_0 - i\gamma_m) \hat{\sigma}_i^\dagger \hat{\sigma}_i + g \sum_{i=1}^N (\hat{\sigma}_i^\dagger \hat{a} + \hat{\sigma}_i \hat{a}^\dagger), \quad (2.31)$$

where the finite lifetimes of photons and material's excitations have been introduced as an imaginary self-energy of the bare modes:

$$\begin{cases} \omega_0 \rightarrow \omega_0 - i\gamma_m \\ \omega_c \rightarrow \omega_c - i\gamma_c \end{cases}. \quad (2.32)$$

The fact that an imaginary self energy will result in gain or decay of a the quantum coupled state can be seen by looking at the time evolution of the coupled fields (Equations 2.29, 2.30): while quantum phase oscillates at the frequency of the eigen-modes, the amplitude can increase or decrease according to any imaginary part of the energy.

From the eigen-modes  $\tilde{\omega}_{\text{LP,UP}}$  of the dissipative-like Hamiltonian 2.31 we can hence derive the collective Rabi splitting as a function of the bare decaying rates ( $\gamma_c, \gamma_m$ ):

$$\tilde{\Omega}_{\text{R}} = \tilde{\omega}_{\text{UP}}(\omega_c = \omega_0) - \tilde{\omega}_{\text{LP}}(\omega_c = \omega_0) = \sqrt{4Ng^2 - (\gamma_c - \gamma_m)^2}. \quad (2.33)$$

To see directly in the time domain how bare dissipations affect the coherent Rabi cycle characteristic of the strong coupling regime, we evaluate the time-dependent emission of the coupled cavity field [60]:

$$I_{\text{cav}}(t) = \langle \hat{a}^\dagger(t) \hat{a}(t) \rangle = \frac{4\sigma(0)^2 Ng^2}{|\tilde{\Omega}_{\text{R}}|^2} e^{-(\gamma_c + \gamma_m)t} \sin\left(\frac{\tilde{\Omega}_{\text{R}}}{2}\right) \sin\left(\frac{\tilde{\Omega}_{\text{R}}^*}{2}\right). \quad (2.34)$$

Note that in the previous expression we have considered a non-driven cavity (i.e.  $a(0) = 0$ ) in resonant condition ( $\omega_c = \omega_0$ ). The calculated emission spectra for a representative material's mode in the THz range is presented in Figure 2.5 (oscillators parameters inside the legend).

We note that the dissipations cause an exponential decay of the beating Rabi modulation occurring at a rate  $1/\Omega_{\text{R}}$  and characteristic of the strong coupling regime. The temporal extent of this coherent energy exchange, which would be infinite in a loss-less cavity, is hence exponentially suppressed by the bare dissipations. This exponential damping of the coherent beating dynamics can make the hybrid system to fall in the weak coupling regime in the limit  $\Omega_{\text{R}} \ll \gamma_c, \gamma_m$ .

### 2.3.1 STRONG-TO-WEAK COUPLING TRANSITION

Recalling the expression of the collective Rabi splitting in dissipative systems  $\tilde{\Omega}_{\text{R}}$  (Equation 2.33), we can identify the boundaries between the strong and the weak coupling regimes.

Importantly, we highlight that the strong light-matter coupling is only achieved when  $4Ng^2 > (\gamma_c - \gamma_m)^2$ , which yields a real value of the collective Rabi splitting.

In the weak coupling regime, for which  $4Ng^2 < (\gamma_c - \gamma_m)^2$ ,  $\tilde{\Omega}_{\text{R}}$  becomes purely imaginary and therefore does not result in any measurable energy splitting. In this

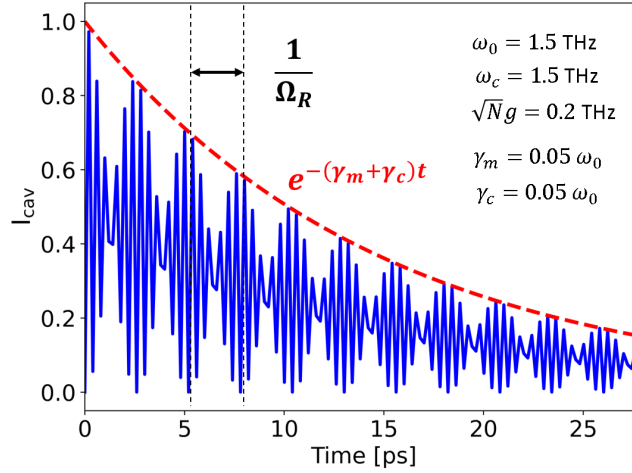


**Figure 2.5: Calculated time-dependent emission of a dissipative THz cavity.** Time-dependent emission spectrum of a non-driven THz cavity calculated from Equation 2.34 showing the exponential damping of the coherent Rabi beating. Parameters of the cavity and material’s oscillators are indicated in legend. The cavity emission has been normalized by its maximum value, occurring at  $t = 0$  ps.

case, the coupling is mapped in a modification of the lifetime of the coupled excitations. In Chapter 6, we will use this feature as a weak coupling signature in the quantum material 1T-TaS<sub>2</sub>.

As the collective coupling  $g\sqrt{N}$  is directly related to the oscillator strength of the targeted excitation (Equation 2.18), the coupling regime is essentially determined by the interplay between the dipolar oscillator strength  $|\mu|$  and the photon/dipole linewidths. Since for our THz cavities (Chapter 3)  $|\mu|$  and the excitation’s linewidth  $\gamma_m$  are fixed and determined by the active material and by the cavity temperature, the coupling regime is mainly governed by the cavity Q factor, which ultimately dictates the photon lifetime  $1/\gamma_c$  (Section 2.1.1).

The effect of Q on the polariton eigen-energies and linewidths is presented in Figure 2.6. The imaginary and real parts of the complex eigen-modes of the dissipative-like Hamiltonian 2.31, corresponding to the polariton broadening and frequency, are shown in Figure 2.6A and B respectively. Plots have been made for a THz cavity in resonant conditions, i.e. for  $\omega_c = \omega_0$ .

The dependence on the cavity quality factor marks two distinct regimes of the light-matter coupling.

- For low-Q cavities, in the weak coupling regime, there is no polariton splitting and hence the system can be still described in terms of the bare dipoles and photons. Nevertheless, their respective linewidths are modified by the coupling with the cavity field, as illustrated in Figure 2.6A. We highlight that, within the weak coupling boundary, the dipole linewidth increases with the cavity Q factor, exhibiting an enhanced emission rate that can be rationalized by the Purcell effect of atomic and molecular physics [13–16]. The Purcell effect predicts indeed a linear scaling of the weakly coupled material’s excitation ( $\gamma_m$ ) as a function of the Q factor of the resonator:

$$\gamma_m(Q) = \gamma_m + F_P Q. \quad (2.35)$$

In the previous equation  $F_P = \frac{3}{4\pi^2 V} \frac{c}{n\omega_c}$  denotes the Purcell factor. Similar trends have been reported in literature also in semiconductor materials weakly coupled

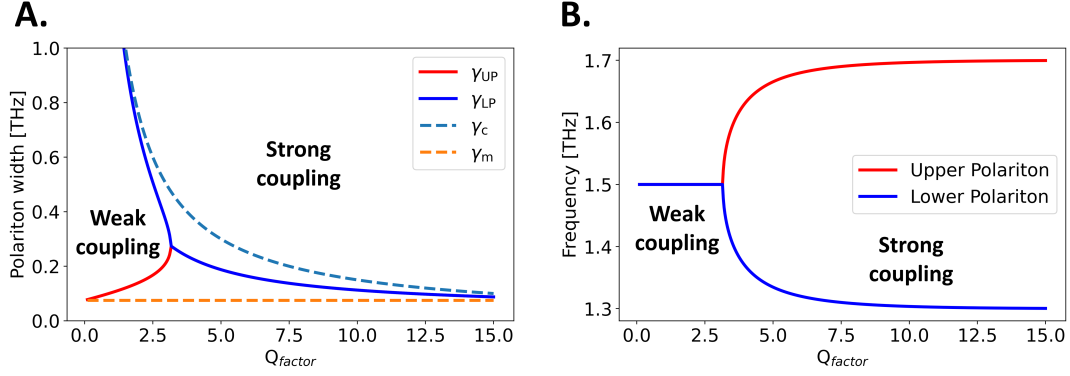


**Figure 2.6: Weak-to-strong coupling transition as a function of the cavity quality factor.** **A.** Calculated polaritons linewidths as a function of the cavity Q factor from the dissipative-like Hamiltonian 2.31. The linewidth of the uncoupled dipoles ( $\gamma_m$ ) and photons ( $\gamma_c$ ) are plotted as dashed lines. **B.** Corresponding evolution of the polaritons frequencies as a function of the Q factor. The polariton splitting marks the weak-to-strong coupling transition. Employed parameters:  $\omega_c = \omega_0 = 1.5$  THz,  $\gamma_m = 0.05\omega_0$ ,  $g\sqrt{N} = \frac{\Omega_R}{2} = 0.2$  THz.

to vacuum cavity fields [23]. Importantly, as highlighted in Figure 2.7, the cavity-induced renormalization of the dipole's linewidth scales with the collective coupling strength  $g\sqrt{N}$ . Indeed, at a fixed Q factor of the cavity,  $\gamma_m$  is more efficiently modified at higher light-matter couplings.

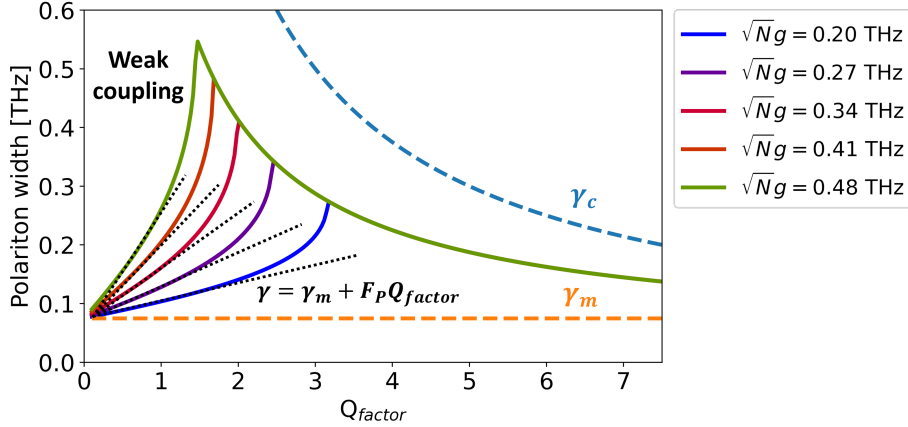


**Figure 2.7: Linewidth enhancement in the weak coupling regime at different coupling strengths.** Dependence of the linewidth of the weakly coupled dipoles on the Q factor for different couplings  $g\sqrt{N}$ . A broadening enhancement (black dashed line) is observed at higher couplings. Employed parameters:  $\omega_c = \omega_0 = 1.5$  THz,  $\gamma_m = 0.05\omega_0$ .

- Conversely, in the strong coupling regime, the eigen-modes splits into two values and the polaritonic concepts presented in Section 2.2.1 are necessary to describe the coupled system. Within this dissipative model, in the strong coupling regime the upper and lower polariton linewidths equal to the average value of the uncoupled dipole and photon linewidths and, hence, decrease at higher Q factors.

From the expression of the dissipation-dependent Rabi splitting (Equation 2.33), it should be highlighted that a difference in the decoherence rates between the dipoles and the cavity photon ( $|\gamma_c - \gamma_m|$ ) causes a reduction of the light-matter coupling. In principle, even if the two uncoupled resonances have large but similar broadening, a Rabi splitting is predicted by the model. However, we must stress that, in order to spectrally resolve the polaritonic states, their individual linewidths has to be less than the splitting between them. This evidence gives therefore two requirements that has to be fulfilled for achieving strong coupling:

$$\begin{cases} |\gamma_c - \gamma_m| < g\sqrt{N} \\ \gamma_c, \gamma_m < g\sqrt{N} \end{cases} . \quad (2.36)$$

The first condition indicates that the effective Rabi splitting can be reduced by the lifetime mismatch between the uncoupled states. The second condition is the requirement that the polariton states has to be spectrally distinguishable in the Fourier domain. The conditions of Equation 2.36 will be exploited in the present thesis to verify the achievement of the strong coupling regime in the studied materials.

## 2.4 MODELLING LINEAR RESPONSE OF LIGHT-MATTER HYBRIDS

In the previous section we have developed the quantum mechanical framework underlying the strong light-matter coupling in both dissipative and non-dissipative cavities. In this section we extend the coupled oscillator model to a cavity response theory in both the classical and the quantum regimes. In particular, we will present how the cavity spectral response, which is our experimental observable, can be derived in a classical Transfer-matrix formalism and in a fully quantum Input-Output theory. Importantly, we will demonstrate that the predictions of the two response theories coincide in a linear regime. This is the regime of non-driven cavities and where the coupling between the optical and material's degrees of freedom can be considered linear.

### 2.4.1 A CLASSICAL APPROACH: THE TRANSFER-MATRIX FORMALISM

The Transfer-matrix is a formalism commonly used in optics to analyse the propagation of electromagnetic waves through a stratified medium characterized by layers of materials with different refractive properties [91–93]. In this classical framework, the transmission and reflection coefficients at the interface between two layers with different optical constants are described by the Fresnel equations and the overall response of the cavity-material hybrid will be the result of the linear interference between multiple reflections and transmissions of light at all the interfaces.

Let us firstly consider the simplest system constituted of two different media with an infinite interface (Figure 2.8A). We will denote with  $n_0$  and  $n_1$  the refractive indexes of the two media. The incident and the transmitted light through the material can be linked through the Snell law:  $n_0 \sin(\theta_0) = n_1 \sin(\theta_1)$ . The complex amplitude of the electric field at a fixed position  $z$  can be expressed as:

$$E(z) = E^+(z) + E^-(z), \quad (2.37)$$

where  $E^+(z)$  and  $E^-(z)$  represent individually electro-magnetic waves travelling along the  $+z$  and the  $-z$  directions, respectively. We can hence define a two dimensional vector  $\Phi$  built upon these complex electric field amplitudes:

$$\Phi(z) = \begin{bmatrix} E^+(z) \\ E^-(z) \end{bmatrix} \quad (2.38)$$

based on which all the presented Transfer-matrix calculations will be performed [69].

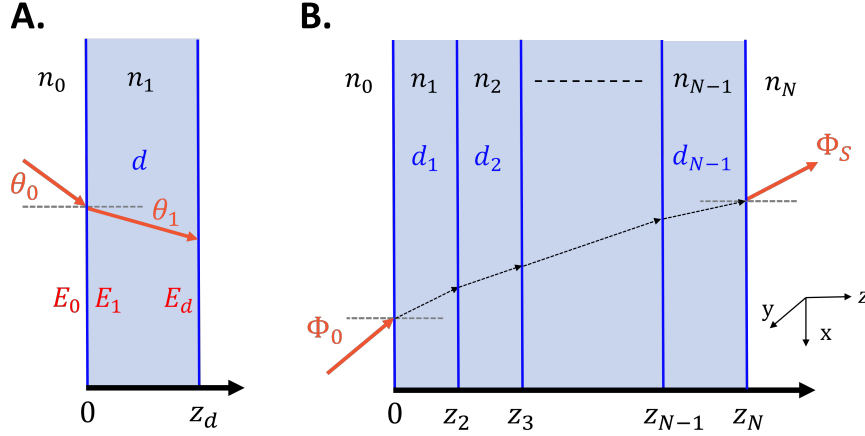


**Figure 2.8: Transmission through a layered structure included in Transfer-matrix simulations.** Transmission through a two-media system (A) and a multilayer system (B).  $d_j$  and  $n_j$  indicates respectively the thickness and the complex refractive index of the  $j^{\text{th}}$  layer.

#### 2.4.1.1 Transfer-matrix at material's interfaces

Firstly, let us consider the light propagating from a medium with refractive index  $n_0$  into a medium having  $n_1$  refractive index. Note that the refractive indexes are complex quantities, hence taking into account both the inductive and the dissipative response of the materials. At the boundaries between the two media, Fresnel's equations apply:

$$r_{0,1} = \begin{cases} \frac{n_0 \cos \theta_0 - n_1 \cos \theta_1}{n_0 \cos \theta_0 + n_1 \cos \theta_1} & (\text{s-pol}) \\ \frac{n_0 \cos \theta_1 - n_1 \cos \theta_0}{n_1 \cos \theta_0 + n_0 \cos \theta_1} & (\text{p-pol}) \end{cases} \quad (2.39)$$

$$t_{0,1} = \begin{cases} \frac{2n_0 \cos(\theta_0)}{n_0 \cos \theta_0 + n_1 \cos \theta_1} & (\text{s-pol}) \\ \frac{2n_0 \cos(\theta_0)}{n_1 \cos \theta_0 + n_0 \cos \theta_1} & (\text{p-pol}) \end{cases} \quad (2.40)$$

where  $r_{0,1}$  ( $t_{0,1}$ ) is the complex reflection (transmission) coefficient at the interface. The s (respectively p) polarization corresponds to an EM wave having its electric field oscillating perpendicular (respectively parallel) to the plane of incidence, defined by the incident ray and the normal to the interface. Clearly, the two polarization cases become identical at normal incidence, i.e. when  $\theta_0 = \theta_1 = 0$ .

In order to obtain the full interference pattern we have also to consider the backwards propagating wave, i.e. the field incident from the medium  $n_1$  into the medium  $n_0$  at the same interface. In this configuration, the reflection and transmission coefficients (respectively  $r_{1,0}$  and  $t_{1,0}$ ) are linked through the Fresnel's law to  $r_{0,1}$  and  $t_{0,1}$  by the relations:

$$r_{1,0} = -r_{0,1} \quad t_{1,0} = \frac{1 - r_{0,1}^2}{t_{0,1}}, \quad (2.41)$$

which imply:

$$r_{1,0}r_{0,1} + t_{1,0}t_{0,1} = 1 \quad (2.42)$$

As depicted in Figure 2.8A, let us label with  $E_0$  and  $E_1$  the longitudinal electric field amplitude at the two boundaries of the material's interface. By considering the EM wave incident on the interface from the  $+z$  direction we will have  $E_1^- = 0$ . Therefore, the reflection and transmission coefficients can be expressed as the ratios between the electric field amplitudes at each side of the interface:

$$r_{0,1} = \frac{E_0^-}{E_0^+} \quad t_{0,1} = \frac{E_1^+}{E_0^+}. \quad (2.43)$$

Similarly, for the back-travelling wave incident from the  $-z$  direction (for which  $E_0^+ = 0$ ), we get:

$$r_{1,0} = \frac{E_1^+}{E_1^-} \quad t_{1,0} = \frac{E_0^-}{E_1^-}. \quad (2.44)$$

From the expressions of the complex reflectivity and transmittivity (Equations 2.43, 2.44) and considering the full interference pattern, i.e. waves incident from both  $\pm z$  directions, we can write the electric field in the  $n_0$  medium as a function of the electric in the  $n_1$  medium through the following "interface Transfer-matrix" equation:

$$\begin{bmatrix} E_0^+ \\ E_0^- \end{bmatrix} = \begin{bmatrix} \frac{1}{t_{0,1}} & -\frac{r_{1,0}}{t_{0,1}} \\ \frac{r_{0,1}}{t_{0,1}} & t_{1,0} - \frac{r_{0,1}r_{1,0}}{t_{0,1}} \end{bmatrix} = \begin{bmatrix} E_1^+ \\ E_1^- \end{bmatrix} \quad (2.45)$$

By recalling Equation 2.41, the above single-layer Transfer-matrix equation can be simplified to:

$$\begin{bmatrix} E_0^+ \\ E_0^- \end{bmatrix} = \frac{1}{t_{0,1}} \begin{bmatrix} 1 & r_{0,1} \\ r_{0,1} & 1 \end{bmatrix} = \begin{bmatrix} E_1^+ \\ E_1^- \end{bmatrix}, \quad (2.46)$$

which, recalling the definition of the  $\Phi$ -vector in Equation 2.38, becomes:

$$\Phi_0 = I_{0,1} \Phi_1 \quad (2.47)$$

with

$$\Phi_0 = \begin{bmatrix} E_0^+ \\ E_0^- \end{bmatrix} \quad \Phi_1 = \begin{bmatrix} E_1^+ \\ E_1^- \end{bmatrix} \quad (2.48)$$

and

$$I_{0,1} = \frac{1}{t_{0,1}} \begin{bmatrix} 1 & r_{0,1} \\ r_{0,1} & 1 \end{bmatrix}. \quad (2.49)$$

$I_{0,1}$  is therefore the Transfer-matrix at the interface of a single-layer, where the refractive properties changes from  $n_0$  to  $n_1$ . The previous matrix representation will be exploited in the following to derive the full Transfer-matrix of the multilayer cavity-like structure, where all the single-layer interferences will be taken into account (Figure 2.8B).

### 2.4.1.2 Transfer-matrix for free propagation

The next step towards the derivation of the multi-layer Transfer-matrix is getting the matrix expression describing the free field propagation between adjacent dielectric interfaces.

Let us hence consider light propagating in the medium  $n_1$  within a distance  $d$ , as illustrated in Figure 2.8A. Labelling with  $E_d$  the electric field amplitude after the free propagation inside the medium  $n_1$ , we will have:

$$\begin{bmatrix} E_1^+ \\ E_1^- \end{bmatrix} = \begin{bmatrix} e^{-in_1kd\cos(\theta_1)} & 0 \\ 0 & e^{-in_1kd\cos(\theta_1)} \end{bmatrix} = \begin{bmatrix} E_d^+ \\ E_d^- \end{bmatrix}, \quad (2.50)$$

where  $k$  is the vacuum wavevector. The propagation equation 2.50 can be equivalently written in the  $\Phi$ -vector form as:

$$\Phi_1 = L_{1,d}\Phi_d. \quad (2.51)$$

Here

$$L_{1,d} = \begin{bmatrix} e^{-in_1kd\cos(\theta_1)} & 0 \\ 0 & e^{-in_1kd\cos(\theta_1)} \end{bmatrix} \quad (2.52)$$

is defined as the Transfer-matrix of free field propagation for a distance  $d$  within a material with complex refractive index  $n_1$ .

Combining the interface propagation (Equation 2.47) with the free field propagation within dielectric boundaries (Equation 2.51) we get:

$$\Phi_0 = I_{0,1}L_{1,d}\Phi_d = M_{0,1,d}\Phi_d, \quad (2.53)$$

where  $M_{0,1,d} = I_{0,1}L_{1,d}$  is the Transfer-matrix describing the single-layer structure of Figure 2.8A. This matrix structure is the basic element for constructing the optical response of a multilayer system. The optical response of the multilayer system will be discussed in the following section.

### 2.4.1.3 Transfer-matrix of a multilayer system

As outlined in Figure 2.8B, a multilayer system, as can be schematized the cavities employed in this thesis, is constructed by stacking a number of individual single-layer units analogous to the one shown in Figure 2.8A.

The whole system contains  $N$  layers, each of which has a finite thickness  $d_j$  and a complex refractive index  $n_j$  ( $j = 1, \dots, N$ ). This  $N$ -layer structure is surrounded by a medium  $n_0$  on the left, and a medium  $n_{N+1}$  on the right, both of which are semi-infinite. The interference within the whole multilayer structure can be described by the  $\Phi$ -vector equation:

$$\Phi_0 = S\Phi_S, \quad (2.54)$$

where

$$S = \left( \prod_{j=1}^N M_{j-1,j,d_j} \right) I_{N,N+1} = \left( \prod_{j=1}^N I_{j-1,j} L_{j,d_j} \right) I_{N,N+1}. \quad (2.55)$$

Here  $\Phi_0$  ( $\Phi_S$ ) is the  $\Phi$ -vector at the left (right) boundary of the  $N$ -layer system, as labelled in Figure 2.8B.  $S$  is instead the overall Transfer-matrix of the multilayer system accounting for the interferences at each dielectric boundary.

#### 2.4.1.4 Optical properties of the multilayer system

Once the general Transfer-matrix  $S$  for a multi-layer system has been constructed, it is straightforward to obtain the linear optical properties, i.e. transmission and reflection of the whole system. The full  $\Phi$ -vector equation 2.54 explicitly reads:

$$\begin{bmatrix} E_0^+ \\ E_0^- \end{bmatrix} = \begin{bmatrix} S_{11} & S_{12} \\ S_{21} & S_{22} \end{bmatrix} = \begin{bmatrix} E_S^+ \\ E_S^- \end{bmatrix}, \quad (2.56)$$

where  $S_{11}$ ,  $S_{12}$ ,  $S_{21}$ ,  $S_{22}$  are the four matrix elements of the Transfer-matrix  $S$ . The latter depend on the thickness  $d_j$  and on the complex refractive index  $n_j$  of each layer.

In order to obtain the linear response of the full multilayer structure, let us consider a s-polarized optical wave entering the stacked system from the left boundary and leaving it through the right interface. In this case,  $E_S^- = 0$  because there is no back-travelling light after the right boundary. The total transmitted  $t_s$  and reflected  $r_s$  amplitudes are therefore:

$$t_s = \frac{E_S^+}{E_0^+} = \frac{1}{S_{11}} \quad r_s = \frac{E_0^-}{E_0^+} = \frac{S_{21}}{S_{11}}. \quad (2.57)$$

As  $r_s$  and  $t_s$  contain both the real and imaginary parts of the amplitude ratios, they actually characterize both the amplitude and the phase response of the layered structure. If we focus only on the intensity, the full spectral transmission  $T(\omega)$  and reflection  $R(\omega)$  can be calculated as:

$$T(\omega) = |t_s(\omega)|^2 = \left| \frac{1}{S_{11}(\omega)} \right|^2 \quad R(\omega) = |r_s(\omega)|^2 = \left| \frac{S_{21}(\omega)}{S_{11}(\omega)} \right|^2, \quad (2.58)$$

where the  $\omega$  dependence is inherited from the frequency-dependent refractive indexes of the single layers ( $n_j(\omega)$ ). The Transfer-matrix formalism hence allows to predict the full optical response of a multilayer cavity, having in input only the cavity geometry (i.e. the layer thicknesses) and the complex dielectric constants of the constituting layers.

#### 2.4.1.5 Comparison with the quantum oscillator model

In the following we demonstrate that in the linear regime, i.e. for a non-driven cavity with linear light-matter coupling [60, 94, 95], the polariton features extracted from the coupled oscillator quantum model (Section 2.2.1) match with the classical predictions of the Transfer-matrix method. The Transfer-matrix formalism can be hence considered as a "local" dielectric model [60], where the overlap integral between the material and photon wave-functions, which determines the coupling strength within the cavity (Equation 2.18), is taken into account through the refractive properties of the cavity constituents and through the boundary conditions set by the cavity geometry.

For this comparison we will exploit the model Terahertz cavity setting presented in Figure 2.9A, where an absorber's slab of thickness  $d_m$  is put within two thin gold mirrors ( $d_{Au} = 2$  nm,  $n_{Au}(\omega)$  from literature [96]). In this model setting, the cavity frequency is set by the mirrors distance which in turns determines the thickness of the air spacer  $d_{air}$ . For simplicity, we will model the material's optical response  $n_m(\omega)$  as a strongly damped Lorentzian oscillator [97]:

$$n_m(\omega) = \sqrt{1 + \frac{\omega_p^2}{\omega_0^2 - \omega^2 - i\omega\gamma_m}}, \quad (2.59)$$

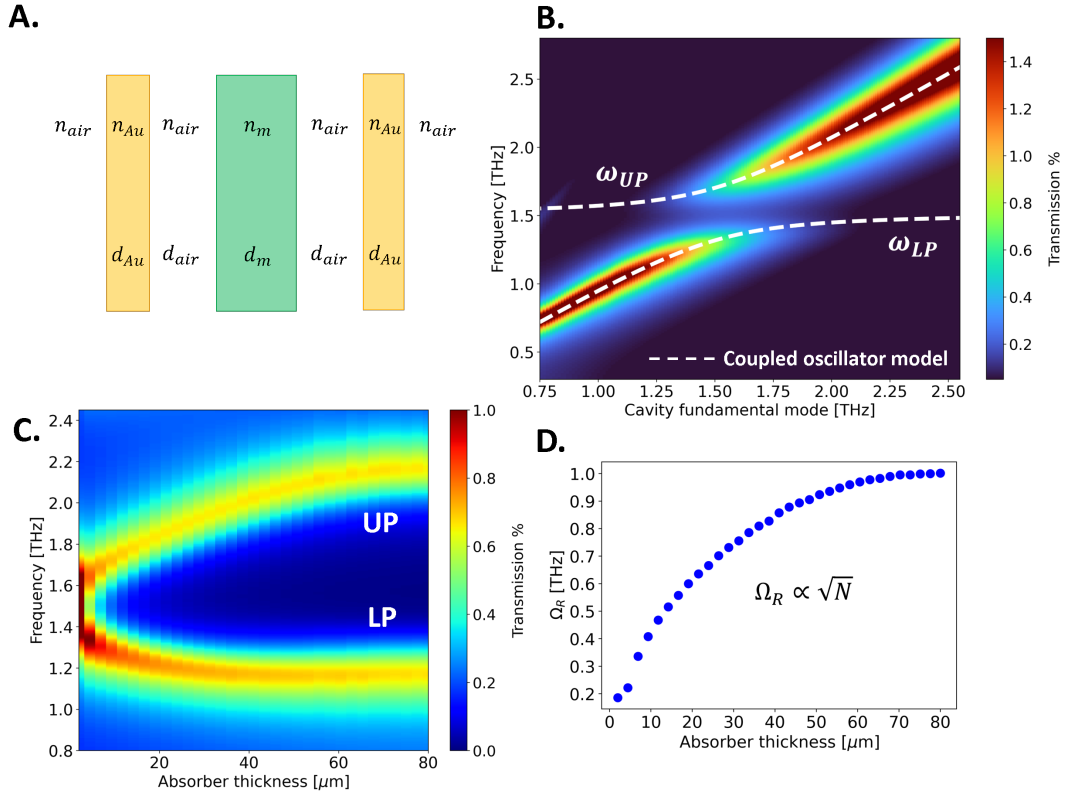


**Figure 2.9: Transfer-matrix calculations of the linear response of a hybrid THz cavity and comparison with the coupled oscillator model.** **A.** Schematic multilayer structure of the THz cavity employed in the classical simulations. **B.** Dispersion of the polariton transmission as a function of the cavity frequency simulated with the classical Transfer-matrix method. The eigen-frequencies of the upper and lower polaritons estimated from the coupled oscillator model (Equation 2.22) are plotted as white dashed lines. **C.** Polariton transmission simulated with the Transfer-matrix method as a function of the absorber’s thickness for a fixed cavity frequency  $\omega_c = 1.5$  THz. Note that, in the different simulations, the material thickness is compensated by a reduction of the mirrors distance in order to maintain the resonance condition of the cavity unaltered. **D.** Rabi splitting as a function of the absorber’s thickness estimated from the spectral responses in C. A square root scaling, analogous to the Tavis-Cummings quantum formulation, is observed.

where we have representatively set  $\omega_0 = 1.5$  THz,  $\omega_p = 0.9$  THz, and  $\gamma_m = 0.05\omega_0$ .

The polariton dispersion obtained with the Transfer-matrix method is presented in Figure 2.9B, where the simulated spectral transmission is plotted as a function of the cavity fundamental frequency. Simulations have been made at normal incidence ( $\theta_0 = 0$ ), which is the geometry adopted for all the experiments presented in the thesis.

We note that, by matching the Rabi splitting of the coupled oscillator model ( $\Omega_R = 2g\sqrt{N}$ ) to the splitting obtained on resonance with the Transfer-matrix method, the dispersion of the polariton eigen-modes (Equation 2.22) matches the simulated transmission peaks. This crucial result implies that, within a linear framework, the bright peaks detected in transmission are associated to the spectral response of the hybrid modes originating from the quantum superposition with the cavity field. This evidence is fundamental since the linear transmission will be the experimental observable adopted in the thesis to track the strong coupling regime in different samples.

Importantly, the splitting between the upper and lower polariton branches simulated with the Transfer-matrix method increases with the active layer thickness  $d_m$  (Figure 2.9C). The Rabi splitting  $\Omega_R$  as a function of the absorptive material thickness, estimated from the linear transmission spectra of Figure 2.9C, is presented in Figure 2.9D. We highlight that the estimated  $\Omega_R$  scales with the square root of the thickness of the layer embedded within the cavity. This gives a further connection between the classical Transfer-matrix method and the quantum Tavis-Cummings model. Indeed, the Tavis-Cummings model predicts, in the linear case, a scaling of the Rabi splitting as  $\sqrt{N}$ , being  $N$  the number of emitters within the cavity volume (Equation 2.24). In a condensed matter rephrasing of the Rabi interaction, the number of emitters should be hence replaced by the total oscillator strength of the active material, which indeed scales with its thickness.

#### 2.4.2 A QUANTUM APPROACH: THE INPUT-OUTPUT FORMALISM

In the previous section we have proved that in a linear regime the classical Transfer-matrix formalism reproduces the spectral response of the hybrid polaritons.

In this section we present a fully quantum formalism, the Input-Output theory IO [98–103], which provides a direct connection between the microscopic dynamics of the hybrid cavities and their time and frequency domain signals measured in experiments.

In a nutshell, the Input-Output formalism allows for the treatment of the properties of light-matter hybrids beyond their coupling to the photonic ground state. In particular, by treating the injection of photons into the cavity and their ejection through a simple linear coupling, which is described quantum-mechanically as a beam splitter operator, it is possible to describe the time evolution of the optical properties of the light-matter hybrids. IO theory allows for a formal description of the injection of photons in cavity as well as for their emission, which is treated at the same level of approximation.

Being a fully quantum theory, the IO formalism can be easily extended to describe non-linear couplings in driven cavities, where instead the linear Transfer-matrix method can't be applied.

In the following we provide a brief review of the IO theory and utilize it to derive the fully quantum equation of motion for the cavity photonic field in the presence of a resonant material's excitation. We will then apply the quantum formalism to obtain the transmission spectrum of the polaritonic modes, i.e. our experimental observable, and prove that in a linear regime it matches the classical Transfer-matrix results.

To model the material's within the cavity, let us consider a set-up of  $N$  independent dipole-allowed excitations strongly coupled to a single mode of a co-planar Fabry-Pérot resonator. The resonator modes are weakly coupled to the external bath EM modes on the left and right-hand sides of the cavity transverse direction. The total Hamiltonian of the hybrid system can be expressed as the sum of three distinct contributions [98, 99]:

$$\hat{H} = \hat{H}_c + \hat{H}_m + \hat{H}_{int}. \quad (2.60)$$

$\hat{H}_c$  and  $\hat{H}_m$  are the Hamiltonians modelling the bare cavity and material dynamics weakly coupled to their corresponding external baths.  $\hat{H}_{mc}$  describes instead the light-matter interaction within the cavity volume (cfr Equation 2.17). Each term of the full Hamiltonian of the hybrid cavity ( $\hat{H}$ ) will be described in the following sections.

## 2.4.2.1 Equation of motion of the empty cavity operator

Let us consider a planar Fabry-Pérot cavity, as the one employed in our experiments, with a single relevant mode. We will suppose the reshaped EM modes within the cavity volume to be weakly-coupled to the EM bath occupying the space external to the cavity. Having a weak coupling with the external bath implies that only linear transmission of photons from the vacuum to the cavity (and vice-versa) is allowed [98, 103]. We will suppose the cavity to have a transverse length  $L$  along the  $z$  axis, and the vacuum electromagnetic modes to live in the semi-infinite spaces to the left and right-side of the cavity. The empty cavity dynamics is governed by the Hamiltonian [98]:

$$\begin{aligned} \hat{H}_c = & \omega_c \hat{a}^\dagger \hat{a} + \int_{-\infty}^{+\infty} d\omega' \omega' \left[ \left( \hat{a}_{\omega'}^L \right)^\dagger \hat{a}_{\omega'}^L + \left( \hat{a}_{\omega'}^R \right)^\dagger \hat{a}_{\omega'}^R \right] + \\ & + \int_{-\infty}^{+\infty} d\omega' \sqrt{\frac{\gamma_c(\omega')}{4\pi}} \left[ \left( \hat{a}_{\omega'}^L \right)^\dagger \hat{a} + \left( \hat{a}_{\omega'}^R \right)^\dagger \hat{a} + \text{h.c.} \right]. \end{aligned} \quad (2.61)$$

Here  $\hat{a}$  is the annihilation operator of the single cavity mode of frequency  $\omega_c$ ,  $\hat{a}_\omega^{L(R)}$  annihilates the left (right) photons of the bath of frequency  $\omega$ , and  $\kappa(\omega)$  is the weak coupling constant with the vacuum EM bath. This is assumed to be independent on the cavity side<sup>4</sup>. The Heisenberg equation of motion connecting the external EM field operators to the cavity mode operator  $\hat{a}(t)$  reads [98]:

$$\partial_t \hat{a}_\omega^L(t) = -i\omega \hat{a}_\omega^L(t) - i\sqrt{\frac{\gamma_c(\omega)}{4\pi}} \hat{a}(t). \quad (2.62)$$

The latter is a linear equation and can be solved given the initial conditions on the fields. Let us now suppose that the cavity-bath coupling is frequency-independent, i.e.  $\gamma_c(\omega) = \gamma_m$ . This assumption is reasonable, as the cavity mode interacts significantly only with a small subset of the external vacuum EM modes, where the variation of  $\gamma_c(\omega)$  is negligible [104]. We highlight that in this fully quantum formalism the coupling constant between the cavity field and the external EM bath plays an analogous role to the photon dissipation rates ( $\gamma_c$ ) introduced semi-classically in the Rabi model (see Section 2.3).

In the case of frequency-independent coupling with the external bath, the temporal evolution of the cavity photon operator  $\hat{a}(t)$  reads:

$$\partial_t \hat{a}(t) = -i \left( \omega_c - i\frac{\gamma_c}{2} \right) \hat{a}(t) - \sqrt{\frac{\gamma_c}{2}} \hat{a}_{\text{in}}(t). \quad (2.63)$$

Here we have introduced the input electromagnetic field operator  $\hat{a}_{\text{in}}(t)$  [98]:

$$\hat{a}_{\text{in}}(t) = \hat{a}_{\text{in}}^L(t) + \hat{a}_{\text{in}}^R(t), \quad (2.64)$$

being

$$\hat{a}_{\text{in}}^{L(R)}(t) = \frac{i}{\sqrt{2\pi}} \int_{-\infty}^{+\infty} d\omega' e^{-i\omega'(t-t_i)} \hat{a}_{\omega'}^{L(R)}(t_i) \quad t > t_i. \quad (2.65)$$

The input operators represent the optical driving of the cavity at a certain time  $t$  due to the past external electromagnetic state described by the operators  $\hat{a}_\omega^{L(R)}(t_i)$ . By following the same procedure, we can obtain also the effective dynamics of the cavity mode in terms of the external EM field at future times  $t_f > t$ :

$$\partial_t \hat{a}(t) = -i \left( \omega_c + i\frac{\gamma_c}{2} \right) \hat{a}(t) - \sqrt{\frac{\gamma_c}{2}} \hat{a}_{\text{out}}(t) \quad t < t_f. \quad (2.66)$$

<sup>4</sup> We have introduced also the unphysical negative frequencies of the external EM field modes just to simplify the mathematical treatment. This has no practical consequences, since in a weak coupling approximation the relevant EM modes are those near-resonant with the cavity mode [99].

Here, in analogy with the input operators of Equation 2.65, we have introduced the cavity output operators as:

$$\hat{a}_{\text{out}}(t) = \hat{a}_{\text{out}}^{\text{L}}(t) + \hat{a}_{\text{out}}^{\text{R}}(t) \quad (2.67)$$

$$\hat{a}_{\text{out}}^{\text{L(R)}}(t) = \frac{i}{\sqrt{2\pi}} \int_{-\infty}^{+\infty} d\omega' e^{i\omega'(t_f-t)} \hat{a}_{\omega'}^{\text{L(R)}}(t_f). \quad (2.68)$$

Equations 2.63 and 2.66 respectively give the forward and backward temporal dynamics of the empty cavity weakly coupled to the external electromagnetic bath. Moreover, they imply the Input-Output relation:

$$\hat{a}_{\text{out}}(t) - \hat{a}_{\text{in}}(t) = \sqrt{2\gamma_c} \hat{a}(t), \quad (2.69)$$

which links the temporal evolution of the input and output fields to the cavity field operator  $\hat{a}(t)$  via the coupling constant with the bath ( $\gamma_c$ ). Note that a similar relationship holds also for the left and right bath degrees of freedom:

$$\hat{a}_{\text{out}}^{\text{L}}(t) - \hat{a}_{\text{in}}^{\text{L}}(t) = \sqrt{2\gamma_c} \hat{a}(t) = \hat{a}_{\text{out}}^{\text{R}}(t) - \hat{a}_{\text{in}}^{\text{R}}(t) \quad (2.70)$$

#### 2.4.2.2 Equation of motion of the material's field

After having derived the quantum evolution of the empty cavity field as a function of the input and output operators of the vacuum bath, we will discuss in the following the temporal evolution of the quantized material's field. The material's system is modelled as a set of  $N$  harmonic oscillators weakly interacting with a macroscopic bath represented by a collection of non-interacting harmonic oscillators [98]. The interaction of the material's modes with the macroscopic bath phenomenologically models the bare dissipations of the material's excitations. The Hamiltonian for the material subsystem, weakly coupled to its environment, reads [98]:

$$\hat{H}_m = \omega_0 \sum_{i=1}^N \hat{\sigma}_i^\dagger \hat{\sigma}_i + \sum_{i=1}^N \int_{-\infty}^{+\infty} d\omega' \omega' \left( \hat{r}_{\omega'}^i \right)^\dagger \hat{r}_{\omega'}^i + \sum_{i=1}^N \sqrt{\gamma_m} \int_{-\infty}^{+\infty} \frac{d\omega'}{\sqrt{2\pi}} \left[ \left( \hat{r}_{\omega'}^i \right)^\dagger \hat{\sigma}_i + \text{h.c.} \right]. \quad (2.71)$$

Here  $\hat{\sigma}_i$  is the annihilation operator of the  $i^{\text{th}}$  material's dipole,  $\hat{r}_{\omega}^i$  the annihilation operator of the  $i^{\text{th}}$  material's bath mode with frequency  $\omega$ , and  $\gamma_m$  the dissipative coupling constant of each dipole mode to the environment. As for the photonic degrees of freedom, we will suppose the coupling with the material's bath to be weak, hence implying a linear interaction between the  $\hat{\sigma}_i$  and  $\hat{r}_{\omega}^i$  fields for each dipole mode. Since the matter Hamiltonian  $\hat{H}_m$  is separable and the bath's degrees of freedom are coupled linearly with each dipole mode, the equation of motion of the matter field can be derived analogously to the cavity field equation of the previous section. The only difference with respect to the derivation of the cavity field lies in the fact that the cavity modes interact with distinct left and right baths, while there is no such distinction for the material's system [98, 99]. The equation of motion of each dipolar field reads:

$$\partial_t \hat{\sigma}_i(t) = -i \left( \omega_0 - i \frac{\gamma_m}{2} \right) \hat{\sigma}_i(t) - \sqrt{\gamma_m} \hat{\sigma}_i^{\text{in}}(t), \quad (2.72)$$

where the input operator for each material's excitation reads:

$$\hat{\sigma}_i^{\text{in}}(t) = i \int_{-\infty}^{+\infty} \frac{d\omega'}{\sqrt{2\pi}} e^{-i\omega'(t-t_i)} \hat{r}_{\omega'}^i(t_i), \quad t > t_i. \quad (2.73)$$

We highlight that, as in the case of the empty cavity evolution, each dipolar mode satisfies the Input-Output relation:

$$\hat{\sigma}_i^{\text{out}}(t) - \hat{\sigma}_i^{\text{in}}(t) = \sqrt{\gamma_m} \hat{\sigma}_i(t), \quad (2.74)$$

where the output material's operator reads:

$$\hat{\sigma}_i^{\text{out}}(t) = i \int_{-\infty}^{+\infty} \frac{d\omega'}{\sqrt{2\pi}} e^{-i\omega'(t_f-t)} \hat{r}_{\omega'}^i(t_f), \quad t < t_f. \quad (2.75)$$

#### 2.4.2.3 Equation of motion of the light-matter hybrids

In order to get the quantum equation of motion for the strongly coupled light-matter hybrids, we resort to the full Hamiltonian 2.60. We will work under a linear light-matter coupling, which implies that the interaction Hamiltonian  $\hat{H}_{\text{int}}$  can be written in the rotating wave approximation [73] as:

$$\hat{H}_{\text{int}} = g \sum_{i=1}^N \left( \hat{\sigma}_i^\dagger \hat{a} + \hat{a}^\dagger \hat{\sigma}_i \right), \quad (2.76)$$

being  $g$  the harmonic coupling strength. We stress that by employing a fully quantum description any non-linear light-matter coupling, as well as non-linear couplings with the external baths, can be added. For simplicity, we will work here in a fully linear framework. This assumption will enable us to compare the obtained results with the classical Transfer-matrix predictions (Figure 2.9). By supposing, as in the experimental setting, that there are no incoming EM fields from the right side of the cavity, i.e.  $\hat{a}_{\text{in}}^{\text{R}} = 0$ , the coupled equations of motion, which link the cavity and material's fields and take into account the linear dissipations with the baths, read:

$$\begin{cases} \partial_t \hat{a}(t) = -i \left( \omega_c - i \frac{\gamma_c}{2} \right) \hat{a}(t) - \sqrt{\frac{\gamma_c}{2}} \hat{a}_{\text{in}}^{\text{L}}(t) - ig \sum_{i=1}^N \hat{\sigma}_i(t) \\ \partial_t \hat{\sigma}_i(t) = -i \left( \omega_0 - i \frac{\gamma_m}{2} \right) \hat{\sigma}_i(t) - ig \hat{a}(t) \end{cases}. \quad (2.77)$$

The corresponding frequency-domain solutions of the coupled field equations will be exploited in the following to obtain the linear transmission of the hybrid polariton modes.

#### 2.4.2.4 Linear transmission within the Input-Output quantum model

In this section we apply the described Input-Output quantum framework to estimate the linear transmission spectrum of the coupled polaritons. This derivation is important since the linear transmission will be the main experimental observable employed in the thesis to track the strong coupling features. Importantly, we will demonstrate that, within a linear coupling between the matter and the cavity oscillators, the fully quantum IO model reproduces the classical linear response predicted by the Transfer-matrix (Section 2.4.1).

Within the quantum IO formalism, the transmission spectrum of the hybrid cavity is given by:

$$T(\omega) = \frac{|\langle \hat{a}_{\text{out}}^{\text{R}}(\omega) \rangle|^2}{|\langle \hat{a}_{\text{in}}^{\text{L}}(\omega) \rangle|^2}. \quad (2.78)$$

By solving the equation of motions of the coupled fields (Equation 2.77) in the frequency domain, it follows that the output optical field operator  $\hat{a}_{\text{out}}^{\text{R}}(\omega)$  can be written in terms of the spectrum of the input optical field  $\hat{a}_{\text{in}}^{\text{L}}(\omega)$  as:

$$\hat{a}_{\text{out}}^{\text{R}}(\omega) = -i\frac{\gamma_c}{2} \frac{(\omega - \omega_0 + i\frac{\gamma_m}{2})}{(\omega - \omega_c + i\frac{\gamma_c}{2})(\omega - \omega_0 + i\frac{\gamma_m}{2}) - Ng^2} \hat{a}_{\text{in}}^{\text{L}}(\omega). \quad (2.79)$$

Therefore, the linear transmission spectrum (Equation 2.78) is given in the Input-Output model by the expression:

$$T(\omega) = \frac{|\langle \hat{a}_{\text{out}}^{\text{R}}(\omega) \rangle|^2}{|\langle \hat{a}_{\text{in}}^{\text{L}}(\omega) \rangle|^2} = \frac{\gamma_c^2}{4} \frac{|(\omega - \omega_0 + i\frac{\gamma_m}{2})|^2}{|(\omega - \omega_c + i\frac{\gamma_c}{2})(\omega - \omega_0 + i\frac{\gamma_m}{2}) - Ng^2|^2}. \quad (2.80)$$

We clarify that this approach gives an approximation of the linear spectral transmission  $T(\omega)$  of the hybrid modes. Indeed, we have assumed the optical leakage rate of the cavity ( $\gamma_c$ ) to be independent of frequency and in-plane wave vector. Moreover, we have neglected the variation of the in-plane wave vector of the cavity with the detuning. Therefore, the above result is expected to hold only for a small neighbourhood of frequencies around the empty cavity resonance [99].

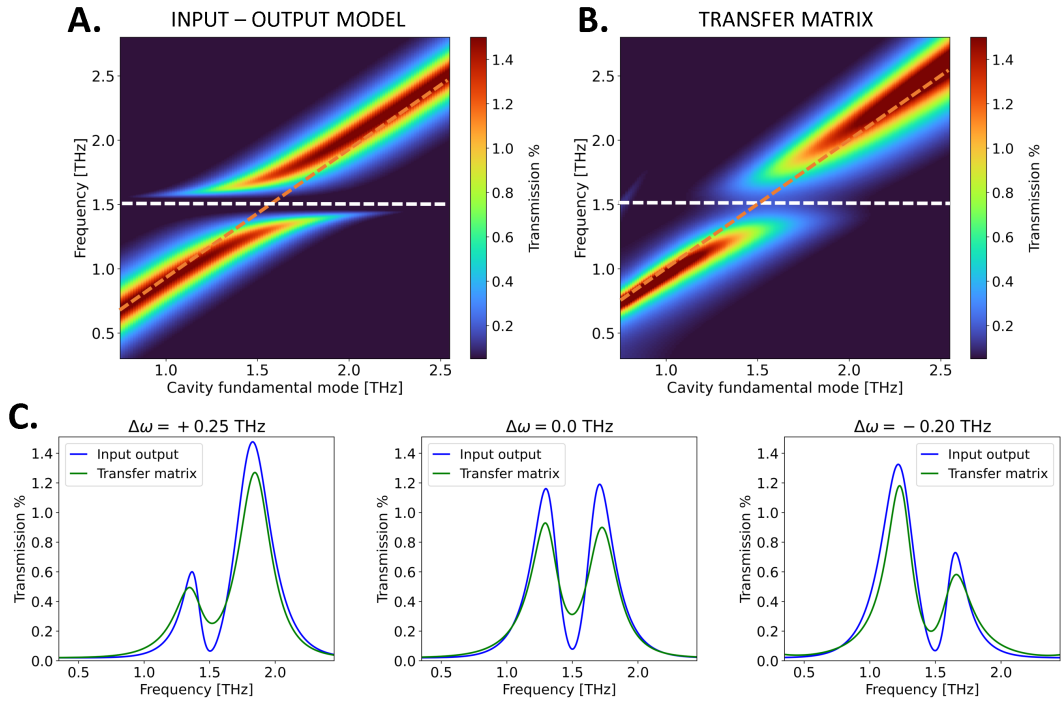


**Figure 2.10: Polariton dispersion simulated with the quantum Input-Output model in the linear regime and comparison with the classical Transfer-matrix method.** **A.** Linear transmission of the hybrid modes as a function of the cavity frequency calculated with the Input-Output formalism (Material's oscillator parameters:  $\omega_0 = 1.5$  THz,  $\gamma_c = \gamma_m = 0.05\omega_0$ , Collective coupling:  $g\sqrt{N} = 0.2$  THz). **B.** Dispersion of the polariton transmission simulated with the classical Transfer-matrix formalism (adopted parameters as in Figure 2.9B). **C.** Selected transmission spectra at different detunings  $\Delta\omega = \omega_c - \omega_0$  calculated with the IO formalism (blue lines) and with the Transfer-matrix method (green lines).

In order to highlight the connection between the IO model in the linear regime and the classical Transfer-matrix formalism, we present in Figure 2.10 the comparison of the linear polariton dispersion within the THz cavity setting of Figure 2.9A simulated with the two methods. We highlight that, by matching the Rabi splitting obtained on resonance with the Transfer-matrix method (Figure 2.9B) to the collective coupling constant of the IO formalism, the fully quantum IO model reproduces the frequency dispersion of the hybrid modes obtained within the classical Transfer-matrix framework. A deviation in the estimation of the polaritons linewidths is attributed to a non-constant frequency loss of the mirrors. The latter enters indeed in the Transfer-matrix method inside the frequency-dependence of the mirrors refractive index. This effect has not been taken into account in the present IO quantum model, since a frequency-independent coupling between the cavity and the EM bath has been supposed.

In conclusion, we have demonstrated that, despite its completely classical character, the linear Transfer-matrix theory remains a very accurate tool at describing the linear response of light-matter hybrids in terms of the cavity geometry and the static refractive properties of its constituents. This fact should not be too surprising since, in the case of a weak external interaction, one could always cast a linear response theory which will effectively describe the quantum mechanical microscopic response of the system. Within the cavity framework, this external weak interaction is represented by the photon exchange with the EM external bath. Obviously, the linear Transfer-matrix response will not describe the dynamics of coupled cavities where non-linearities emerge or where quantum statistics become important. In those cases a fully quantum theory, as the Input-Output previously described, would be the most accurate one.

# EXPERIMENTAL APPARATUS: TUNABLE CRYOGENIC TERAHERTZ CAVITY

---

We report in this chapter the set-up employed in the thesis to study the optical properties of light-matter hybrids. These are constituted of crystalline samples embedded within a Terahertz Fabry-Pérot cavity. The experimental assembly developed offers the unique opportunity to study the weak and strong coupling regimes between a tunable optical cavity in cryogenic environment and low energy degrees of freedom, such as phonons, magnons, or charge fluctuations.

We clarify that this cavity setting does not allow to reach the high compression of the electric field obtained within other kind of resonators such as split-ring resonators [64], array-defects cavities [32], or plasmonic cavities [88]. However, its crucial strength lies in its unique possibility of tuning the cavity resonance in a cryogenic environment, thus enabling to study the coupling at low temperature of a vast number of Terahertz excitations.

We describe in this chapter the developed set-up that allows for the positioning of crystalline samples in a Terahertz optical cavity of different quality factors, the tuning of the cavity length at cryogenic temperatures, and its optical characterization with a broadband time domain THz spectrometer ( $\sim 0.1 - 6.0$  THz). The built THz spectrometer allows, at the same time, for the characterization of the cavity optical characteristics (fundamental mode and quality factor) and the study of the linear response of the light-matter hybrids at low temperatures.

## 3.1 CRYOGENIC CAVITY ASSEMBLY

A detailed scheme of the built variable-length cryogenic THz cavity is presented in Figure 3.1. This is composed of two cryo-cooled piezo-controlled movable mirrors between which the sample is inserted. The movement of each of the the two cavity mirrors is ensured by three piezo actuators (N472-11V, Physik Instrumente) with a total travel range of 7 mm and a minimum incremental motion of 50 nm with a designed resolution of 5 nm. The independent movement of each of the three piezo actuators ensures the independent horizontal and vertical alignment of the mirrors while the simultaneous motion of the three results in a rigid translation of the whole mirror. Importantly, since both the mirror positions are controlled by the piezoelectric mechanics, the set-up includes both the possibility of tuning independently the cavity length and the sample position with respect to the mirrors.

The tunability of the cavity length sets the frequency of the cavity fundamental mode. Instead, the tunability of the sample position with respect to the mirrors allows us to maximize the coupling of the cavity photons with the targeted excitation, since the coupling energy scales with the absolute cavity field [42, 105] (see Section 2.2.1).

The mirrors are mounted on copper holders, and they are cryo-cooled by means of copper braids directly connected to the cold finger of the cryostat. Since the piezo actuators temperature operational range is 283–313 K, the piezo actuators are thermally decoupled from the mirror supports. The thermal decoupling is realized by placing between the piezo actuators and the mirror holders a PEEK disk on which the actuators actually act and three ceramic cylinders. These materials are thermal insulators, and they have a low thermal expansion coefficient in the operational temperature range of the cryostat (10 – 300 K). These features ensure the mirrors to be thermally insulated as well as an alignment stability of the cavity in the operational temperature range. We tested the set-up under nitrogen-cooled conditions and proved that in the temperature range of 80 – 300 K, the thermal decoupling between the cryo-cooled mirrors and the piezo actuators is efficient, thus making the set-up suitable to perform cavity length-dependent studies in cryogenic environment.

The chamber, shown in Figure 3.1A, is mounted on a flow cryostat, which is supported by a mechanical assembly allowing for the movement of the whole sample in the  $x$ ,  $y$ , and  $z$  directions. We stress that the mechanical translation of the sample is particularly crucial for the experiment since it allows us to perform THz transmission measurements of the empty cavity by simply moving the vertical/horizontal position of the whole chamber in Figure 3.1A. The chamber shown in Figure 3.1A is enclosed in a vacuum chamber allowing for optical access for transmission. The cryostat windows are two 2 mm crystalline quartz windows, which are suitable for the THz range. The vacuum conditions are ensured via a turbo pumping system (Pfeiffer HiCube). Pressures of  $10^{-6}$  mbar can be reached at room temperature, while at cryogenic temperature, the typical working pressure is  $10^{-7}$  mbar. The temperature is normally read on the sample holder and on the mirrors mounts by means of cryogenic silicon diodes. A temperature controller provided with a feedback circuit enables to modify the sample temperature so that a complete temperature scan can be performed at a fixed cavity length.

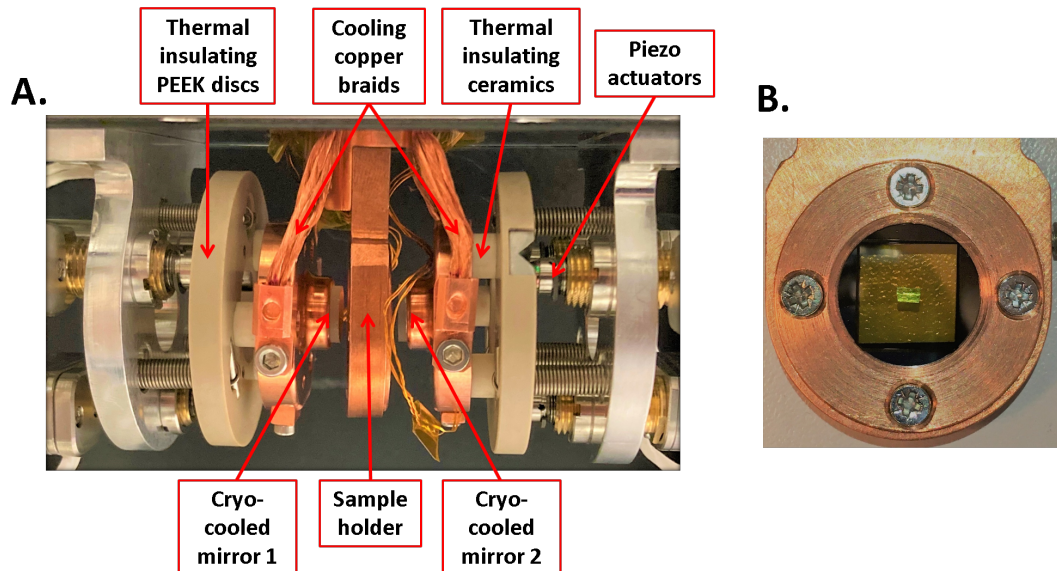


**Figure 3.1: Tunable cryogenic Terahertz cavity.** **A.** Detailed illustration of the cryogenic Terahertz cavity. The cavity mirrors are kept in thermal contact with the sample holder while they are insulated from the piezoelectric mechanics. **B.** Illustration of the sample holder. The sample is mounted between two transparent silicon nitride membranes of 2  $\mu\text{m}$  thickness.

### 3.1.1 SEMI-REFLECTING MIRRORS FABRICATION

The cavity semi-reflecting mirrors were fabricated by evaporating a thin bilayer of titanium-gold (2-10 nm) on a 2 mm thick crystalline quartz substrate, resulting in a transmission amplitude of 20 % across the THz spectral range of the experiment with no apparent spectral features. In detail, the deposition of the thin film coating has been achieved by classical E-beam evaporation. The substrates were first cleaned using standard procedure based on RCA-1 ( $\text{NH}_4\text{OH}-\text{H}_2\text{O}_2-\text{H}_2\text{O}$  1:1:5,  $75^\circ\text{C}$ , and 10'), rinsed by de-ionized (DI) water, and dried under  $\text{N}_2$  blow. Right before the transfer in the evaporator chamber, the substrates were treated by oxygen plasma (P:20 W, B:50 V, and t:1'). The first 2 nm thin layer of titanium was used to increase the adhesion of the following gold layer. The deposition rate for the titanium layer was  $0.1 \text{ \AA/s}$ , while for the gold we deposited the first 2 nm at a rate of  $0.1 \text{ \AA/s}$  and the other 8 nm at a rate of  $0.3 \text{ \AA/s}$ . At these deposition rates, we estimated an error in the film thickness of  $\sim 5\%$ , which translates in a 0.1 nm error for the 2 nm titanium film and 0.5 nm error for the 10 nm gold film.

### 3.1.2 SAMPLE'S MOUNTING

The sample is mounted between the semi-reflecting mirrors in a copper sample holder directly connected to the cold finger of the cryostat and sealed between two silicon nitride membranes (LP-CVD grown) with a window size of  $11 \times 11 \text{ mm}^2$  and a thickness of  $2 \text{ }\mu\text{m}$  (Figure 3.1B). The membranes are supported on a  $13 \times 13 \text{ mm}^2$  silicon frame that has a thickness of  $500 \text{ }\mu\text{m}$ . Importantly, the membranes are transparent in the THz frequency range employed in the experiments and do not show any spectral dependence. This is proved in Figure 3.2, where we present the transmission of the free standing silicon nitride membranes within the employed THz range. No absorption-like spectral features are indeed revealed.

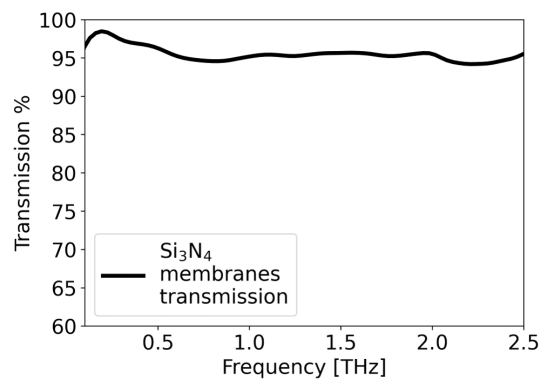


**Figure 3.2:** Measured THz transmission of the silicon nitride membranes within the employed spectral range.

## 3.2 TERAHERTZ TIME-DOMAIN SPECTROSCOPY

We characterize the tunable cryogenic cavity and eventually the light-matter hybrids through linear THz spectroscopy. In this section we outline the main features of the technique and the advantages with respect to standard FTIR to track the light-matter coupling features. We then present the built THz spectrometer and the procedure to extract the optical constants from the measurements of the THz transients.

### 3.2.1 THE TERAHERTZ DOMAIN

The Terahertz (THz) region of the electromagnetic spectrum, extending from approximately 0.1 THz to 30 THz, is of major importance for the study of correlated systems, since it is in this low frequency region that many of the phenomena influencing electronic properties of complex materials are found [106–108]. Whereas probing the ground state excitations may unveil the underlying mechanism of these complex phenomena, the characteristic energy scales of different elementary excitations and collective modes in many of these materials lie within the THz range. Bound states such as excitons and Cooper pairs have energies in the THz range, as do phonons and charge fluctuations. Moreover, by investigating the THz spectral region, information may be gained on scattering rates in semiconductors and superconductors and confinement in low-dimensional solids [106].

In the last two decades the THz region has opened up through the advent of THz time-domain spectroscopy. This technique has overcome the problems of infra-red spectroscopy techniques, which all lack brightness in the THz range, by providing sources with a broad bandwidth in the THz region and by enabling direct measurements of the dielectric function of materials without resorting to Kramers-Kronig methods [109]. The principle of THz time-domain spectroscopy is founded on the generation of THz transient fields using ultrafast laser pulses, which are then detected using optical gating. This allows for a direct measurement of the THz electric field of the pulse itself, which is used to reconstruct the real and imaginary parts of the optical constants without extrapolations or approximations. Within the cavity framework, having an intrinsic phase-resolved probe is also crucial, since it allows for a temporal reconstruction of the cavity-mediated dynamics, such as the coherent energy exchange characteristic of the strong coupling regime (Figure 2.5). These features are indeed hidden in intensity-based FTIR techniques [18, 30, 61, 110–112].

### 3.2.2 TERAHERTZ GENERATION AND DETECTION

#### 3.2.2.1 THz generation: the photo-conductive antenna

Let us consider a slab of a material excited at normal incidence by a time-dependent optical pulse. The electromagnetic radiation  $E_{\text{rad}}(t)$  emitted from the slab in the far-field limit, i.e. when the spatial position at which the field is detected is much larger than the ratio of the dimension of the emitter over the emitted wavelength [113], follows the Maxwell's equations:

$$E_{\text{rad}}(t) \propto \left( \frac{\partial \mathbf{J}(t)}{\partial t} + \frac{\partial^2 \mathbf{P}(t)}{\partial t^2} \right). \quad (3.1)$$

Here  $\mathbf{J}(t)$  is the time-varying isotropic conduction current and  $\mathbf{P}(t)$  the polarization, both induced by the time-dependent photo-excitation. Therefore, by properly selecting the medium and the excitation pulse, it is possible to either induce a time-dependent charge current or a time-varying optical polarization, so that the emitted electromagnetic radiation lies in the Terahertz range. The first can be induced in photo-conductive switchers, while the latter in non-linear optical media.

We will focus in this section on the photo-conductive switching method, which is the process to generate the THz pulses employed in the experiments.

The photo-switching is commonly realized in a photo-conductive antenna (PCA) [114–116]. A photo-conductive antenna typically consists of a grown semiconductor material with metallic electrodes separated by a few microns deposited on the surface, as illustrated in Figure 3.3A. An ultrafast laser pulse (temporal duration  $\sim 50$  fs) is used to excite carriers within this gap, which are then accelerated by the applied bias electric field  $V_{bias}$ . The photo-excited carriers are then rapidly recaptured by defect trap sites through a recombination process. This process of generation, acceleration and recombination undergone by the charge carriers occurs over the time range of a few picoseconds, hence leading to the emission of broadband THz radiation. A representative temporal evolution of the pump pulse envelope, of the induced photo-current  $\mathbf{J}(t)$ , and of the resulting THz field are presented in Figure 3.3B. It is worth stressing that the semiconductor substrate and the input laser used are interconnected, as the photon energy of the pulse has to be above the band gap of the semiconductor to efficiently generate conductive carriers.

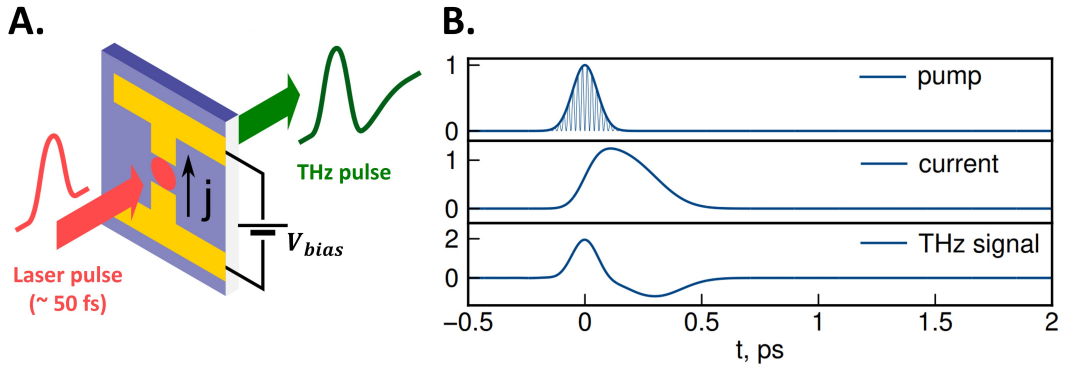


**Figure 3.3: Mechanism of THz generation in a photo-conductive antenna.** **A** Sketch of the THz pulses generation through ultrafast optical excitation of the antenna. The ultrafast laser pulse ( $\sim 50$  fs) excites carriers which are accelerated by the potential  $V_{bias}$ . The resulting charge separation induces the emission of the THz field. **B**. Typical electrical and optical response of the photo-conductive antenna to an optical pump pulse of femtosecond time duration (Picture taken from [117]).

The typical dependence of the output THz power spectrum generated in the semiconductor-based photo-conductive antenna is given by [118]:

$$P_{THz}(\omega_{THz}) \sim \frac{1}{1 + (\omega_{THz}\tau_{eff})^2}. \quad (3.2)$$

Here  $\tau_{\text{eff}}$  represents the effective lifetime of the photo-carriers, which is equal to the lifetime of the non-equilibrium charge carriers in the semiconductor. From Equation 3.2, we notice that the shorter the lifetime  $\tau_{\text{eff}}$  is, the greater efficiency of THz generation can be obtained. GaAs (Gallium Arsenide) grown by molecular beam epitaxy on a low temperature substrate (LT-GaAs) is usually chosen as a photo-conductive material, as this grown method allows to obtain a material with a larger number of defects and hence with shorter lifetimes of out-of-equilibrium charge carriers ( $< 200$  fs) [118].

The THz emitter employed in the experiments presented in this thesis is fabricated on a semi-insulating GaAs substrate by depositing the metal electrodes having an interdigitated finger-like structure [119–122]. Each electrode is  $\sim 1$  cm long and  $10 \mu\text{m}$  wide. The gap between two nearby electrodes, which is also the active region, is  $10 \mu\text{m}$ . The total area of the emitter is  $1 \times 1 \text{ cm}^2$ . Due to such a narrow electrode gap, a bias of just a few volts on the electrodes creates an electric field of the order of a few kV/cm in the active region. Now, photo-excitation of the active regions creates charge carriers in GaAs, which accelerate due to the presence of an applied electric field and emit THz radiation having polarization parallel to the applied electric field. To avoid the destructive interference of THz radiated from two neighbouring active regions, each alternate active region is covered with a metallic layer to avoid the photo-excitation and, hence, out-of-phase THz generation from those regions.

### 3.2.2.2 THz detection: Electro-Optical Sampling

The full temporal structure of the THz pulses are commonly detected through Electro-Optical Sampling (EOS) techniques [123, 124]. EOS is essentially the inverse process of the optical rectification, mixing the THz pulse with an optical gating pulse in a non-linear medium through the Pockels effect. In the Pockels effect, a non-linear polarization  $\mathbf{P}$  is induced in an electro-optical medium according to:

$$P_i(\omega) = 2 \sum_{jk} \chi_{ijk}^{(2)} E_j(\omega) E_k(\omega), \quad (3.3)$$

being  $\chi_{ijk}^{(2)}$  the non-linear susceptibility tensor. Therefore, a static field induces a birefringence in the medium proportional to the applied field amplitude. Thus, by measuring the degree of birefringence, the applied field strength can be determined. This is the principle of the EOS technique.

The generated THz field and the optical gating pulse co-propagate through the electro-optical medium. By assuming a matching between the THz phase velocity and the optical group velocity, the short optical pulse experiences a constant electric field due to the presence of the THz field and its polarization rotates as a consequence of the field-induced birefringence. The rotation degree is proportional to the THz field strength so that, if the THz and the gating pulse temporally overlap, a measurement of the polarization rotation results in a direct measurement of the THz electric field. This is achieved by propagating the optical pulse through a quarter-wave plate aligned such that in the absence of the THz field the linearly polarized sampling beam becomes circularly polarized and then through a Wollaston prism. The Wollaston prism splits the optical pulse into two ortogonally polarized components, which are subsequently detected by two photodiodes (Figure 3.4), balanced in order to have no differential signal when no THz is present. Conversely, when the THz field is present, the polarization of the optical gating pulse slightly rotates and the polarization is hence elliptical after the quarter-wave plate. In the presence of the THz the two detectors are therefore unbalanced and

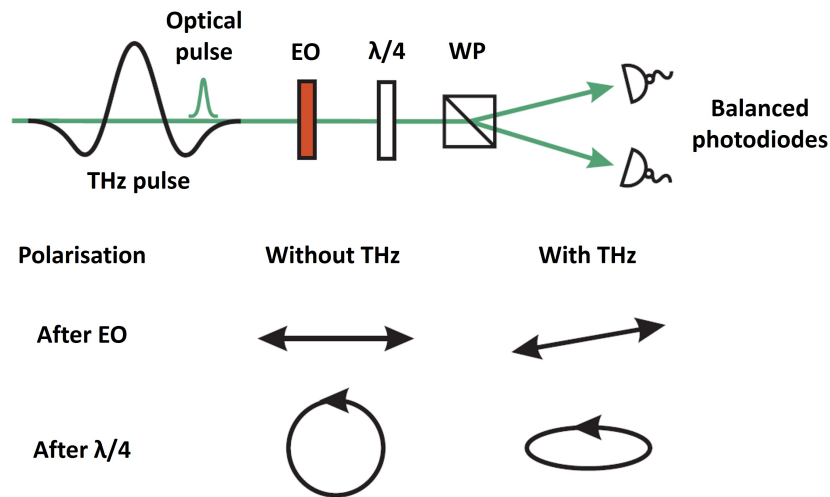


**Figure 3.4: Schematic layout of electro-optical sampling (EOS)** EO: Non linear Electro-optic crystal,  $\lambda/4$ : Quarter-wave plate, WP: Wollaston prism. The effect of the presence of the THz field on the polarization of the gating optical pulse are illustrated beneath.

the differential intensity read on the diodes maps the ellipticity of the sampling beam and, subsequently, the instantaneous THz electric field (Figure 3.4). By scanning the relative temporal delay between the optical and the THz pulses and measuring the THz-induced differential polarization components of the gating beam, it is therefore possible to temporally map the THz pulse.

### 3.2.3 TERAHERTZ TIME-DOMAIN SPECTROMETER

The layout of the built THz spectrometer based on THz generation in a GaAs-based photo-conductive switcher is shown in the schematic diagram of Figure 3.5.

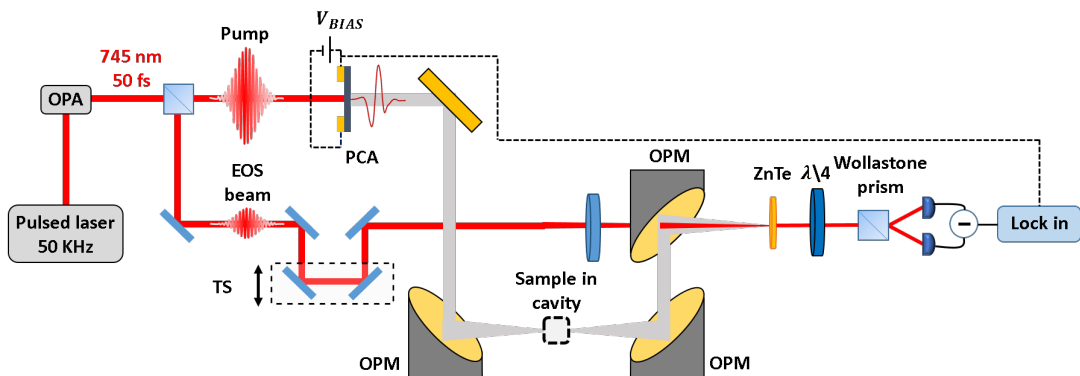


**Figure 3.5: Schematic layout of the Terahertz time-domain spectrometer.** OPA: Optical Parametric Amplifier, PCA: Photo-Conductive Antenna, TS: Translation Stage, OPM: Off-Axis Parabolic mirror,  $\lambda/4$ : Quarter-wave plate.

Ultrashort laser pulses (50 fs pulse duration and 745 nm central wavelength) from a commercial 50 kHz pulsed laser + Optical Parametric Amplifier (OPA) system (Pharos +

Orpheus-F, Light Conversion) are split into two to form an intense optical beam for THz generation (6  $\mu\text{J}/\text{pulse}$ ) and a weak readout pulse (< 100 nJ/pulse) for time-resolved Electro-Optical Sampling.

Single-cycle THz pulses are generated via the acceleration of the photoinduced carriers in a large-area GaAs-based photoconductive antenna (PCA). The acceleration of the free carriers induced by the pump is achieved by biasing the PCA with a square-wave bias voltage  $V_{\text{bias}}$  triggered with the laser at a frequency of 1.25 kHz. We employed a biasing square wave with a voltage peak of 8.0 V and a 50 % duty cycle. For an efficient THz generation using 6  $\mu\text{J}$  pump pulse energy, an area of around 6 mm diameter on the  $1 \text{ cm}^2$  large emitter is illuminated using a collinear pump beam. Since the diameter of the excitation area is comparatively much larger than the THz wavelength, the radiated THz beam has a similar wavefront as the pump beam on the emitter and, hence, follows the same beam path as the pump beam.

The emitted collimated THz beam is then focused on the sample mounted inside the cavity, which is placed in the focal plane of two off-axis parabolic mirrors (OPMs). The THz field and the readout pulse are then combined and focused on a 0.5 mm ZnTe crystal, which acts as the electro-optical crystal. After the electro-optical crystal, the probe beam, variable delayed in time through a translation stage (TS), is analyzed for its differential polarization changes induced by THz in the ZnTe crystal, which maps the time evolution of the ultrafast THz field. This is carried out by standard Electro-Optical Sampling (EOS), by splitting the two probe polarizations with a Wollaston prism and measuring the differential intensity recorded on a pair of photodiodes (Section 3.2.2.2). The resulting differential signal is then detected using a lock-in amplifier (SR830, Stanford Research System) referenced at the frequency of the bias voltage ( $V_{\text{bias}}$ ). We estimated the signal-to-noise ratio of the detected THz field to be  $4.6 \times 10^4$  and the temporal phase stability to be  $\leq 30$  fs.

The entire system is purged with nitrogen to eliminate THz absorption coming from the water vapour in the ambient atmosphere. We show in Figure 3.6A the measured electric field of the generated THz pulse and its calculated Fourier spectrum (Figure 3.6B). As shown, the input field is, indeed, a nearly single-cycle THz pulse with the spectral content reaching 6 THz, as highlighted in the logarithmic scale plot in the inset of Figure 3.6B.

### 3.2.4 DETERMINING THZ OPTICAL PROPERTIES

The power of THz time-domain spectroscopy relies in its ability to record both amplitude and phase information by direct sampling of the electric field. This provides amplitude and phase information on the transmission (or reflection) coefficients of the targeted sample, which in turns yields both real and imaginary parts of the complex dielectric function within the spectrum of the THz pulse. This aspect is of major advance over the FTIR techniques commonly used in the cavity field [18, 30, 61, 110–112], which only provide power spectra and rely on Kramers-Kronig methods to determine the optical constants.

In this section we outline the basic procedure for obtaining the complex dielectric constant and complex optical conductivity of a medium from measurements of the THz transient field. Since the samples of interest for this thesis are all transparent within the THz range, all experiments are carried out using transmission measurements only. Therefore, only the transmittivity will be considered in the following treatment, though the analysis can be analogously applied to the reflection coefficients.

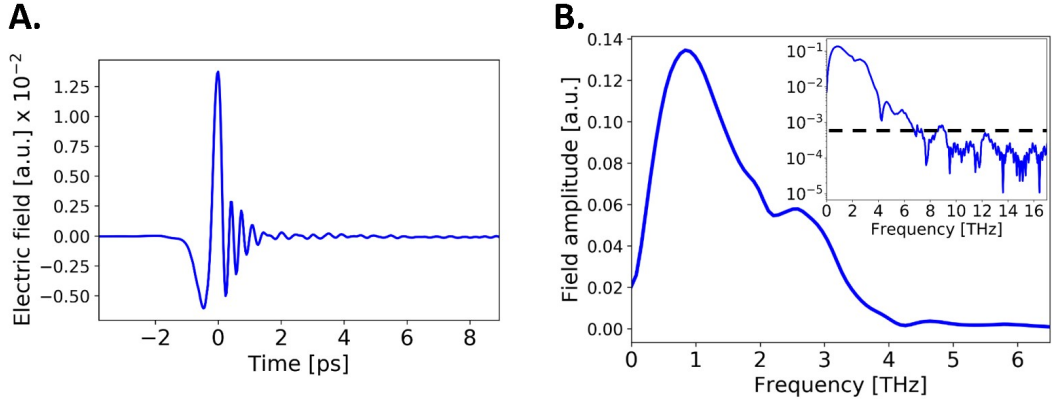


**Figure 3.6: Employed THz pulses generated by the photo-conductive antenna.** **A.** Free space nearly single-cycle THz field employed in the experiments detected through Electro-Optical-Sampling (EOS) in a 0.5 mm ZnTe crystal. **B.** Fourier transform of the nearly single-cycle THz field in free space. In the inset, the Fourier spectrum is plotted in logarithmic scale to highlight the spectral content of the THz field up to  $\sim 6$  THz. The black dashed line in the logarithmic plot marks the spectral noise level.

### 3.2.4.1 Complex optical constants

The optical properties of a given medium can be described by the dielectric constant  $\tilde{\epsilon}(\omega)$ , the optical conductivity  $\tilde{\sigma}(\omega)$ , and the complex refractive index  $\tilde{n}(\omega)$ , all of which are, in general, complex quantities:

$$\begin{aligned}\tilde{\epsilon}(\omega) &= \epsilon_1(\omega) + i\epsilon_2(\omega), \\ \tilde{\sigma}(\omega) &= \sigma_1(\omega) + i\sigma_2(\omega), \\ \tilde{n}(\omega) &= n(\omega) + i\kappa(\omega),\end{aligned}\tag{3.4}$$

where  $n(\omega)$  is the refractive index and  $\kappa(\omega)$  the absorption coefficient [125]. The complex refractive index is related to the complex dielectric constant through the relation:

$$\tilde{n}^2(\omega) = \tilde{\epsilon}(\omega).\tag{3.5}$$

The general relation between the dielectric constant and the complex conductivity can be hence shown to be:

$$\tilde{\epsilon}(\omega) = \epsilon_1(\omega) + i\frac{\sigma_1(\omega)}{\omega\epsilon_0},\tag{3.6}$$

where  $\epsilon_0$  is the free space permittivity,  $\epsilon_1(\omega)$  describes the motion of bound charges, and  $\sigma_1(\omega)$  describes that of free charges, in the limit of low near-DC driving frequencies. Nonetheless, at higher frequencies, especially in the optical range, the response of free and bound charges to fast oscillating fields changes significantly from the lower frequency case, and the distinction between free and bound charges becomes one of convention [126]. It is therefore possible to redefine the relation between the dielectric constant and the complex conductivity in order to include the response of all the charges (bound and free) into the conductivity term:

$$\tilde{\epsilon}(\omega) = 1 + i\frac{\tilde{\sigma}(\omega)}{\omega\epsilon_0}.\tag{3.7}$$

The previous relation also allows in converting back and forth between  $\tilde{\epsilon}(\omega)$  and  $\tilde{\sigma}(\omega)$ , since the real and imaginary parts of  $\tilde{\epsilon}(\omega)$  and  $\tilde{\sigma}(\omega)$  can be expressed in terms of each other as:

$$\begin{aligned}\sigma_1(\omega) &= \omega\epsilon_0\epsilon_2(\omega) \\ \sigma_2(\omega) &= \omega\epsilon_0(1 - \epsilon_1(\omega))\end{aligned}\quad (3.8)$$

The latter relations will be exploited to map the THz absorptive ( $\sigma_1$ ) and inductive ( $\sigma_2$ ) contributions to the dielectric response of the targeted materials.

### 3.2.4.2 Analysis of the THz time domain measurements

After having established the definitions of the optical constants and their mutual relations, we show in this section how to recover them from the experimental measurements. The experimental procedure involves the measurements of electric fields transmitted through the samples under investigation. In all the investigated samples we will work under the so called "thin film approximation". In this configuration the sample's optical length is less than the geometrical length of the THz pulse. Therefore, in this case it is not possible to distinguish in the time-domain trace the multiple reflections of the THz field within the sample's surfaces. For the THz fields employed in the experiments we estimate a pulse width in free space of  $\tau_{\text{THz}} \sim 0.25$  ps, corresponding to an optical thickness of  $75 \mu\text{m}$ .

By denoting with  $t_{12}$  and  $t_{21}$  the complex Fresnel coefficients associated to the light passing into and out of the sample, the THz field transmitted through the sample  $E_s(\omega)$  can be expressed as a function of the incident THz field  $E_0(\omega)$  as:

$$\begin{aligned}E_s(\omega) &= E_0(\omega)t_{12}t_{21}e^{i\frac{\tilde{n}(\omega)\omega d}{c}} \\ &= E_0(\omega)t_{12}t_{21}e^{-\frac{\kappa(\omega)\omega d}{c}}e^{i\frac{n(\omega)\omega d}{c}}\end{aligned}\quad (3.9)$$

where  $d$  is the sample's thickness.

By dividing the Fourier spectrum of the THz pulse passing through the sample  $E_s(\omega)$  by the Fourier spectrum of a reference spectrum passing through air, we can obtain the complex transfer function<sup>1</sup>:

$$H(\omega) = \frac{E_s(\omega)}{E_r(\omega)} = T(\omega)e^{i\phi(\omega)} = t_{12}t_{21}e^{-\frac{\kappa(\omega)d}{2}}e^{id(n(\omega)-1)\frac{\omega}{c}}. \quad (3.10)$$

By supposing that the targeted material is low absorptive, the imaginary part of the Fresnel coefficients can be neglected, and the real and imaginary part of the material's refractive index can be expressed in terms of  $\phi(\omega)$  and  $T(\omega)$  as:

$$n(\omega) = 1 + \frac{\phi(\omega)c}{\omega d} \quad (3.11)$$

$$\kappa(\omega) = -\frac{1}{d} \ln \left( \frac{(n(\omega) + 1)^2}{4n(\omega)} T(\omega) \right). \quad (3.12)$$

We note that for calculating the complex refractive index one needs to extract the phase  $\phi(\omega)$  from the experimental transfer function  $H(\omega)$  through the equation:

$$\phi(\omega) = \arctan \left( \frac{\text{Re}(H(\omega))}{\text{Im}(H(\omega))} \right). \quad (3.13)$$

<sup>1</sup> In the present equation we have set  $n_{\text{air}} = 1$  and supposed normal incidence, so that the angular dependence of the Fresnel coefficients can be neglected (see Equation 2.40).

Because of the periodicity of the  $\arctan$  function the phase is hence not continuous and displays jumps of  $2\pi$ , which has to be corrected through a phase unwrapping procedure.

We present in Figure 3.7 an example of optical constants extraction, corresponding to the low temperature phase of a  $15\ \mu\text{m}$  1T-TaS<sub>2</sub> sample (see Chapters 6, 5 for further details). The measured transmitted THz field is shown in Figure 3.7A, while the extracted real and imaginary part of the optical conductivity are shown in Figures 3.7B and 3.7C, respectively. Both the absorptive ( $\sigma_1$ ) and the inductive ( $\sigma_2$ ) response of the material mark the presence of optical THz phonons whose origin will be discussed in Chapters 6, and 5.

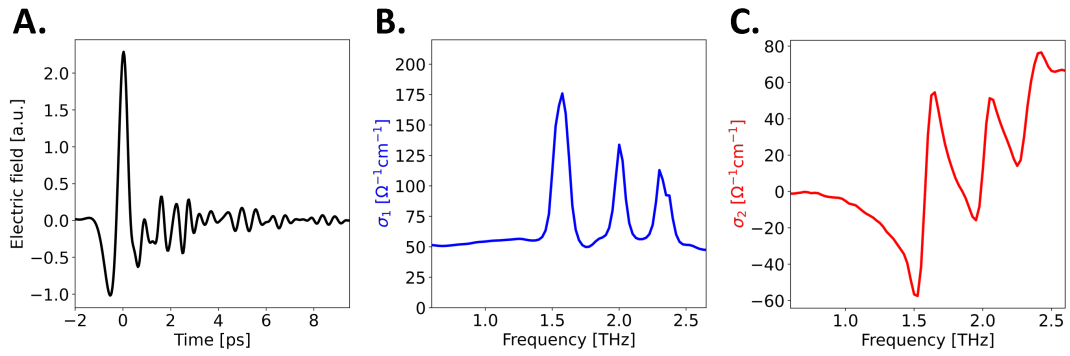


**Figure 3.7: Extraction of THz optical constants.** **A.** Time domain THz field transmitted through a  $15\ \mu\text{m}$  1T-TaS<sub>2</sub> sample at 80 K. **B.** Extracted real part of the optical conductivity  $\sigma_1(\omega)$ . **C.** Extracted imaginary part of the optical conductivity  $\sigma_2(\omega)$ .

### 3.3 CHARACTERIZATION OF THE BARE TERAHERTZ CAVITY

We present in this section the characterization of the optical properties of the tunable THz cavity. Firstly, we will present the estimation of the quality factor of the employed Fabry-Pérot cavities, which sets the photon confinement. Secondly, we will characterize how the cavity resonance evolves in temperature and illustrate the procedure for correcting the thermal drift of the cavity length employed in all the temperature scans presented in the thesis.

#### 3.3.1 EMPTY CAVITY CHARACTERIZATION AT LOW TEMPERATURE

In this section, we present the characterization of the response of the empty THz cavity at low temperature (80 K), i.e. when the THz field passes only through the silicon nitride membranes within the mirrors. With this characterization, the quality factor of the cavity can be determined. As described in Section 2.1.1, the cavity quality factor is a crucial parameter for the experiment, setting the photon lifetime inside the cavity

and, hence, the coupling strength between the cavity mode and the targeted material resonance.

In order to minimize the photon losses and, hence, maximizing the cavity quality factor, the two cavity mirrors were set parallel to each other and perpendicular to the THz incoming beam. This was obtained by aligning the multiple reflections of the pump beam, which is made collinear with THz by the generation process. The alignment was then finely tuned by maximizing the THz field peaks in the time domain trace associated with the multiple reflections of the THz beam within the cavity.

The results of the characterization are presented in Figure 3.8 where we plot the time domain THz field transmitted through the Fabry–Pérot empty cavity and the corresponding spectral content for three representative values of the cavity length.

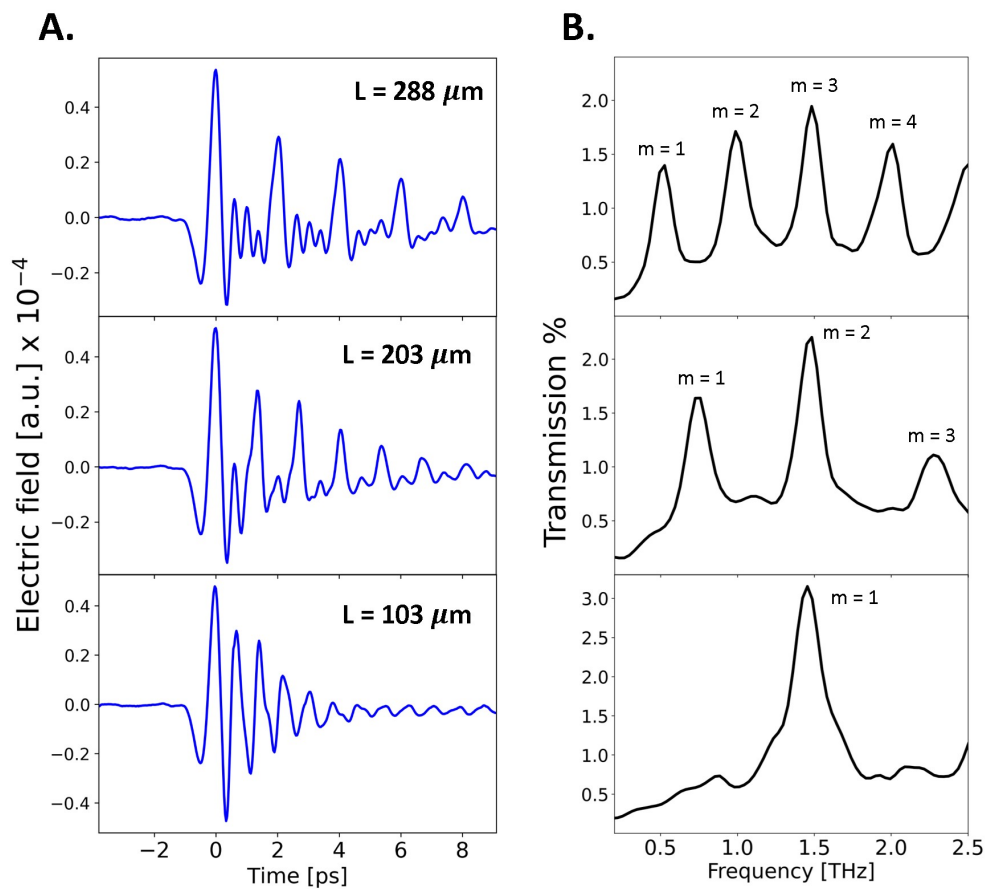


**Figure 3.8:** THz spectroscopy of the empty cavity at 80 K for representative distances  $L$  between the cryogenic mirrors **A**. Measured time-resolved THz fields transmitted through the empty cavity at 80 K. **B**. Corresponding transmission spectra showing the tunability of the cavity fundamental resonance mode ( $m = 1$ ). For the presented measurements the thickness of the gold layer on the semi-reflecting mirrors is  $d_{Au} = 10 \text{ nm}$ .

The transmission spectra are obtained by taking the ratio between the Fourier spectrum of the time domain THz traces shown in Figure 3.8A and the reference free-space spectrum shown in Figure 3.6B. The latter was measured once at the beginning of each measurement campaign and once at the end. This is justified by the amplitude and

phase stability of the free-space THz field discussed in Section 3.2.3. We estimated the contribution to the cavity transmission error due to an amplitude variation in the reference THz field in the spectral range 0.5 – 2.5 THz to be  $\sim 45$  times less than the relative amplitude variation in the cavity field.

The time-dependent detected fields (Figure 3.8A) show that when the nearly single-cycle THz pulse passes through the cavity, it is repeatedly reflected by the mirrors with a round-trip time set by the cavity length. This causes the nearly single-cycle THz field to be stretched to a multi-cycle decaying oscillating field with a decay time set by the cavity quality factor. This results in transmission spectra (Figure 3.8A) exhibiting interference Fabry-Pérot modes with their frequency determined the  $\omega_m = \frac{c}{2nL} m$ , where  $L$  is the length of the cavity,  $n$  the refractive index of the medium inside the cavity, and  $m$  is the mode number. The estimated quality factor of the cavity at 80 K, defined as the ratio between the fundamental cavity mode and its bandwidth at a fixed cavity length, is  $Q \sim 6.0$ .

Cavities with higher quality factors can be produced by depositing a thicker gold layer on the quartz mirror substrates. Increasing the thickness of the gold layer will increase the bare cavity quality factor and, hence, lead to a sharper cavity resonance. On the other hand, increasing the layer thickness will decrease the intensity of the transmitted signal and overall the signal-to-noise ratio of the detected THz field. It should be noted that the ideal gold layer thickness should be chosen as a trade-off between the two quantities and depends on the experimental goals.

### 3.3.2 THERMAL EVOLUTION OF THE CAVITY RESONANCE

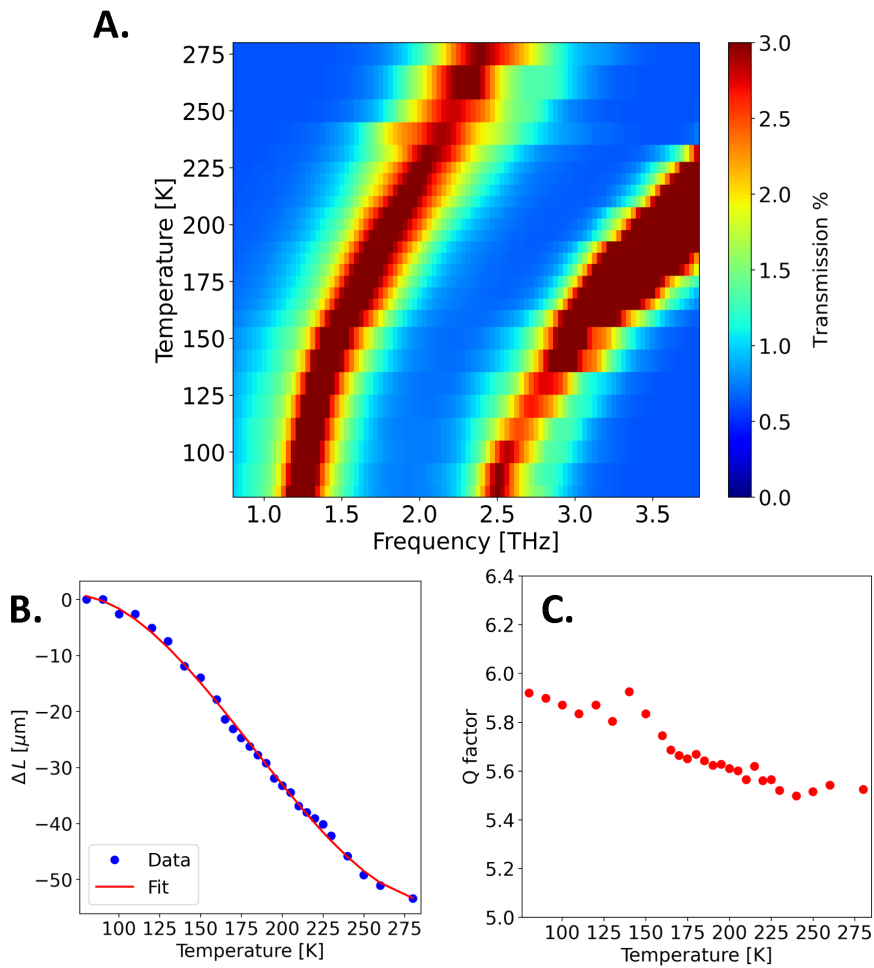
The developed THz cavity allows for performing temperature-dependent studies of the light-matter hybrids. It is therefore crucial to characterize how the bare cavity properties evolve with temperature to subsequently correct possible thermal drifts.

Figure 3.9A presents the thermal evolution of the empty cavity transmission measured in the range 80 – 280 K. A thermal drift of the cavity resonance is detected. The thermal drift is quantified in Figure 3.9B where we present the thermal variation of the cavity length  $\Delta L$  estimated from the cavity transmission resonances. Overall, a length variation of  $\sim 55 \mu\text{m}$  is detected within the employed temperature range, consistent with a linear thermal expansion of the copper mirrors mounts [127].

Importantly, as shown in Figure 3.9C, the thermal drift of the cavity length does not significantly affect the quality factor of the cavity. This implies that the cavity alignment, which in turn sets the  $Q$  factor of the Fabry-Pérot resonator, can be considered temperature-independent.

Given these evidences, we schematic present in the following the procedure to account for thermal drifts of the cavity resonance which, obviously, become more important at higher cavity frequencies. The employed procedure for correcting this thermal drift and subsequently obtain a temperature scan at a fixed cavity mode is the following:

- We set the bare cavity frequency at 80 K by measuring its THz interference spectrum (Figure 3.8).
- For the cavity length set at 80 K, we run the temperature scan and measure the temperature-dependent THz transmission of the coupled cavity.
- For each spectrum obtained at fixed temperature we assign an effective cavity length. This can be estimated by fitting the thermal variation of the cavity length  $\Delta L$  for a representative empty cavity resonance (see the polynomial fit of Figure



**Figure 3.9: Temperature dependence of the empty cavity properties** **A.** Evolution of the empty cavity THz transmission as a function of the temperature (measured on the sample’s mount). **B.** Thermal shift of the cavity length ( $\Delta L$ ) estimated from the THz transmission spectra in **A.** In blue solid the corresponding polynomial fit. **C.** Quality factor of the empty cavity as a function of the temperature estimated from the THz transmission in **A.** As in Figure 3.8, the thickness of the gold layer on the semi-reflecting mirrors is  $d_{\text{Au}} = 10$  nm.

3.9C). In this way, each cavity spectrum can be labelled through its temperature and through its effective cavity length.

- We collect all the cavity spectra sharing the same effective cavity length and construct the corrected temperature scan, in which the thermal drift of the cavity resonance is removed.

In conclusion, the developed set-up allows to study the Terahertz optical properties of low energy degrees of freedom in crystalline solid samples coupled with a tunable optical cavity in cryogenic environment. The unique feature implemented in the set-up lies in its capability of tuning the cavity resonance at cryogenic temperatures. The light-matter hybrids are characterized with a broadband THz nearly single-cycle field generated in a photo-conductive switcher and with a frequency content of up to 6 THz.

The use of broadband THz fields is particularly crucial in this sense as it allows for the simultaneous characterization of the empty cavity and the cavity hybridized with the contained material.

The capability of the set-up of tuning the cavity resonance combined with its capability of performing temperature-dependent studies in a wide range of cryogenic temperatures makes it a versatile platform for the study of how light-matter hybridization of different low energy excitations may affect the macroscopic properties of complex materials, as we will show in the following chapters.



# VIBRATIONAL STRONG COUPLING IN $\text{CuGeO}_3$

---

In view of the intriguing possibilities offered by electronic strong coupling as a mean to modify the excited state properties of complex systems, achieving analogous behaviours within the electronic ground state manifold, i.e. through the strong coupling of vibrational transitions [27, 30, 110, 128–132], would be a crucial step towards new material science and chemistry.

When photons are hybridized with specific vibrational modes, the physical and optical properties of those vibrations, such as the excited state lifetime [133], emissivity [134], Raman scattering dynamics [135], and phonon non-linearities [136] in the ground electronic state can change. Since the frequency of the normal mode vibration shifts under strong coupling with the cavity field, the ground state potential well can be as well modified [18, 137]. This fascinating perspective has stimulated the condensed matter community to apply the vibrational strong coupling framework in phonon-assisted collective phenomena in quantum materials, such as superconductivity [57], ferromagnetism [58], or ferroelectricity [51, 52].

We report here the experimental demonstration of the vibrational strong coupling regime in the benchmark material  $\text{CuGeO}_3$ . Crystalline  $\text{CuGeO}_3$  is an ideal platform wherein to test the potentiality of the developed set-up to detect the features associated with the strong coupling of THz vibrational excitations. Indeed, it is a dielectric material exhibiting a strong optical-active phonon mode in the THz range with smoothly varying line parameters as a function of the temperature. We are therefore in a suitable setting to detect how the signatures of vibrational strong coupling directly emerge in the measured THz spectrum and to verify the consistency of the experiments with the light-matter interaction models presented in Chapter 2.

Firstly, we demonstrate the strong coupling of the  $\text{CuGeO}_3$  optical phonon at cryogenic temperature (80 K). The strong coupling within the cavity leads to the formation of new phonon-polariton modes which we experimentally observe in the time domain as a normal mode beating, corresponding in the Terahertz spectrum to an avoided crossing. We further validate the strong coupling regime by comparing the experimental results with the predictions of the coupled oscillator model and with Transfer-matrix classical simulations, which we prove to reproduce the measured polariton dispersion. We lastly vary the temperature and prove that the line changes of the bare phonon are mapped in a thermal modification of the linewidth and frequency of the vibro-polariton lines. This leads to a slight enhancement of the Rabi splitting at high temperature which we relate to a decrease of the bare phonon lifetime.

## 4.1 THZ SPECTROSCOPY OF $\text{CuGeO}_3$ NORMAL PHASE

In this section the static Terahertz properties of the benchmark material  $\text{CuGeO}_3$  are presented.  $\text{CuGeO}_3$  is an insulating crystal belonging to the family of cuprates. Its room temperature crystalline structure is presented in Figure 4.1A and takes the name

of "normal" or "undistorted" phase. The building blocks of the crystal structure are the  $\text{Cu}^{2+}$  and  $\text{Ge}^{4+}$  chains parallel to the  $c$  axis. These chains are bounded together through the oxygen atoms and form layers parallel to the  $b$ - $c$  plane weakly coupled along the  $a$  axis [138–141].  $\text{CuGeO}_3$  is extensively studied for its peculiar magnetic behaviour revealing the onset of a spin-Peierls phase (below 14 K) in which the lattice distortion is accompanied by the formation of a spin-singlet ground state and by the creation of an energy gap in the spectrum of magnetic excitations [139, 140, 142–144].

A full review of the spin-Peierls physics in  $\text{CuGeO}_3$  goes beyond the scope of the chapter.  $\text{CuGeO}_3$  is indeed chosen as a playground to explore vibrational strong coupling at THz frequencies since it exhibits a strong Cu-O optical-active vibrational mode within the employed THz range ( $\omega_{\text{phonon}} \sim 1.45$  THz). This mode is associated with the rotation (accompanied by a slight internal distortion) of the  $\text{GeO}_4$  tetrahedra around the axis defined by the oxygen sites and presents a  $B_{2u}$  symmetry [139, 145], which makes it IR-active. The optical activity of the targeted phonon mode is a crucial ingredient in the strong coupling framework [146]. Indeed, it is the dipole moment change associated to the vibrational excitation which, in terms of the phonon normal coordinates  $Q_k$  can be written as:

$$\mu = \mu_{Q_k=0} + \left( \frac{\partial \mu}{\partial Q_k} \right)_{Q_k=0} Q_k, \quad (4.1)$$

which couples to the cavity electric field.

The targeted  $B_{2u}$  mode shows an anomalous monotonic blue shift across the undistorted phase when the temperature is increased from 14 K to 300 K together with a line broadening due to phonon thermal population [139, 140]. These features make therefore this phonon a suitable benchmark target to measure how the temperature dependence of its line parameters is mapped onto the vibro-polariton states when the phonon is strongly coupled with a resonant cavity mode.

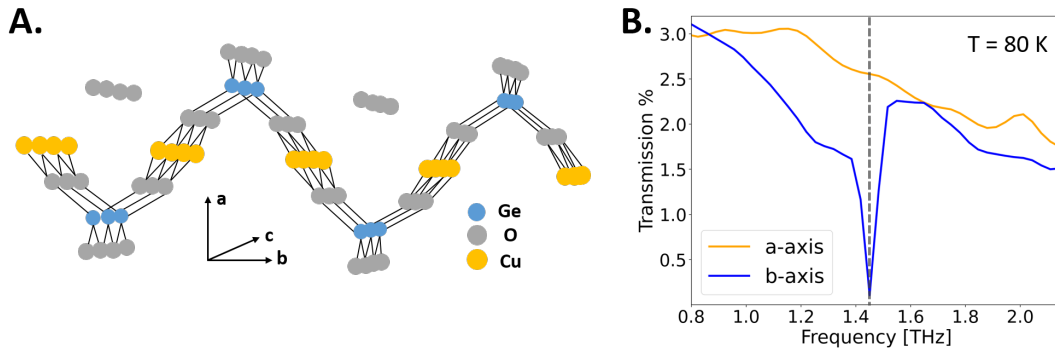


**Figure 4.1: Terahertz linear spectroscopy of  $\text{CuGeO}_3$ .** **A.**  $\text{CuGeO}_3$  crystal structure in the normal phase. **B.**  $\text{CuGeO}_3$  static transmission at 80 K of THz light polarized along the  $a$  and the  $b$  axis measured in the open cavity configuration. Along the  $b$  axis an IR-active phonon is detected at 1.45 THz.

Due to symmetry selection rules [145] the targeted  $B_{2u}$  phonon can be measured only with a THz electric field polarized perpendicular to the magnetic chains (and hence lying along the  $b$  axis), while no absorption is present at the phonon energy when the THz radiation is polarized along the chains (and hence along the  $a$  axis). For this reason

the sample was oriented in order to have the  $b$  axis lying along the same direction of the input THz field.

The frequency-dependent transmission at 80 K of the 20  $\mu\text{m}$  thick  $\text{CuGeO}_3$  crystal employed in this study is presented in Figure 4.1B in the cases when the THz field is polarized along the  $a$  and along the  $b$  axis. The 80 K  $b$  axis transmission spectrum exhibits a sharp absorption at  $\omega_{\text{phon}} = 1.45$  THz associated with the  $B_{2u}$  mode, while no absorption is present when the THz electric field lies along the  $a$  direction.

We clarify that both the transmission spectra presented in Figure 4.1B are measured in the open cavity configuration, i.e. when the distance between the two cavity mirrors is such that the fundamental cavity frequency lies far below the targeted phonon. In this setting, the frequency of the cavity fringes is smaller than the frequency resolution of the spectrum and the measured sample transmission can be regarded as the free space one with only a damping coefficient ( $\sim 5\%$  transmission) due to the absorption of the two semi-reflecting mirrors.

## 4.2 PHONON STRONG COUPLING EVIDENCES AT 80 K

After having characterized the bare phonon response we examined the 80 K response of the sample placed in the center of cavities with resonances across the phonon absorption. We will firstly examine the resonant configuration, i.e. when the distance between the mirrors is set in order to have the first-order cavity mode resonant with the  $\text{CuGeO}_3$  vibrational mode. We will then change the cavity resonance, map the vibro-polariton dispersion and prove that it exhibits the anti-crossing feature characteristic of the strong coupling regime (cfr Section 2.2).

### 4.2.1 RESONANT CAVITY MEASUREMENTS

We present in Figure 4.2 the THz transmission spectrum obtained when the cavity is resonant to the targeted 1.45 THz  $\text{CuGeO}_3$  phonon. The spectrum of the coupled system (blue solid line) is plotted together with the free space phonon transmission (red dashed line) and the empty cavity transmission at the phonon frequency (black dashed line). The estimated quality factor of the empty cavity at 80 K, defined as the ratio between the fundamental cavity mode ( $\omega_{\text{cav}} = 1.45$ ) and its FWHM<sup>1</sup>, is  $Q = 6.3$ .

We note that the hybrid sample-cavity system exhibits a splitting in its spectral response around the phonon frequency with a frequency separation greater than both the dissipative response of the free space phonon and the cavity linewidth, which quantifies the photon dissipative rates inside the bare cavity. The measured double-peaked spectral structure is a peculiar feature of a normal-mode splitting arising from the strong coupling between the cavity and the vibrational mode [17–20, 22, 23, 25–28, 30–33, 61].

We stress that the spectrum measured within the resonant cavity cannot be simply ascribed to a trivial phonon absorption from a field with the spectral content of the empty cavity field (black dashed line in Figure 4.2). The absorption at the phonon frequency from a spectrally-shaped THz field would also yield a double-peaked structure. However, in that case the separation between the two peaks will be dominated by the phonon linewidth rather than by the strength of the coupling between the phonon and the cavity field. In the measured spectrum, the phonon linewidth is significantly narrower than the observed splitting, hence validating the fact that the two measured bright peaks can be associated with the hybrid vibro-polariton states.

<sup>1</sup> Full Width Half Maximum.

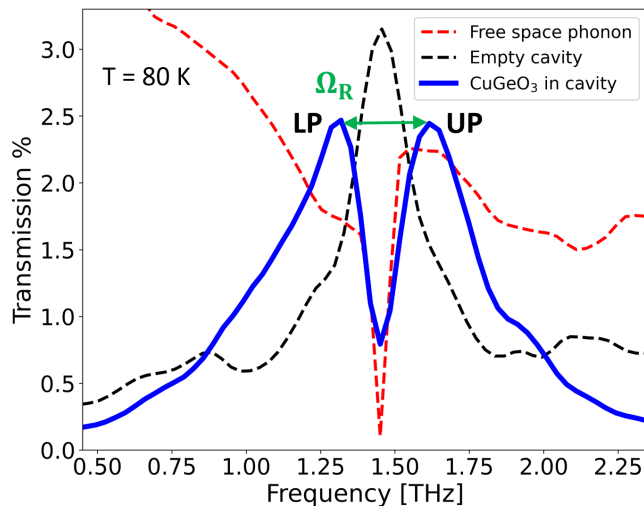


**Figure 4.2: Normal-mode splitting of  $\text{CuGeO}_3$  phonon-polaritons at 80 K.** Static transmission of  $\text{CuGeO}_3$  at 80 K in a cavity of length with the fundamental frequency resonant to the phonon one. Strong coupling between the phonon and the cavity modes results in a spectral splitting into two new modes: Upper Polariton (UP) and Lower Polariton (LP) with a separation  $\Omega_R$  greater than either the free space phonon linewidth (red dashed curve) and the empty cavity linewidth at the resonance frequency (black dashed curve).

The energy separation between the two vibro-polariton states (Rabi splitting) is estimated to be  $\Omega_R = 0.32$  THz. The measured Rabi splitting at 80 K is approximately the 22 % of the bare phonon frequency ( $\omega_{\text{phon}} = 1.45$  THz), placing the hybridized system closed to the ultrastrong coupling regime [17].

Thanks to the intrinsic phase-resolution of THz spectroscopy, the fingerprints of the vibrational strong coupling regime are visible also in the THz field exiting the coupled cavity. In order to illustrate this, we present in Figure 4.3 the comparison of the measured THz fields exiting the bare cavity (Figure 4.3A) and the bare material (Figure 4.3B) with the THz field detected at the output of the resonant hybrid system (Figure 4.3C). We note that, while in the bare systems the THz field decays as a single exponential with the lifetime set by the bare cavity and phonon dissipations, in the strongly coupled configuration the signal is an exponentially decaying field modulated by a periodic beating of period  $1/\Omega_R = 3.1$  ps (cfr Figure 2.5). This periodic modulation corresponds to coherent Rabi oscillations and indicates that there is a coherent energy exchange between photons and phonons at a rate  $\Omega_R = 0.32$  THz occurring inside the resonant cavity. We note, indeed, that if there were no splitting associated with the strong coupling regime, the cavity and the vibrational mode would be frequency-degenerate at resonance and therefore exhibit no temporal beating.

We highlight that Rabi oscillations occurring under strong coupling of molecular excitations were previously observed probing the excited state population with non-equilibrium pump-probe studies [147]. Conversely, here we are able to detect the Rabi oscillations directly in the static electric field transmitted through the coupled cavity.

As shown in Figure 4.4A, in addition to the two vibro-polaritons, the second-order cavity mode ( $m = 2$ ) is also located within the input THz bandwidth. Therefore, the input THz pulse probes a superposition of the polaritonic states with the second-order uncoupled cavity mode. This gives rise to higher frequency components within the raw output field (Figure 4.4B) which may hide the coherent Rabi oscillations. For this reason, we have filtered the raw time-domain signal with a band-pass filter [32] in order

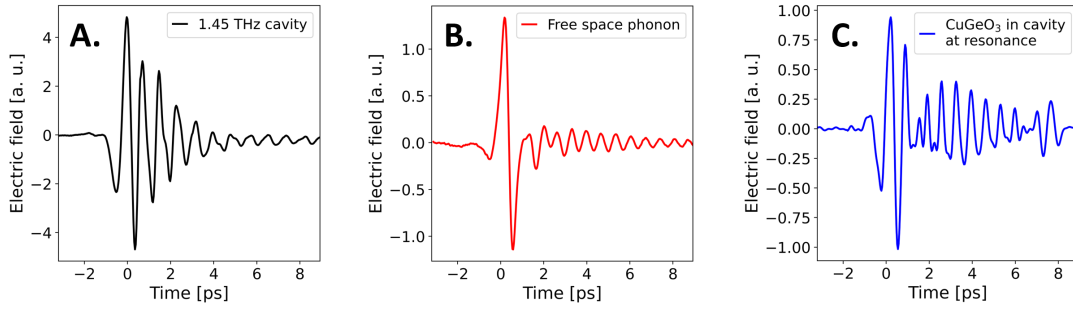


**Figure 4.3: Time-domain THz fields exiting the uncoupled systems and the strongly coupled system.** **A.** THz trace measured at the output of the resonant 1.45 THz empty cavity. **B.** Measured time-resolved THz field transmitted through the 20  $\mu\text{m}$   $\text{CuGeO}_3$  sample in the open cavity configuration. **C.** Raw THz field exiting the coupled 1.45 THz cavity. Coherent Rabi oscillations associated with the strong coupling regime can be seen in the raw field.

to exclude all the frequencies outside the 0.4 – 2.5 THz range. The filtered time-domain field is presented in Figure 4.4C. As can be seen, this filtering procedure of the time-domain data allows us to examine the evolution of the emitted field at frequencies around the resonance (1.45 THz) and, hence, to highlight more clearly the coherent energy exchange between photonic and phononic degrees of freedom associated with strong coupling.

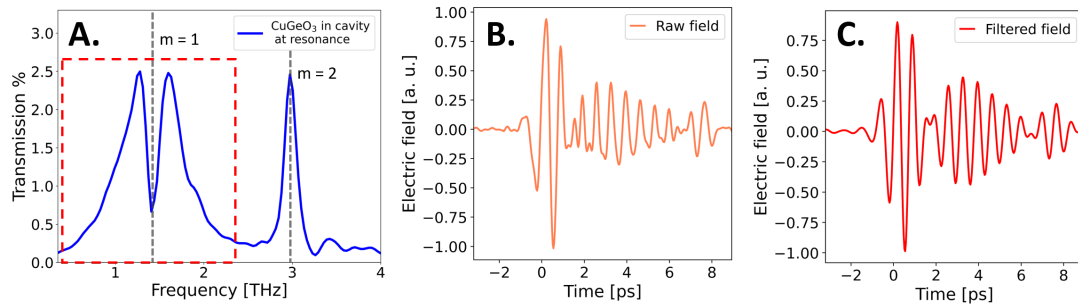


**Figure 4.4: Spectral filtering of the cavity fields.** **A.** Full frequency transmission spectrum showing the first order cavity mode strongly coupled to the phonon and the second order uncoupled mode. In the dashed box the filtering region. **B.** Raw THz field exiting the cavity at resonance. **C.** THz field obtained filtering in the region 0.4 – 2.5 THz the resonant raw field shown in B.

It is important to highlight that the measured Rabi splitting between the polaritonic modes (Figure 4.2) is not induced by the incoming THz pulse. The THz field instead acts only as a probe for the coupled states generated with the interaction with the cavity mode [18, 94]. Therefore, in order to verify that the Rabi splitting is not induced by the THz pulses, we repeated the measurement in the resonant condition with lower strengths of the incoming THz field. This was achieved by tuning the bias of the photoconductive antenna. Figure 4.5 shows the power spectra and the corresponding transmissions for five different strengths of the incoming THz field. The results show that, for the THz field strengths employed in the experiment, there is no dependence of the polaritonic resonances and linewidths on the THz intensity. This confirms that the THz field acts only as a probe of the coupled modes.

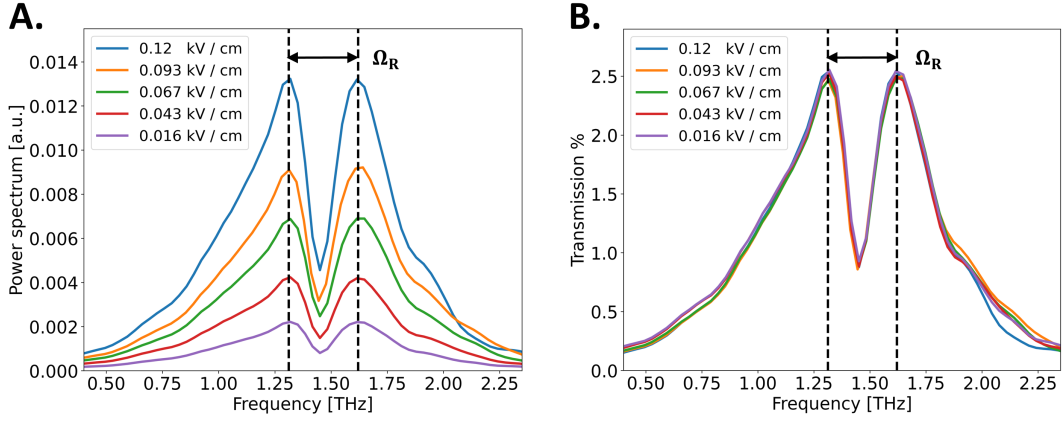


**Figure 4.5: Dependence of the phonon-polariton modes on the strength of the THz field. A.** Power spectra at the output of the resonant cavity measured with different input pulse intensities. **B.** Corresponding transmission spectra. The black vertical lines mark the measured Rabi splitting  $\Omega_R$ .

#### 4.2.2 TUNABLE CAVITY MEASUREMENTS: MAPPING POLARITON DISPERSION

After having characterized the signatures of the vibrational strong coupling of the  $B_{2u}$  phonon in the resonant cavity condition, we tuned the resonance of the cavity at 80 K and measured the anti-crossing behaviour between the two polaritonic states.

This is a distinctive feature of the strong coupling regime and corresponds to the creation of two separate polaritonic branches that do not intersect when the cavity resonance lies within the absorption band of the targeted excitation [17–20, 22, 23, 25–28, 30–33] (cfr Figure 2.4). We tracked the emergence of the two polariton branches by symmetrically tuning the position of the two mirrors around the resonant cavity mode ( $\omega_{\text{cav}} = 1.45$  THz), which is, therefore, tuned across the phonon frequency.

In Figure 4.6A we plot the THz transmission for each configuration of the mirrors and the obtained dispersion of the polaritonic branches as a function of the cavity frequency. The measured evolution of the transmission spectra shows that when the cavity is tuned away from the vibrational resonance at 1.45 THz, the frequencies of the polariton modes shift with respect to the resonant case (Figure 4.2), and their relative spectral weight is also modified. Indeed, as highlighted in Figure 4.6A, when the frequency of the cavity fundamental mode is different with respect to the phonon one, the energies of the two polariton branches approach the ones of the uncoupled system (black and red dashed lines of 4.6A). Conversely, under the resonant condition ( $\omega_{\text{cav}} = \omega_{\text{phon}}$ ) the measured difference between the polariton energies and the uncoupled systems ones is maximum. This results in the measured avoided crossing around the vibrational mode frequency.

In 4.6B we present the evolution of the filtered time-domain THz fields exiting the cavity for different detuning  $\Delta\omega = \omega_{\text{cav}} - \omega_{\text{phon}}$  around the phonon frequency. The data show that tuning the cavity mode away from the vibrational resonance is mapped in the time domain with a damping of the coherent Rabi oscillations with respect to the resonant case  $\Delta\omega = 0$ .

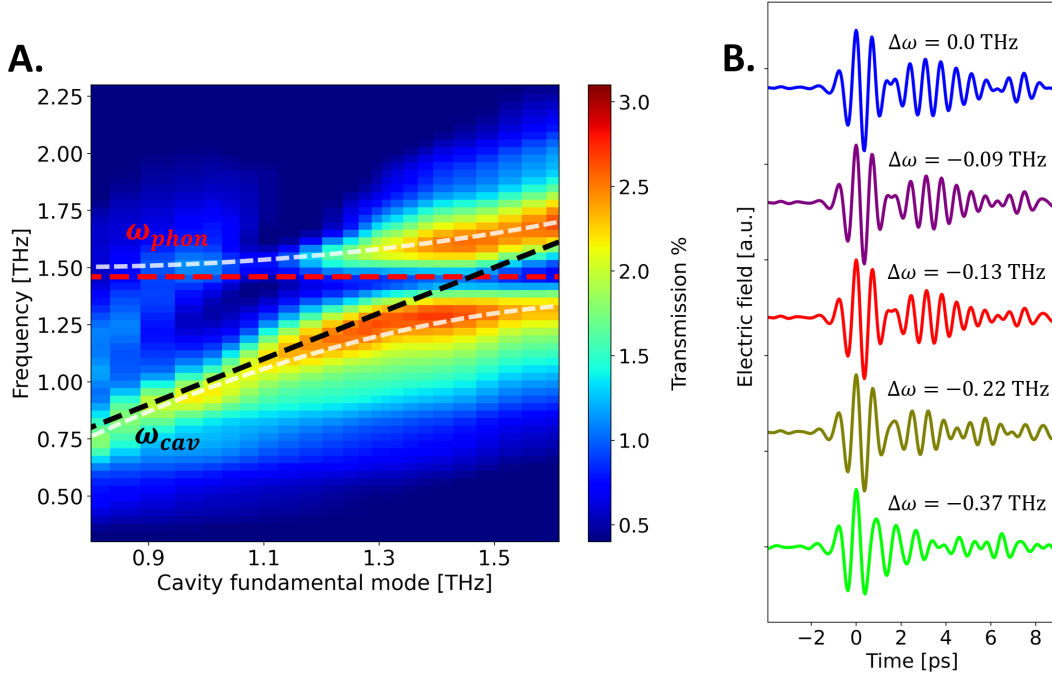


**Figure 4.6: Dependence of the phonon-polariton states on the cavity frequency.** **A.** Frequency dispersion of CuGeO<sub>3</sub> phonon-polaritons at 80 K. The red dashed line marks the uncoupled phonon frequency  $\omega_{\text{phon}} = 1.45$  THz, while the black dashed one marks the uncoupled cavity mode  $\omega_{\text{cav}}$ . **B.** Evolution of the filtered THz fields exiting the cavity at 80 K for different detunings  $\Delta\omega = \omega_{\text{cav}} - \omega_{\text{phon}}$ .

### 4.3 MODELLING PHONON STRONG COUPLING IN CuGeO<sub>3</sub>

In the previous section we have experimentally proved the strong coupling regime of the B<sub>2u</sub> mode in CuGeO<sub>3</sub> at 80 K. In this section we will take advantage of the linear models presented in Chapter 2 to simulate the experimental spectra. In particular, we will exploit the coupled oscillator model to estimate the mixing wave-function components of the polaritonic states and the Transfer-matrix method to simulate the full transmission spectra at all the detunings and gain insight about the polaritons' linewidth. We will lastly prove that, thanks to the high oscillator strength of the targeted mode, the employed quality factor ( $Q = 6.3$ ) is sufficient to overcome the strong coupling threshold.

#### 4.3.1 ESTIMATION OF THE COMPONENTS OF THE POLARITON WAVE-FUNCTIONS

Let us model the vibrational strong coupling in CuGeO<sub>3</sub> as the interaction between  $N$  dipole-active phonons with a single tunable cavity mode. Recalling the Tavis-Cummings approximation within the coupled oscillator model (Section 2.2.1) the upper and lower polariton wave-functions ( $|LP\rangle, |UP\rangle$ ) can be expressed on the uncoupled phonon/cavity

bases as follows (cfr Equation 2.25):

$$\begin{aligned} |\text{LP}\rangle &= \chi_{\text{cav}}^{\text{LP}}(\Delta\omega)|G, 1\rangle + \chi_{\text{phon}}^{\text{LP}}(\Delta\omega) \sum_{i=1}^N |e_i, 0\rangle \\ |\text{UP}\rangle &= \chi_{\text{cav}}^{\text{UP}}(\Delta\omega)|G, 1\rangle + \chi_{\text{phon}}^{\text{UP}}(\Delta\omega) \sum_{i=1}^N |e_i, 0\rangle \end{aligned} \quad (4.2)$$

In Equation 4.2 we have indicated with  $|G, 1\rangle$  the purely cavity state in which we have no phonon excitations and one photon inside the cavity, and with  $\sum_{i=1}^N |e_i, 0\rangle$  the purely vibrational state in which the cavity is in its ground state  $|0\rangle$  and each vibrational dipole is in its first excited state  $|e_i\rangle$ . Importantly, for each value of the cavity detuning  $\Delta\omega$ , the coefficients of the polaritonic wave-functions expressed in Equation 4.2 must satisfy the relation :

$$\begin{cases} \chi_{\text{phon}}^{\text{LP}}(\Delta\omega) = \chi_{\text{cav}}^{\text{UP}}(\Delta\omega) \\ \chi_{\text{cav}}^{\text{LP}}(\Delta\omega) = -\chi_{\text{phon}}^{\text{UP}}(\Delta\omega) \end{cases} \quad (4.3)$$

$|\chi_{\text{cav}}^{\text{LP/UP}}(\Delta\omega)|^2$  and  $|\chi_{\text{phon}}^{\text{LP/UP}}(\Delta\omega)|^2$  are therefore the cavity and phononic fraction of the lower/upper polariton wave-function [79] and can be expressed as a function of the collective coupling constant  $g_c = g\sqrt{N} = 2\Omega_R$  as:

$$\begin{aligned} |\chi_{\text{cav}}^{\text{LP/UP}}(\Delta\omega)|^2 &= \frac{1}{1 + \left( \frac{E_{\text{LP/UP}}(\Delta\omega) - \omega_{\text{phon}}}{g_c} \right)^2} \\ |\chi_{\text{phon}}^{\text{LP/UP}}(\Delta\omega)|^2 &= \frac{1}{1 + \left( \frac{g_c}{E_{\text{LP/UP}}(\Delta\omega) - \omega_{\text{phon}}} \right)^2} \end{aligned} \quad (4.4)$$

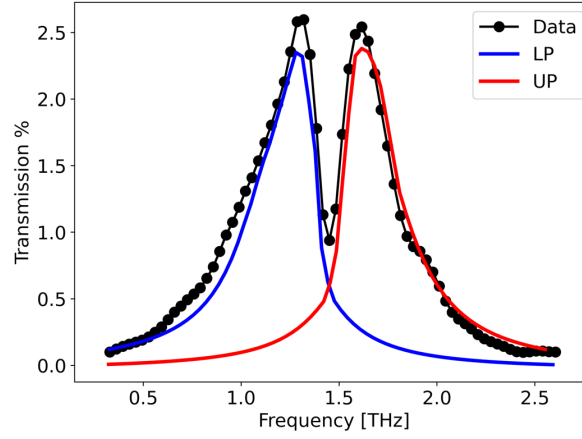
where  $\Omega_R$  is the Rabi splitting measured in the resonant configuration ( $\Delta\omega = 0$ ). For the present setting we estimated  $\Omega_R = 0.32$  THz (Figure 4.2). Therefore, by extracting the vibro-polariton energies from the dispersion measured in Figure 4.6A and using Equation 4.4 we can estimate within the coupled oscillator framework the wave-function components of the hybrid states.

Figure 4.8A shows the measured frequencies of the upper and lower polariton branches as a function of the cavity fundamental frequency. The latter have been obtained by fitting for each value of the cavity length a two oscillator asymmetric Voigt function [148, 149] to the experimental transmission spectra of Figure 4.6A<sup>2</sup>. A representative fitted spectrum is presented in Figure 4.7.

The estimation of the phonon and cavity fractions of the lower and upper polariton branches are shown in Figures 4.8B, and 4.8C respectively. We note that, as the lower polariton branch approaches the vibrational energy  $\omega_{\text{phon}}$ , its phononic (cavity) fraction increases (decreases). Conversely, as the upper polariton branch approaches the cavity dispersion  $\omega_{\text{cav}}$ , its cavity (phononic) fraction increases (decreases). Within the coupled oscillator framework we are therefore able to demonstrate that the CuGeO<sub>3</sub> vibro-polaritons exhibit more phonon-like or cavity-like physical properties depending

<sup>2</sup> We modelled the asymmetry with a Voigt lineshape with a frequency-dependent linewidth

$\Gamma(\omega) = \frac{2\Gamma_0}{1 + e^{\alpha(\omega - \omega_0)}}$ , where  $\alpha$  is the asymmetry parameter,  $\Gamma_0$  the frequency-independent linewidth, and  $\omega_0$  the central frequency of the oscillator.



**Figure 4.7: Fitted polariton spectrum of strongly coupled  $\text{CuGeO}_3$ .** Fit of the transmission spectrum of the strongly coupled  $B_{2u}$  phonon with a two mode asymmetric Voigt function. In black dot the raw data, in blue (red) the deconvoluted lower (upper) polariton components of the experimental spectrum.

on the detuning. This aspect is of major importance for the polaritonic field in processes like polariton Bose-condensation [80–82] or polariton lasing [83–85].

Importantly, as highlighted in Figures 4.8B and 4.8C, the estimated cavity (phonon) fractions of the upper and lower polariton wave-functions crosses when the detuning of the cavity approaches the frequency of the vibrational mode  $\omega_{\text{phon}} = 1.45$  THz, i.e. near the resonant configuration. In this case we note that  $|X_{\text{cav}}^{\text{LP}}|^2 \simeq |X_{\text{cav}}^{\text{UP}}|^2 \simeq 0.5$ , and  $|X_{\text{phon}}^{\text{LP}}|^2 \simeq |X_{\text{phon}}^{\text{UP}}|^2 \simeq 0.5$ . Our estimation confirms therefore that on resonance the vibro-polariton states are in a superposition of a half cavity state  $|G, 1\rangle$  and a half excited phonon state  $\sum_{i=1}^N |e_i, 0\rangle$ .

To further consolidate the estimations presented in Figure 4.8, we computed the sum of the cavity and photon components of the upper and lower branches as a function of the detuning. We show that the normalization condition  $|X_{\text{cav}}^{\text{LP}}|^2 + |X_{\text{cav}}^{\text{UP}}|^2 = |X_{\text{phon}}^{\text{LP}}|^2 + |X_{\text{phon}}^{\text{UP}}|^2 = 1$  is satisfied within the errors for the estimated phonon fraction (Figure 4.9A), and, symmetrically, for the cavity fraction (4.9B). This validates the accuracy of the estimations presented in Figure 4.8.

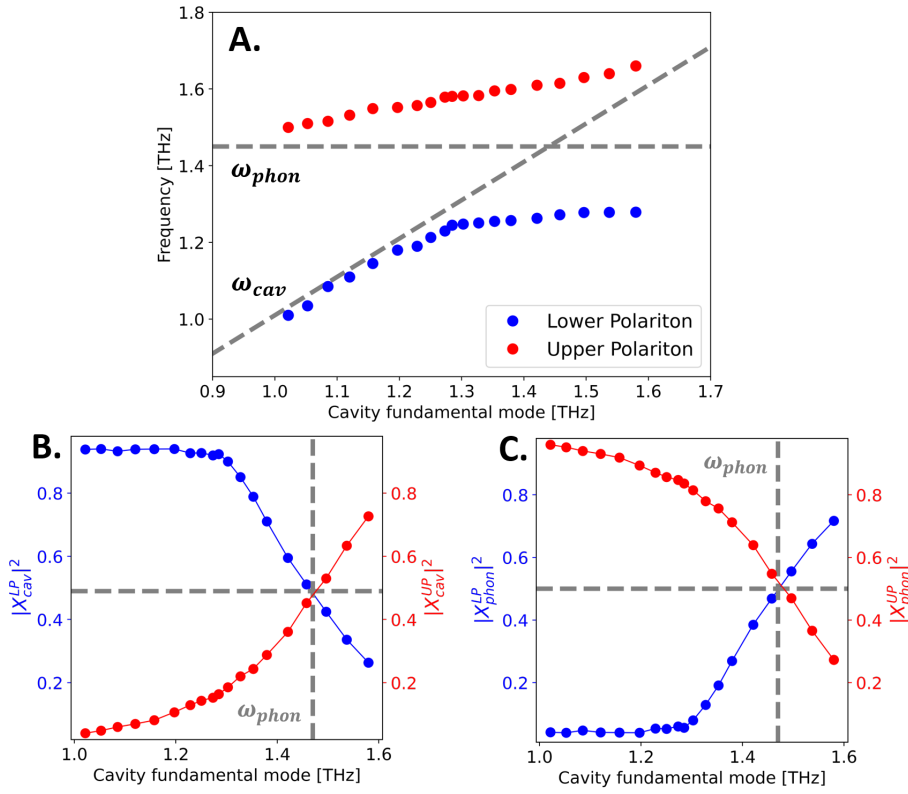


**Figure 4.8: Estimated wave-function components of the cavity-phonon hybrid states.** **A.** THz vibro-polariton branches of strongly coupled CuGeO<sub>3</sub>. The points correspond to the measured polariton peaks, obtained by scanning the cavity resonance across the phonon absorption (marked by the horizontal dashed line). **B.** Photon fraction of the lower (blue) and upper (red) polariton wave-function as a function of the cavity frequency obtained. **C.** Phonon fraction of the lower (blue) and upper (red) polariton wave-function as a function of the cavity fundamental mode. The polariton wave-function components presented in B. and C. have been estimated within the coupled oscillator model (Equation 4.4).

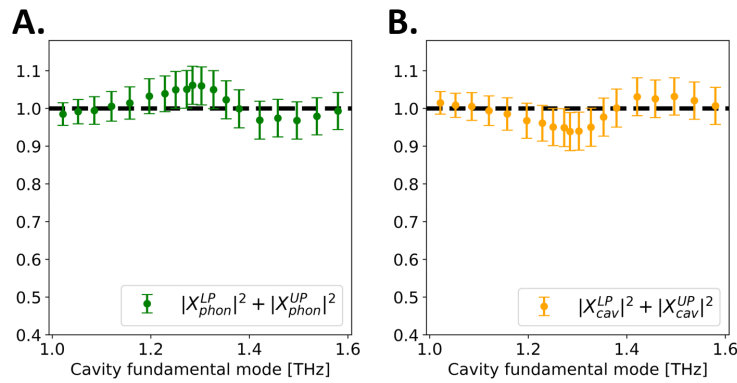


**Figure 4.9: Sum of the cavity and phonon fraction of the polaritonic wave-functions.** **A.** Sum of the photon fraction of the upper and lower polariton wave-functions. **B.** Symmetrical sum of the phonon fraction of the upper and lower polariton wave-functions. The black dashed line marks the normalization condition  $|X_{cav}^{LP}|^2 + |X_{cav}^{UP}|^2 = |X_{phon}^{LP}|^2 + |X_{phon}^{UP}|^2 = 1$ .

### 4.3.2 TRANSFER-MATRIX SIMULATIONS

In order to simulate the full transmission spectra of the coupled cavity at 80 K we exploited the classical Transfer-matrix method, which, in the linear regime, gives the same predictions of the fully quantum model [60, 94, 95] (see Section 2.4.1).

For the simulations, we used the experimentally measured refractive index of gold [96] to model the cavity mirrors and then tuned the thickness of the gold layer to match the polaritons' linewidth measured on resonance (Figure 4.2). We followed this procedure since it should be noted that the polaritons' linewidth is greater than the bare cavity mode (black line in Figure 4.10A), even though the bare phonon is sharper, and hence longer lived, than the cavity mode. Within a coupled oscillator framework we would have instead expected the polaritons' lifetime corresponding to the average of the coupled modes [60, 150] (see Section 2.2.1). This is evidence can be ascribed to the fact that the empty cavity spectrum shown in black in Figure 4.10A is not representative of the effective cavity mode because it is measured outside the CuGeO<sub>3</sub> sample and, therefore, does not take into account all the incoherent scattering losses due to the presence of the sample's full dielectric environment. By fitting with the Transfer-matrix method the polaritons' linewidth on resonance we can therefore extract the effective cavity resonance (red dashed line of Figure 4.10B) which has been adopted for all the simulations. The latter corresponds to an empty cavity with mirrors having the gold layer with an effective thickness  $d_{eff} = 1.8$  nm.

The interaction of the single cavity mode with the phonons can be modelled classically by including in the Transfer-matrix simulations the frequency-dependent complex dielectric function of the sample [151]. The complex dielectric function  $\tilde{\epsilon}(\omega)$  of CuGeO<sub>3</sub> is accurately described in the THz range by a Lorentz-Drude model [97]:

$$\tilde{\epsilon}(\omega) = \epsilon_{\infty} + \sum_{j=1}^n S_j \frac{\omega_{0j}^2}{\omega_{0j}^2 - \omega^2 - i\omega\gamma_j}. \quad (4.5)$$

The first term  $\epsilon_{\infty}$  represents the high frequency part of the dielectric constant. Conversely, the second term gives the contribution to the dielectric constant from the  $j^{\text{th}}$  Lorentzian phonon oscillator, where  $S_j$  is the oscillator strength,  $\omega_{0j}$  is the vibrational frequency, and  $\gamma_j$  the phonon linewidth. Note that, since the system is insulating [139, 140], there is no Drude contribution to the static dielectric function.

Table 4.1 lists the fit parameters for Equation 4.5 for bare CuGeO<sub>3</sub> at 80 K. The data and the corresponding fit for the 20  $\mu\text{m}$  CuGeO<sub>3</sub> sample are shown in Figure 4.10B.<sup>3</sup>

$\epsilon_{\infty} = 2.5$	j	$\omega_{0j}$ [THz]	$\gamma_j$ [THz]	$S_j$
	1	1.45	0.076	0.41
	2	4.97	0.052	0.46

**Table 4.1: Lorentz fit parameters for bare CuGeO<sub>3</sub> at 80 K.** The higher frequency phonon has been added to fit the transmission background around the B<sub>2u</sub> low energy phonon.

<sup>3</sup> We precise that the spectrum presented in Figure 4.10B is measured in the open cavity configuration. Before fitting the data we have therefore divided the spectrum for the total transmission of the mirrors (5 %), which is frequency-independent in the employed frequency range.

In Figure 4.10C we present the simulated Transfer-matrix results for the coupled system (green lines) and their comparison with the measured spectra (blue lines) for three representative values of the detuning  $\Delta\omega$ . In the simulations, we fixed all the parameters except for the thickness of the air gap between the sample surfaces and the tunable mirrors which therefore sets the cavity fundamental resonance. In the simulations, the exact detuning for each cavity length has been extracted by removing the contribution of the vibrational resonance to the dielectric function of  $\text{CuGeO}_3$  and taking into account only its background index of refraction.

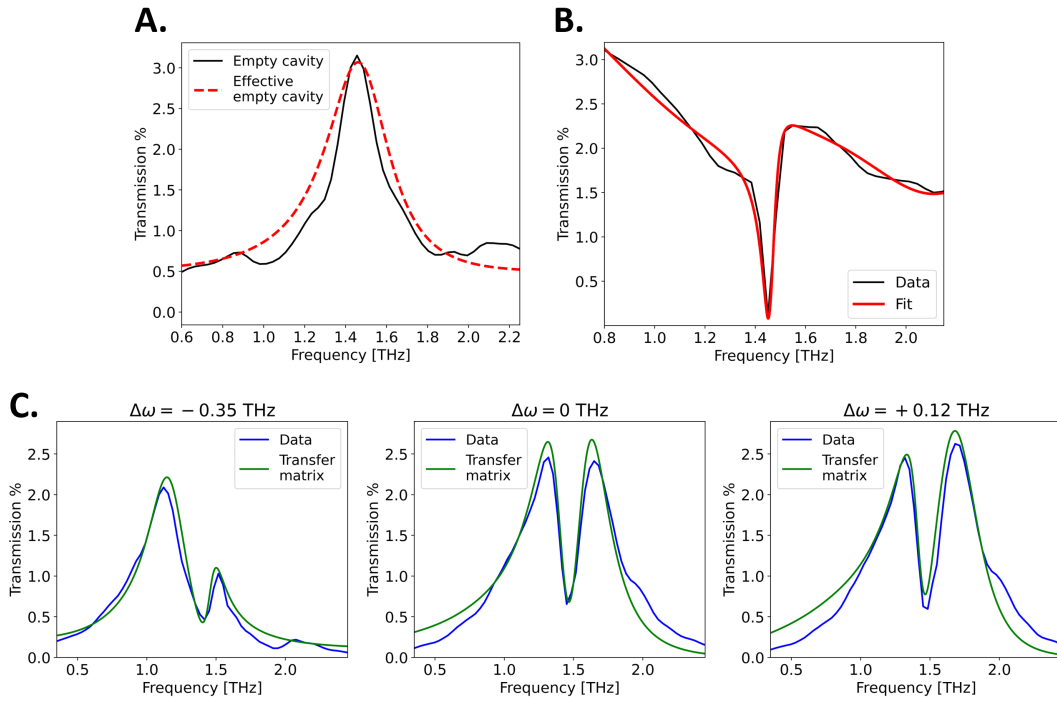


**Figure 4.10: Comparison of the cavity transmission spectra with the Transfer-matrix model**  
**A.** Comparison between the measured empty cavity spectrum at resonance (black line) and the effective empty cavity spectrum (red dashed line) adopted in the simulations to take into account the incoherent broadening of the cavity line. **B.** Phonon transmission at 80 K in the open cavity geometry (black line) and its fit with a Lorentz model (red line). **C.** Selected cavity transmission spectra at different detunings  $\Delta\omega$  (blue lines) and their comparison with the Transfer-matrix simulations (green lines).

The full comparison between the measured and the simulated vibro-polariton dispersion at 80 K is presented in Figure 4.11.

We stress that the Transfer-matrix formalism predicts the spectral response of the cavity in the linear regime [60, 152], therefore the agreement between the experimental and simulated transmission spectra further indicates that the THz field does not govern the strong coupling effect but acts instead only as a probe for the coupled oscillators.

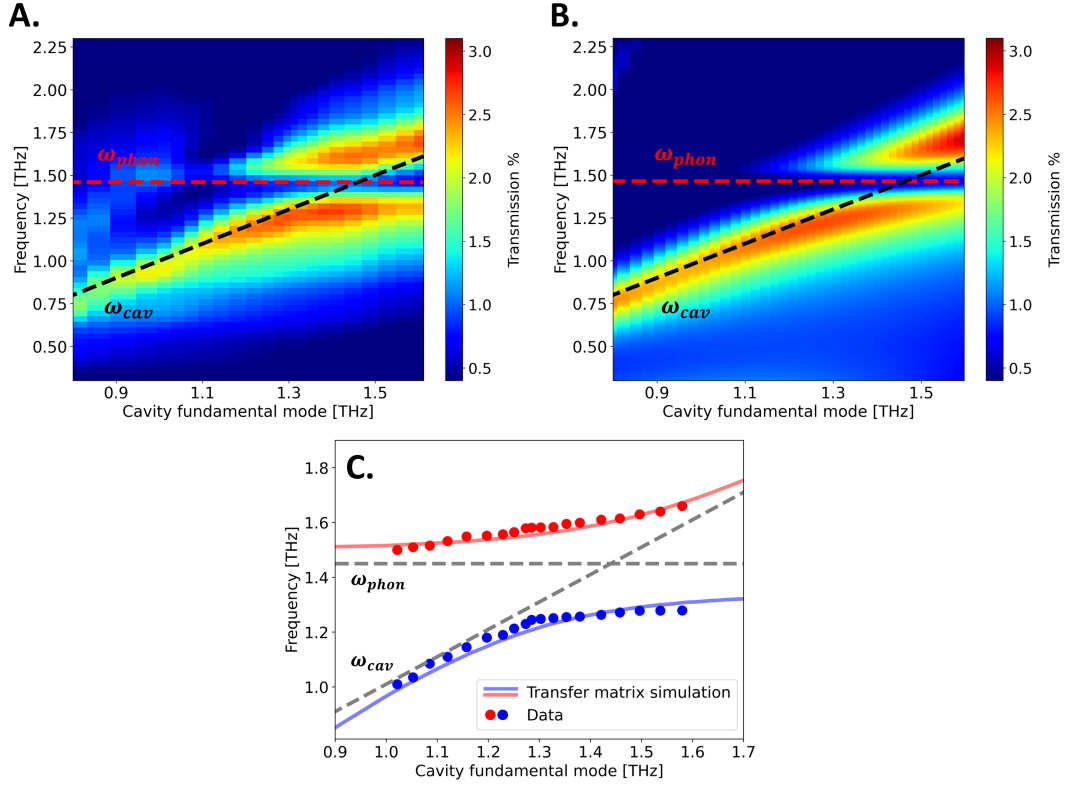


**Figure 4.11: Comparison of the measured vibro-polariton dispersion at 80 K with the Transfer-matrix simulation. A.** Measured dispersion of CuGeO<sub>3</sub> phonon-polaritons at 80 K. **B.** Polariton dispersion at 80 K simulated with the Transfer-matrix method. **C.** Measured upper (red circles) and lower polariton (blue circles) frequencies as a function of the cavity fundamental mode. The solid curves show the polariton frequencies simulated with the Transfer-matrix model.

### 4.3.3 EVOLUTION OF THE POLARITONS LINEWIDTH

We demonstrate here that the features associated to the strong coupling of the B<sub>2u</sub> phonon emerge also by looking at the linewidths of the polariton modes. It should be indeed noted that the broadening of the vibro-polaritons depends on the detuning of the cavity, given that it results from the contribution of the phonon/cavity linewidths weighted by the relative phonon/cavity fraction [60, 150].

The estimated polariton linewidths, defined as the FWHM of the deconvoluted polaritonic peaks in transmission (Figure 4.7), are presented in Figure 4.12. We note that the lower polariton branch is getting narrower when approaching the vibrational mode at  $\omega_{phon} = 1.45$  THz, whilst the upper polariton peak becomes broader moving towards the resonant cavity condition.

This evidence can be rationalized within the coupled oscillator framework (Section 2.2.1) noting that the polariton lifetime approaches the phonon (resp. cavity) one when the phononic (resp. photonic) fraction of its wave-function increases. This is highlighted in Figure 4.12B where we note that the linewidths of the two polariton branches cross in correspondence of the phonon frequency, while they tend to the broadening of the uncoupled modes in off-resonance conditions.

We stress that the measured detuning dependence of the polaritons' broadening can't be ascribed to a change in the Q factor of the effective cavity mode (orange dashed

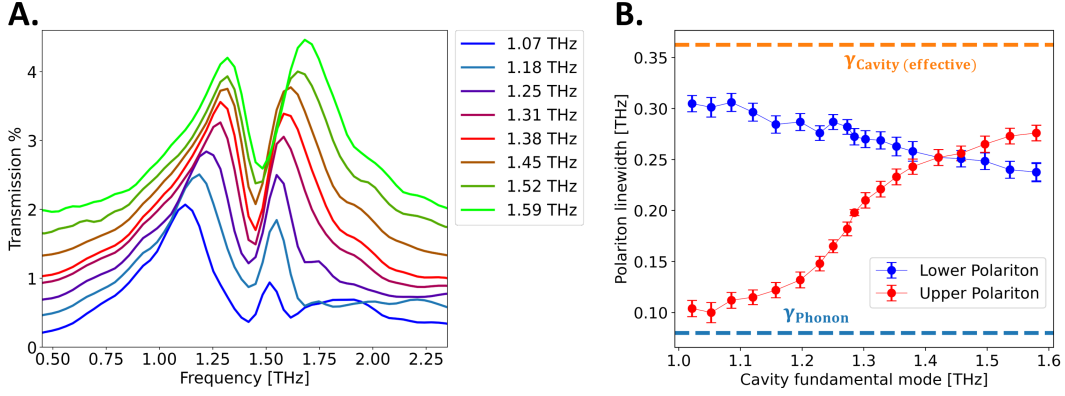


**Figure 4.12: Measured upper and lower polariton linewidths as a function of the cavity frequency.** **A.** Experimental evolution of the cavity transmission spectra at 80 K with cavity fundamental frequencies (indicated in legend) across the phonon resonance. The spectra have been vertically shifted for clarity. **B.** Estimated FWHM of the polariton modes as a function of the cavity mode. The light blue dashed line indicates the bare phonon linewidth, while the orange dashed line corresponds to the FWHM of the effective cavity mode shown in in Figure 4.10A.

line of Figure 4.12B) estimated with the Transfer-matrix method. A mode broadening of the cavity resonance would indeed not explain the narrowing of the lower polariton branch when the detuning approaches the vibrational frequency. Indeed, if the polariton lifetimes were dominated by the change of the cavity lifetime we would have expected the linewidth of both the polariton branches to follow the same trend upon changing the detuning.

Therefore, the narrowing (broadening) of the lower (upper) polariton branch as the detuning approaches the phonon frequency can be considered a further prove of the strong-coupling regime. Indeed, this narrowing (broadening) can be rationalized as an increasing contribution of the bare phonon (bare cavity) lifetime to the lower (upper) polariton lifetime.

#### 4.3.4 DEPENDENCE OF THE COUPLING ON THE QUALITY FACTOR

In this section we exploit the quantum coupled oscillator model (Section 2.2.1) to demonstrate that, thanks to the high oscillator strength of the B<sub>2u</sub> mode, the employed quality factor of the bare cavity (Q = 6.3) is sufficient to overcome the strong coupling threshold.

We recall that, within the coupled oscillator framework, the polariton splitting measured in the resonant configuration  $\Delta\omega = 0$  can be expressed as a function of the bare dissipation channels as:

$$E_{\text{UP}}(\Delta\omega = 0) - E_{\text{LP}}(\Delta\omega = 0) = \sqrt{4g_c^2 - (\gamma_{\text{phonon}} - \gamma_{\text{cav}})^2} \quad (4.6)$$

where:

$$\begin{aligned} E_{\text{LP}}(\Delta\omega = 0) &= \omega_{\text{phonon}} - \frac{1}{2} \left( \sqrt{4g_c^2 - (\gamma_{\text{phonon}} - \gamma_{\text{cav}})^2} - i(\gamma_{\text{phonon}} + \gamma_{\text{cav}}) \right) \\ E_{\text{UP}}(\Delta\omega = 0) &= \omega_{\text{phonon}} + \frac{1}{2} \left( \sqrt{4g_c^2 - (\gamma_{\text{phonon}} - \gamma_{\text{cav}})^2} - i(\gamma_{\text{phonon}} + \gamma_{\text{cav}}) \right) \end{aligned} \quad (4.7)$$

In Equations 4.6 and 4.7  $\gamma_{\text{phonon}} = 0.076$  THz is the bare CuGeO<sub>3</sub> phonon linewidth,  $\gamma_{\text{cav}}$  the effective cavity linewidth (see Figure 4.10A) and  $g_c = g\sqrt{N}$  the collective coupling constant which can be expressed as a function of the experimental Rabi splitting  $\Omega_R$  as  $g_c = 2\Omega_R = 2 \times 0.32$  THz = 0.64 THz. Since at fixed temperature (80 K) the collective coupling  $g_c$  and the phonon linewidth are fixed, the coupling regime is governed by the cavity quality factor  $Q \propto 1/\gamma_{\text{cav}}$  which dictates the lifetime of the photon inside the cavity.

The effect of the quality factor on the vibro-polariton eigenenergies of CuGeO<sub>3</sub> at 80 K, according to Equation 4.7 and for the experimental parameters written above, is presented in Figure 4.13. The real and imaginary parts of  $E_{\text{LP}}$  and  $E_{\text{LUP}}$ , corresponding to the polariton energy and linewidth, are shown in Figure 4.13A and Figure 4.13B respectively.

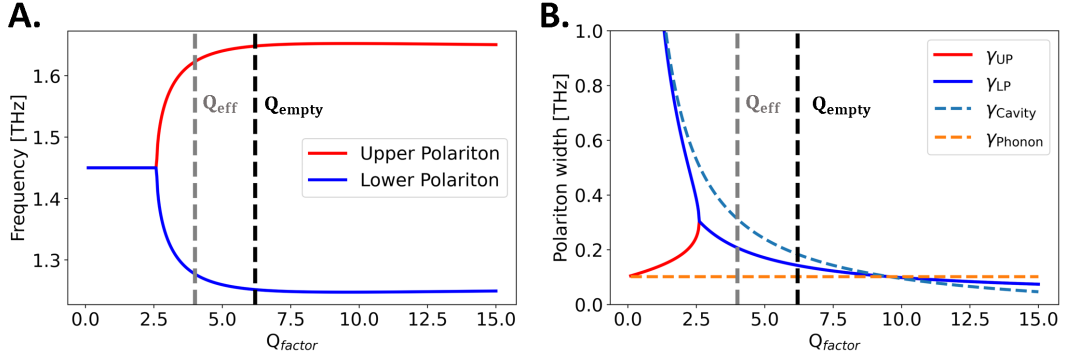


**Figure 4.13: Estimated frequency and linewidth of CuGeO<sub>3</sub> vibro-polaritons as a function of the quality factor of the bare cavity.** **A.** Calculated splitting of CuGeO<sub>3</sub> phonon-polaritons at 80 K from the coupled oscillator model. **B.** Calculated linewidth of CuGeO<sub>3</sub> phonon-polaritons at 80 K from the coupled oscillator model. Both the calculation has been made in the resonant condition ( $\Delta\omega = 0$ ). The black dashed line indicates the measured quality factor of the resonant empty cavity ( $Q_{\text{empty}}$ ), while the grey dashed line the effective quality factor ( $Q_{\text{eff}}$ ) which takes into account the incoherent broadening of the empty cavity resonance. The effective quality factor of the bare cavity is estimated to be in the strong coupling region, confirming the observed polariton splitting.

The coupled oscillator calculations show that for a bare quality factor  $Q_{\text{empty}} = 6.3$  (corresponding to an effective quality factor  $Q_{\text{eff}} = 4.0$ ) the phonon is strongly coupled to the cavity mode, as can be seen by the energy splitting of the two polariton branches. Within this model we note that, for our effective quality factor, the predicted broadenings of the polariton peaks ( $\gamma_{\text{LP}}, \gamma_{\text{LUP}}$ ) equal the average value of the uncoupled phonon and photon linewidths.

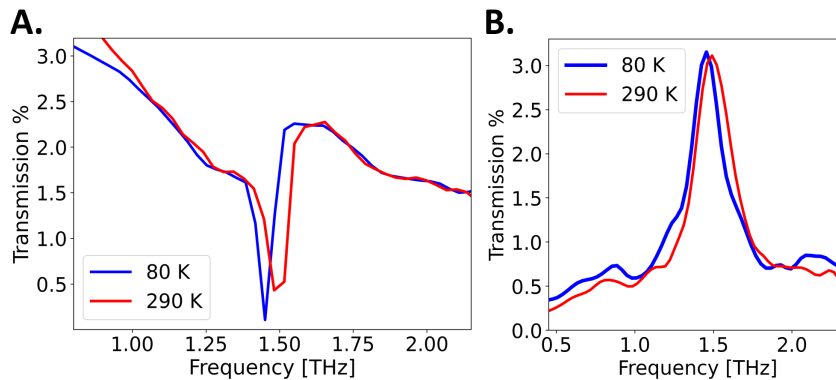
We stress that an effective quality factor  $Q_{\text{eff}} = 4.0$  is sufficient for having the relation  $\gamma_{\text{LP}}, \gamma_{\text{LUP}} < \Omega_R$  satisfied. The latter condition is indeed necessary to make the two strongly coupled modes distinguishable in the frequency spectrum (see Equation 2.36).

#### 4.4 TEMPERATURE EVOLUTION OF THE VIBRO-POLARITON MODES

In the previous section we have demonstrated the vibrational strong coupling of the  $B_{2u}$  phonon of  $\text{CuGeO}_3$  at 80 K. In this section we present the study of the temperature evolution of the strongly-coupled polaritonic modes above the spin-Peierls transition.

The targeted  $B_{2u}$  mode shows an anomalous monotonic blue shift across the  $\text{CuGeO}_3$  normal phase when the temperature is increased from 14 K to 300 K. This anomalous blue shift is associated with a line broadening due to the phonon thermal distribution [139, 140].

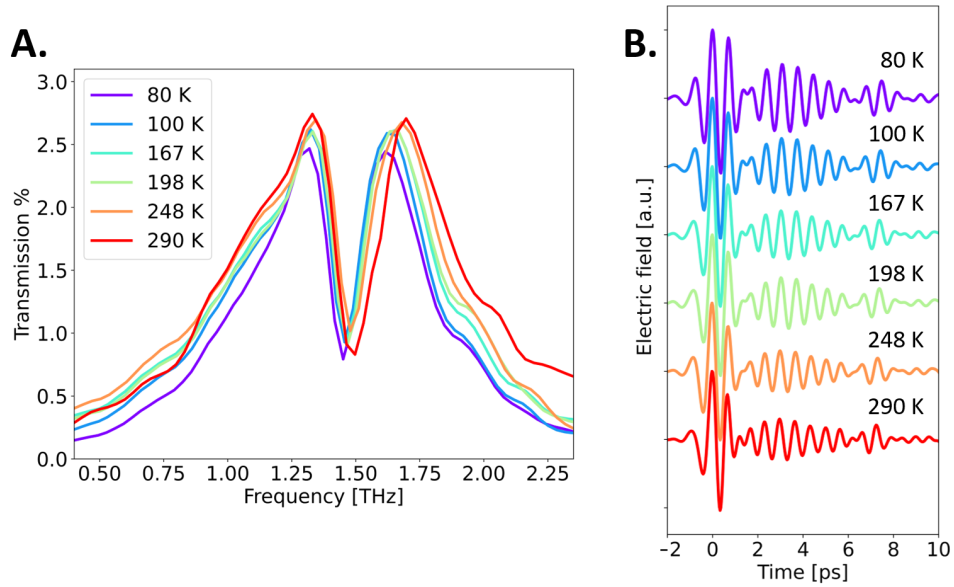
Figure 4.14A reports the comparison between the bare phonon transmission at 80 K and 290 K in the open cavity geometry. We detected a blue shift of the vibrational Cu-O mode of approximately the 3 % and a linewidth broadening of  $\sim 50$  %. We stress that, as presented in Figure 4.14B, no significant change in the broadening of the bare cavity is instead measured upon increasing the temperature. This is a crucial aspect in the temperature-dependent analysis since it implies that, within a linear approximation<sup>4</sup>, any change in the parameters of the polaritonic modes has to be linked to a change of the bare phonon resonance.



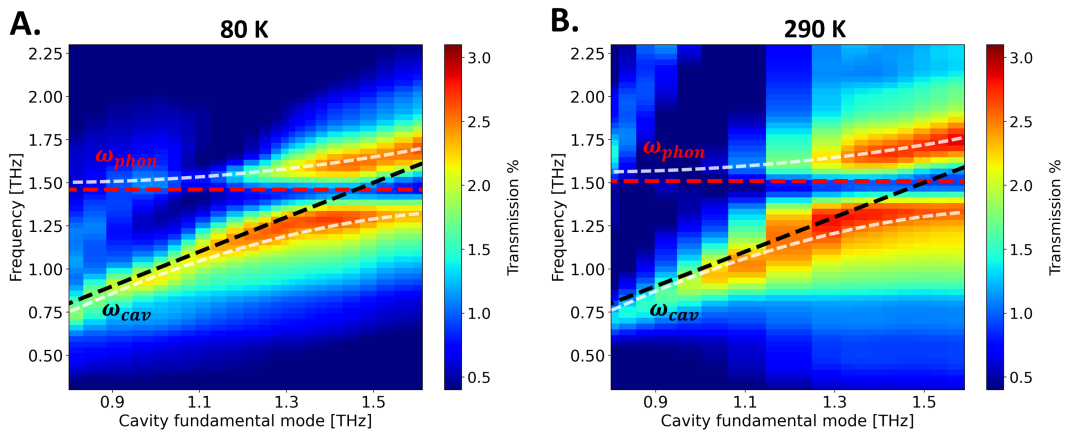
**Figure 4.14: Change in temperature of the bare phonon and of the bare cavity mode. A.** 80 K and 290 K THz transmissions of the bare  $\text{CuGeO}_3$  phonon in the open cavity configuration. A relative blue shift of the phonon mode together with an increase of the linewidth is detected going from 80 K to 290 K **B.** Resonant bare cavity transmission measured at 80 K and 280 K. No significant change of the linewidth of the bare cavity is measured.

Figure 4.15 presents the full temperature evolution of the polariton spectra across the undistorted phase of  $\text{CuGeO}_3$ . We note that, upon increasing the temperature, the splitting frequency  $\omega_0$  between the two polariton modes shifts towards higher frequencies and the linewidths of the two polaritons become broader. We highlight in Figure 4.15B that the reduction of the polaritons lifetime upon increasing the temperature can be directly visualized in the time-domain THz fields exiting the cavity. At higher temperatures we measured indeed a reduction of the Rabi oscillations' envelope which is associated to a shorter polaritons' lifetime.

<sup>4</sup> The linear regime has been demonstrated in Figure 4.5 by studying the fluence dependence of the probing THz field on the polaritonic modes.



**Figure 4.15: Frequency and time-domain temperature-dependent spectra of  $\text{CuGeO}_3$  polariton modes at resonance.** **A.** THz transmission spectra of  $\text{CuGeO}_3$  phonon within a resonant cavity measured at different temperatures. **B.** Temperature-dependent THz time traces detected at the output of the resonant cavity and filtered in the range 0.4 – 2.5 THz.



**Figure 4.16: Comparison between low and high temperature dispersion of the vibro-polaritons in  $\text{CuGeO}_3$ .** **A.** Vibro-polariton dispersion in  $\text{CuGeO}_3$  at 80 K. **B.** Vibro-polariton dispersion in  $\text{CuGeO}_3$  at 290 K.

We further proved that the measured polariton broadening is related to an intrinsic modification of the phononic resonance by mapping the full polariton dispersion as a function of the cavity detuning at 80 K and 290 K. The measured dispersions are presented in Figure 4.16. The results show that at 290 K the polaritons linewidths are greater than the 80 K ones for each detuning. This further demonstrates that the measured broadening of the polariton resonances can't be ascribed to a change of the cavity mode upon temperature increasing.

The temperature evolution of the measured parameters of the polariton modes (splitting frequency  $\omega_0$ , linewidth  $\gamma$  and Rabi splitting  $\Omega_R$ ) is presented in Figure 4.17. Upon increasing the temperature, we estimated a monotonic blue shift of the splitting frequency (Figure 4.17A) and a monotonic broadening of both the upper and lower polariton resonances with a similar trend (Figure 4.17B).

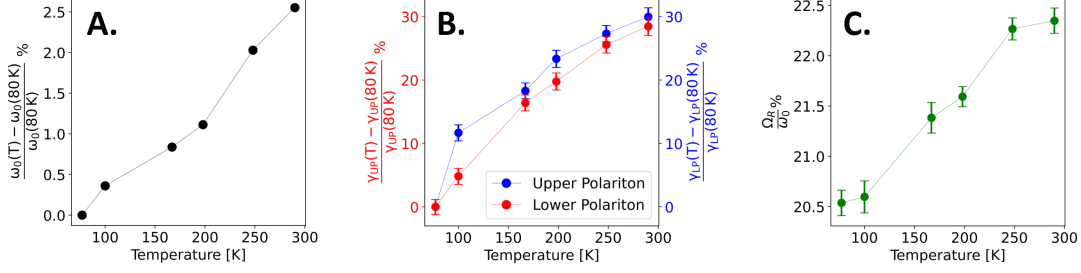


**Figure 4.17: Temperature dependence of the polariton parameters.** Temperature dependence of the percentage change in splitting frequency  $\omega_0$  (A), linewidth  $\gamma_{UP,LP}$  (B), and normalized Rabi splitting  $\Omega_R/\omega_0$  (C) of the CuGeO<sub>3</sub> phonon-polariton modes.

As highlighted in Figure 4.17C, we note that also the Rabi splitting between the vibropolaritons slightly changes with temperature. This can be interpreted by recalling the dependence of the Rabi splitting on the bare dissipation rates ( $\gamma_{cav}$ ,  $\gamma_{phon}$ ):

$$\Omega_R = \sqrt{4g_c^2 - (\gamma_{phon} - \gamma_{cav})^2} \quad (4.8)$$

Equation 4.8 indicates that, if the polariton resonances are sharp enough to be resolved, the Rabi splitting can be enhanced by a smaller mismatch between the bare linewidths ( $\gamma_{cav} - \gamma_{phon}$ ).

To further validate the previous predictions we performed Transfer-matrix simulations of the strongly-coupled cavity at different temperatures. As demonstrated in Figure 4.14, we can assume that the only input parameter which significantly changes with temperature is the dielectric function  $\epsilon(\omega)$  of CuGeO<sub>3</sub>. We present in Figures 4.18A and 4.18B the comparison between the 80 K and the 290 K phonon transmission with the corresponding Lorentz-Drude fit (Equation 4.5). We list in Table 4.2 the fit parameters for bare CuGeO<sub>3</sub> at 290 K.

$\epsilon_\infty = 2.5$	j	$\omega_{0j}$ [THz]	$\gamma_j$ [THz]	$S_j$
	1	1.50	0.115	0.39
	2	4.92	0.143	0.38

**Table 4.2: Lorentz fit parameters for bare CuGeO<sub>3</sub> at 290 K.** The higher frequency phonon has been added to fit the transmission background around the B<sub>2u</sub> low energy phonon.

Figure 4.18D presents the results of the Transfer-matrix simulations at 80 K and 290 K using for the dielectric constant of  $\text{CuGeO}_3$  the Drude-Lorentz parameters shown Tables 4.1 and 4.2 respectively.

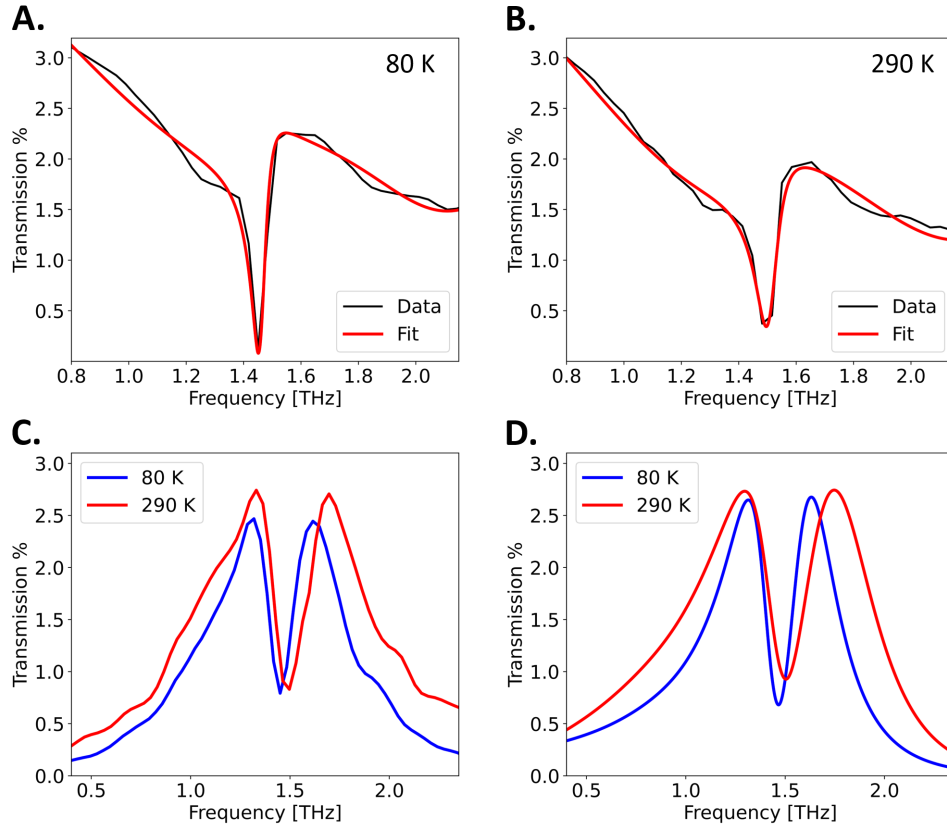


**Figure 4.18: Comparison between the measured and the simulated polaritonic spectra at 80 K and 290 K.** A. Phonon transmission at 80 K in the open cavity geometry and its fit with the 80 K Lorentz model. B. Phonon transmission at 290 K in the open cavity geometry and its fit with the 290 K Lorentz model. C. Comparison between the polariton spectra measured on resonance at 80 K and 290 K. D. Transfer-matrix simulations of the vibro-polariton spectra at 80 K and 290 K exploiting the  $\text{CuGeO}_3$  dielectric function obtained from the fits in A. and in B.

As highlighted by the comparison with the experimental transmission spectra (Figure 4.18C), the Transfer-matrix method reproduces the measured temperature-dependent polaritonic features. Indeed, the simulations predict a blue-shift of the splitting frequency together with a line broadening of the polaritonic modes. Moreover, an increase of the Rabi splitting is predicted upon raising the temperature.

We highlight that a framework in which the increase of the Rabi splitting at high temperature is due to a line broadening of the  $B_{2u}$  mode is consistent with the simulations. Indeed, by looking at the Lorentz fit parameters at 80 K and 290 K, we note that there is no significant change of the oscillator strength of the targeted mode, whereas a 50 % modification of its linewidth is estimated.

We can therefore conclude that the measured increase of the Rabi splitting (Figure 4.17C) can be justified, within the coupled oscillator framework, by the broadening of

the bare  $B_{2u}$  mode upon temperature increasing (Figure 4.14A). Indeed, since in our experimental configuration the effective cavity mode is larger than the bare phonon resonance at each temperature, we will have:

$$|\gamma_{\text{cav}} - \gamma_{\text{phon}}(80 \text{ K})| > |\gamma_{\text{cav}} - \gamma_{\text{phon}}(290 \text{ K})|.$$

This, following Equation 4.8, justifies the increase of the Rabi splitting at higher temperatures. The results point therefore to a scenario in which the temperature change of the Rabi splitting is mainly linked to a thermal change of the lifetime of the  $B_{2u}$  phonon mode and not to a modification of its oscillator strength.

## 4.5 CONCLUSIONS

In conclusion, we have demonstrated the THz signatures of the vibrational strong coupling regime of an IR-active phonon in the normal phase of  $\text{CuGeO}_3$ . Strong coupling with the cavity field results in the formation of hybrid vibro-polariton states which we directly observed in the time-domain as a normal mode beating, characteristic of the coherent energy exchange between the vibrational and the optical degrees of freedom. By varying the temperature across the undistorted phase of  $\text{CuGeO}_3$  we detected a thermal modification of the vibro-polariton lines, associated to a change in the bare phonon lifetime. The thermal change of the phonon dissipative rates leads to a slight enhancement of the Rabi splitting between the polaritons at higher temperatures. The results validate therefore the capability of the set-up to track temperature-dependent strong coupling features of THz excitations.

# CAVITY CONTROL OF THE METAL-TO-INSULATOR TRANSITION IN 1T-TaS<sub>2</sub>

---

The weak and strong coupling regimes described in Chapter 2, which can be obtained by placing quantum materials into resonant optical cavities, provide a unique platform to control quantum cooperative properties of matter. We present in this chapter the first experimental evidence of the reversible cavity control of a metal-to-insulator phase transition in a correlated solid state material. The large modification of the linear response observed by placing the dichalcogenide charge density wave material 1T-TaS<sub>2</sub> in tunable low energy Terahertz cavities enables a reversible touchless control of the metal-to-insulator phase transition. We revealed that a switch between conductive and insulating behaviour can be obtained by mechanically tuning the distance between the cavity mirrors and their alignment. Our finding uncovers a new path to control the macroscopic transport properties of quantum materials by changing their electromagnetic environment.

## 5.1 MOTIVATION

Light-matter interaction provide the means to control and manipulate the collective properties of complex materials. In commonly explored approaches materials are driven into highly non-equilibrium transient states where the materials are characterized by the response of excited quasi-particles, giving rise to new functionalities [3–10]. In recent years, the modification of the electromagnetic environment introduced by placing materials into resonant optical cavities is emerging as a suggestive possibility for controlling material properties at equilibrium and without out-of-equilibrium driving.

The proposal of employing light-matter coupling in optical cavities to control the properties of solid-state complex materials has stimulated in the last years a wealth of theoretical proposals [11], ranging from: enhanced superconductivity through cavity-mediated electron pairing [43–48], cavity control of the competing order between charge density wave and superconducting phases [49], cavity control of excitons [50], enhanced ferroelectricity [51–54], and cavity control of magnetic order [55].

From the experimental point of view, it has been recently proved that vacuum fields in the strong coupling regime [42] can reshape material properties even without external illumination, e.g. by changing the magneto-transport in a two dimensional material [38], suppressing the topological protection of the integer quantum Hall effect [56], or even modifying the critical temperatures in conventional and unconventional superconductors [57, 58]. These effects can be rationalized within the framework of strong light-matter coupling presented in Chapter 2 in which the coherent energy exchange between the cavity field and the resonant material excitations leads to changes of thermodynamical potentials [153].

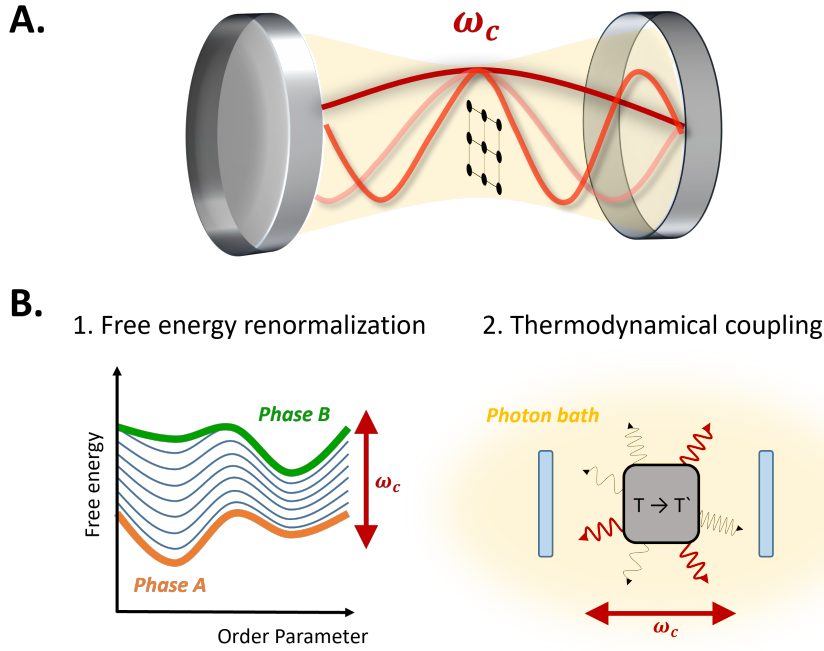


**Figure 5.1: Mechanisms of cavity control of quantum materials.** **A.** Sketch of a material embedded in the middle of a tunable optical cavity with controllable fundamental frequency  $\omega_c$  and alignment. **B.** Coupling of the material's excitations with the cavity field can act on the sample's thermodynamics within two different scenarios: it can either renormalize the free energy of one material phase with respect to the other (left panel) or reshape the material's spectral emission and subsequently rescale its temperature (right panel).

Confining materials into optical cavities provides new means to control the phase transformations in correlated systems in different mechanisms (Figure 5.1).

- On one hand, the selective coupling of the cavity modes to the excitation of a given phase can renormalize the free energy of that phase with respect to that of other ones, thereby modifying the temperature at which the phase transition occurs (left panel of Figure 5.1B).
- On the other hand, the optical cavity can reshape the exchange energy between the material and the thermal reservoir of photons in which the material is immersed [154]. In general, thermal emission can be associated with a black-body at a certain temperature which exchanges energy with its environment in the radiative form. The spectral energy density of a black-body  $u(\omega, T)$  can be expressed as [155]:

$$u(\omega, T) = E(\omega)n(\omega, T)D(\omega), \quad (5.1)$$

where  $E(\omega)$  and  $n(\omega, T)$  are respectively the mode energy and its occupation, and  $D(\omega)$  the density of states of the electromagnetic field, which can be reshaped by the cavity boundary conditions. In analogy with the Purcell effect [13–16], by engineering the local density of states of the electromagnetic environment at the sample position through tunable optical cavities, it is therefore possible to modify the absorption and emission of the coupled sample and subsequently its temperature [156–158]. The illustration of this second scenario is depicted in the right panel of Figure 5.1B.

We investigate here the metal-to-insulator transition in the transition metal dichalcogenide 1T-TaS<sub>2</sub> embedded into low energy cavities at THz and sub-THz frequencies.

Firstly, we will review the physics underlying the metal-to-insulator transition in 1T-TaS<sub>2</sub> and show how the onset of metallicity in the system is mapped onto the THz linear response, which is the employed observable (Chapter 3). We will then report the experimental evidences which hints towards a cavity-driven control of the phase transition. In particular, we will show that, while long wavelength cavities (up to  $\sim 25$  GHz) favour the metallic phase, the coupling with cavities at higher frequencies results in an effective stabilization of the dielectric charge density wave phase, giving rise to a peculiar non-monotonic renormalization with respect to the free space material. For the employed experimental setting, the modification of the effective critical temperature of the phase transition ( $\sim 70$  K) overcomes the intrinsic hysteresis in the material and enables a reversible touchless control of the metal-to-insulator phase transition, which we will prove to be sensitive to the cavity alignment. Moreover, to see whether our observation could be rationalized within the free energy scenario or within the cavity-mediated heating scenario, we performed an independent measurement campaign to address cavity-mediated changes of the sample's temperature. We will show that the sample's temperature measurements within the cavity are qualitatively consistent with the THz observations. This evidence points towards the Purcell-like scenario (Figure 5.1B, right panel) to be the dominant one in describing the cavity-driven control of the metal-to-insulator transition in 1T-TaS<sub>2</sub>. We will conclude the present chapter by presenting the full set of experimental tests performed to demonstrate the cavity-induced origin of the observed renormalization of the phase transition.

## 5.2 TERAHERTZ SPECTROSCOPY OF 1T-TaS<sub>2</sub> ACROSS THE CHARGE ORDERING TRANSITION

Transition metal dichalcogenides (TMDs) have the basic chemical structure MX<sub>2</sub>, where M is a transition metal and X a chalcogenide. From the structural point of view, TMDs form sheets of X-M-X sandwiches, which are weakly bound together by van der Waals forces. This weak interlayer coupling provides the quasi-two-dimensional character characteristic of TMDs [159]. The coordination of the metal atom in the sandwich can take on either an octahedral or trigonal prismatic shape. There are many potential polytypes resulting from the various sandwich stackings [159], with the most basic being the pure octahedral (1T) and pure trigonal prismatic (2H) structures.

Among all the quasi-two-dimensional transition metal dichalcogenides, the 1T polytype TaS<sub>2</sub> (1T-TaS<sub>2</sub>) is one of the most widely studied in the recent years. The basic crystalline structure of 1T-TaS<sub>2</sub> is depicted in Figure 5.2A. 1T-TaS<sub>2</sub> is notable for being one of the first quasi-2D materials in which a charge-density-wave state (CDW) was observed [160].

1T-TaS<sub>2</sub> exhibits four thermodynamical phases characterized by significant differences in the charge order and mobility [161], and in the CDW commensuration [162]. This temperature-dependent charge order originates from the competition of Coulomb repulsion, lattice strain, interlayer hopping, and Fermi surface nesting [163–165].

At high temperatures ( $T > 550$  K) the system presents the features of a simple metal and no charge-density-wave is present. As 1T-TaS<sub>2</sub> is cooled down below  $T = 550$  K, a CDW distortion occurs. The charge-density-wave is incommensurate with the underlying lattice within the temperature range  $550 \text{ K} > T > 350 \text{ K}$  (IC phase). Figure 5.2B

presents the crystalline structure of the Ta plane. The unit cell of the undistorted and IC phases is depicted in the upper left corner.

The frustration arising from the incommensurability of the IC state with the underlying lattice causes the IC-CDW to transform into a nearly commensurate (NC) structure at  $T \sim 350$  K in which patches of commensurately ordered hexagonal-shaped polarons are periodically separated by conductive domain walls [163, 166, 167]. Within the commensurate domain-like regions, the lattice distortion creates polaron clusters of Ta atoms in the so called "star of David" formation, with each star cluster finding itself at the corner of a new  $\sqrt{13}a \times \sqrt{13}a$  superlattice unit cell (Figure 5.2B).

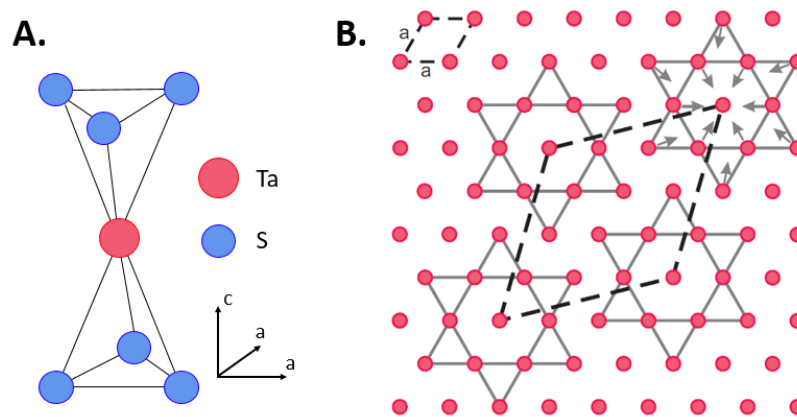


**Figure 5.2: Crystalline structure of 1T-TaS<sub>2</sub>.** A. Octahedral coordination unit forming the S-Ta-S layers. B. Sketch of the Ta plane. Without the CDW, the unit cell is that shown by the dashed line in the upper left corner. With the CDW, star-of-David cluster polaron formation takes place, shown by the solid lines. Arrows show the displacement of Ta atoms and the dashed line connecting the stars gives the new superlattice cell.

By further lowering the temperature below  $\sim 180$  K a transition to an insulating state occurs. The metallic domain walls, related to the discommensuration network of the CDW regions, disappear and the system becomes a fully commensurate charge-density-wave (C-CDW) Mott insulator [164]. The illustrations of the melting of the discommensurate CDW regions, associated with the metal-to-insulator charge ordering transition, are presented in the insets of Figure 5.3B.

Importantly, while in the nearly-commensurate CDW phase the metallic response is determined by domain wall fluctuations, below the critical temperature, in the commensurate CDW phase, domain walls lock to the crystal structure giving rise to an insulating response [164, 168].

It is worth noting that the free energy landscape of 1T-TaS<sub>2</sub> is much more complicated than the simple free energy sketch of Figure 5.1B: the phase transitions in 1T-TaS<sub>2</sub> are multiple and sensitive to the thermal history of the sample. For example, it has been recently reported [169] that upon heating from the C-CDW phase, an additional intermediate trigonal (T) phase with in-plane charge stripes occurs at  $\sim 220$  K and persists up to  $\sim 280$  K, when the NC-CDW is re-established.

We employed time-domain THz spectroscopy to track the temperature dependent charge order of 1T-TaS<sub>2</sub> for different cavity configurations. As described in Chapter 3,

THz spectroscopy is a powerful tool to track the metal-to-insulator transition associated to the metallic domain wall suppression since it is able to measure contact-less the quasi-static dielectric response associated to the presence of free conductive charges characteristic of a metallic state.

We present in Figure 5.3A the temperature dependent THz linear transmission of 1T-TaS<sub>2</sub> in free space upon heating and cooling, which captures the first order transition between the NC-CDW metallic phase and the C-CDW insulating phase. The presented THz transmission measurements have been performed on a  $\sim 15 \mu\text{m}$  thick single-crystal sample.

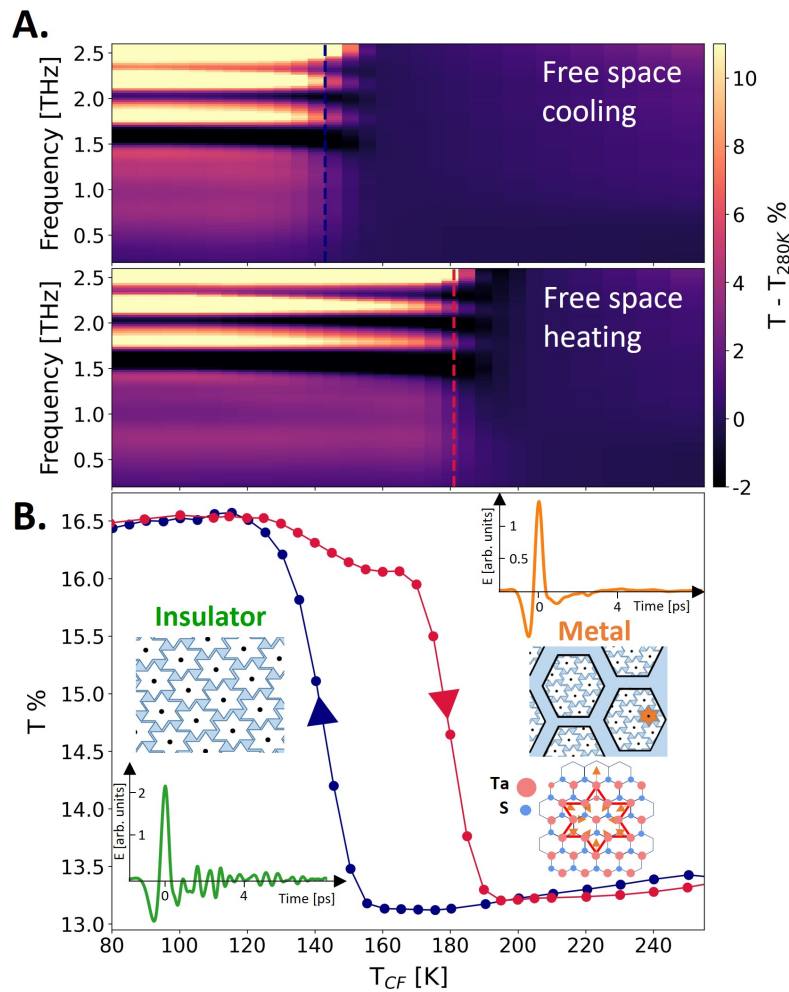


**Figure 5.3: THz linear spectroscopy of 1T-TaS<sub>2</sub> metal-to-insulator transition measured in free space.** A. THz linear transmission spectra in free space at different temperatures across 1T-TaS<sub>2</sub> metal-to-insulator transition (temperature scans performed by cooling (upper panel) and heating (lower panel)). In order to highlight the phase transition each spectrum has been subtracted from the 280 K THz transmission. B. Temperature dependence of the integrated low frequency transmission ( $0.2 \text{ THz} < \omega < 1.5 \text{ THz}$ ), marking the metal-to-insulator transition and its hysteresis. The temperature scale indicates the readout of the thermocouple in thermal contact with the cryostat cold finger. In the insets the time domain THz fields are shown for the metallic and the insulating phases, together with the illustration of the in-plane lattice modulations characteristic of the insulating C-CDW phase and of the metallic NC-CDW phase.

The optical features associated to the phase transition, which are visible within the THz range, are:

- The increase of the low frequency transmission ( $\sim 0.2 \text{ THz} < \omega < 1.5 \text{ THz}$ ) below the critical temperature. This is consistent with a transition to an insulating behaviour. The Drude-like response of free carriers is indeed reduced in the dielectric phase, which in turn gives rise to a decreased absorption within the quasi-static spectral region [170, 171].
- The emergence below  $T_c$  of IR-active optical phonons at 1.58 THz, 2.02 THz, and 2.35 THz which are allowed by the symmetry of the fully commensurate charge-density-wave. As highlighted by the full temperature scans of Figure 5.3A and by the THz time-domain traces measured in the two phases (insets of Figure 5.3B), the CDW vibrations are screened by the free carriers and therefore not visible in the metallic NC phase. As reported in [170], the screened phonon modes are followed at higher frequencies by a pseudogap-like increase of the optical conductivity which evolves in a gapped response in the dielectric state.

Importantly, as highlighted in Figure 5.4, the above features, associated to the charge ordering transition and unveiled by THz transmission, are directly linked to the thermal evolution of the optical conductivity  $\sigma_1(\omega)$ . The latter is a crucial parameter since it quantifies the absorptive contribution of the THz excitations to the 1T-TaS<sub>2</sub> dielectric function (Chapter 3), which is strongly affected by the metal-to-insulator transition.

In all the following discussion, we will use the temperature dependence of the integrated low frequency transmission ( $0.2 \text{ THz} < \omega < 1.5 \text{ THz}$ ) as a marker which tracks the charge order dynamics in 1T-TaS<sub>2</sub> and hence the metal-to-insulator phase transition (Figure 5.3B). We prove in Figure 5.5 that the measured low frequency transmission is mapped directly on the evolution of the Drude contribution to the optical conductivity  $\sigma_1(\omega)$ , representative of the free carriers response. This comparison clarifies that, at energies below the lowest-lying phonon, the integrated transmission is indeed a good indicator of the metallicity of the system and can be hence exploited to track the phase transition in different cavity configurations.

The full temperature dependence of the integrated low frequency transmission ( $0.2 \text{ THz} < \omega < 1.5 \text{ THz}$ ) for the material in free space is shown in Figure 5.3B. The difference between the results obtained upon heating and cooling the sample in free space marks the hysteresis associated to the first order phase transition. The phase transition in free space upon heating from the insulating state occurs at 181 K and at 143 K upon cooling from the metallic phase. Note that the smooth transition observed could be ascribed to the presence intrinsic inhomogeneities and strain in the system which smear out the first order transition [172–174]. A discussion on inhomogeneities, on the waiting protocol to track the phase transition, and on the determination of the critical temperature is detailed in Section 5.5 of the present chapter.

We note that the effective critical temperature measured in the employed set-up differs with respect to the literature value [164] of about 35 K. This difference is attributed to the difference between the internal temperature of the sample ( $T_S$ ) and the temperature of cryostat's cold finger ( $T_{CF}$ ), due to the high thermal dissipation of the silicon nitride membranes between which 1T-TaS<sub>2</sub> is embedded. The membranes makes therefore the sample significantly isolated from the ambient radiation. A finite elements simulation of the membrane's thermal profile, accounting for the incoherent thermal load at the sample position, is in quantitative agreement with the measured temperature shift. Further details on the simulations of incoherent radiation heating within the

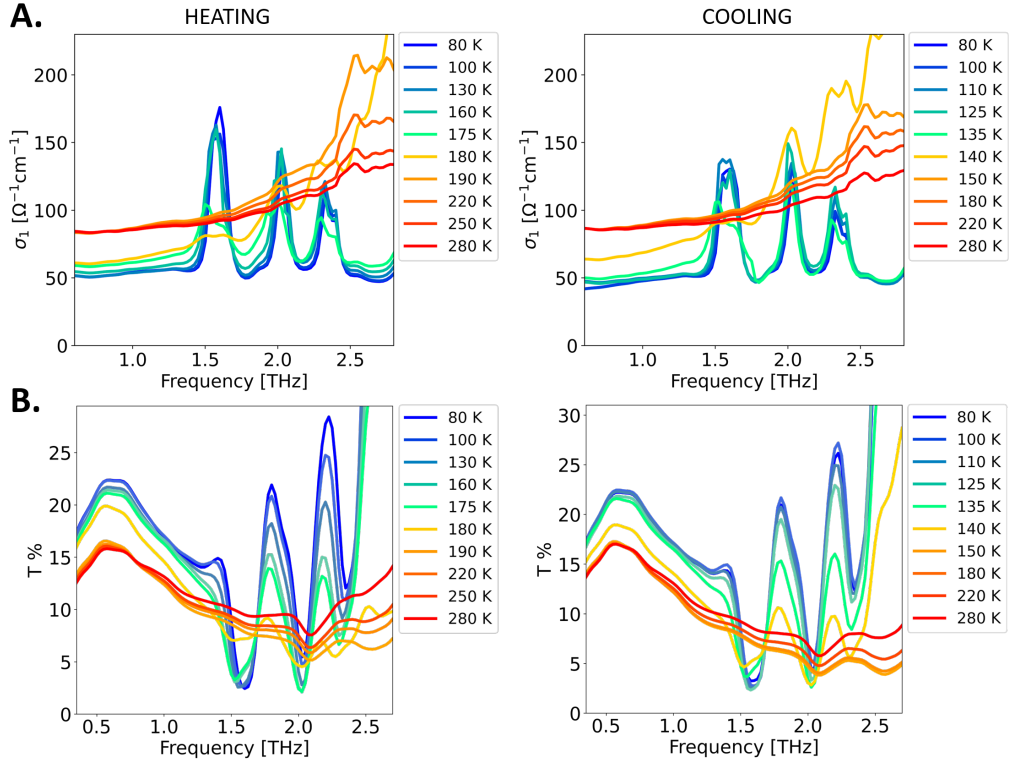


**Figure 5.4: Optical conductivity and THz transmission of 1T-TaS<sub>2</sub> across the metal-to-insulator phase transition.** **A.** Real part of the optical conductivity ( $\sigma_1$ ) measured in free space upon heating (left panel) and cooling (right panel) the sample from the insulating and metallic phase, respectively. **B.** THz transmission measured in free space at different temperatures upon heating (left panel) and cooling (right panel) the sample. Temperature evolution of  $\sigma_1$  measured upon cooling the sample from the metallic phase.

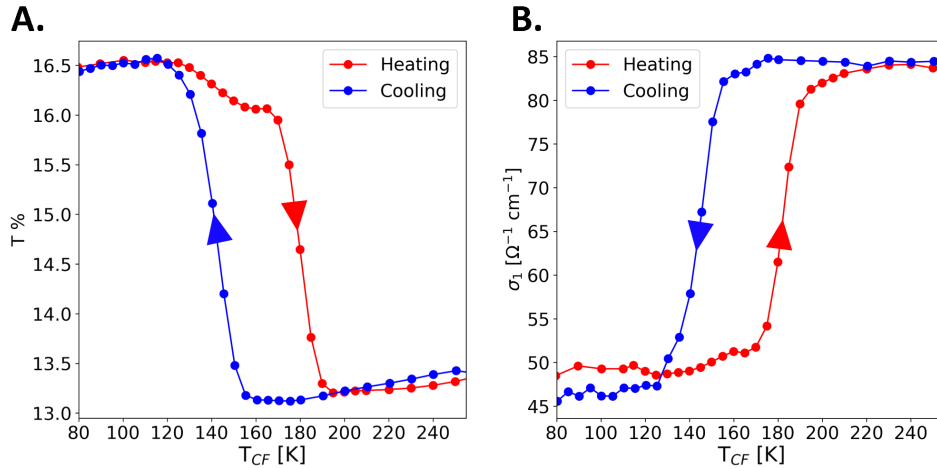


**Figure 5.5: Hysteretic behaviour of the charge ordering transition in THz transmission and optical conductivity  $\sigma_1$ .** **A.** Low-frequency transmission ( $0.2 \text{ THz} < \omega < 1.5 \text{ THz}$ ) upon heating and cooling the sample. **B.** Real part of the optical conductivity  $\sigma_1$  integrated in the same frequency range upon heating and cooling. The hysteretic behaviour of the phase transition is the same for both the observables.

cavity will be discussed in Section 5.7 of the present chapter. Despite the measured rigid shift, we stress that this critical temperature sets the absolute free space reference for all the cavity-dependent studies, since it is independent of geometrical variations of the cavity chamber (see Section 5.8.4).

An aspect which is important to highlight here is that a simultaneous measurement of the actual sample's temperature inside of the cavity ( $T_S$ ) and THz transmission is not viable. This is due to both practical and fundamental aspects. On a practical level, the placement of a physical thermometer within the cavity would absorb the THz pulses and make the transmission measurements unfeasible. On a fundamental level, any material object placed within the optical cavity will perturb the cavity characteristics and therefore the response of the light-matter assembly. For this reason, we have designed an experimental protocol in which for the THz characterization we measure the temperature on the support of the sample outside of the cavity which we denote as  $T_{CF}$ . Due to the mismatch between the sample and the cold finger temperature suggested by the free space measurements (Figure 5.3), we will refer to the critical temperatures detected through THz spectroscopy as effective critical temperatures ( $T_c^{eff}$ ). The latter will be defined as the temperature of the cold finger support ( $T_{CF}$ ) at which the phase transition is observed for a given experimental configuration. The results of the independent campaign to address the actual sample's temperature  $T_S$ , which are crucial to distinguish which of the two possible cavity-mediated scenarios of Figure 5.1 is dominant, will be discussed separately.

### 5.3 CAVITY-DRIVEN RENORMALIZATION OF THE PHASE TRANSITION

We present in this section the results pointing to a cavity renormalization of the metal-to-insulator transition when the system is resonant to cavities within the sub-THz region.

Figure 5.6 shows the temperature dependent THz linear transmission of 1T-TaS<sub>2</sub> in free space and embedded in the centre of an optical cavity with resonant frequency  $\omega_c = 11.5$  GHz and quality factor  $Q \sim 4$ . The details of the quality factor characterization of the sub-THz cavities employed in the experiments are presented in the "Methods" section of the present chapter (Section 5.5.1).

The comparison in Figure 5.6 highlights that the placement of the sample in such a cavity results in a shift of the effective critical temperature  $T_c^{eff}$  for the metal-to-insulator phase transition, which is observed at 136 K (109 K) upon heating (cooling) the coupled sample. It should be noted that the cavity-mediated shift in the effective transition temperature depends on the thermal cycle. Indeed, a renormalization of the apparent phase transition temperature of 44 K is observed if the critical temperature is approached from the dielectric state (heating), while a shift of 33 K is obtained coming from the metallic phase (cooling). Overall, this results in a cavity-mediated shrinking of the hysteresis of 11 K.

It is important to stress that the effective critical temperature measured within the cavity is independent from the input intensity of the THz field. The THz field acts therefore only as a probe for the cavity-coupled system and does not introduce a detectable thermal load at the sample position. We will justify this crucial statement in Section 5.8.5 by presenting measurements of the coupled cavity probed with different THz field strengths.

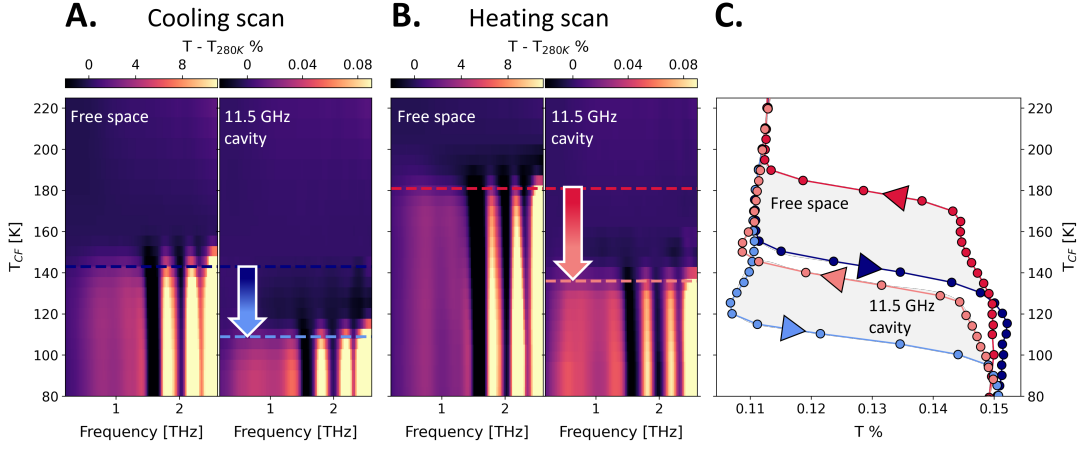


**Figure 5.6: Cavity-driven renormalization of the effective critical temperature of the metal-to-insulator phase transition.** Temperature dependent THz transmission upon cooling (A) and heating (B) for a sample held in free space (left) and one placed in the middle of the 11.5 GHz cavity (right). C. Comparison between the hysteresis in free space and within the 11.5 GHz cavity plotted as the integrated cavity transmission in the range  $0.2 \text{ THz} < \omega < 1.5 \text{ THz}$ . The free-space data have been arbitrarily translated along the horizontal axis to overlap with the cavity integrated transmission. A possible cavity-driven renormalization of the effective critical temperature of 44 K (33 K) towards lower temperatures is measured upon heating (cooling) the sample. This results in a cavity-mediated shrinking of the phase transition hysteresis of 11 K.

### 5.3.1 CAVITY ALIGNMENT DEPENDENCE

In order to show that the observed renormalization of the phase transition (Figure 5.6) hints towards a cavity-mediated effect, we varied the cavity geometry and measured the effective critical temperature  $T_c^{eff}$  as a function of the alignment of the cavity mirrors. The rationale for this is that any misalignment of the cavity will reduce the photon interaction time within the cavity and hence the cavity-driven change of sample properties. We quantify the cavity misalignment as the sum of the misalignment angles of the two cavity mirrors  $\theta$  with respect to the parallel mirrors configuration.

We stress that misaligning the mirrors only slightly modifies the cavity fundamental frequency ( $\Delta\omega_c \sim 0.14 \text{ GHz/deg}$ ) (see Section 5.8.3), but it reduces the quality factor of the cavity and hence its optical losses. This will subsequently decrease the light-matter interaction time within the cavity. Figure 5.7A illustrates the THz time domain fields in the C-CDW phase for different misalignment angles  $\theta$ . In the dashed box the THz reflection associated to the cavity round trip is highlighted. We note that upon misalignment the peak associated to the cavity round trip reduces its intensity. This is consistent with the decrease of the photon lifetime within the cavity and hence with the reduction of the quality factor of the bare cavity. The dependence of the cavity Q factor as a function of the misalignment angle has been estimated in Figure 5.7B. The estimation has been performed by approximating the exponential decay with a linear fit.

The temperature dependence of the low frequency THz transmission ( $0.2 \text{ THz} < \omega < 1.5 \text{ THz}$  integration range) at different mirrors alignment is shown in Figure 5.8A for the heating and cooling temperature scans. We highlight that changing the optical losses through the cavity alignment in turn reduces the renormalization of the observed critical temperature (Figure 5.6) towards the free space value (Figure 5.3).

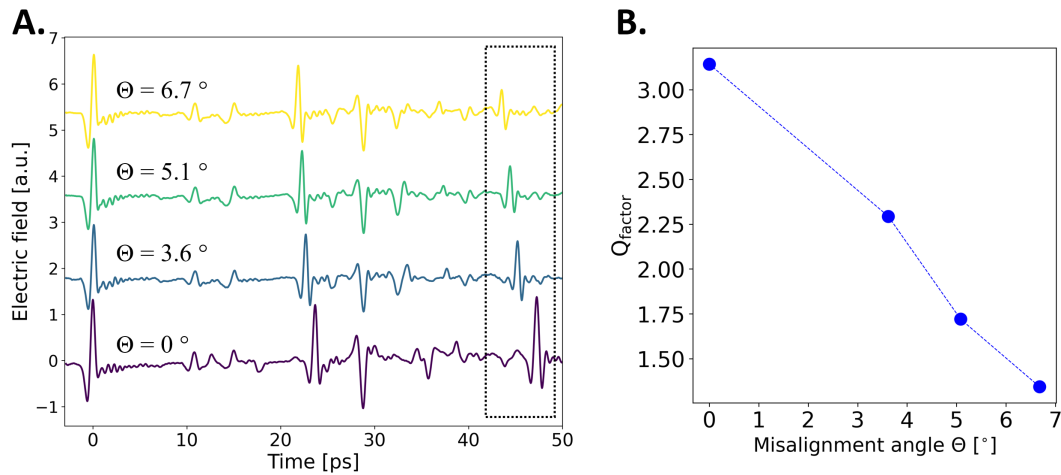


**Figure 5.7: Variation of the cavity quality factor as a function of the total misalignment angle of the mirrors.** **A.** THz time domain fields passing through the sample within the cavity for different misalignment angles  $\theta$ . In the dashed box we highlight the THz reflection associated to the cavity round trip. **B.** Estimated cavity quality factor as a function of the misalignment angle. The Q factor has been estimated by approximating the exponential decay of the cavity field with a linear fit.

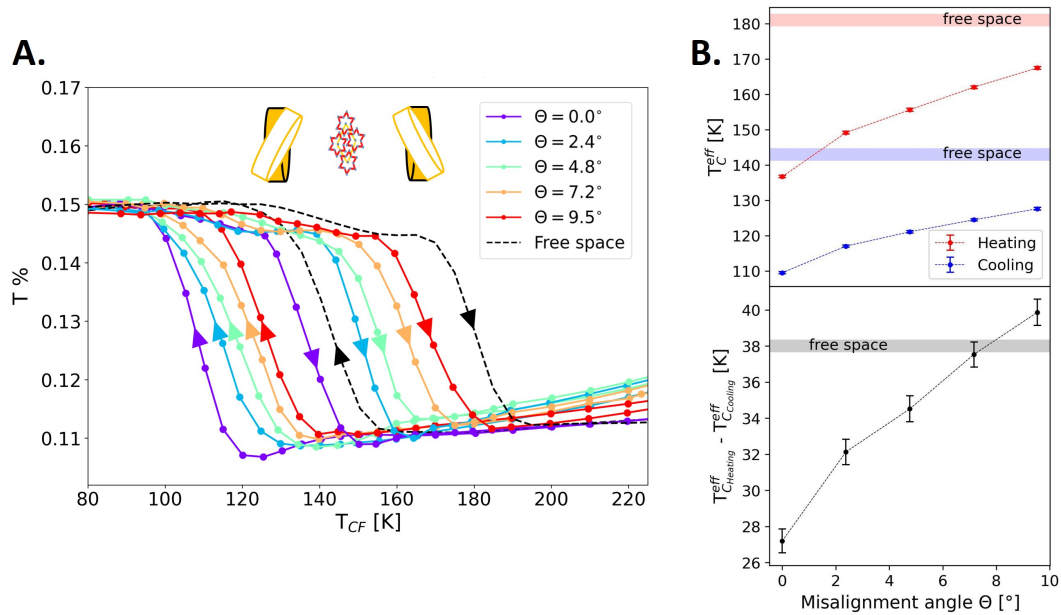


**Figure 5.8: Dependence of the effective critical temperature on the cavity alignment.** **A.** Dependence of the metal-to-insulator phase transition as a function of the cavity alignment for the 11.5 GHz cavity. The hysteric sweeping curves are plotted for each misalignment angle  $\theta$  as the integrated low frequency transmission ( $0.2 \text{ THz} < \omega < 1.5 \text{ THz}$ ). **B.** Estimation of the effective critical temperature as a function of the cavity alignment. Top panel: effective critical temperature upon heating (red) and cooling (blue) the sample as a function of the misalignment angle of the cavity. The shaded horizontal lines indicate the free-space reference. Bottom panel: corresponding hysteresis. The black shaded line marks the hysteresis measured in the free space material.

This effect is quantified in the upper panel of Figure 5.8B where we present the evolution of the effective critical temperature as function of the cavity alignment for the heating and cooling temperature scans. We note that, as highlighted in the lower panel of Figure 5.8B, misaligning the cavity mirrors not only changes  $T_c^{\text{eff}}$ , but also increases the hysteresis of the metal-to-insulator transition. The latter approaches the free space hysteresis value when the mirrors are highly misaligned. This further suggests that the modification of the sample thermodynamics is associated to the boundary conditions introduced by the cavity environment.

Moreover, in order to further validate the effect of the alignment on the metal-to-insulator transition, we proved that a switch between the metallic and the dielectric linear response can be obtained at fixed temperature ( $T_{\text{CF}}$ ) by changing the cavity alignment. The results of this test are presented in Figure 5.9A across the heating charge ordering transition and in Figure 5.9B across the cooling transition. In the first case the cold finger temperature has been set at  $T_{\text{CF}} = 154$  K, while in the latter we set the cold finger at  $T_{\text{CF}} = 116$  K.

The THz linear response measured at fixed  $T_{\text{CF}}$  at the output of the coupled cavity validates the dependence of the hysteretic curves on the mirror orientation presented in Figure 5.8. This can be directly seen in the linear THz response through the emergence (vanishing) of the CDW phonons (oscillations in the THz time domain) upon tuning  $\theta$ .

For the quality factors employed in the experiment (Figure 5.7), the phase switch detected upon tuning the cavity alignment  $\theta$  is not reversible. This is a consequence of the fact that, for the explored mirror angles the change of the effective critical temperature upon changing the cavity alignment does not exceed the free space hysteresis of the material. We show the irreversibility of the phase switch by comparing the THz fields exiting the cavity in the same alignment condition before and after the sample has switched the phase. The experimental evidences of the switch irreversibility are presented in Figure 5.10A (B) in the proximity of the heating (cooling) transition temperature. The THz linear responses exhibit the features of a different phase before and after the alignment-induced switch. This evidence marks the irreversibility of the process for the explored Q factors.

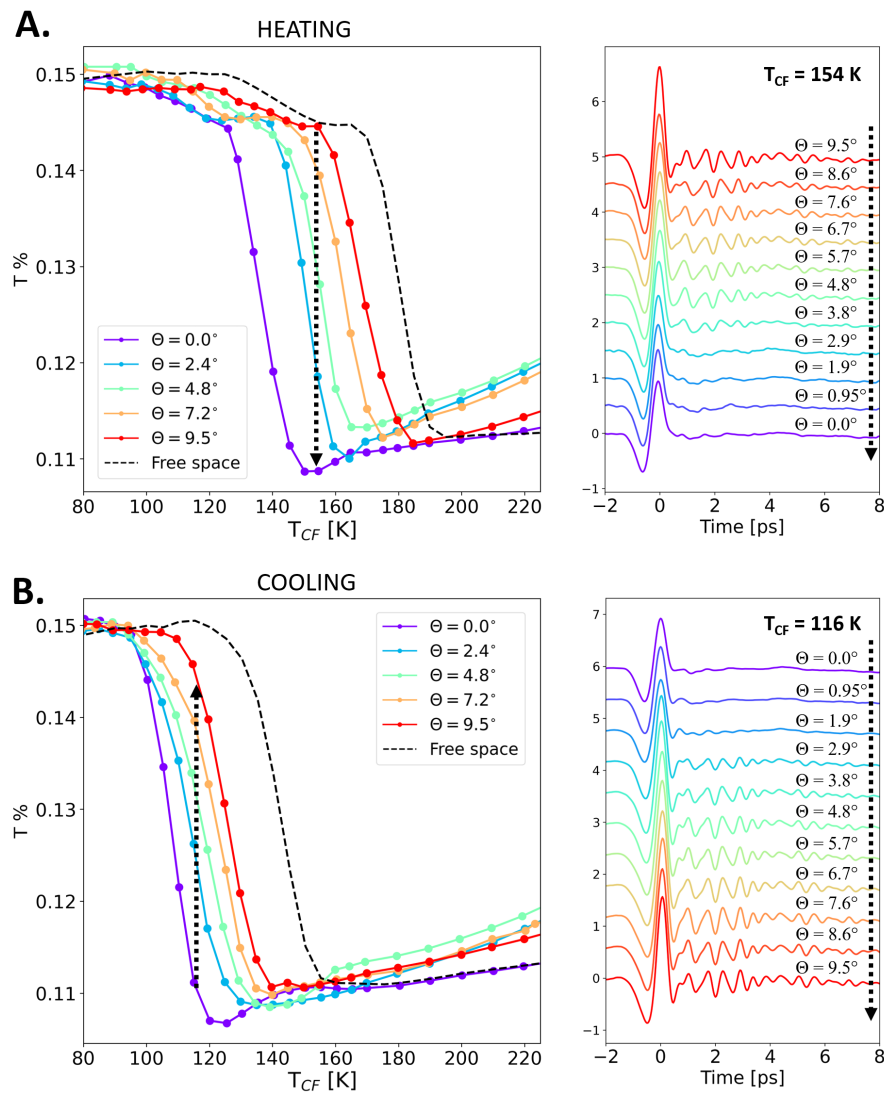


**Figure 5.9: Dependence of the metal-to-insulator transition on the cavity alignment at fixed temperature.** **A.** Right panel: Low frequency THz transmission as a function of the mirrors alignment of the 11.5 GHz cavity measured upon heating the sample. The black dashed arrow indicates the temperature across the heating phase transition employed for this study ( $T_{CF} = 154$  K). Left panel: THz fields detected at the output of the coupled 11.5 GHz cavity at 154 K as a function of misalignment angle of the mirrors. Transition from the dielectric to the metallic state is detected passing from the misaligned to the aligned configuration. **B.** Right panel: Low frequency THz transmission as a function of the mirrors' alignment of the 11.5 GHz cavity measured upon cooling the sample. The black dashed arrow indicates the temperature across the cooling phase transition employed for this study ( $T_{CF} = 116$  K). Left panel: THz fields at the output of the coupled 11.5 GHz cavity at 116 K as a function of the mirrors angle. Transition from the metallic to the insulating state is detected passing from the aligned to the misaligned configuration.

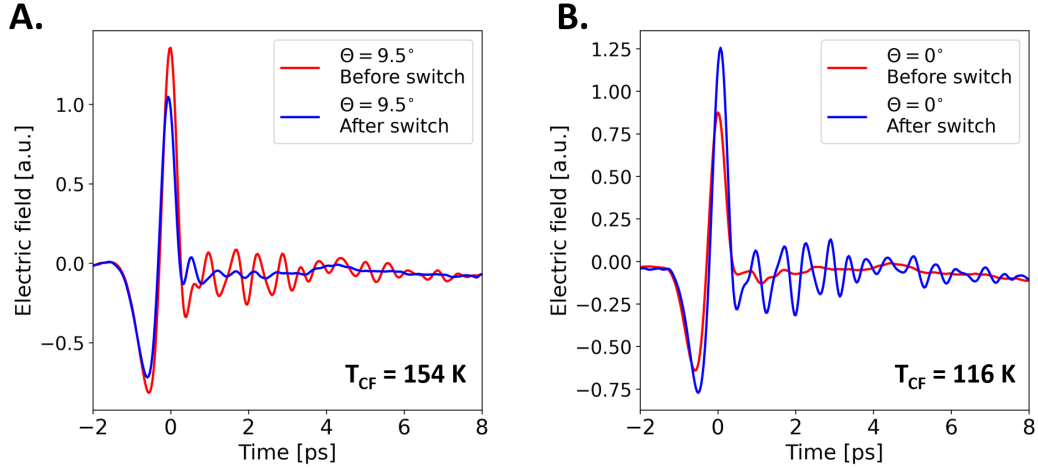


**Figure 5.10: Phase switch irreversibility upon tuning the cavity alignment.** **A.** THz fields exiting the 11.5 GHz cavity misaligned at the maximum angle ( $\theta = 9.5^\circ$ ) before and after the phase switch induced by aligning the cavity (Figure 5.9A). As in Figure 5.9A the cold finger temperature has been set at  $T_{CF} = 154$  K. **B.** THz fields at the output of the aligned 11.5 GHz cavity ( $\theta = 0^\circ$ ) before and after the phase switch induced by misaligning the mirrors (Figure 5.9B). As in Figure 5.9B the cold finger temperature has been set at  $T_{CF} = 116$  K.

### 5.3.2 CAVITY FREQUENCY DEPENDENCE

In order to study how the sample thermodynamics is influenced by the cavity resonant frequency we fixed the cold finger temperature to  $T_{CF} = 150$  K, and hence within the hysteresis of the free space material, and tuned the cavity fundamental mode. This characterization is presented in Figure 5.11. The results reveal that the cavity-driven change of the effective transition temperature  $T_c^{eff}$  overcomes the free space hysteresis (38 K), thus enabling a reversible touchless control of the metal-to-insulator phase transition.

Upon reducing the distance between the mirrors, we detected the phase transition between the metallic and the insulating phase to occur at a cavity frequency of  $\sim 25.0$  GHz. This is highlighted by the THz time domain traces of the insets of Figure 5.11 by the screening of the IR-active phonon modes of the C-CDW insulating phase. After the system has fully switched to the insulating state, we decreased the cavity fundamental frequency and detected a switch to the metallic phase at a lower cavity frequency ( $\sim 13.6$  GHz). This therefore results in the hysteretic behaviour of the low frequency conductance of Figure 5.11 obtained upon reversibly tuning the cavity fundamental mode.

Figure 5.12 summarises the dependence of the effective phase transition temperature (heating and cooling) on the cavity resonant frequency. We measured the effective transition temperature for cavity frequencies ranging from 11.5 GHz until 570 GHz. The raw temperature hysteretic curves employed for the estimation of the effective critical temperatures presented in Figure 5.12 are shown in Figure 5.13 upon heating (A) and cooling (B) the sample. Importantly, the maximum cavity frequency employed lies below the frequency of the lowest IR-active mode of the C-CDW phase (1.58 THz as shown in the frequency spectra of Figure 5.4). We made this choice in order to disentangle the effects due to the coupling to the IR-active optical phonons. A full description of the vibrational coupling with the CDW excitations across the charge ordering transition will be presented in Chapter 6.

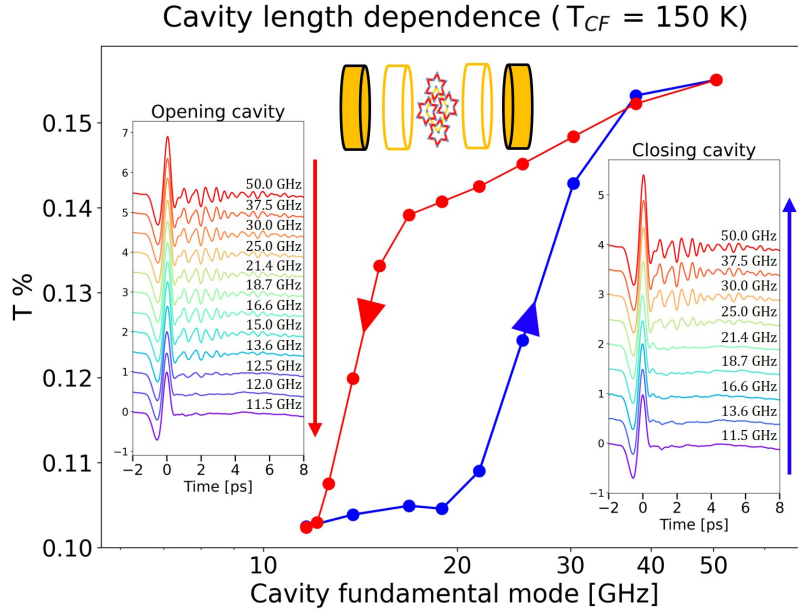


**Figure 5.11: Reversible cavity control of the metal-to-insulator transition at fixed temperature (150 K) upon tuning the fundamental mode.** The hysteresis as a function of the cavity fundamental mode is plotted as the evolution of the integrated low frequency THz transmission ( $0.2 \text{ THz} < \omega < 1.5 \text{ THz}$ ). The insets show the evolution of the time domain THz fields exiting the cavity for different values of the cavity frequency ranging from 50.0 GHz to 11.5 GHz (opening cavity case) and from 11.5 GHz to 50.0 GHz (closing cavity case), demonstrating the reversible switching between the two phases.

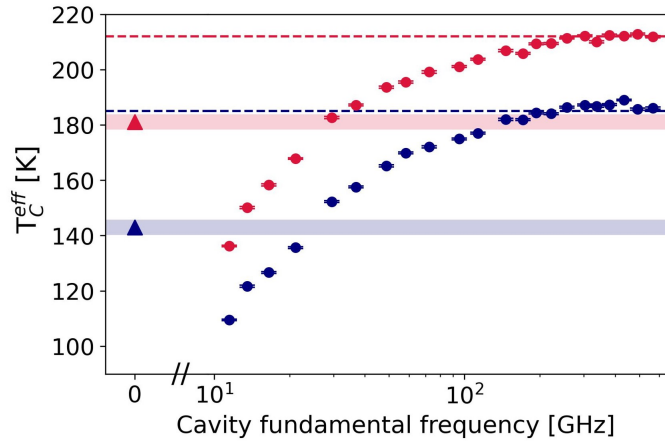


**Figure 5.12: Cavity-driven renormalization of the effective critical temperature as a function of the cavity resonance.** Dependence of the effective critical temperature on the cavity fundamental frequency for the heating and cooling temperature scans. The zero-frequency point represents the free space critical temperature, while the red (blue) dashed line the literature critical temperature [164] for the heating (cooling) temperature scan. The error bar associated to each temperature is the standard deviation of the effective critical temperatures estimated for three consecutive scans.

The results presented in Figure 5.12 show a non-monotonic trend of the effective critical temperature  $T_c^{\text{eff}}$  with respect to the free-space condition. Indeed, while long wavelength cavities (up to  $\sim 25 \text{ GHz}$ ) effectively stabilize the nearly-commensurate metallic

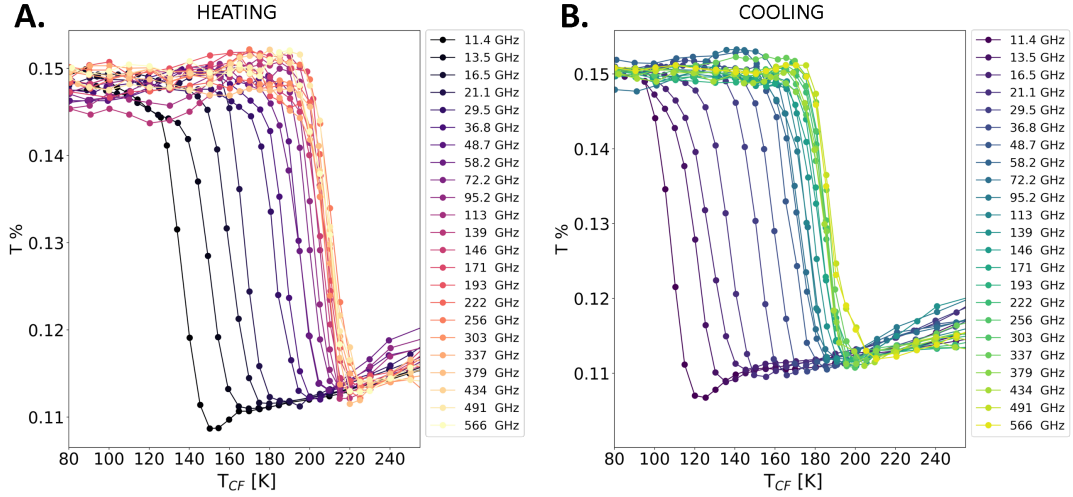


**Figure 5.13: Temperature hysteretic curves as a function of the cavity frequency. A.** Low frequency THz transmission ( $0.2 \text{ THz} < \omega < 1.5 \text{ THz}$ ) for all the cavity frequencies of Figure 5.12 (indicated in legend) measured upon heating the sample. **B.** Corresponding sweeping curves for the cooling temperature scans.

phase, the coupling with higher energy cavities results in an effective stabilization of the insulating C-CDW phase with respect to the material in free space (represented in Figure 5.12 as the zero-frequency point). Overall, we revealed a shift of  $T_c^{\text{eff}}$  of  $\sim 75 \text{ K}$  by moving from the lowest energy cavity employed in the experiment (11.5 GHz) towards the highest one (570 GHz). The measured modification of the effective critical temperature within the employed cavity frequency range exceeds the hysteresis of 1T-TaS<sub>2</sub> in free space (38 K), thus further validating the reversible control of the phase transition presented in Figure 5.11.

We note that the cavity mediated  $T_c^{\text{eff}}$  obtained for the cavity with the lowest frequency achievable in the set-up ( $\omega_c = 11.5 \text{ GHz}$ ) is  $\sim 30 \text{ K}$  below the temperature measured with THz spectroscopy outside of the cavity (Figure 5.12). This marks an effect which cannot be rationalized by incoherent cooling associated to the mirror distance but should rather be associated to the interaction with the cavity-confined field.

Crucially, the exclusion of an incoherent heating mechanism is confirmed by the fact that the dependence of  $T_c^{\text{eff}}$  on the cavity length is qualitatively similar for measurements with cavity mirror at different temperature. This evidence is in stark contrast with an incoherent radiation heating scenario which would give opposite trends with hot and cold cavity mirrors. Measurements with cavity mirrors at different temperatures will be fully discussed in Section 5.8.2.

## 5.4 DISCUSSION

Proven that the observed effect can be related to the peculiar cavity electrostatics and cannot be rationalized through incoherent radiation heating, in the present section we will focus on understanding and discussing if the observations should be rationalized as a cavity-mediated heating (cooling) or a free energy renormalization (i.e. the two scenarios presented in Figure 5.1).

To understand which of the two scenario would play the dominant role in the possible cavity-control of the charge ordering transition it is crucial to have a direct mea-

measurements of the sample's temperature ( $T_S$ ) within the cavity volume. For this aim, we performed an independent measurement campaign dedicated to address cavity mediated changes of sample's temperature. We insert within the cavity a micrometric Cr-Al junction (see the "Methods" section 5.7.1) custom design to minimize the impact on the cavity geometry and measure simultaneously  $T_S$  and  $T_{CF}$  in all experimental conditions in which THz measurements were performed.

A complete discussion of the temperature measurements in all the experimental conditions is presented in Section 5.8. Here, in order to discriminate between the two scenarios, we will present, in analogy with the THz transmission results of Figure 5.12, the dependence of  $T_S$  on the cavity resonance. Figure 5.14 displays the results of the temperature measurements performed within the cryogenic cavity for representative frequencies of the cavity modes.

In Figure 5.14 we plot, for each cavity length, the difference between the temperature measured in thermal contact with the sample within the cavity ( $T_S$ ) and the temperature of the cold finger ( $T_{CF}$ ) as a function of  $T_S$ . Upon changing the cavity frequency, we revealed a non-monotonic trend of the differential temperature  $T_S - T_{CF}$  with respect to the free space configuration. Indeed, while lower frequency cavities induce a coherent heating of the sample, the coupling with higher energy cavity modes decreases the local sample's temperature with respect to the free space material. By tracking  $T_S$  at the cold finger temperature corresponding to the literature  $T_c$  ( $T_{CF} = 215$  K), we revealed a non-monotonic trend as a function of the cavity frequency (inset of Figure 5.14). This trend is *qualitatively* consistent with the THz observations of Figure 5.12. We note that the observed non-monotonic trend of  $T_S - T_{CF}$  with cavity frequency depends on the presence of the sample and it is not observed when the thermocouple is mounted within the two holding membranes without the sample. We will detail this evidence, which in turns proves that the observed effect is sample dependent, in Section 5.8.1.

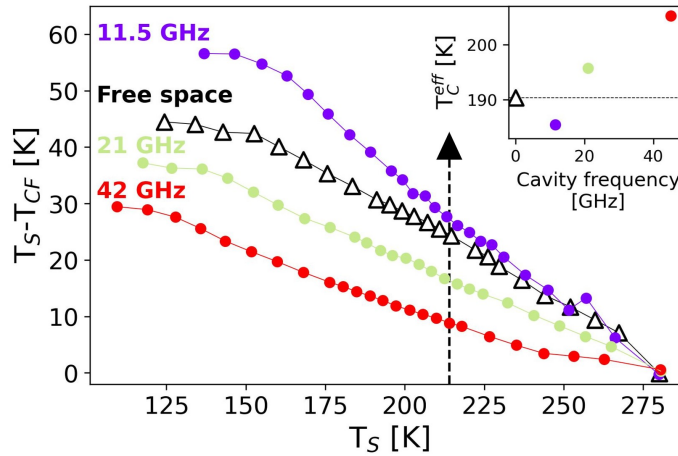


**Figure 5.14: Cavity-driven renormalization of sample's temperature as a function of the cavity resonance.** Difference between the temperature measured on the sample ( $T_S$ ) and on the cold finger ( $T_{CF}$ ) as a function of the sample temperature for different values of the cavity fundamental frequency. Temperatures have been measured upon heating the sample from the C-CDW phase. In the inset, the effective critical temperature, defined as the cold finger temperature at which the sample reaches the nominal critical temperature  $T_{CF} = 215$  K, as a function of the cavity mode.

We stress that the non-monotonic trend, as well as the quantitative variations upon sweeping the cavity mode revealed in Figures 5.12 and 5.14, cannot be justified with an incoherent radiative heating/cooling of the sample. To support this hypothesis, we performed finite elements simulations of the membrane's thermal profile (theoretical details in Section 5.7.2) as a function of the cavity length, repeated the measurements with mirrors at 290 K, revealing, apart from a rigid shift, a trend which is compatible with the cryogenic cavity case. Crucially, a decrease of the sample's effective temperature ( $T_S$ ) upon closing the cavity, regardless the mirrors temperature, is incompatible with an incoherent radiative scenario and points towards a cavity-mediated effect. This evidence will be detailed in Section 5.8.2.

The cavity frequency-dependent hysteresis in Figure 5.8 can be further discussed in light of the temperature measurements reported in Figure 5.14. By keeping fixed the cold finger temperature, the local temperature of the sample decreases upon increasing the cavity frequency. Therefore, closing the cavity effectively corresponds to cool down the sample that is thus driven to the insulating state (blue curve in Figure 5.11). The effect is reversed when, starting from the insulating state, the cavity frequency is decreased (red curve). Closing and opening the cavity can be thus interpreted as an effective coherent temperature scan, therefore leading to the hysteretic behaviour observed in Figure 5.11. Analogously, the alignment dependence presented in Figures 5.8, 5.9 can be linked to a coherent change of the sample temperature induced by the cavity environment, as it depends on the presence of the sample, regardless of the mirrors temperature (see Sections 5.8.3, 5.8.2).

Changing the cavity frequency leads not only to a renormalization of the effective critical temperature, but also to a shrinking of the hysteresis of the phase transition. This is explicitly demonstrated in Figure 5.15A where we plot the comparison of the phase transition hysteresis for two different cavity settings at low and high frequency ( $\omega_c^{\text{low}} = 16.7$  GHz and  $\omega_c^{\text{high}} = 337$  GHz). The measured changes in the effective critical temperature observed upon heating and cooling depend therefore not only on the cavity length, but also on the sample's thermal history (see also the characterizations of Section 5.8.1). This marks a scenario in which the coupling to the cavity is different in the two phases of the material leading to a different cavity driven response. The observed shrinking of the cavity hysteresis with respect to the free space (Figure 5.6 and Figure 5.14) hints to a plausible scenario in which the coupling between the cavity modes and the EM-active modes of the metallic state in 1T-TaS<sub>2</sub> is the driving force of the apparent renormalization of the phase transition. Indeed, such coupling is expected to be different in the two phases displaying a profoundly different dielectric response. The shrinking of the phase transition hysteresis induced by the cavity environment points therefore to a scenario in which the insulating phase is less sensitive to the boundary conditions of the electromagnetic field.

In order to rationalize the shift of the effective critical temperature  $T_c^{\text{eff}}$  observed experimentally, we resort to the thermodynamical picture presented in Figure 5.15B where we schematize the free energies of the metallic NC-CDW phase and of the dielectric C-CDW phase as a function of the temperature. The crossing temperature between the free energies of the two phases sets the critical temperature of the metal-to-insulator phase transition defined as the centre of the first order transition hysteresis. For simplicity, we assume the free energy of the dielectric phase to be weakly dependent on temperature and subsequently consider the change in temperature of the free energy of the metallic phase to be responsible for the phase transition. The schematic temperature dependence of the free energy of the metallic state ( $F_m$ ) and of the dielectric state ( $F_d$ )

in the low and high cavity frequency case, consistent with the experimental observation in Figure 5.15A, are plotted in Figure 5.15B.

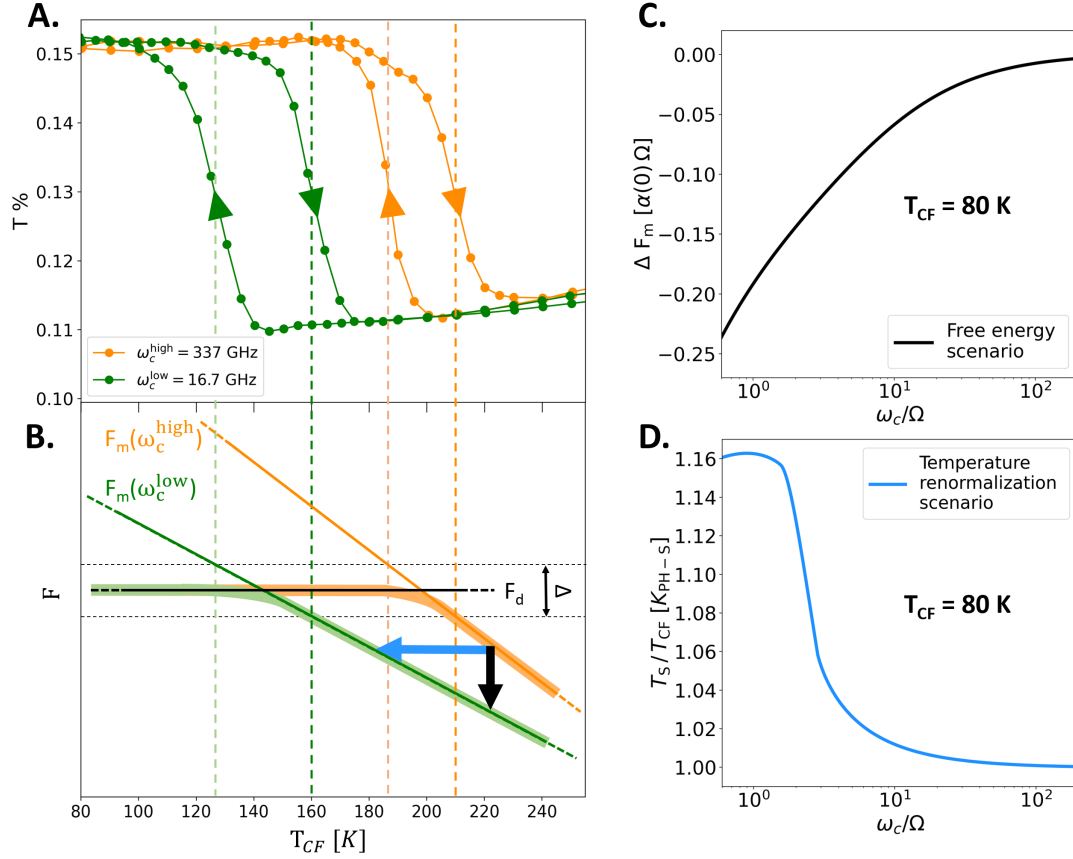


**Figure 5.15: Cavity-driven renormalization of 1T-TaS<sub>2</sub> thermodynamics.** **A.** Comparison of the phase transition hysteresis of 1T-TaS<sub>2</sub> within a low frequency cavity ( $\omega_c^{\text{low}} = 16.7$  GHz) and a high frequency cavity ( $\omega_c^{\text{high}} = 337$  GHz). **B.** Schematic temperature dependence of the free energy of the metallic ( $F_m$ ) and the dielectric ( $F_d$ ) phase at the cavity frequencies  $\omega_c^{\text{low}}$  and  $\omega_c^{\text{high}}$  employed in (A). The activation energy for switching the phase is indicated with  $\Delta$ . The shift of the apparent transition temperature can be rationalized with a cavity-mediated renormalization of the free energy of the metallic state (black vertical arrow) and with a scaling of the sample effective temperature in analogy with the Purcell effect (blue horizontal arrow). **C.** Free energy scenario predictions. Calculated renormalization of the metallic free energy  $\Delta F_m$  as function of the cavity frequency. **D.** Purcell-like effect predictions. Predicted temperature ratio  $\frac{T_S}{T_{CF}}$  upon sweeping the cavity fundamental mode. The estimations of the two cavity-mediated scenarios in (C) and (D) have been calculated at a representative cold finger temperature  $T_{CF} = 80$  K. The cavity frequencies presented in (C) and (D) are normalized by a representative low energy mode frequency  $\Omega = 15$  GHz.

Recalling Figure 5.1, the different coupling of the collective excitations in the material to the cavity modes can renormalize the effective critical temperature  $T_c^{\text{eff}}$  through two mechanisms.

In the first scenario, the hybridization of the cavity modes with the sample could change the energy spectrum of the collective sub-THz modes in the material. In this hypothesis, a coupling between the material and the cavity modes, which is different in the two phases, is the driving force of the renormalization of the phase transition temperature. In this picture, the shift in the transition temperature occurs through a decrease of the free energy of the metallic phase with respect to the insulating one, resulting in a shift of the transition temperature (black vertical arrow in Figure 5.15B). The experimental observation would thus suggest that lowering the cavity resonance could cause a decrease of the free energy of the metallic phase and a reduction of the slope of its temperature dependence, consistent with a cavity-driven shrinking of the hysteresis.

In order to see whether the free energy scenario could give the right trends, we resort to a Dicke-based model with a single cavity mode coupled to a continuum absorption spectrum within the GHz spectral range, where linear conductivity measurements suggest an increased dielectric response [175, 176]. These sub-THz excitations are tentatively associated to domain wall fluctuations of the discommensurate regions [177, 178] which freeze as a consequence of the CDW commensuration [166] and hence they are only active in the metallic NC-CDW phase. We note that the system of domain walls is charged with respect to the background, and this charge may be hence directly coupled to the transverse electric field of the cavity. The full theoretical description and derivation of the free energy model can be found in Section 5.6.1.

Importantly, under a harmonic approximation for the low energy modes in the solid, the free energy difference  $\Delta F_m$  between the light-matter hybrid and the isolated cavity and solid can be understood solely in terms of the frequency dependent polarizability of the system, irrespective of the microscopic nature of the modes in the solid. In order to qualitatively illustrate the mechanism, we tentatively model the low energy spectrum associated to collective domain wall fluctuations as a broad absorption band centred at  $\Omega$ , with  $\Omega$  lying in the GHz range ( $\Omega = 15$  GHz) and exploit the model to extract the free energy renormalization of the metallic phase  $\Delta F_m$ . Figure 5.15C shows the dependence of the free energy renormalization of the metallic phase at 80 K as a function of the cavity frequency when the latter is swept through the spectrum of the collective mode. The model indicates that the free energy of the metallic state is lowered upon lowering the cavity frequency, which would be qualitatively consistent with the decrease of the effective critical temperature upon reducing the cavity frequency, experimentally observed by THz spectroscopy (Figure 5.12). The overall scale of the free energy change shown in Figure 5.15C is proportional to the central frequency of the continuum collective mode  $\Omega$  and to the total dielectric loss within its absorption band ( $\alpha''(0)$ ).

For the quantitative estimate of the free energy mechanisms, we stress that the coupling to a single cavity mode gives only a non-extensive contribution to the free energy [179, 180]. The total effect on the free energy depends on the phase space of the relevant cavity modes which can be shifted within the spectrum of the low energy collective modes. Taking into account this phase space factor, extremely large couplings would be needed for the free energy changes to explain the observed shifts in the phase transition temperature (see Section 5.6.1 for the quantitative estimation).

In this regard, the phase space restriction is no longer valid in the thermodynamical coupling scenario of Figure 5.1, in which an open system is considered and thermal

exchanges between the material, the cold finger and the photon bath are allowed<sup>1</sup>. This, together with the experimental evidence that the cavity can coherently heat up or cool down the sample as a function of the frequency (Figure 5.14) suggests that the second mechanism in Figure 5.1 has the dominant effect on the phase transition.

Within this thermodynamical framework, the gap between the temperature measured on the cold finger ( $T_{CF}$ ) and the sample's temperature ( $T_S$ ) can be changed through a cavity control of the electromagnetic density of states at the sample's position. The re-shaping of the electromagnetic density of the states driven by the cavity (Figure 5.1B) can indeed induce a change of the sample's emission spectrum and hence of its temperature [181] (blue horizontal arrow in Figure 5.15B). For instance, for the studied phase transition, the short cavities move the electromagnetic modes to higher frequency and could effectively decouple the electromagnetic active modes from the vacuum, similarly to the Purcell effect in atomic and molecular physics [13–16]. The sample is in thermal contact with the cold finger through the Si<sub>3</sub>N<sub>4</sub> membranes, but it is also in thermal contact with the external photon bath at 300 K. We assume that the thermal transfer from the cold finger to the sample depends only on the difference between  $T_{CF}$  and  $T_S$  through a cavity-independent thermal coupling constant. Conversely, the thermal load on the sample due to the contact with the external photon bath is mediated by the cavity through a coupling constant  $K_{PH-S}$  depending on the cavity geometry (fundamental frequency  $\omega_c$  and quality factor  $Q$ ) and on the sample dielectric loss within the employed cavity range. In order to qualitatively illustrate the mechanism, we model the infrared spectrum of 1T-TaS<sub>2</sub>, as for the free energy model, as a broad continuum absorption band lying in the GHz range and centred at a representative frequency  $\Omega = 15$  GHz, and exploit the Purcell-based model to extract an effective temperature of the sample  $T_S(\omega_c, Q)$  depending on the cavity geometry. Further details can be found in the theoretical section of the present chapter (Section 5.6.2).

We proved that upon increasing the cavity frequency, i.e. by decoupling the EM active transitions from the cavity fundamental mode, the cavity induces a coherent cooling of the sample, whose temperature reaches the cold finger one at high cavity frequencies. This frequency-dependent trend is shown in Figure 5.15D, where the temperature ratio  $\frac{T_S(\omega_c, Q)}{T_{CF}}$  is plotted as a function of cavity fundamental mode  $\omega_c$  for a cold finger temperature  $T_{CF} = 80$  K. Simulations at different cold finger temperatures, among the ones employed in the experiment, can be found in Section 5.6.2.

The dependence of  $T_S$  on the cavity frequency predicted by the thermodynamical coupling mechanism is qualitatively consistent with the trend of the effective critical temperature observed experimentally with both THz transmission (Figure 5.12) and temperature measurements (Figure 5.14).

Overall, the scenario in which the presence of the cavity leads to a sample temperature change seems to be the dominant effect. Nevertheless, a quantitative accounting of the effect could not be reached and it cannot be excluded that the cavity-driven free energy renormalization participate and makes the effect larger. In this respect it is interesting to observe that both mechanisms, based on the Purcell effect and on the free energy renormalization of the metallic state, give the correct dependence of the phase transition on the cavity frequency. This may provide a useful guide for future quan-

<sup>1</sup> In this regard, a simple yet effective example that clarifies how the phase space argument no longer applies for open systems is our daily experience with the sunbeams: sunlight is always absorbed at momentum  $q = 0$ , but this does not prevent objects from getting warm.

titative theories, which should also take into account the open system as well as the non-linear interaction between the low energy modes in the solid.

## 5.5 MEASURE PROTOCOLS AND DATA ANALYSIS

We present in this section further experimental details about the measurements presented before. In particular, we will characterize the quality factor of the cavities employed in the experiments, the waiting time protocol adopted to track the phase transition and the procedure employed to determine the effective critical temperatures for different cavity settings.

### 5.5.1 CHARACTERIZATION OF THE SUB-THZ EMPTY CAVITIES

In order to estimate the quality factor of the sub-THz cavities employed in the experiments presented in Section 5.3, we characterized the response of the empty cavity, i.e. when the THz field passes only through the Si<sub>3</sub>N<sub>4</sub> membranes within the mirrors.

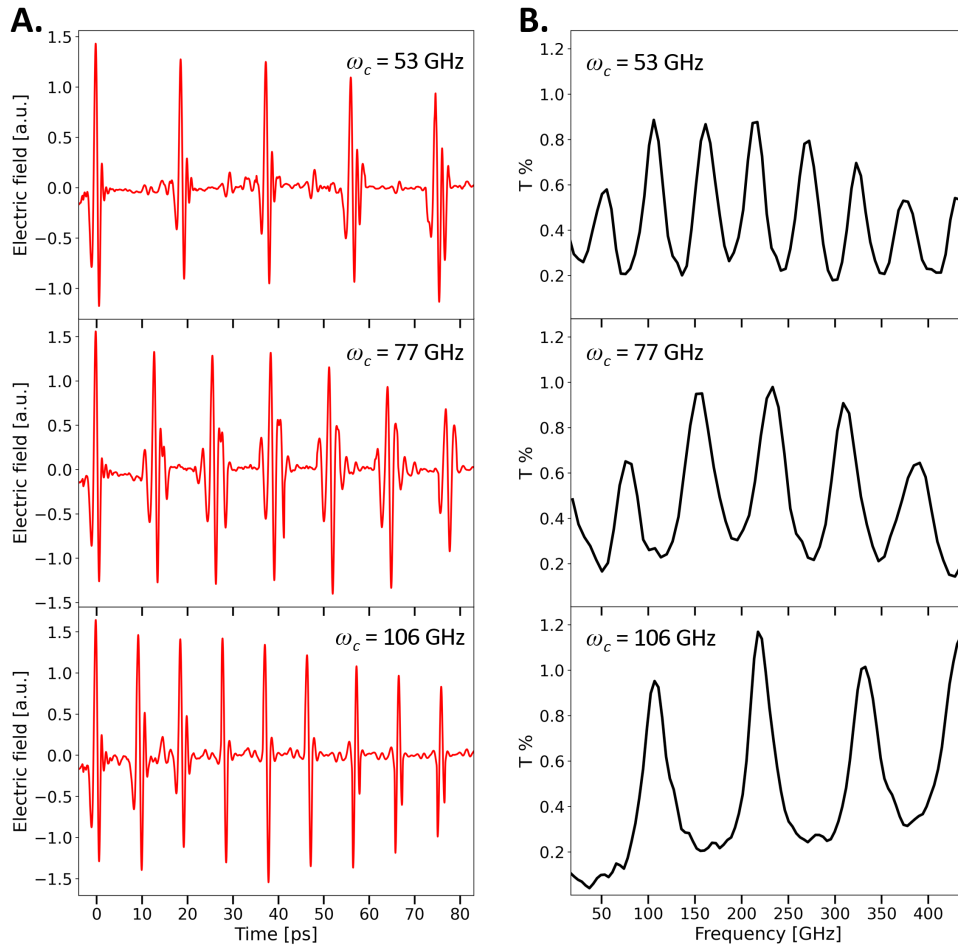


**Figure 5.16: THz characterization of the sub-THz empty cavities.** **A.** Time domain THz fields measured at the output of the empty cavity for three representative cavity frequencies  $\omega_c$  indicated in legend. **B.** Cavity transmission spectra calculated from the fields shown in A. proving the tunability of the cavity fundamental mode. For the presented measurements, as for all the measurements presented in the chapter, the thickness of the gold layer on the semi-reflecting mirrors is  $d_{Au} = 15$  nm.

As pointed out in the theoretical section 2.1.1 of Chapter 2, the quality factor quantifies the bare optical dissipations within the cavity volume and hence set the coupling strength between the cavity field and the targeted material excitation.

In Figure 5.16 we plot the time domain THz fields transmitted through the sub-THz Fabry-Perot cavity (Figure 5.16A) and the corresponding spectral content (Figure 5.16B) for three representative values of the cavity fundamental mode  $\omega_c$  among the ones used in the experiment ( $\omega_c = 53, 77, 106$  GHz). The cavity transmission spectra exhibit indeed interference Fabry-Pérot modes with a tunable fundamental frequency set by the cavity length.

For the three representative cavities shown in Figure 5.16 we estimated the quality factors  $Q$  to be 3.3, 3.6 and 3.5 for the 53, 77, and 106 GHz cavity, respectively. The latter were calculated as the ratio between the fundamental cavity frequency and its bandwidth defined as the full width half maximum of the transmission peak of the fundamental mode. This estimation proves that, for all the cavity lengths that we studied, the bare quality factor (and hence the incoherent photon losses) can be considered independent on the cavity fundamental frequency.

### 5.5.2 CHARACTERIZATION OF THE SAMPLE THERMALIZATION TIME

In order to prove that all the measurements have been performed in a stationary regime, we estimated the thermalization time of the sample by delaying the THz acquisition by different amounts of time. Figure 5.17 shows that no significant variation in the effective critical temperature and in the slope of the phase transition occurs for  $\Delta t \geq 2$  min. All the measured THz traces in the experiment are the result of a 20 minute integration time at each temperature step with a 5 minutes waiting time before the first THz acquisition. Therefore, we can safely rule out that the observed inhomogeneous-like feature of the phase transition is due to a measurement waiting time less than the sample thermalization and it can be instead likely ascribed to intrinsic inhomogeneities of the sample, which can smear out the charge ordering transition [172, 173]. Another factor

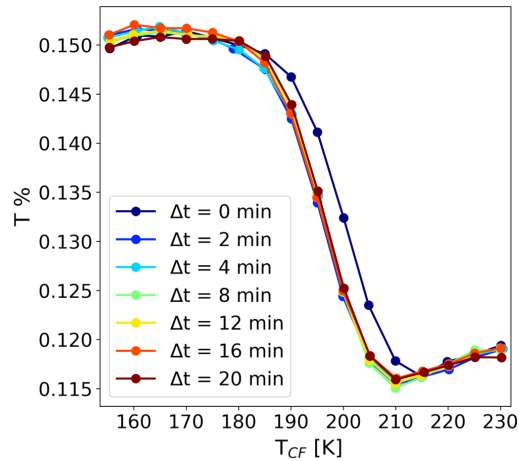


**Figure 5.17: Dependence of the metal-to-insulator phase transition on the waiting time.** The temperature evolution of the low frequency transmission ( $0.2 \text{ THz} < \omega < 1.5 \text{ THz}$ ) is plotted for different waiting times before starting the THz acquisition.

which could be responsible for the smearing out of the metal-to-insulator transition in single-crystal 1T-TaS<sub>2</sub> samples is substrate strain. Strain plays indeed a large role in the charge ordering transition, and can shift and broaden the transition temperature substantially [174, 182]. Additionally, when mounted on membranes, homogeneity of the temperature, in particularly the in-plane one, may also broaden the transition.

We stress that none of these inhomogeneous-like effects have any bearing on the shifts of  $T_c^{\text{eff}}$  discussed. In fact, the well-documented sensitivity of the discommensuration melting transition temperature to external influences speaks in favour of the cavity-mediated effects being genuine.

### 5.5.3 DETERMINATION OF THE EFFECTIVE CRITICAL TEMPERATURE

In this section we present the method used to extract from the THz transmission data the effective critical temperatures of 1T-TaS<sub>2</sub> in free space and within the THz cavities.

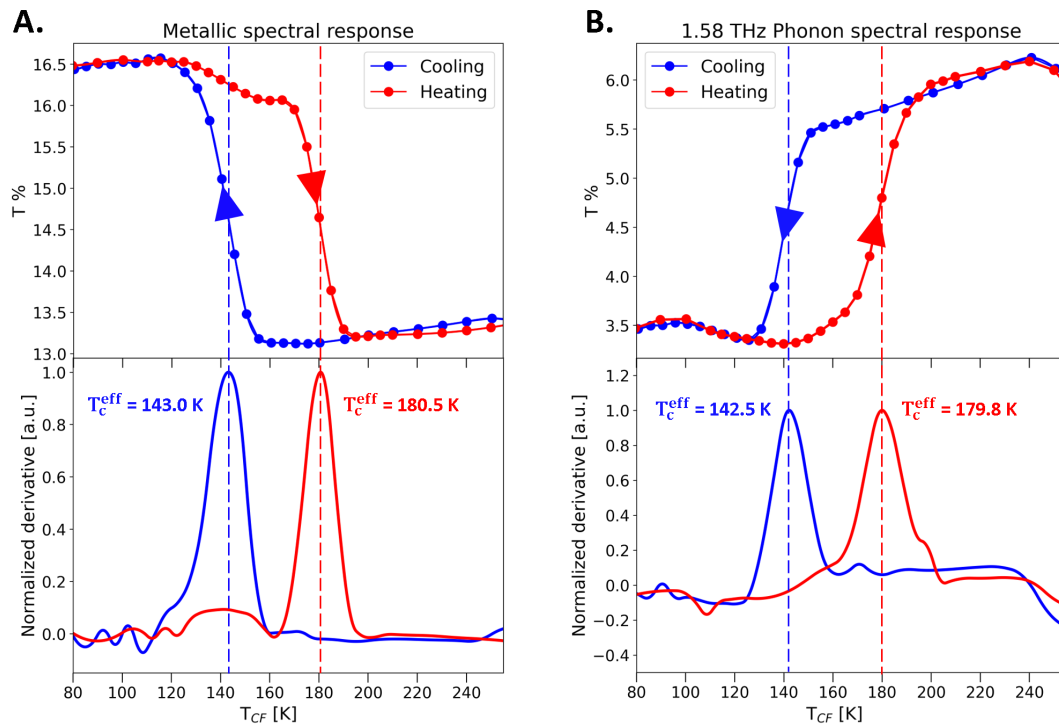


**Figure 5.18: Determination procedure of the effective critical temperature of the metal-to-insulator transition.** **A.** In the top panel the temperature evolution of the integrated low frequency transmission ( $0.2 \text{ THz} < \omega < 1.5 \text{ THz}$  integration range) upon heating and cooling. In solid line the interpolated evolution. In the lower panel the derivative of the interpolated curve whose maximum sets the effective critical temperature of the phase transition. **B.** In the top panel the temperature evolution of the integrated 1.58 THz phonon transmission ( $1.53 \text{ THz} < \omega < 1.62 \text{ THz}$  integration range) and its interpolation. In the lower panel the derivative of the interpolated phonon response across the phase transition.

Figure 5.18A shows the temperature evolution of the integrated low frequency transmission ( $0.2 \text{ THz} < \omega < 1.5 \text{ THz}$ ) associated to the onset of the metallicity. Figure 5.18B

shows instead the temperature evolution of the transmitted spectral weight around the 1.58 THz phonon integrated in the range 1.53 THz – 1.62 THz. This integration range corresponds to the phonon bandwidth. In order to estimate the effective critical temperature at each cavity length, we interpolated the metallic and phononic temperature response and calculated the derivative of the interpolated curve. The obtained temperature-derivative for the free space sample is presented in the lower panels of Figure 5.18A and Figure 5.18B for the metallic and phononic response, respectively.

We set the effective critical temperature of the phase transition ( $T_c^{eff}$ ) to be the maximum of the derivative of the interpolated curve. The error associated to each  $T_c^{eff}$  is the standard deviation of the critical temperatures estimated for three consecutive scans. The robustness of this procedure is validated by the fact that the effective critical temperatures estimated from the metallic response are compatible with the ones estimated from the phonon spectral response.

## 5.6 THEORETICAL MODELS

We present in this section the full theoretical models, developed to describe the two proposed mechanisms through which the cavity field can act on the phase transition (Figure 5.1).

### 5.6.1 FREE ENERGY PICTURE

In this section we introduce the phenomenological free energy model, providing a qualitative estimation of the renormalization of the free energy of the metallic NC state due to cavity electrostatics.

Let us consider a solid with given dielectric properties, characterized by the polarizability  $\alpha(\omega)$ , which determines the response of the transverse polarization density of the electric field,  $\mathbf{P}(\omega) = \epsilon_0 \alpha(\omega) \mathbf{E}(\omega)$ . The polarizability  $\alpha(\omega)$  is related to the dielectric function  $\epsilon(\omega)$  as  $\epsilon(\omega) = 1 + \alpha(\omega)$ . A non-zero polarizability implies that there are modes in the solid which can hybridize with the electromagnetic field, which in turn leads to a change of the free energy when the system is put within the cavity. In order to understand the effect of the cavity on the free energy of the system, we evaluate the difference

$$\Delta F = F_{tot} - F_{mat} - F_{cav} \quad (5.2)$$

between the total free energy of the coupled cavity ( $F_{tot}$ ) and the free energies of the uncoupled solid ( $F_{mat}$ ) and of the confined electromagnetic field ( $F_{cav}$ ). A key observation is that, as long as the solid is approximately described by a harmonic theory,  $\Delta F$  can be determined from the knowledge of the experimentally accessible dielectric function alone, independent of microscopic details such as the precise nature of the electromagnetically active modes. In short, the reason is that in a harmonic theory one can exactly integrate out the modes of the solid, so that the resulting effective action of the cavity, which then determines  $\Delta F$ , is given only in terms of the linear response functions of the matter.

We will make a further simplification in line with the present experimental setting, and assume that the volume  $V_m$  of the solid is small compared to the cavity volume  $V$ , i.e.  $\frac{V_m}{V} \ll 1$ . This approximation is valid for the experimental setting since the cavities employed have fundamental frequencies in the sub-THz region, while the sample thickness is  $\sim 15 \mu\text{m}$ . With this approximation, as we will show below, for a single cavity

mode with fundamental frequency  $\omega_c$  the free energy renormalization  $\Delta F$  due to the light-matter coupling (Equation 5.2) is given by  $\Delta F(\omega_c, T) = \frac{V_m}{V} f(\omega_c, T)$ , where

$$f(\omega_c, T) = \frac{1}{\pi} \int_0^{+\infty} d\omega \alpha''(\omega) \omega \frac{b(\omega_c, T)\omega_c - b(\omega, T)\omega}{\omega_c^2 - \omega^2}. \quad (5.3)$$

In the previous equation  $b(\omega, T) = (e^{\frac{\hbar\omega}{k_B T}} - 1)^{-1}$  is the Bose function and  $\alpha''(\omega)$  the imaginary part of the solid polarizability (dielectric loss).

The total free energy change  $\Delta F$  is a thermodynamically extensive quantity, which arises from the coupling to a continuum of cavity modes with transverse momentum  $q$  and a discrete mode index  $n$  (Figure 5.19). For simplicity, instead of summing Equation 5.3 over all cavity modes  $\omega_c \equiv \omega_{q,n}$ , we will first analyse the single mode result (Equation 5.3) for the lowest cavity frequency ( $\omega_c = \frac{\pi c}{L}$ , with  $L$  the cavity length) to understand the qualitative functional dependence of  $\Delta F$  on the temperature and on the cavity parameters. In order to estimate the order of magnitude of the total effect of all modes, the result will then be multiplied with a phase space factor that counts the number of modes  $N_{\text{mode}}$  that are affected by the cavity.

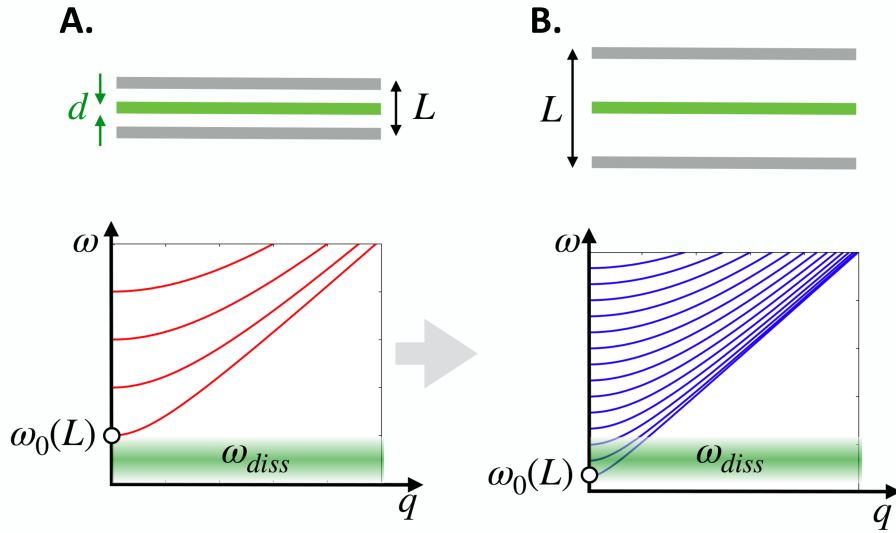


**Figure 5.19: Free energy model setting.** Upper panels: coplanar cavity with a thin slab of matter (thickness  $d$ ) inside a cavity of length  $L$ . Lower panels: Sketch of the cavity modes dispersion and of the absorption solid band (green shaded region centered at  $\omega_{diss}$ ). As  $L$  is increased, modes are pulled inside and below the absorption band of the solid. The cavity fundamental mode is indicated with  $\omega_c(L)$ .

To analyse the free energy renormalization (Equation 5.3), we assume that the solid polarizability  $\alpha(\omega)$  in the sub-THz region, which we tentatively attribute to domain wall fluctuations [177, 178], gives rise to a broad continuum absorption band that can be fitted by the response of a strongly damped oscillator:

$$\alpha(\omega) = \alpha(0) \frac{\Omega^2}{\Omega^2 - \omega^2 - i\omega\gamma}. \quad (5.4)$$

Here  $\Omega$  corresponds to the central frequency of the domain fluctuations mode,  $\gamma$  is the linewidth, and  $\alpha(0)$  is the contribution of the domain wall fluctuations mode to the static polarizability. The latter also measures the total spectral weight in the absorption band and therefore serves as a phenomenological measure of the effective coupling strength. The representative dielectric loss  $\alpha''(\omega)$  due to domain wall fluctuations adopted for the estimations is presented in Fig. 5.20A. We set a central frequency  $\Omega = 15$  GHz and a frequency damping  $\gamma = 20$  GHz, so that no significant contribution of domain wall fluctuations to the solid dielectric loss is present in the THz region ( $\omega > 0.1$  THz).

Figure 5.20B shows the dependence of the free energy renormalization of the metallic phase (Equation 5.3) as a function of the cavity frequency  $\omega_c$  when the latter is swept through the mode centred at  $\Omega$ . The model indicates that the free energy of the metallic state is lowered upon lowering the cavity frequency, which is qualitatively consistent with the decrease of the effective critical temperature upon reducing the cavity frequency observed experimentally. The renormalization of the metallic free energy is larger for larger temperatures, indicating that it is related to the thermal population of the low energy mode. We stress that the temperature in the experiment is well above  $\Omega$ .

Figure 5.20C shows the free energy renormalization as a function of temperature for different cavity frequencies  $\omega_c$  below and above the resonance  $\omega_c = \Omega$ . The free energy of the metallic phase is lowered and becomes steeper when the cavity frequency is lowered (i.e. opening the cavity). This trend is consistent with the interpretation of the experimental observation presented in Figure 5.15B.

It should be stressed, however, that the absolute changes of the total free energy are expected to be rather small. As mentioned above, the single mode result  $\Delta F(\omega_c, T) = \frac{V_m}{V} f(\omega_c, T)$  should be integrated over all modes or, for a simple estimate, multiplied with a phase space factor  $N_{\text{modes}}$ . If the latter is simply taken to account for all the modes below a certain cutoff  $\omega_{\text{cut}}$  in a volume  $V$ , we have  $N_{\text{modes}} = \frac{V}{\lambda_{\text{cut}}^3}$ , up to constants of order one. Therefore, the free energy change  $N_{\text{modes}} \times \frac{V_m}{V} f(\omega_c, T)$  per volume  $V_m$  is given by the amount  $f(\omega_c, T)$  per volume  $\lambda_{\text{cut}}^3$ . The changes of  $f(\omega_c, T)$  upon modifying the cavity frequency are of the order of  $\alpha(0)\Omega$  (see Figure 5.20), thus corresponding to an energy density  $\frac{\alpha(0)\Omega}{\lambda_{\text{cut}}^3}$ . This value has to be compared with the condensation energy density of the phase transition, which is  $Q \sim 6 \text{ J/mm}^3 \sim 3.6 \times 10^{10} \text{ eV}/\mu\text{m}^3$  [183]. With  $\Omega$  in the sub-meV range, very large couplings  $\alpha(0)$  would be needed, even with a cut-off  $\lambda_{\text{cut}}$  in the optical range (which is clearly an upper bound, as optical frequencies are hardly affected by the present THz cavity setting).

We therefore conclude that although the free energy renormalization in the cavity  $\Delta F$  follows the correct trend (lowering the free energy of the nearly commensurate phase as the cavity is opened), it is not sufficient to explain the experimental observation. While it will certainly be also interesting to investigate future theoretical interpretations which go beyond the harmonic theory, this puts more emphasis on the second mechanism, which is based on an electrodynamical control of cavity dissipations, similar to Purcell effect (Figure 5.1).

Finally, let us conclude this theoretical section with the explicit derivation of Equation 5.3. Let us start from a general harmonic model in which one mode of the electromagnetic field couples to a continuum of modes in the solid. The Hamiltonian is a general Dicke-type Hamiltonian:

$$H = \frac{1}{2} \sum_{\alpha} \left( \Omega_{\alpha}^2 \left[ p_{\alpha} + \frac{\kappa \gamma_{\alpha}}{\Omega_{\alpha}^2} \Pi \right]^2 + x_{\alpha}^2 \right) + \frac{1}{2} \left( \Pi^2 \omega_q^2 + X^2 \right), \quad (5.5)$$

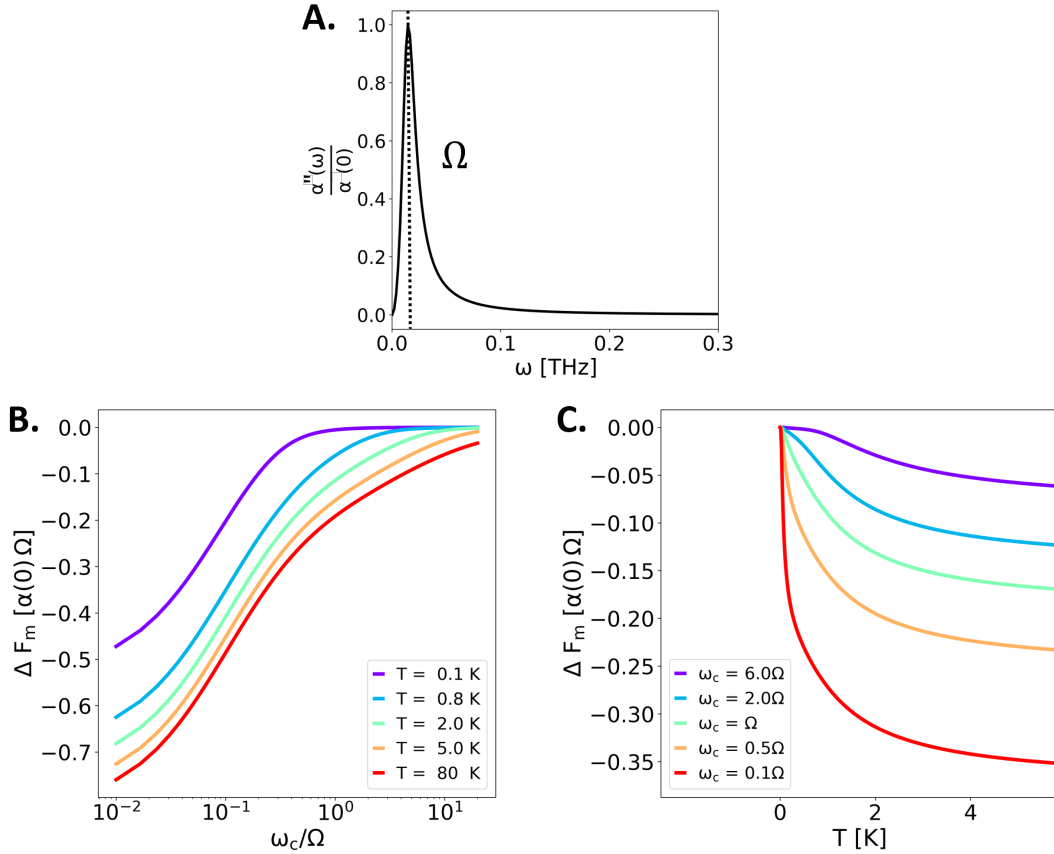


**Figure 5.20: Cavity-induced renormalization of the free energy of the metallic phase.** **A.** Dielectric loss spectrum  $\alpha''(\omega)$  ( $\Omega = 15$  GHz,  $\gamma = 20$  GHz) employed for the calculations. The spectrum has been normalized by the static contribution to the polarizability  $\alpha(0)$ . **B.** Renormalization of the metallic free energy  $\Delta F_m$  as a function of the cavity frequency for different temperatures. The cavity frequencies  $\omega_c$  are normalized by  $\Omega = 15$  GHz. **C.** Renormalization of the metallic free energy  $\Delta F_m$  as a function of the temperature for different cavity frequencies above and below resonance  $\omega_c = \Omega$ .

where  $X$  and  $\Pi$  are the canonical quadratures of the electromagnetic field, and  $p_\alpha$  and  $x_\alpha$  the quadratures of the modes in the solid. The solid normal modes have frequencies  $\Omega_\alpha$  in the absence of the coupling to the cavity field. The electromagnetic field quadrature  $\Pi$  is related to the vector potential (which is spatially homogeneous throughout the solid) by the relation

$$\hat{\mathbf{A}} = \hat{\mathbf{n}} \sqrt{\frac{1}{\epsilon_0 V}} \Pi, \quad (5.6)$$

where we have indicated with  $V$  the cavity mode volume, and with  $\hat{\mathbf{n}}$  the polarization direction. The electric field operator is connected to the vector potential by the temporal derivative  $\hat{\mathbf{E}} = -\partial_t \hat{\mathbf{A}}$ . The complete square light-matter coupling in Equation 5.5, with coupling constants  $\gamma_\alpha$ , corresponds to a minimal coupling of the modes in the solid to the vector potential. The coupling between the solid oscillators and the single cavity mode scales as  $\kappa \gamma_\alpha$  where  $\kappa^2 = \frac{V_\alpha}{V}$  is the volume fraction of the cavity filled with the 1T-TaS<sub>2</sub> sample. Note that, as mentioned above, the final result for  $\Delta F$  will be expressed in terms of the polarizability, so that the detailed choice of the parameters  $\Omega_\alpha$  and  $\gamma_\alpha$  does not enter.

The aim is now to calculate the free energy difference  $\Delta F$  within this model. Denoting with  $\eta_\alpha$  and  $\eta_\alpha^{(0)}$  the normal modes energies of the coupled and uncoupled system, respectively, the free energy difference (Equation 5.2) is simply given by

$$\Delta F = \frac{1}{\beta} \sum_{\alpha} \left[ \ln \left( 1 - e^{-\beta \eta_\alpha} \right) - \ln \left( 1 - e^{-\beta \eta_\alpha^{(0)}} \right) \right], \quad (5.7)$$

where  $\frac{1}{\beta} \ln(1 - e^{-\beta \eta})$  is the free energy of an oscillator with frequency  $\eta$ . The  $\eta_\alpha^2$  are given by the eigenvalues of the dynamical matrix  $\mathcal{D}$  corresponding to the Hamiltonian 5.5:

$$\mathcal{D} = \begin{pmatrix} \widetilde{\omega}_c^2 & \kappa \gamma_1 & \kappa \gamma_2 & \dots \\ \kappa \gamma_1^* & \Omega_1^2 & 0 & \dots \\ \kappa \gamma_2^* & 0 & \Omega_2^2 & \dots \\ \vdots & \vdots & \vdots & \ddots \end{pmatrix}. \quad (5.8)$$

Here  $\widetilde{\omega}_c^2$  is the shifted cavity frequency  $\widetilde{\omega}_c^2 = \omega_c^2 + \kappa^2 \sum_a \frac{|\gamma_a^2|}{\Omega_a^2}$  as a consequence of the coupling with the solid degrees of freedom. We determine these normal modes perturbatively in the solid volume fraction  $\kappa^2 \ll 1$ . The perturbative expansion for the cavity mode (entry 0 in the dynamical matrix of Equation 5.8) reads

$$\eta_0^2 = \omega_c^2 + \kappa^2 \sum_a \frac{|\gamma_a^2|}{\Omega_a^2} + \kappa^2 \sum_a \frac{|\gamma_a^2|}{\omega_c^2 - \Omega_a^2}, \quad (5.9)$$

while for the matter modes we have:

$$\eta_a^2 = \Omega_a^2 + \kappa^2 \frac{|\gamma_a^2|}{\Omega_a^2 - \omega_c^2}. \quad (5.10)$$

One can then linearize Equation 5.7 in  $\delta \eta$ , leading to  $\Delta F = \kappa^2 \sum_{\alpha} b \left( \eta_{\alpha}^{(0)} \right) \delta \eta_{\alpha}$ , and insert the perturbative expressions of the cavity (Equation 5.9) and of the solid (Equation 5.10) eigenmodes. With some straightforward manipulations, this gives the results of Equation 5.3, with the function  $\alpha''(\omega)$  of the form:

$$\alpha''(\omega) = \pi \sum_a \frac{|\gamma_a|^2}{2\Omega_a^3} [\delta(\omega - \Omega_a) - \delta(\omega + \Omega_a)]. \quad (5.11)$$

Finally, we need to confirm that this expression (Equation 5.11) is precisely the imaginary part of the polarizability within the model of Equation 5.5. A simple link is made via the dielectric loss. When the system is driven with a time-dependent field, the absorbed energy per volume is the time-average of  $\mathbf{E}(t) \partial_t \mathbf{P}(t)$ . With the above definition of the polarizability, the loss under a field  $\mathbf{A}(t) = \hat{n} \mathbf{A}_\omega e^{-i\omega t} + \text{h.c.}$  is

$$\Gamma(\omega) = 2\omega^3 \epsilon_0 \alpha''(\omega) |\mathbf{A}_\omega|^2. \quad (5.12)$$

On the other hand, in the model (Equation 5.5) we can calculate the energy absorption due to a time dependent classical vector potential, which by means of Equation 5.6 is introduced by replacing  $\Pi \rightarrow \Pi + \sqrt{V \epsilon_0} \mathbf{A}(t)$ . Fermi's golden rule (or equivalently the Kubo linear response formalism [184]) gives

$$\Gamma_{\mathbf{A}}(\omega) = |\mathbf{A}_\omega|^2 2\omega \sum_a |\gamma_a|^2 \chi''_{aa}(\omega) \epsilon_0 V \kappa^2 = V_m |\mathbf{A}_\omega|^2 2\omega \sum_a |\gamma_a|^2 \chi''_{aa}(\omega) \epsilon_0 \quad (5.13)$$

with  $\chi''_{\alpha\alpha}$

$$\chi''_{\alpha\alpha}(\omega) = \frac{\pi}{2\Omega_\alpha} [\delta(\omega - \Omega_\alpha) - \delta(\omega + \Omega_\alpha)], \quad (5.14)$$

the spectral function of the single mode  $\alpha$ . Comparing the two expressions in Equation 5.12 and Equation 5.13, shows that Equation 5.11 is the actual result for the polarizability.

### 5.6.2 CONTROL OF DISSIPATIONS THROUGH CAVITY ELECTRODYNAMICS

In this section we discuss in detail the theory beyond the Purcell-like scenario, i.e. the scenario in which the changes in the effective critical temperature of 1T-TaS<sub>2</sub> could be related to a control of the sample's dissipations through the cavity electrodynamics. In this scenario, the reshaping of the electromagnetic density of states at the sample position due to the cavity electrodynamics could result in a modification of the sample's thermal load and subsequently of its temperature.

In order to estimate the Purcell-based effect, we proceed as indicated in Figure 5.21A. The sample is in thermal contact with the cold finger through the membranes, but it is also in thermal contact with the external photon bath at  $T_{\text{PH}} = 300$  K. We assume that the thermal transfer from the cold finger to the sample depends only on the difference between the cold finger temperature ( $T_{\text{CF}}$ ) and the sample effective temperature ( $T_{\text{S}}$ ). Conversely, we assume that the thermal load on the sample due to the contact with the external photon bath is mediated by the cavity, in analogy with the Purcell effect [13–16]. Under these hypotheses, we can write two rate equations describing respectively the cavity-independent heat flow between the cold finger and the sample:

$$Q_{\text{CF-S}} = K_{\text{CF-S}}(T_{\text{CF}} - T_{\text{S}}), \quad (5.15)$$

and the cavity-mediated heat transfer between the sample and the external photon bath:

$$Q_{\text{PH-S}}(\omega_c, Q) = K_{\text{PH-S}}(\omega_c, Q)(T_{\text{PH}} - T_{\text{S}}). \quad (5.16)$$

In the previous equations  $K_{\text{CF-S}}$  represents the cavity-independent coupling constant between the cold finger and the sample, while  $K_{\text{PH-S}}(\omega_c, Q)$  the coupling constant between the sample and the photon bath, which depends on the cavity geometry, i.e. on the fundamental frequency  $\omega_c$  and on the quality factor  $Q$ .

The coupling constant  $K_{\text{PH-S}}(\omega_c, Q)$  between the sample and the photon bath can be expressed as the joint density of states of the solid  $\rho_{\text{Solid}}(\omega)$  and of the cavity  $\rho_{\text{Cavity}}$ , with the latter multiplied by the Boltzmann distribution at the photon bath temperature  $T_{\text{PH}} = 300$  K:

$$K_{\text{PH-S}}(\omega_c, Q) = \int_0^{+\infty} d\omega \rho_{\text{Cavity}}(\omega_c, Q)(\omega) \cdot \rho_{\text{Solid}}(\omega) e^{-\frac{\omega}{k_B T_{\text{PH}}}}. \quad (5.17)$$

Let us model the sub-THz absorption of the sample, as for the free energy scenario presented in Section 5.6.1, with a continuum broad mode centred at  $\Omega = 15$  GHz and with a spectral linewidth  $\gamma = 20$  GHz, which we tentatively associate with the domain wall fluctuations of the non-commensurate regions. Under this hypothesis, the solid density of state in the sub-THz region can be expressed through the dielectric loss per unit frequency as:

$$\rho_{\text{Solid}}(\omega) = \frac{\alpha''(\omega)}{\Omega} = \alpha(0) \frac{\Omega\gamma\omega}{(\omega^2 - \Omega^2)^2 + (\gamma\omega)^2}. \quad (5.18)$$

The multimode cavity density of states takes instead the following form:

$$\rho_{\text{Cavity}}(\omega_c, Q)(\omega) = \sum_{n=0}^{+\infty} \frac{\gamma_{\text{cav}}}{(\omega - n\omega_c)^2 + (\gamma_{\text{cav}})^2}, \quad (5.19)$$

where  $\gamma_{\text{cav}}$  represents the linewidth of the bare cavity, which is related to the quality factor  $Q$  by the relation  $Q = \frac{\omega_c}{\gamma_{\text{cav}}}$ . The quality factor of the empty cavity is set by the experimental conditions (see Section 5.5.1).

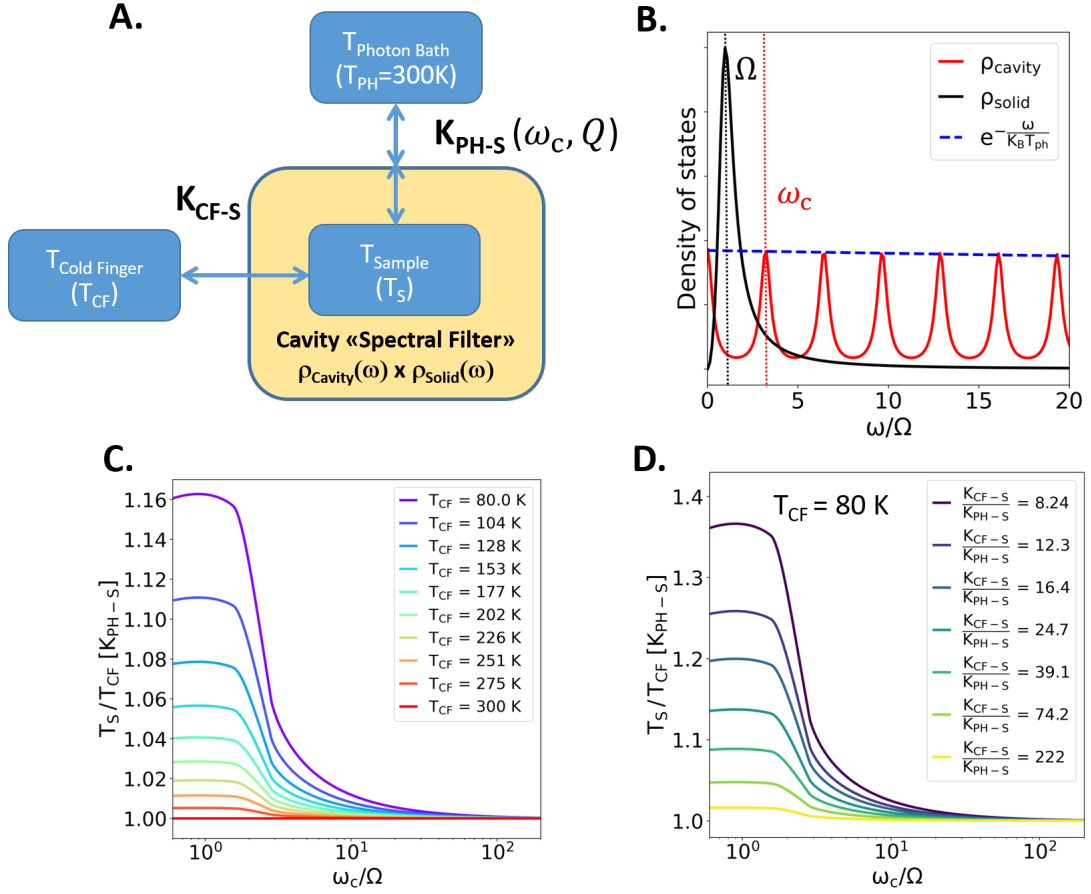


**Figure 5.21: Cavity control of sample dissipations.** **A.** Schematic representation of the thermal loads on the sample determined by its coupling with the cold finger through the cavity-independent factor  $K_{\text{CF-S}}$  and with the photon thermal bath through the cavity-dependent factor  $K_{\text{PH-S}}(\omega_c, Q)$ . **B.** Density of states of the solid (peaked at the mode frequency  $\Omega$ ) and of the cavity (peaked at multiples of the fundamental mode  $\omega_c$ ). The cavity density of states is multiplied by the Boltzmann distribution at the temperature of the photon bath  $T_{\text{PH}} = 300$  K. **C.** Dependence of the temperature ratio  $\frac{T_S(\omega_c, Q)}{T_{\text{CF}}}$  as function of the cavity frequency for different temperatures of the cold finger  $T_{\text{CF}}$ . The renormalization of the absolute temperature scales with  $K_{\text{PH-S}}(\omega_c, Q)$ , which is related to the mode oscillator strength. **D.** Evolution of the temperature ratio  $\frac{T_S(\omega_c, Q)}{T_{\text{CF}}}$  upon tuning the cavity frequency for different values of the cavity-independent coupling constant  $K_{\text{CF-S}}$  at a fixed cold finger temperature  $T_{\text{CF}} = 80$  K. The values of the cavity-independent constant  $K_{\text{CF-S}}$  indicated in the legend are normalized by  $K_{\text{PH-S}}(\omega_c, Q)$  evaluated at  $\omega_c = \Omega$ .

We present in Figure 5.21B a plot of the solid density of state and of the cavity density of states multiplied by the Boltzmann distribution at the photon bath temperature  $T_{\text{PH}} = 300$  K.

Under stationary conditions, the thermal flow from the cold finger to the sample  $Q_{\text{CF-S}}$  equals the cavity-mediated heat transfer between the sample and the photon bath  $Q_{\text{PH-S}}(\omega_c, Q)$ , that is  $Q_{\text{CF-S}} + Q_{\text{PH-S}}(\omega_c, Q) = 0$ . At equilibrium, we can subsequently calculate an effective sample temperature  $T_s(\omega_c, Q)$ , which takes the form:

$$T_s(\omega_c, Q) = \frac{K_{\text{PH-S}}(\omega_c, Q)T_{\text{PH}} + K_{\text{CF-S}}T_{\text{CF}}}{K_{\text{PH-S}}(\omega_c, Q) + K_{\text{CF-S}}}. \quad (5.20)$$

The temperature ratio between the sample and the cold finger  $\frac{T_s(\omega_c, Q)}{T_{\text{CF}}}$  as a function of the cavity fundamental mode is plotted in Figure 5.21C for different cold finger temperatures. We stress that the renormalization of the sample effective temperature in the employed cavity frequency range scales with the cavity-solid joint density of states  $K_{\text{PH-S}}(\omega_c, Q)$ , and hence with the total spectral weight within the solid absorption band  $\alpha(0)$ . Larger cavity-induced renormalization of the sample's temperature are hence expected for a larger oscillator strength of the sub-THz collective mode.

We note that, upon increasing the cavity frequency, i.e. by decoupling the electromagnetic active sub-THz modes from the cavity fundamental mode, the model predicts a decrease of the temperature ratio  $\frac{T_s(\omega_c, Q)}{T_{\text{CF}}}$  consistent with a decrease of the effective temperature at the sample's position. In particular,  $T_s$  tends to  $T_{\text{CF}}$  at high cavity frequencies, i.e. when the cavity field is far off-resonance with the low energy mode. We highlight that this trend is qualitatively consistent with the experimental observations of Figure 5.12 and Figure 5.14.

As marked in Figure 5.21C, the cavity-mediated modification of the sample-photon bath dissipations is more efficient when the temperature difference between the cold finger and the photon thermal bath is larger. For a given cavity configuration (frequency  $\omega_c$  and quality factor  $Q$ ) the model predicts therefore a greater shift of the sample's temperature at lower temperatures. This prediction could therefore qualitatively justify the cavity-mediated shrinking of the hysteresis (Figure 5.15A, B). Indeed, since  $T_c^{\text{heating}} > T_c^{\text{cooling}}$ , we expect the Purcell-like effect (Figure 5.21C) to be more efficient at  $T_c^{\text{cooling}}$  with respect to  $T_c^{\text{heating}}$ , thus leading to an effective shrinking of the hysteretic behaviour.

In Figure 5.21D we prove that the trend highlighted in Figure 5.21C is qualitatively independent on the thermal coupling constant between the sample and the cold finger  $K_{\text{CF-S}}$ . A change in  $K_{\text{CF-S}}$  in the employed cavity frequency range acts only as a scaling factor of the cavity frequency trend. The results shown in 5.21D has been calculated for a representative cold finger temperature  $T_{\text{CF}} = 80$  K.

Importantly, we note that the renormalization of the sample effective temperature induced by the cavity is more efficient when the thermal coupling between the sample and the cold finger  $K_{\text{CF-S}}$  is smaller. At very high thermal couplings ( $K_{\text{CF-S}}$ ) we expect indeed the contribution to the sample's temperature of the cavity-dependent interaction with the photon bath, and hence the renormalization of  $T_s$ , to be negligible.

## 5.7 METHODS

In this section we present the experimental details of the temperature measurement within the cavity and we give the details of the finite elements simulations employed to analyse the incoherent thermal dynamics inside the cavity. These methods will be jointly exploited in the next section 5.8 to extensively prove the cavity-induced origin of the phase transition control.

### 5.7.1 MEASUREMENT OF THE TEMPERATURE WITHIN THE CAVITY

We stressed while presenting the experimental evidences of the cavity-driven control of the phase transition (Section 5.3) that the temperature indicated in all the reported measurements is the cold finger readout. When performing THz optical measurements, this choice is mandatory because any thermosensitive device introduced in the cavity would not only impede the THz transmission, but also modify the sample environment. On the other hand, measuring the actual temperature of the sample is crucial to discriminate between the two cavity-mediated scenarios that we proposed (see Section 5.6 for further theoretical details).

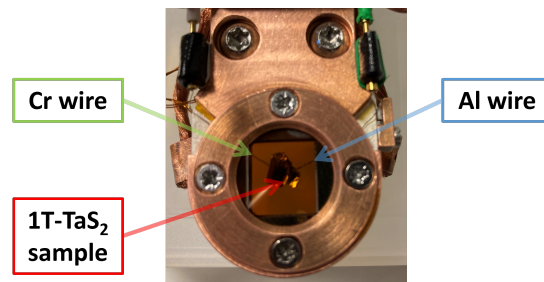


**Figure 5.22:** Cr-Al thermocouple junction sealed within the membranes and in thermal contact with the sample.

To this aim, we directly measured the temperature – both of the membrane and the sample – in the cavity by sealing of a home-made 20  $\mu\text{m}$  Cr-Al junction within the membranes. In Figure 5.22 we show a picture of the thermocouple arrangement within the sample mount. Importantly, in order to not have offsets in the temperature readout, all the wires connecting the junction to the output of the cryostat head were made of Cr and Al of  $\sim 120 \mu\text{m}$ . The only discontinuity point is represented by the gold male-female connectors at the output of the sample holder which, as we verified, give no temperature discrepancy.

We highlight that, in this experimental setting, the THz optical measurements cannot be performed; it is therefore not possible to monitor the THz response of the sample as function of its actual (measured) temperature. All the temperature measurements discussed must be then considered a separate characterization of the temperature of the sample in a cavity geometry which is nevertheless identical to the one used in all the THz measurements.

### 5.7.2 FINITE ELEMENT SIMULATIONS OF INCOHERENT THERMAL HEATING

To estimate the effect of the incoherent thermal radiation within the cavity, we performed finite elements simulations exploiting the COMSOL MULTIPHYSICS software. By simulating the incoherent thermal load at the membrane position, we are indeed able to gain insight on the membrane's thermal profile for different cavity configurations and hence exclude trivial scenarios in which the sample's temperature is modified by purely geometrical factors related to the cavity settings.

Let us model the membrane as a grey body having emissivity  $\epsilon$ , reflectivity  $\rho$ , absorptivity  $\alpha$ , and temperature  $T$ , and let us assume the incoherent radiative properties of the membrane to be fully described by these four parameters  $\epsilon$ ,  $\rho$ ,  $\alpha$ ,  $T$ . The net inward heat flux  $Q$  at certain point  $\mathbf{x}$  on the membrane's surface will be given by the difference between the total arriving radiative flux  $G$  (irradiation) and the total outgoing radiative flux  $J$  (radiosity):

$$Q(\mathbf{x}) = G(\mathbf{x}) - J(\mathbf{x}). \quad (5.21)$$

The radiosity  $J$  is the sum of the reflected and emitted radiation from the membrane and can be described through the Stefan-Boltzmann equation as:

$$J(\mathbf{x}) = \rho G(\mathbf{x}) + \epsilon \sigma T^4. \quad (5.22)$$

By imposing now that the membrane is in thermodynamical equilibrium with the surroundings, i.e. the emissivity  $\epsilon$  is equal to the absorptivity  $\alpha$ , we can rewrite the reflectivity  $\rho$  as:

$$\alpha = \epsilon = 1 - \rho. \quad (5.23)$$

Thus, the net inward radiative flux of the membrane can be expressed only as a function of  $G$ ,  $\epsilon$ , and  $T$  as:

$$Q(\mathbf{x}) = \epsilon \left( G(\mathbf{x}) - \sigma T^4 \right). \quad (5.24)$$

Equation 5.24 has been used in COMSOL as radiation boundary condition for the membrane's surface.

The total surface radiation  $G$  includes radiation from both the ambient surroundings and from other surfaces. A generalized equation for the irradiative flux is:

$$G(\mathbf{x}) = G_m(\mathbf{x}) + F_{\text{amb}}(\mathbf{x}) \sigma T_{\text{amb}}^4, \quad (5.25)$$

where  $G_m$  is the mutual irradiation arriving from other surfaces in the modelled geometry,  $T_{\text{amb}} = 300$  K is the temperature of the surrounding environment schematized as a radiative black body, and  $F_{\text{amb}}$  is the ambient view factor. The view factor parameter describes the portion of the view from each point that is covered by ambient conditions. Conversely,  $G_m$  is determined by the geometry and the local temperatures of the surrounding surface boundaries. Including the expression of the irradiation  $G$  inside Equation 5.24, the general expression of the net radiative load at the specific point  $\mathbf{x}$  on the membrane is:

$$Q(\mathbf{x}) = \epsilon \left( G_m(\mathbf{x}) + F_{\text{amb}}(\mathbf{x}) \sigma T_{\text{amb}}^4 - \sigma T^4 \right) \quad (5.26)$$

This equation has been used by COMSOL to compute the net radiative transfer at each point  $\mathbf{x}$  of the membrane's surface [185]. We stress that Equation 5.26 results in

a linear equation system in  $Q(\mathbf{x})$  that must be solved in parallel with the heat transfer equation for the temperature  $T$ :

$$Q(\mathbf{x}) = -k\nabla^2 T(\mathbf{x}) \quad (5.27)$$

in order to extract the membrane's thermal profile  $T(\mathbf{x})$ . In the previous expression  $k$  represents the membrane's thermal conductivity.

Firstly, we discuss here the simulated thermal profile of a single silicon nitride membrane held in free space. For simplicity we assumed 2D circular geometry for the membrane. We imposed the boundary conditions in order to have the membrane's edge at the same temperature of the cold finger. The thermal profile along the radial coordinate of the free space membrane will be hence controlled by the balance between the membrane's emissivity  $\epsilon$  and the thermal load due to ambient black body radiation at  $T_{\text{amb}} = 300$  K. For the simulations we set the silicon nitride emissivity at  $\epsilon = 0.3$  [186], supposing no wavelength dependence across the mid-infrared spectral range, where the black-body radiation of the membrane is located for the employed temperatures ( $80 < T < 300$  K). Figure 5.23 illustrates the simulated thermal profile of the membrane in free space, together with a cut along the radial direction.

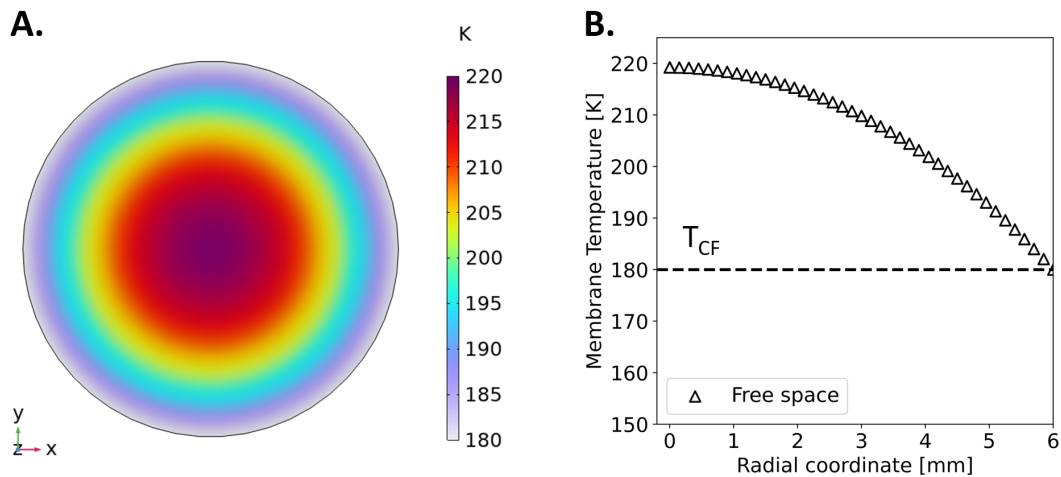


**Figure 5.23: Finite elements simulation of the membrane's thermal dissipations in free space.** **A.** Simulated 2D temperature profile of the membrane in free space. **B.** Radial dependence of the membrane's temperature held in free space. The cold finger temperature has been set at  $T_{\text{CF}} = 180$  K.

We highlight that by setting the cold finger temperature at the temperature at which the phase transition in  $1\text{T-TaS}_2$  is observed in free space ( $T_{\text{CF}} = 180$  K), we can retrieve a temperature in the middle of the membrane (and hence at the sample position) corresponding to the literature  $T_c$  [164]. The simulation therefore confirms the assumption that the measured rigid shift of the free space critical temperature (Figure 5.3) with respect to the literature one has to be attributed to the high thermal impedance of the  $\text{Si}_3\text{N}_4$  membranes between which the sample is embedded. This high thermal impedance does not hence allow the membranes to efficiently re-radiate the ambient black-body radiation.

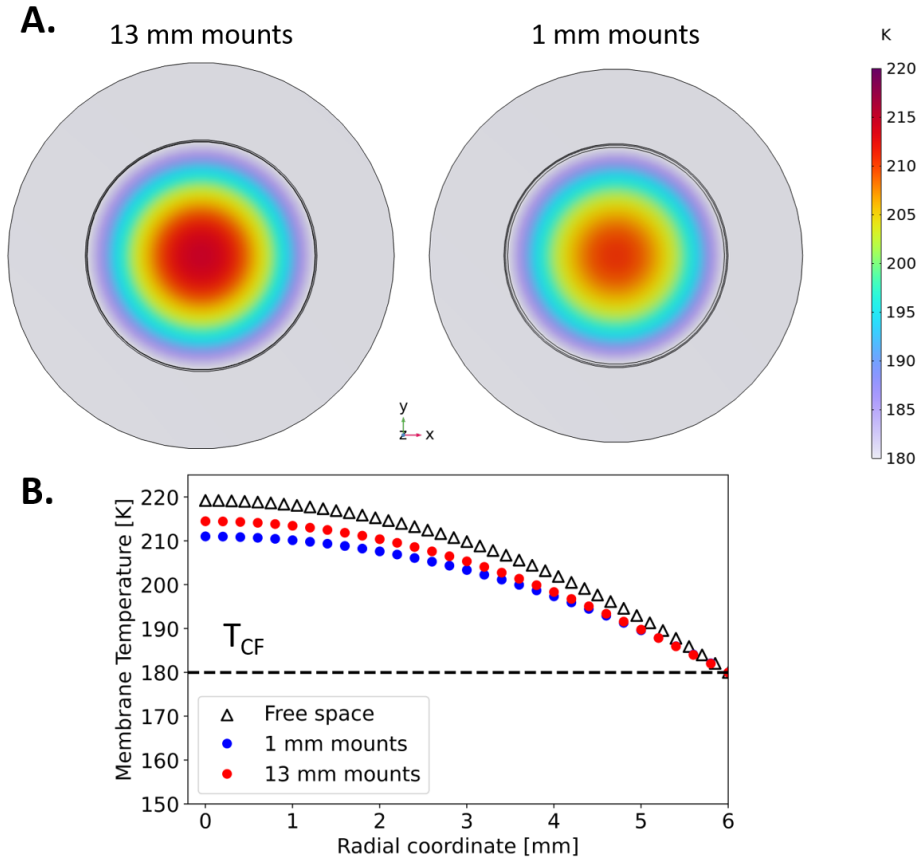


**Figure 5.24: Finite elements simulation of membrane's temperature as a function of the relative position of the mirror mounts. A.** 3D thermal profile of the membrane for two representative distances between the mirror mounts (13 mm and 1.0 mm). **B.** Cut of membrane's thermal profile along the radial direction for the two mounts' distances presented in A. The cold finger temperature has been set at  $T_{CF} = 180$  K, as well as the mounts temperature.

Importantly, as shown in Figure 5.24, the simulations confirm that the incoherent thermal load on the membranes is not significantly influenced by the distance between the cryogenic mirror mounts. This further excludes a trivial scenario in which is the geometrical variation of the cavity mounts which screens the ambient radiation and subsequently changes the membrane's temperature.

## 5.8 TESTS FOR THE CAVITY-INDUCED ORIGIN OF THE PHASE TRANSITION CONTROL

The main experimental evidence reported in this chapter is that the effective critical temperature of the metal-to-insulator transition in  $1T\text{-TaS}_2$  can be modified by tens of kelvin by placing the sample within a sub-THz cavity. We have demonstrated that the renormalization of the effective critical temperature depends both on the cavity length and the cavity alignment (Section 5.3).

The novelty of the experiment, which represents one of the few attempts in the literature to study how the properties of solid-state complex systems can be modified by the light-matter coupling, calls for a thorough characterization of the effect with the

aim of ruling out possible experimental artifacts and trivial scenarios. In particular, the most straightforward explanation could be that the huge shift of the effective critical temperature is due to an incoherent radiation heating of the sample, placed within the cavity and therefore in scarce thermal contact with the cold finger.

In the following, we will detail that this is not the case. By jointly discussing results of the finite elements simulations and of the temperature measurements, we will prove that a coherent light-matter interaction which modifies the cavity electro-dynamics may be the dominant effect for explaining our experimental observations.

To facilitate the discussion, we will address specific questions that may arise and argue how the complementary tests that we carried out hint towards a cavity-mediated scenario.

### 5.8.1 DOES THE SAMPLE AFFECT THE TEMPERATURE DIFFERENCE BETWEEN THE COLD FINGER AND THE CAVITY CENTER?

In a trivial scenario in which the sample experiences an incoherent radiation heating, also the membranes are expected to behave similarly in response to the modification of the cavity parameters. In order to rule out this possibility, we measured the temperature of the sample and the temperature of just the membranes (i.e., without placing the sample between them) by means of the thermocouple for different cavity fundamental modes.

Figure 5.25 presents the results of the temperature measurements performed within the cavity when the thermocouple is sealed on the sample (Figure 5.25A) and when it is held just between the two  $\text{Si}_3\text{N}_4$  membranes (Figure 5.25B). The temperature measurements, for each cavity setting, are plotted as the difference between the temperature measured on the sample/membrane ( $T_S/T_{\text{Membrane}}$ ) and the one recorded on the cold finger ( $T_{\text{CF}}$ ) as a function of  $T_S$  or  $T_{\text{Membrane}}$ .

We highlight two distinctive trends, characteristic of the presence of the sample:

- The absolute temperature renormalization passing from the lower to higher cavity frequency is significantly higher on the sample with respect to the membrane. For the lowest cold finger temperature ( $T_{\text{CF}} = 80$  K) we indeed measured a renormalization of the sample's temperature of  $\sim 27$  K moving the cavity fundamental mode from 11.5 GHz to 42.8 GHz. Conversely, between the two cavity configurations we measured only a  $\sim 9$  K renormalization of the membrane's temperature.
- The temperature renormalization induced by the cavity in the sample is non-monotonic with respect to the free-space case. Indeed, for high frequency cavities the sample's temperature within the cavity is lower with respect to the sample's temperature measured in free space. This is qualitatively consistent with the critical temperature trend as function of the cavity fundamental mode revealed by THz spectroscopy (Figure 5.12). Conversely, this anomalous non-monotonic behaviour is not observed on the membranes, where the membrane's temperature measured within the cavity is lower than the free space case for all the cavity frequencies studied. In particular, we observe that the membrane's temperature measured for the larger cavity length (11.5 GHz) approaches the trend measured in free space.

In Figure 5.25C we present the differential temperature  $T_S - T_{\text{CF}}$  for a fixed cold finger temperature as a function of the cavity fundamental frequency. To perform this

length dependent study the cold finger temperature has been set at  $T_{CF} = 150$  K, as for the THz transmission measurements (Figure 5.11).

As expected from the full temperature scans presented in Figure 5.25A, B we revealed a renormalization of the sample's effective temperature of  $\sim 18$  K by sweeping the cavity mode from 11.5 GHz to 42.8 GHz. On the other hand, for the same frequency range, we detected a significantly smaller change in the membrane's temperature ( $\sim 5$  K).

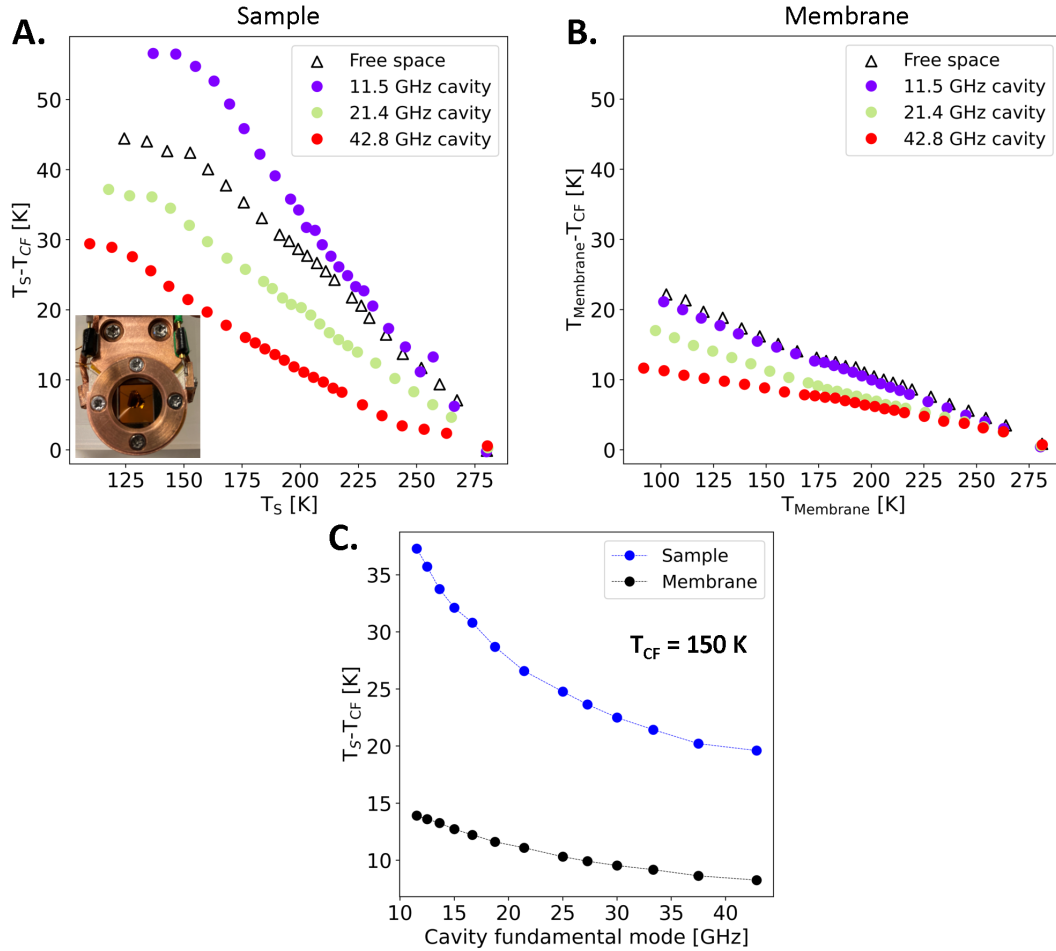


**Figure 5.25: Temperature measurements within the cavity.** **A.** Difference between the temperature measured on the sample ( $T_S$ ) and on the cold finger ( $T_{CF}$ ) as a function of the sample temperature. Temperatures have been measured upon heating the sample from the dielectric C-CDW phase. **B.** Difference between the membrane temperature and the cold finger temperature when the thermocouple is held just between the two membranes. **C.** Difference between the temperature measured on the thermocouple and on the cold finger as a function of the cavity frequency for a fixed cold finger temperature ( $T_{CF} = 150$  K). In blue the measurements performed with the thermocouple put on the sample, while in black with the thermocouple held between the membranes.

A further confirmation that the reported effect is related to the cavity-mediated interaction of the sample with the confined field comes from the direct measurement of the sample's temperature both in heating and cooling conditions. Should the temperature

renormalization depend on an incoherent heating, no differences would be expected in the two scanning conditions. This is in fact what we observed on the membrane (Figure 5.26A) where the difference between  $T_{\text{Membrane}}$  and  $T_{\text{CF}}$  is identical when heating up or cooling down within the cavity. However, the sample's temperature shows a different trend for the heating/cooling directions (Figure 5.26B). In particular, while we do not observe any systematic discontinuity when heating up the sample, a kink at the nominal critical temperature  $\sim 215$  K is always present when cooling down the sample at different cavity lengths. In the temperature range  $\sim 160 - 215$  K we also observe a constant temperature difference between the sample and the cold finger. The thermodynamical meaning of this effect is not clear, but the observation of this hysteretic behaviour, which is not present on the bare membranes, proves that the effects discussed are peculiar of the sample.

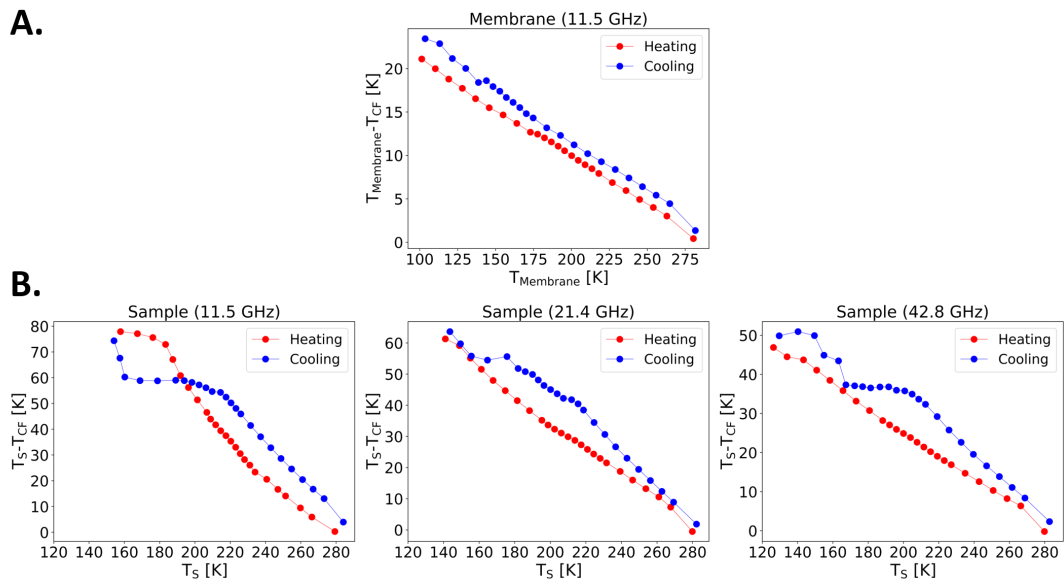


**Figure 5.26: Temperature measurements upon heating and cooling.** A. Difference between the membrane and the cold finger temperature within a 11.5 GHz cavity upon heating (red curve) and cooling (blue curve). Same as (A) but for the sample's temperature in three different cavity configurations. The cavity frequency for each configuration is indicated in the plot title.

### 5.8.2 DOES THE TEMPERATURE OF THE CAVITY MIRRORS AFFECT THE SAMPLE TEMPERATURE?

A possible source of incoherent thermal load are the cavity mirrors, whose presence might affect the temperature of the sample. In order to exclude this incoherent heating effect, we carried out a characterization of the phase transition shift with cavity frequency as a function of the mirrors temperature. We made this test by comparing the cryo-cooled mirrors configuration ( $T_{\text{mirror}} = 95$  K<sup>2</sup>) with the 290 K mirrors one. The

<sup>2</sup> This is the lowest reachable temperature of the mirrors for the present experiment, measured when the cold finger is at  $T_{\text{CF}} = 80$  K.

relation between the mirrors and the sample's temperature in the two cases is presented in Figure 5.27.

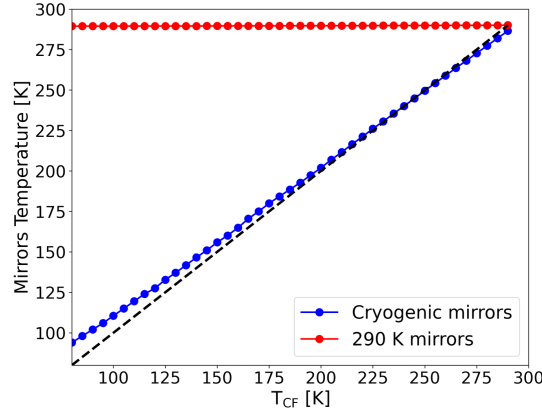


**Figure 5.27: Temperature of the mirrors in the cryogenic configuration and in the room temperature case.** Relation between the cold finger temperature and the mirrors temperature in the cryo-cooled mirrors configuration and in the 290 K mirrors configuration. The black dashed line marks the diagonal.

Figure 5.28 shows the temperature dependent THz transmission upon heating 1T-TaS<sub>2</sub> embedded in the middle of cavities with three different frequencies ( $\omega_c = 11.5, 21.2, 48.8$  GHz). In Figure 5.28A the temperature scans are performed with the cavity mirrors at 290 K, while in Figure 5.28B they are performed in the configuration with cryo-cooled mirrors. The dependence of the effective critical temperature on the cavity frequency is presented in Figure 5.29 for the two configurations.

It is evident that, despite a rigid temperature shift independent on the cavity frequency ( $\sim 35$  K), the effective critical temperature of the phase transition is pushed up with the 290 K mirrors upon increasing the cavity frequency, displaying a trend which is analogous to the one measured with the cryogenic mirrors. Crucially, this further hints that the effective T<sub>c</sub> shift is an effect due to the cavity electromagnetic confinement. If not, in the 290 K mirrors configuration we would have expected to increase the incoherent thermal load on the sample upon closing the cavity and hence push down the apparent critical temperature of the phase transition.

In order to clarify this point, we simulated with the finite elements software COMSOL the membrane's thermal profile embedded in three cavities having different lengths. The employed 3D geometry can be found in Figure 5.30A and Figure 5.31A for cryogenic and ambient temperature mirrors, respectively.

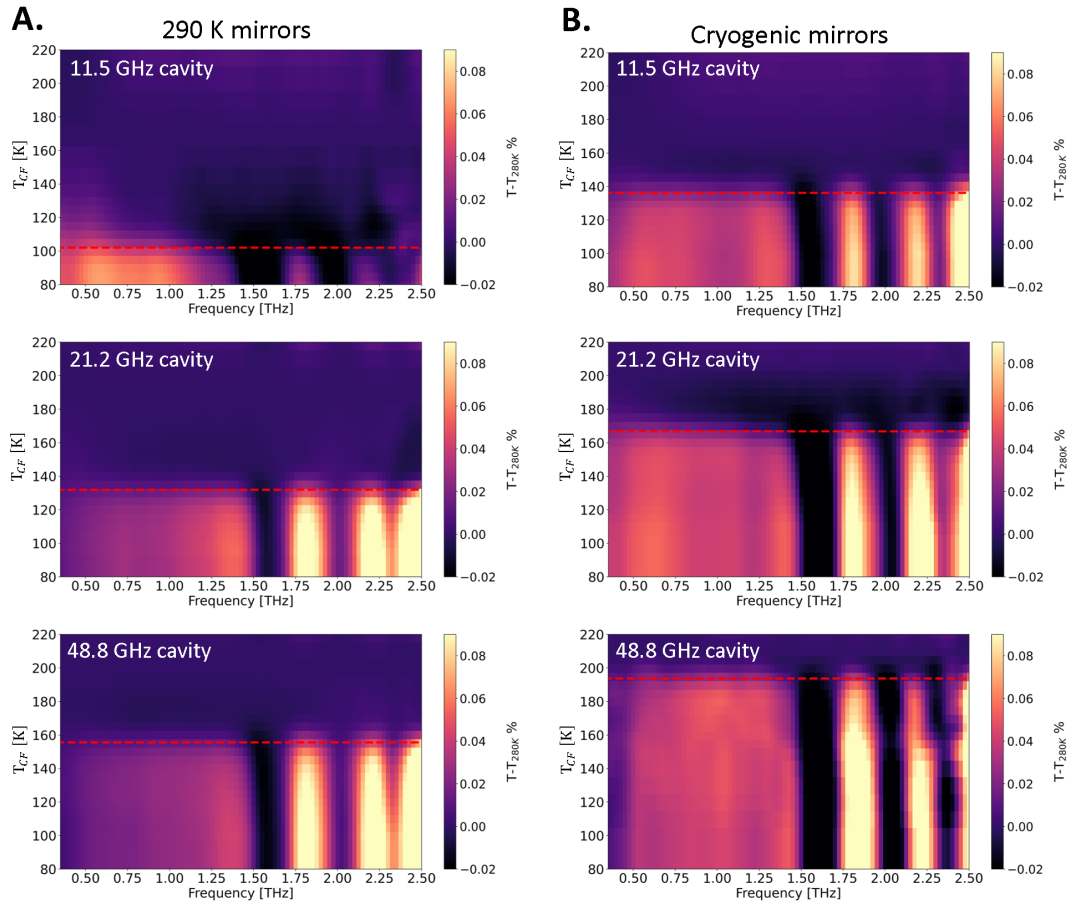


**Figure 5.28: Dependence of the phase transition on the temperature of the cavity mirrors revealed by THz spectroscopy. A.** Heating temperature scans for three representative cavity frequencies ( $\omega_c = 11.5, 21.2, 48.8$  GHz) in the 290 K mirrors configuration. **B.** Corresponding heating temperature scans for the cryogenic mirrors configuration.

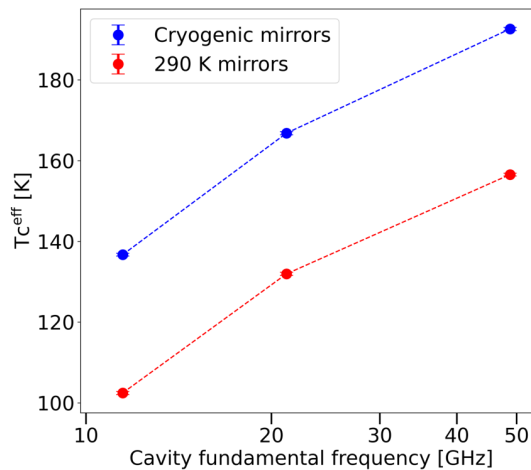


**Figure 5.29: Dependence of the heating critical temperature on the cavity fundamental frequency for the 290 K and cryogenic mirrors configurations.** In blue (red) the effective critical temperature measured upon heating the sample from the dielectric phase for the cryogenic mirrors (290 K mirrors) configuration. The effective critical temperatures have been extracted for the THz scans of Figure 5.28.

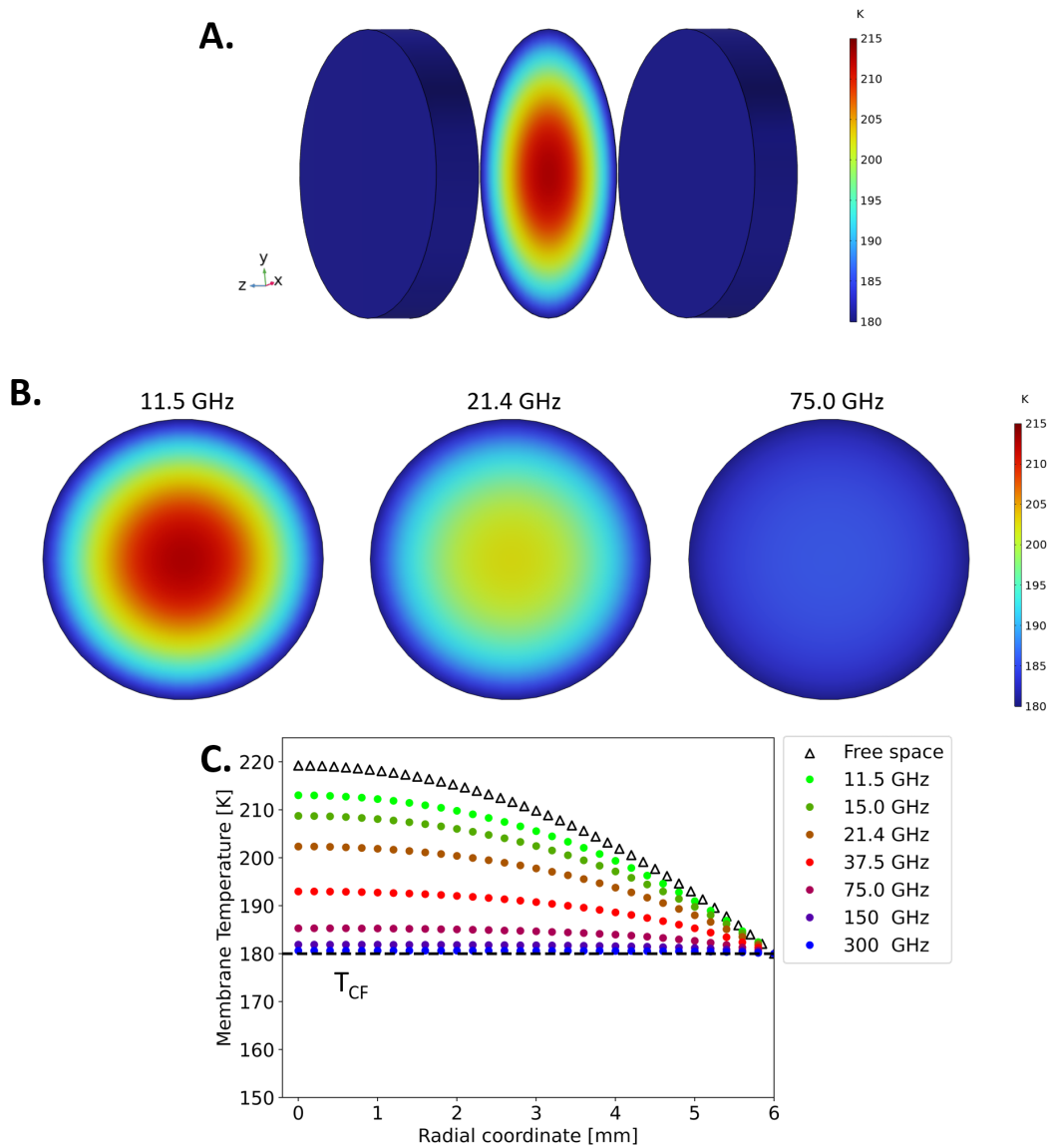


**Figure 5.30: Finite elements simulation of the membrane's temperature as a function of the cavity fundamental frequency in the cryogenic mirrors configuration.** **A.** 3D thermal view of the cryogenic cavity employed for the simulations. **B.** 2D thermal profile of the membrane within the cryogenic cavity for three representative cavity frequencies (11.5, 21.4, 75.0 GHz) employed in the experiment. **C.** Radial profile of the membranes held within the cryogenic cavity for different values of the cavity fundamental mode (indicated in legend). The cold finger temperature ( $T_{CF}$ ) and the mirrors temperature have been set at 180 K.

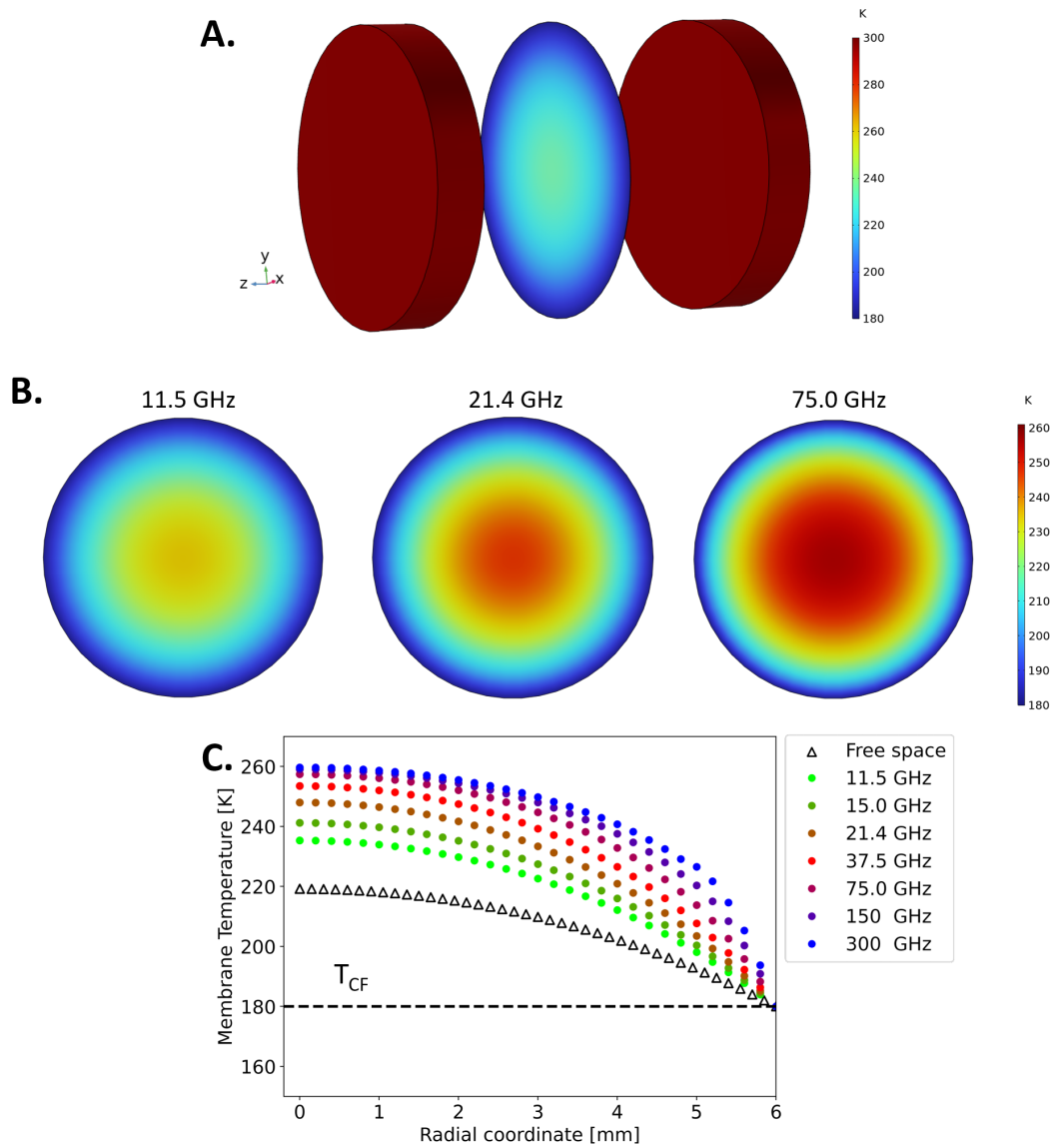


**Figure 5.31: Finite elements simulation of membrane's temperature as a function of the cavity fundamental frequency in the 300 K mirrors configuration. A.** 3D thermal view of the membrane held between the 300 K mirrors. **B.** 2D thermal profile of the membrane within the 300 K mirrors for three representative cavity frequencies (11.5, 21.4, 75.0 GHz) employed in the experiment. **C.** Radial profile of the membranes in the 300 K mirrors configuration for different values of the cavity fundamental mode (indicated in legend). The cold finger temperature ( $T_{CF}$ ) has been set to 180 K.

The radial profiles plotted in Figure 5.30C and Figure 5.31C show that, upon closing the cavity and thus increasing the cavity frequency, the shielding of ambient radiation is efficient only with the cryogenic mirrors, whereas in the 300 K mirror case the incoherent radiation from the mirror surfaces dominates the thermal load on the membrane. We stress that this trend is opposite to the one measured by THz spectroscopy (Figure 5.29).

Finite element simulations emphasize that the non-monotonic trend of the phase transition renormalization revealed by both THz linear spectroscopy (Figure 5.12) and direct temperature measurements (Figure 5.14) cannot be rationalized within an incoherent thermal scenario. Crucially, this evidence is valid for both the cryogenic and room temperature mirrors configurations. In both the scenarios, the finite elements simulations predict indeed a modification of the sample's temperature due to incoherent heating which is monotonic with respect to the free space value. Indeed, upon reducing the cavity length the effective sample's temperature monotonically decreases in the cryogenic mirrors case (Figure 5.30C), while it monotonically raises within the ambient temperature mirrors (Figure 5.31C).

Together with THz linear transmission, we characterized the effect of the mirrors temperature on the phase transition by tracking the sample's temperature as a function of the cavity frequency and of the cavity alignment.

Figure 5.32 shows a comparison of the differential temperature between the cold finger and the sample when the latter is held between the cryogenic cavity (Figure 5.32A) and between the cavity with 290 K mirrors (Figure 5.32B). The measured trend is qualitatively consistent with the effective critical temperature trend measured by THz spectroscopy (Figure 5.29). Indeed, despite a cavity-independent shift of the sample's temperature due to the different incoherent thermal load, in the 290 K mirrors case the sample's temperature is pushed down with a similar trend of the cryogenic mirrors case upon increasing the cavity frequency.

For the lowest cold finger temperature ( $T_{CF} = 80$  K) and in the 290 K mirrors case we measured a renormalization of the sample's temperature of  $\sim 31$  K by sweeping the cavity mode from 11.5 GHz to 42.8 GHz, which is similar to the  $\sim 27$  K measured within the cryogenic cavity. A similar trend between the 290 K and cryo-cooled cases is measured by fixing the cold finger at 150 K and tracking the differential temperature  $T_S - T_{CF}$  as a function of the cavity fundamental mode (Figure 5.32C). As highlighted in the comparative plots of Figure 5.32C, the renormalization of the sample's temperature measured either within the cryogenic cavity and with the 290 K mirrors is not consistent with the trend measured on the bare membranes, where a  $\sim 3$  times smaller renormalization is observed moving the cavity mode at 150 K from 11.5 GHz to 42.8 GHz (black points of Figure 5.32C).

Importantly, we further prove that the cavity-mediated change of sample's temperature is independent on the mirrors temperature by repeating the misalignment test with the 290 K mirrors. In Figure 5.33 we present the comparison of the differential temperature  $T_S - T_{CF}$  as function of the cavity alignment in the cryo-cooled and in the 290 K mirrors case. We show that, despite a rigid shift due to the incoherent thermal load introduced by the 290 K mirrors, the renormalization of the sample's temperature due to the cavity alignment is  $\sim 3.5$  times larger than the one measured on the bare membranes for both the mirrors temperature configurations. This further hints that the observed effect is ascribable to a selective effect of cavity electrostatics to the sample's thermodynamics.

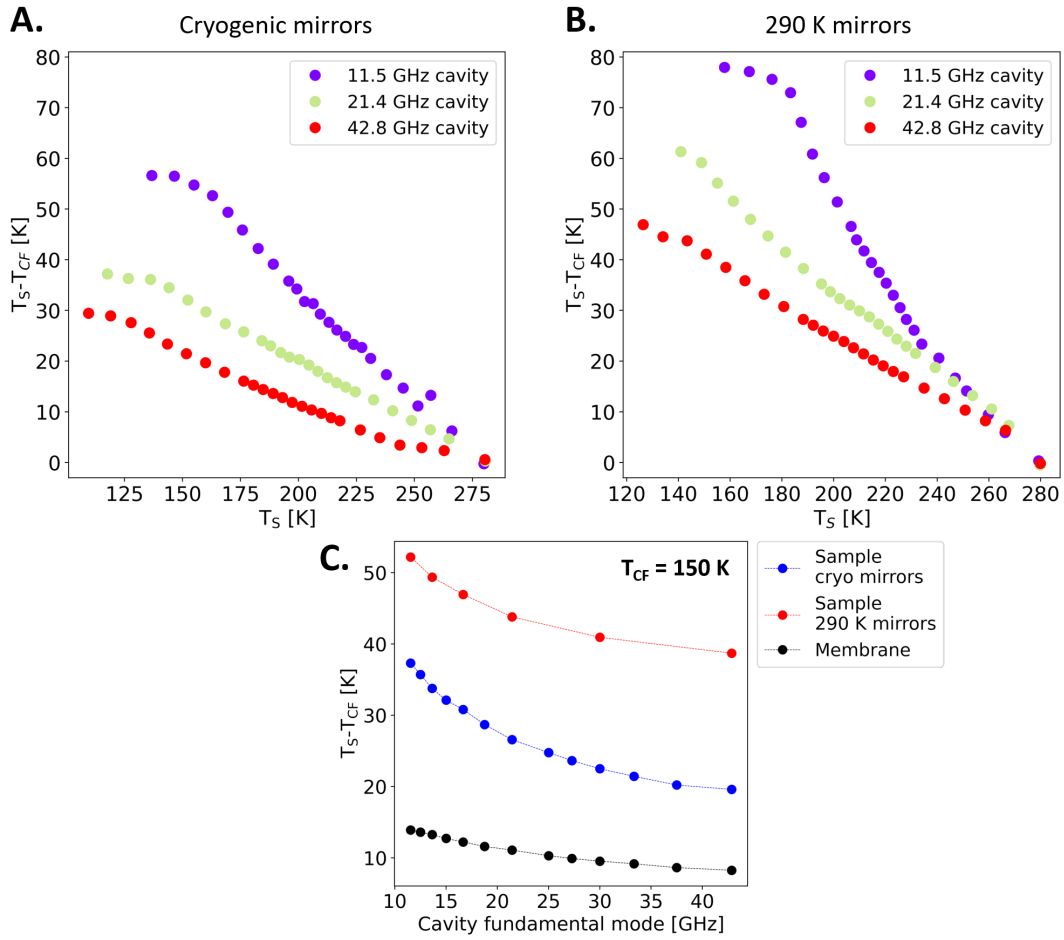


**Figure 5.32: Temperature measurement within the cavity as a function of the mirrors temperature.** **A.** Evolution of the difference between the temperature measured on the sample ( $T_S$ ) and on the cold finger ( $T_{CF}$ ) as a function of the sample temperature in the cryo-cooled mirrors configuration. **B.** Differential temperature  $T_S - T_{CF}$  as a function of the sample's temperature measured in the 290 K mirrors configuration. In both cases the temperatures have been measured upon heating the sample from the C-CDW phase. **C.** Differential temperature  $T_S - T_{CF}$  for a fixed cold finger temperature ( $T_{CF} = 150$  K) as a function of the cavity fundamental frequency. In blue the measurements performed within the cavity with cryogenic mirrors, while in red with 290 K mirrors. In black, for reference, the differential temperature measured within the membranes in the cryogenic mirrors configuration.

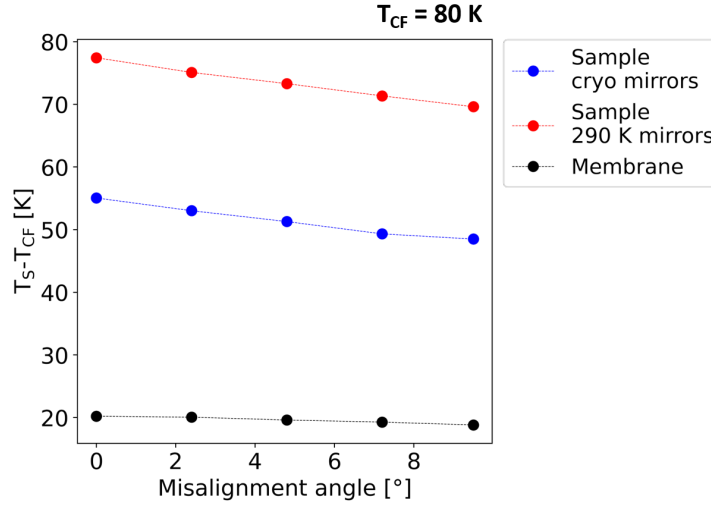


**Figure 5.33: Temperature measurements within the cavity as a function of the cavity alignment for different mirror temperatures.** Differential temperature  $T_S - T_{CF}$  as a function of the alignment measured for the sample held within cryogenic mirrors (blue) and 290 K mirrors (red). In black, for comparison, the differential temperature measured on the membranes. For the present measurements the cold finger has been set at  $T_{CF} = 80$  K.

### 5.8.3 DOES THE CAVITY ALIGNMENT MODIFY THE SAMPLE TEMPERATURE?

A further parameter which was shown to affect the effective critical temperature of the metal-to-insulator transition is the alignment of the cavity (Figure 5.8), which ultimately sets its quality factor (Figure 5.7). In order to demonstrate that this is not just a pure geometrical effect, we characterize in the following the response of the sample to the cavity misalignment.

First of all, we proved that the effective change of the phase transition temperature due to the cavity alignment cannot be ascribed to a change of the cavity length. In order to do so, we estimated the change of the cavity frequency at the sample position as a function of the misalignment angle of the mirrors. Figure 5.34A illustrates the THz time-domain traces in the C-CDW phase for different misalignment angles  $\theta$ . In the dashed box we highlight the THz reflection associated to the cavity round trip whose temporal distance from the main transmitted peak sets the cavity length. We note that upon misalignment the peak associated to the cavity round trip not only reduces its intensity as a consequence of the increase of optical losses (cfr Figure 5.7), but also exhibits a temporal shift associated to a modification of the cavity length.

The dependence of the cavity frequency shift on the misalignment angle  $\theta$  and the corresponding linear fit are shown in Figure 5.34B. We estimated the change of the fundamental frequency upon tuning the angle  $\theta$  to be  $\Delta\omega_c = 0.14$  GHz/deg for the 11.5 GHz cavity. This implies that the 11.5 GHz cavity misaligned at the maximum angle ( $\theta = 9.5^\circ$ ) has an equivalent fundamental frequency of 12.8 GHz. We therefore set the cavity frequency at 12.8 GHz and compare the effective critical temperature obtained in this configuration with the one measured on the sample embedded within the 11.5 GHz cavity misaligned at  $\theta = 9.5^\circ$ . We measured the shift of the effective critical temperature between the two cavity configurations to be  $\Delta_{MIS} = 21$  K. This phase transition shift is

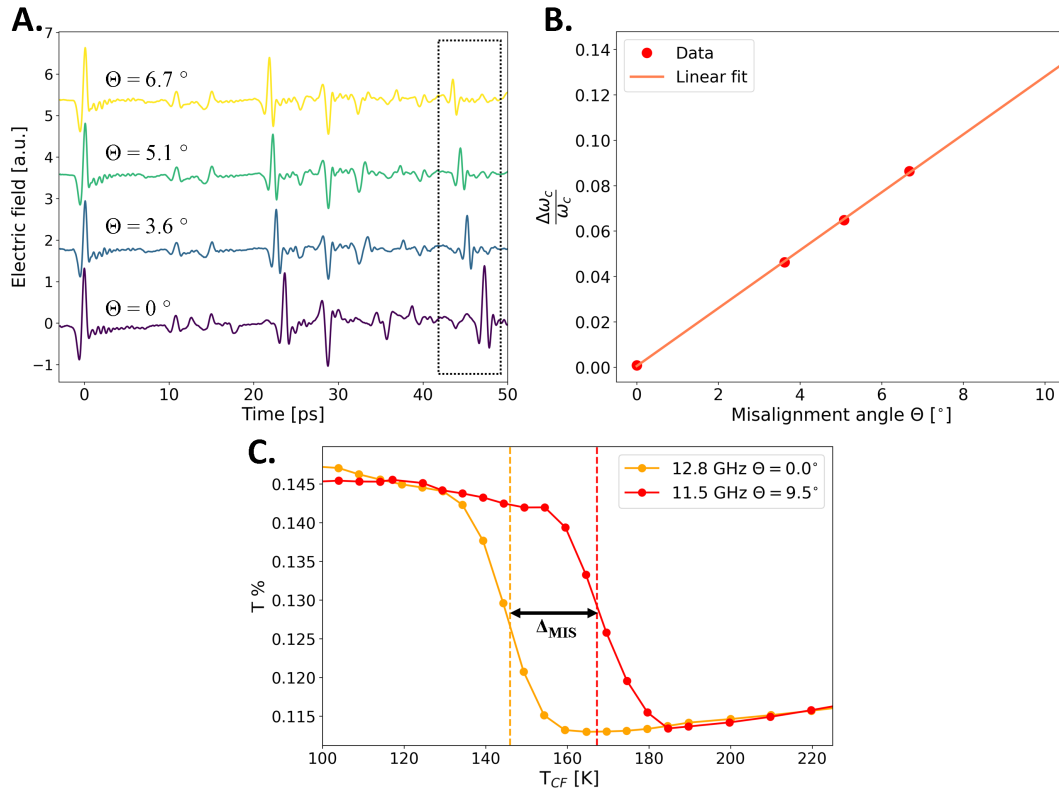


**Figure 5.34: Variation of the cavity fundamental frequency as a function of the total misalignment angle of the cavity.** **A.** THz fields measured at the output of the coupled cavity for different misalignment angles  $\theta$ . In the dashed box we highlight the THz reflection associated to the cavity round trip, which slightly shifts in time upon misaligning the mirrors. **B.** Relative shift of the cavity frequency as a function of the misalignment angle obtained from the THz fields shown in A and corresponding linear fit. **C.** Comparison between the temperature dependent low frequency transmission ( $0.2 \text{ THz} < \omega < 1.5 \text{ THz}$ ) in the 11.5 GHz misaligned cavity ( $\theta = 9.5^\circ$ ) and in the 12.8 GHz aligned one. The measured shift of the effective critical temperature  $\Delta_{MIS} = 21 \text{ K}$  quantifies the  $T_c$  shift due to cavity misalignment.

due to the cavity misalignment (Figure 5.34C), as it cannot be justified just in terms of a change in the cavity length.

Furthermore, by means of the finite elements simulations, we proved that the renormalization of the effective critical temperature cannot be explained by simply assuming an incoherent thermal heating. In fact, as shown in Figure 5.35, no temperature shift of the membrane is expected when the cavity mirrors are in the maximum misaligned configuration employed in the experiment ( $\theta = 9.5^\circ$ ).

Finally, in order to verify how the sample's temperature is affected by the cavity environment, we measured  $T_S$  as a function of the cavity alignment for a cavity fundamental mode of 11.5 GHz (Figure 5.36). By setting the cold finger temperature to 80 K, we detected a variation of 6.5 K in the sample's temperature by switching from the aligned to the maximum misaligned condition. Conversely, we measured only a 1.6 K temperature renormalization when the thermocouple is held only between the two membranes. We notice that the measured renormalization of the sample's temperature is however smaller than the shift of the effective transition temperature measured by THz spec-

troscopy (Figure 5.8). This effect can be ascribed to the presence of the thermocouple which may slightly perturb the local thermal environment of the sample.

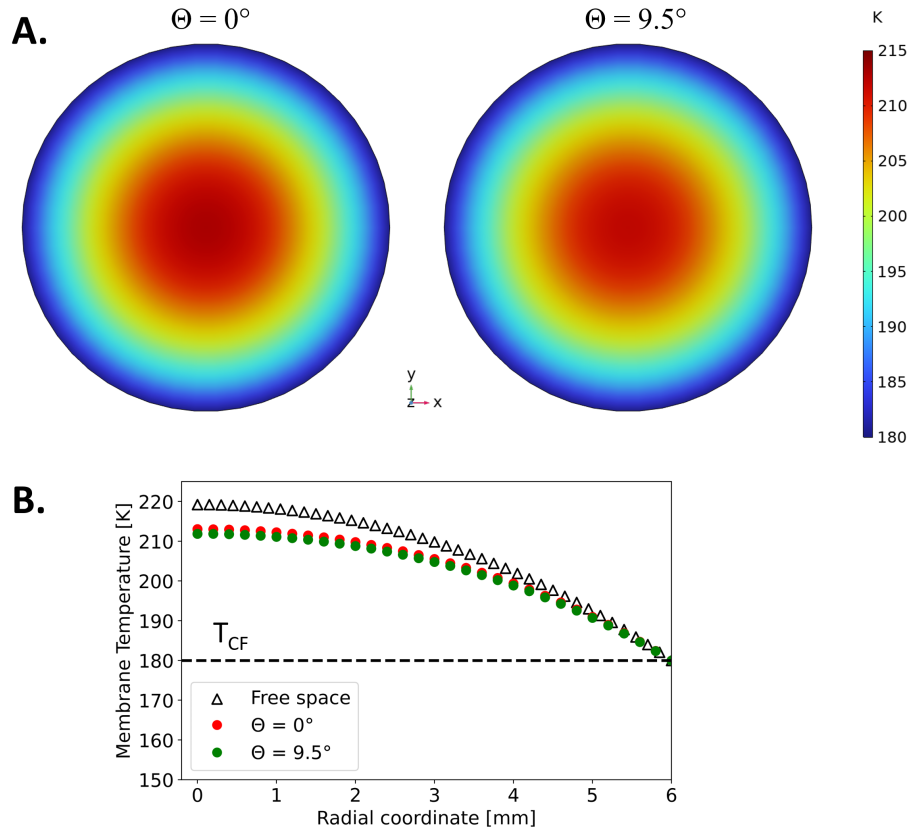


**Figure 5.35: Finite elements simulation of the membrane's temperature as a function of the cavity alignment.** **A.** 2D thermal profile of the membrane within the cryogenic cavity in the aligned configuration ( $\theta = 0^\circ$ ) and in the maximum misaligned configuration employed in the experiment ( $\theta = 9.5^\circ$ ). **B.** Membrane's thermal profile along the radial coordinate for the two alignment conditions. The cold finger temperature ( $T_{CF}$ ) and the mirrors temperature have been set to 180 K.

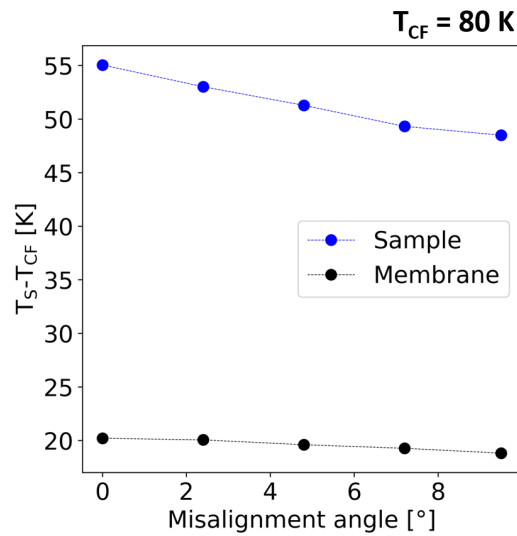


**Figure 5.36: Temperature measurements within the cavity (11.5 GHz) as a function of the cavity alignment.** In blue the dependence of the difference between the temperature measured on the sample ( $T_S$ ) and on the cold finger ( $T_{CF}$ ) as a function of the mirror alignment. In black, for comparison, the same differential temperature  $T_S - T_{CF}$  measured on the membranes. For the presented measurements we set the cold finger at  $T_{CF} = 80$  K.

#### 5.8.4 DOES THE EXTERNAL RADIATION INFLUENCE THE SAMPLE TEMPERATURE?

In order to prove that the shift of the effective critical temperature upon tuning the cavity resonance is not an effect merely due to the geometry of the cavity chamber, we removed the cavity mirrors and tracked the phase transition of the sample in free space at two different positions of the mirrors mounts (Figure 5.37). For this characterization we compared the mirrors mounts distance corresponding to a 9 mm (16.7 GHz) cavity with the one corresponding to a 1 mm (150 GHz) cavity. No significant shift of the effective  $T_c$  ( $\sim 2$  K) is measured between the two configurations. This proves that the thermal load on the sample is not influenced by the distance from the cryogenic mirrors mounts, and hence that the effective critical temperature shift upon tuning the cavity mode (Figure 5.12) cannot be ascribed to a geometrical variation of the cavity chamber. Therefore, the critical temperatures measured in free space (Figure 5.3) effectively sets the absolute free space reference for all the cavity-dependent studies.

We also demonstrated that the leading effect is not related to a geometrical screening of the mid-infrared black-body ambient radiation, whose amount within the cavity can be geometrically modified by tuning the mirror distance. To rule out this scenario, we screened with metallic foils the cavity chamber and, by means of the Cr-Al junction, tracked the differential temperature between the sample and the cold finger as a function of the cavity frequency. As highlighted in Figure 5.38, a similar temperature trend is detected in both the shielded and non-shielded configurations. This, together with the evidence of Figure 5.37, further validates that the reported evidence cannot be simply explained in terms of a geometrical screening of the ambient black-body radiation and more likely hints at a coherent light-matter coupling scenario.

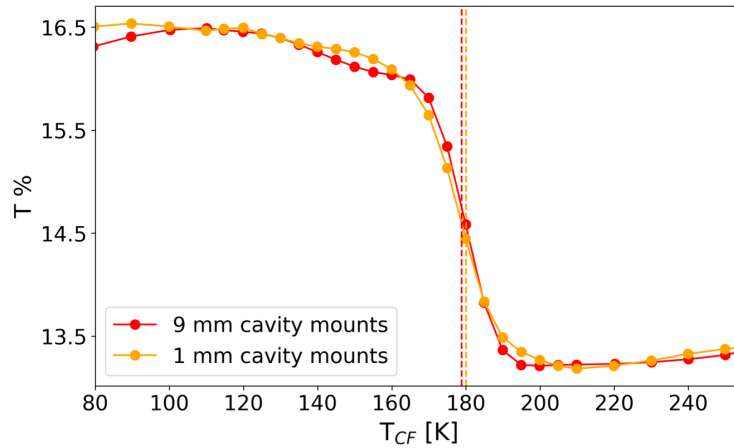


**Figure 5.37: Dependence of the effective phase transition temperature on the cavity geometry (without mirrors).** The low frequency transmission ( $0.2 \text{ THz} < \omega < 1.5 \text{ THz}$ ) in free space is plotted for two representative distances between the mirrors mounts and the sample. No significant shift in TC is observed ( $\sim 2 \text{ K}$ ).

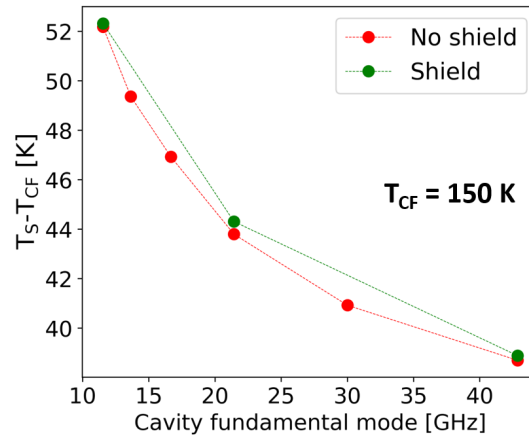


**Figure 5.38: Effect of the shielding of ambient radiation on the sample's temperature.** Differential temperature between the sample and the cold finger as a function of the cavity fundamental mode. Red (green) points correspond to sample temperatures measured without (with) shielding the cavity environment with metallic foils. The test has been made with the mirrors temperature set at 290 K.

### 5.8.5 DOES THE THz THERMAL LOAD AFFECT THE OBSERVED TRANSITION TEMPERATURE?

In order to verify that the phase transition within the cavity is not influenced by the thermal load introduced by the THz radiation, we repeated the same temperature scan with different intensities of the THz pulses. This was achieved by varying the bias voltage of the photo-conductive antenna (see Section 3.2.2 for the details on THz generation).

Figure 5.39 shows the cooling temperature scans for the sample within a cavity of a representative frequency of 36.8 GHz for two different peak strengths of the input THz field (0.1 KV/cm, and 0.03 KV/cm). A negligible shift of the effective critical temperature ( $< 1.0 \text{ K}$ ) is measured, confirming that the employed THz pulse only acts as probe and does not introduce a detectable thermal load at the sample position. For this

reason, in order to maximize the signal to noise ratio of the detected THz field, all the measurements presented were performed at a THz input peak strength of 0.1 KV/cm.

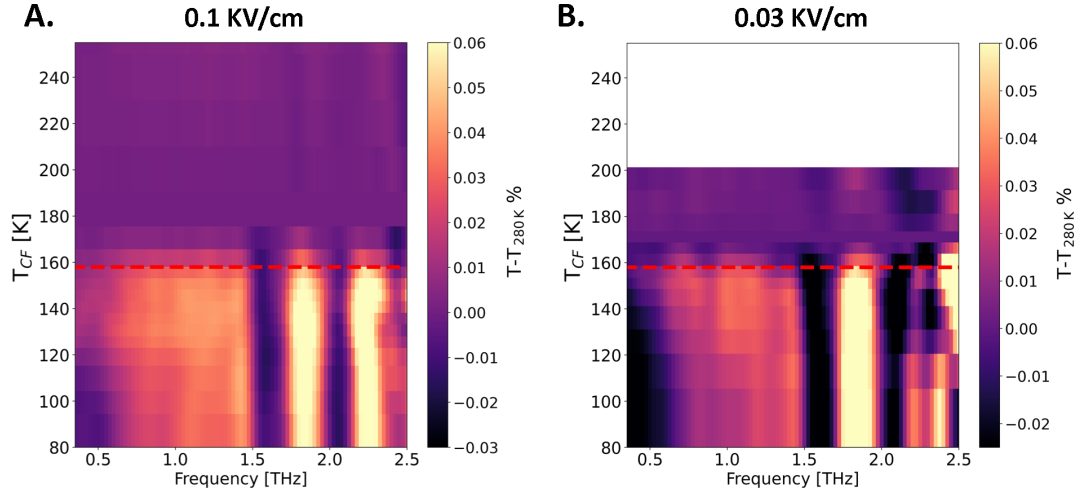


**Figure 5.39: Dependence of the metal-to-insulator transition on the THz probing intensity.** Cooling temperature scans for the sample within a cavity of a representative frequency of 36.8 GHz for two different intensities of the THz probing field: 0.1 KV/cm (A) and 0.03 KV/cm (B). A negligible shift of the effective critical temperature ( $< 1.0$  K) between the two THz intensities is detected.

A further confirmation of the negligible effect of the THz thermal load on the reported evidence is given by directly measuring the temperature of the membrane in the absence and in the presence of the THz field. In Figure 5.40, we plot the temperature difference between the cold finger and the center of the membrane (measured by means of the junction). We revealed that, even with the maximum THz intensity employed in all the transmission measurements (0.1 kV/cm), the temperature difference  $T_{\text{Membrane}} - T_{CF}$  changes by less than 1 K.

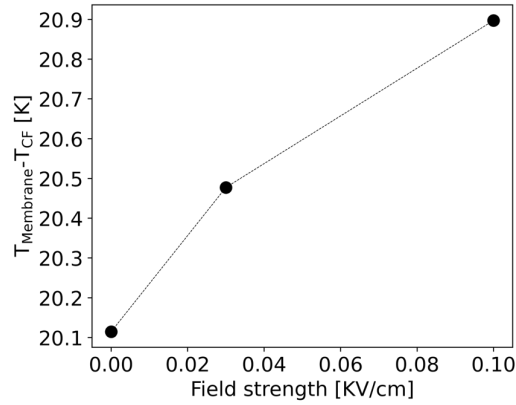


**Figure 5.40: Dependence of the membrane temperature on the THz intensity.** Measured difference between the temperature of the membrane and the temperature of the cold finger in the absence (0 kV/cm) and in the presence of THz radiation with two different field strengths (0.03 kV/cm and 0.1 kV/cm).

## 5.9 CONCLUSIONS

In summary, our results show that the metal-to-insulator transition in the quantum material 1T-TaS<sub>2</sub> can be reversibly controlled through low energy THz cavities. In particular, we reveal that, while long wavelength cavities (up to  $\sim 25$  GHz) effectively favour the metallic phase, the coupling with cavities at higher frequencies results in a stabilization of the insulating charge density wave phase. Overall, for the present setting the effective critical temperature associated to the charge ordering transition in 1T-TaS<sub>2</sub> can be shifted by more than 70 K by tuning the cavity resonant frequency. Such a giant modification overcomes the intrinsic hysteresis in the material and enables a reversible touchless control of the metal-to-insulator phase transition. The control of the phase transition is sensitive to the cavity alignment and hence to the optical losses within the cavity volume. This evidence further validates that the observed effect can be linked to the cavity electrodynamics.

The modification of the sample thermodynamics depends not only on the cavity geometry (alignment and fundamental mode), but also on the sample thermal history. This points to a scenario in which the cavity preferentially couples to the excitations of one of the two phases (tentatively the domain wall fluctuations of the metallic phase) and can modify the effective sample temperature in a Purcell-based mechanism or renormalize its free energy. The complementary THz transmission and temperature measurements, performed for different cavity settings, point to a scenario in which the coupling of the material excitations with the cavity field can coherently renormalize the sample's temperature. Further studies are needed to provide a quantitative estimate of the cavity-dependent total radiative heat load experienced by the sample within the THz optical cavity. As suggested by the described Purcell-like mechanism, an increased sensitivity in this respect could be provided by cavity design featuring a better thermal insulation between the sample and the cold finger.

Overall, our results deliver a new control parameter in the rich phase diagram of complex materials and open the way in the nascent field of cavity quantum materials [11] for tailoring equilibrium collective properties in correlated systems by engineering their electromagnetic environment.

# STRONG COUPLING SIGNATURES ACROSS 1T-TaS<sub>2</sub> METAL-TO-INSULATOR TRANSITION

---

Strong coupling between confined light fields and solid state excitations is creating increasing attention owing to the potential that such coupling regime offers as a new tool to control the equilibrium energy landscape of materials [11, 18, 61, 128, 187–190]. In the condensed matter framework, the core aspect that has raised much interest in light-matter hybrids in the strong coupling regime is the fact that polaritonic states can be regarded as highly delocalized states. This delocalization arises from the fact that in complex systems many oscillators are placed the cavity mode volume, and therefore can simultaneously interact with a common mode that can induce quantum correlations among the spatially separated dipoles.

The macroscopic collective nature of the hybrid light-matter states in the strong coupling limit has resulted in a variety of photonic effects and applications, such as Bose-Einstein condensation of exciton polaritons [81], low threshold lasing [84], superradiance [191], spectral control of quantum dot emission [192], and polaritonic enhancements for spectroscopic analysis [193].

Moreover, recent experiments with organic semiconductors [194] have demonstrated a dramatic enhancement of charge conductivity when molecules are strongly coupled within plasmonic cavities. These experiments, together with recent theoretical works [39, 40, 195], have demonstrated how the dissipative properties of conductive charges can be controlled by the cavity environment. These evidences has led to the suggestion that cavity electrodynamics can be exploited also in condensed matter platforms with the goal of controlling their macroscopic charge transport.

We report here experimental evidences of how the change in the equilibrium charge transport in the quantum material 1T-TaS<sub>2</sub> across its metal-to-insulator transition affects cavity electrodynamics. In particular, we will study the case in which the cavity is coupled with the Drude excitation associated to the free charges response and compare it with the configuration in which the cavity field is strongly coupled to the phonons of the C-CDW insulating phase.

We reveal that when the cavity frequency is tuned in order to be in resonance with the continuum Drude its quality factor, which quantifies the dissipative rates, is sensitive to the 1T-TaS<sub>2</sub> phase. Indeed, we measured a lifetime of the cavity photons which decreases passing from the dielectric to the metallic state. This evidence is consistent with an increased low frequency optical conductivity associated to a Drude-like response of the free carriers [161, 170, 171]. We will show that this points to a scenario in which the free charges couple to the cavity field and subsequently enhance the dissipative rates within the cavity.

Conversely, when the cavity is tuned resonantly to the IR-active vibrations of the C-CDW low temperature phase, we reveal the THz signatures of a multi-polariton mixing. The estimated components of the polaritonic wave-functions show that the measured polaritons of the C-CDW phase have character from all the vibrational resonances

within the used spectral range as a consequence of the photon-mediated hybridization. In particular, we detected two weakly dispersive middle polariton states resulting from the cavity-mediated mixing of two non-degenerate CDW phonons.

The measured Rabi splitting between the hybridized phonons closes across the metal-to-insulator transition as a consequence of the screening of the free charges. Intriguingly, near the critical temperature the dissipations in the cavity-coupled system are such that the weak vibrational coupling regime can be established. This will be proved by the evidence of a decrease of the quality factor of the coupled cavity when the latter is tuned across the spectral region of the CDW phonons.

Our evidences further emphasise the crucial role that dissipations play in cavity electrodynamics. In particular, the evidence that changing the dissipative rate of the conductive carriers induces a transition from strong to weak coupling uncovers a new path [129, 196–199] towards the tuning of the coupling regime in cavity-confined systems.

## 6.1 COUPLING WITH THE DRUDE EXCITATION

As discussed in Section 5.2, the low energy physics of 1T-TaS<sub>2</sub> is dominated by the response of the free charges. The latter are responsible of the polaronic-like transport observed in the non-commensurate CDW phase which gives rise to macroscopic metallic features [164, 200].

The metal-to-insulator phase transition, associated to the melting of the discommensuration network of the charge density wave [166, 168, 201], is associated with a significant decrease of the Drude-like optical conductivity in the low frequency region. This is highlighted in Figure 6.1A where we present a comparison between the real part of the optical conductivity  $\sigma_1$  measured in the insulating and in the metallic phase of 1T-TaS<sub>2</sub>. A relative decrease of the quasi-static conductivity of  $\sim 40\%$  is detected passing from the metallic to the dielectric state.

### 6.1.1 CAVITY DISSIPATIONS ACROSS THE CHARGE ORDERING TRANSITION

In this section, we experimentally show how the change in the conductive properties of 1T-TaS<sub>2</sub> is mapped onto the dissipative response of a cavity strongly coupled with the Drude continuum excitation.

For this study, the cavity was tuned within the spectral region highlighted in Figure 6.1A ( $0.3 \text{ THz} < \omega < 1.1 \text{ THz}$ ). Indeed, within this frequency region, the linear THz response is dominated by the response of the Drude carriers and no possible polaritonic interference with the CDW phonons can emerge at low temperatures. We are therefore in a suitable configuration to study how the Drude-like conductivity affects the features of a cavity mode strongly coupled with the free carriers.

As presented in Figure 6.1A, within the targeted spectral region the THz fields exiting the coupled cavity present a single decaying oscillating mode characteristic of the multiple round-trips within the cavity. The decay time of the cavity field sets the lifetime of the trapped photons and hence the dissipation rate of the cavity-confined material. The linear transmission of the coupled cavity, corresponding to the THz field shown in Figure 6.1A, is presented in Figure 6.1B. In the employed frequency region ( $0.3 \text{ THz} < \omega < 1.1 \text{ THz}$ ) the THz transmission of the hybrid system presents therefore the features of a single cavity mode, whose linewidth quantifies the dissipations of the coupled system. Importantly, for the cavity frequencies employed for this analysis,

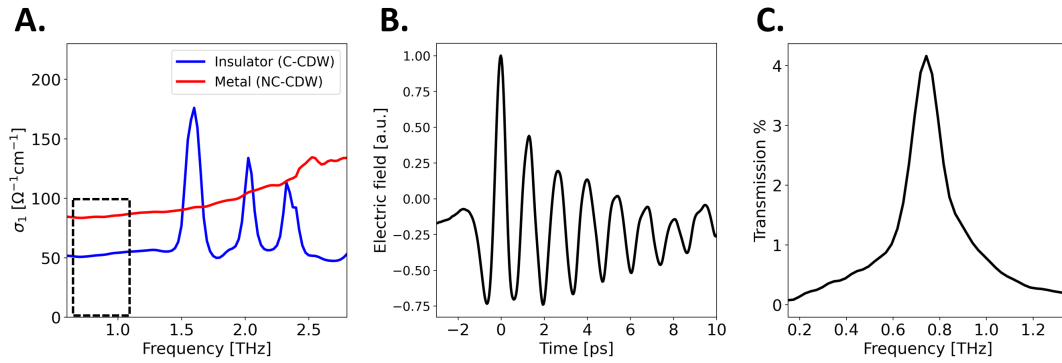


**Figure 6.1: Selection of the spectral region for the Drude coupling analysis.** **A.** Real part of the optical conductivity  $\sigma_1(\omega)$  extracted in the insulating ( $T = 80$  K) and in the metallic ( $T = 280$  K) phase of  $1T\text{-TaS}_2$ . The dashed box indicates the spectral region associated to the decreased free electrons Drude conductivity across the metal-to-insulator transition. **B.** Representative THz field measured at 80 K at the output of a cavity tuned within the Drude excitation region (dashed box in A.). **C.** THz transmission calculated from the THz field presented in B. In the selected spectral region a single cavity mode is measured.

the THz features of a single cavity mode are detected at each temperature. Indeed, the fundamental cavity mode lies far below the energy of the lowest CDW phonon. This ensures the CDW phonons to be screened by the cavity interference and hence exhibit no features of polaritonic-like coupling with the cavity field.

We present in Figure 6.2 the temperature evolution of a representative cavity mode within the Drude region ( $\omega_c = 0.75$  THz) measured upon heating (A, B) and cooling (C, D) the sample. We note that the metal-to-insulator transition, occurring at  $\sim 215$  K upon heating and at  $\sim 180$  K upon cooling, significantly affects the cavity dissipations. Conversely, no relevant shift of the mode frequency is observed. This is highlighted in the THz transmission spectra measured as a function of the temperature (Figure 6.2A, C). The temperature-dependent spectra reveal that the cavity mode is sharper in the C-CDW phase, while its linewidth becomes larger when the system switches to the metallic state.

As highlighted in the time-domain fields of Figure 6.2B, D, the linewidth modification across the phase transition is directly linked to a change in the photon dissipations within the cavity. Indeed, the photons lifetime inside the cavity appears shorter when they are coupled with the Drude oscillator of the metallic phase, whereas a longer dissipative dynamics is observed in the dielectric phase. This can be seen by comparing the decay times of the multi-cycle THz fields exiting the coupled cavity. We note that the dielectric phase better sustains the cavity oscillations, while the increase of the free charge conductivity, associated to the transition to the metallic state, suppresses the coherence time within the cavity, leading to a faster dissipation of the cavity field.

Therefore, by studying the coupling with the Drude oscillator (Figure 6.2), we are in a suitable configuration to map the dissipative response of the free charges of  $1T\text{-TaS}_2$  onto the dissipative processes of the cavity photons. In order to highlight this insightful connection we present in Figure 6.3 the comparison between the temperature evolution of the cavity linewidth and the average optical conductivity  $\sigma_1$  in the Drude range ( $0.3 \text{ THz} < \omega < 1.1 \text{ THz}$ ). The conductivity  $\sigma_1$  has been calculated for the 0.75 THz cavity. Cavity linewidths have been estimated by fitting the transmission spectra presented in Figure 6.2 with a Voigt lineshape.

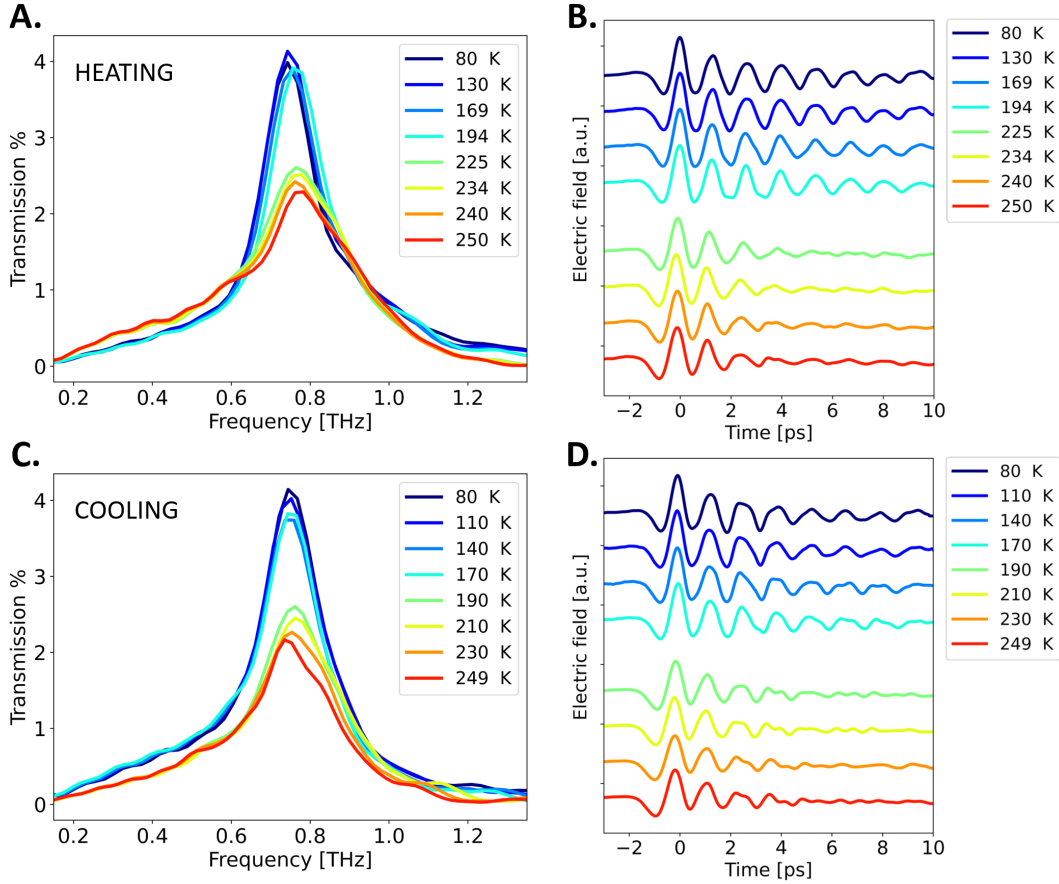


**Figure 6.2: Modification of cavity dissipations in the Drude spectral region of 1T-TaS<sub>2</sub>.** **A.** Evolution of the cavity mode tuned in the Drude spectral region of 1T-TaS<sub>2</sub> ( $\omega_c = 0.75$  THz). The cavity spectra were measured upon heating the sample from the dielectric C-CDW phase. **B.** Measured THz fields exiting the 0.75 THz cavity for the heating temperature scan. **C.** Temperature dependence of the 0.75 THz cavity mode upon cooling the sample from the metallic NC-CDW phase. **D.** THz fields measured at the output of the 0.75 THz cavity for the cooling temperature scan.

Intriguingly, the temperature evolution of the cavity linewidth (Figure 6.3A) exhibits a discontinuity around 185 K (210 K) upon cooling (heating) the sample. These discontinuous jumps in the cavity dissipations are consistent with the temperature dependence of the average Drude-like conductivity, which marks the charge ordering transition (Figure 6.3B).

Importantly, the dependence of the cavity dissipative rates on the material phase is not sensitive to the choice of the cavity frequency within the Drude region (Figure 6.1A). In order to prove it, we detuned the cavity at a different frequency ( $\omega_c = 0.5$  THz) and mapped the shape of the cavity mode across the metal-to-insulator transition. The measured THz transmission spectra relative to the 0.5 THz cavity are presented in Figure 6.4A for the cooling temperature scan. Figure 6.4B presents the temperature dependence of the cavity linewidth when the latter is tuned at 0.5 THz and at 0.75 THz. We note that, for both frequencies, the cavity linewidth manifests a discontinuity around the cooling critical temperature ( $\sim 180$  K), which marks the transition to the insulating state. This evidence supports the robustness of the discussed effect, proving

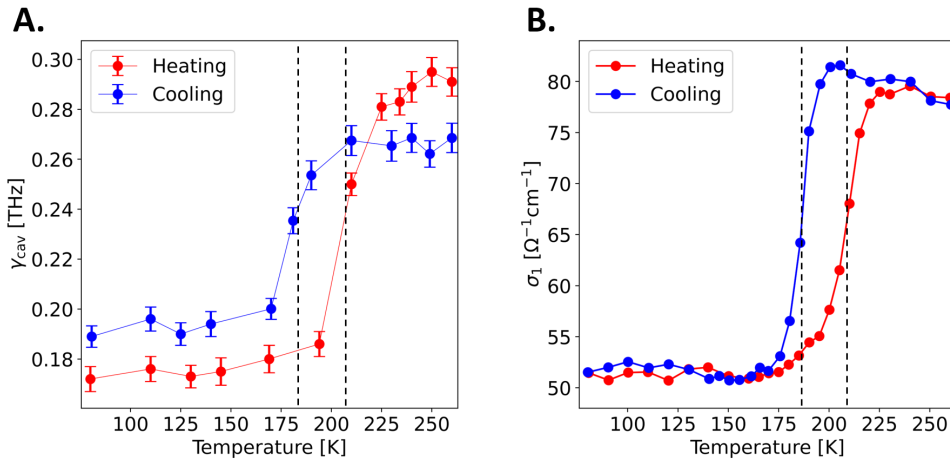


**Figure 6.3: Comparison between the cavity linewidth and the Drude-like conductivity across 1T-TaS<sub>2</sub> metal-to-insulator transition.** **A.** Temperature dependence of the cavity linewidth ( $\gamma_{cav}$ ) upon heating (red) and cooling (blue). The fundamental cavity mode is set at  $\omega_c = 0.75$  THz. **B.** Corresponding temperature dependence of the low frequency conductivity  $\sigma_1$  integrated in the frequency range  $0.2 \text{ THz} < \omega < 1.45 \text{ THz}$ .

that it is related to the change of sample's conductivity and not to the choice of the cavity fundamental mode.

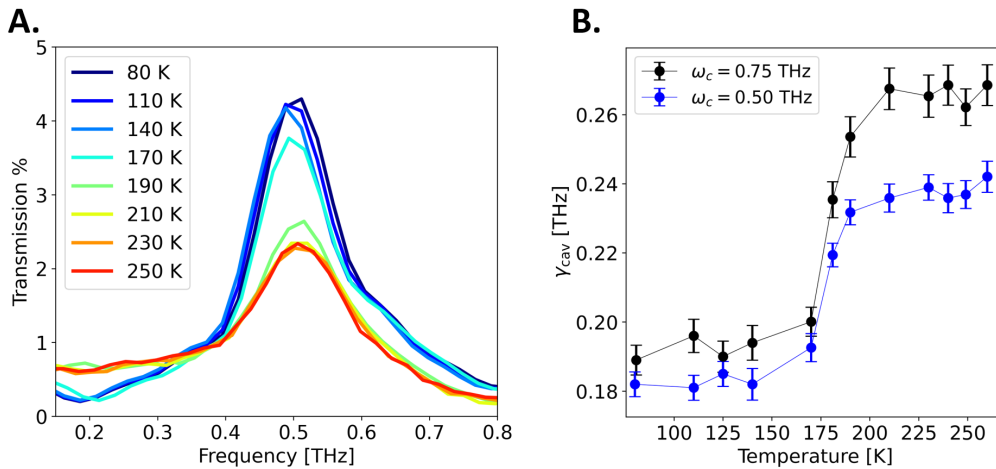


**Figure 6.4: Effect of Drude response on cavity dissipations for different cavity frequencies.** **A.** Temperature dependence of a cavity mode tuned at  $\omega_c = 0.5$  THz measured upon cooling. **B.** Temperature evolution of the cavity linewidth for the 0.5 THz and the 0.75 THz cavity, marking the phase transition.

### 6.1.2 DEPENDENCE OF THE COUPLING ON THE SYMMETRY OF THE CAVITY MODE

In the previous section we have shown that the coupling of the cavity field with the free charges is significantly affected by the material conductance. The metallicity of the system induces indeed phase-dependent dissipative rates within the coupled cavity.

In this section we experimentally demonstrate that the measured change of the cavity dissipations across the charge ordering transition depends on the spatial distribution of the cavity field.

Since the light-matter interaction within the cavity is governed by the overlap between the spatially varying cavity field and the material slab [202–204], we expect the coupling with the Drude excitation to depend on the modal profile within the cavity volume. This is in analogy with the molecular framework where works [105, 205] have demonstrated the influence of the spatial overlap between the location of vibrational absorbers and the optical mode profile of a Fabry-Pérot cavity on the resulting Rabi splitting.

#### 6.1.2.1 Measurements

In order to prove that the phase-dependent modification of the cavity linewidth is sensitive to the mode distribution, we tuned the cavity fundamental mode at a lower frequency ( $\omega_c = 0.4$  THz). With this choice also the first excited cavity mode ( $m = 2$ ) lies within the Drude bandwidth adopted for the analysis (Figure 6.1A). This represents therefore a suitable configuration to simultaneously track the temperature dependent coupling of the Drude oscillator with the ground state ( $m = 1$ ) and with the first excited cavity mode ( $m = 2$ ).

As depicted in Figure 6.5A, the spatial overlap of the dipole-like oscillators of the material with the cavity field is maximum for the ground state mode ( $m = 1$ ), while it approaches zero when the second-order mode ( $m = 2$ ) is coupled. Indeed, the  $m = 1$  mode presents a maximum at the sample position, i.e. the middle of the cavity volume, while the  $m = 2$  field has a node in correspondence with the 1T-TaS<sub>2</sub> position.

The temperature dependence of the THz transmission of the first and second order cavity mode across the metal-to-insulator transition is presented in Figures 6.5B, C for the cooling and heating scans. Comparing the effect that the charge ordering transition has on the ground state and on the second order cavity mode, we note that the line broadening related to the coupling of the cavity field with the Drude oscillator is mode-sensitive. Indeed, while the linewidth of the fundamental mode ( $m = 1$ ), and hence the photon dissipative rate, is enhanced in the metallic state, no significant change of the photon lifetime is measured when the first excited mode ( $m = 2$ ) is coupled to the Drude oscillator.

Figure 6.6 presents the quantitative temperature evolution of the linewidths of the first and second mode across the metal-to-insulator transition. The latter have been estimated by independently fitting the  $m = 1$  and  $m = 2$  cavity resonances with a Voigt lineshape. We note that only the broadening of the ground state cavity resonance marks the hysteresis of the phase transition, while no phase transition features are visible tracking the linewidth of the excited mode.

#### 6.1.2.2 Coupled oscillator analytical model

The relationship between the line broadening of the cavity resonance and the spatial profile of the cavity mode can be rationalized within the coupled oscillator model through

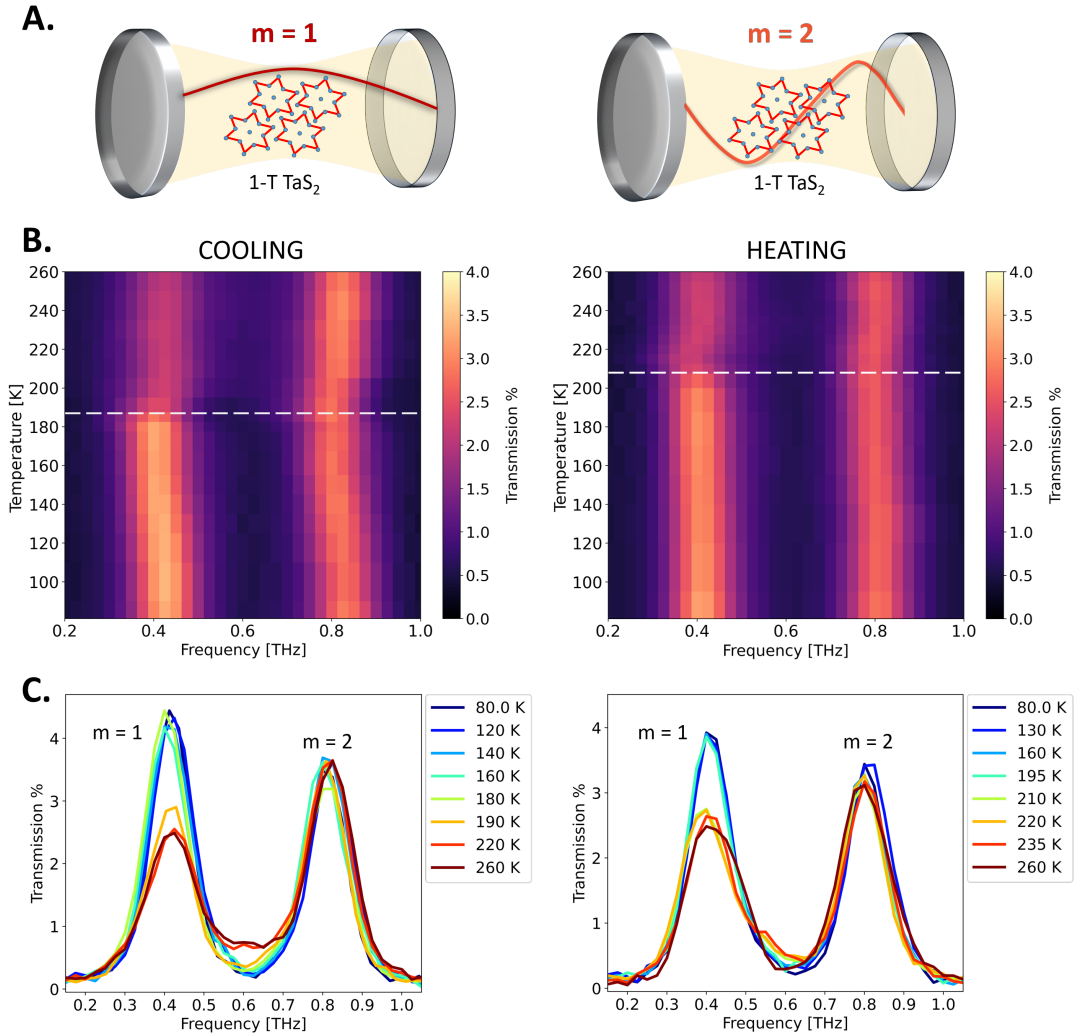


**Figure 6.5: Dependence of the coupling with Drude oscillator on the symmetry of the cavity mode** **A.** Spatial symmetry of the cavity field in its ground state ( $m = 1$ ) and in its first excited state ( $m = 2$ ). The 1T-TaS<sub>2</sub> sample is held in the middle of the cavity volume. **B.** Temperature dependent THz transmission for the sample held within a cavity of fundamental mode  $\omega_c = 0.4$  THz. In the left (right) panel the spectra are measured upon cooling (heating) the sample. **C.** Selected transmission spectra below and above the critical temperature. The line broadening due the coupling with the free carriers is measured only for the first cavity mode ( $m = 1$ ), while no significant changes on the second mode ( $m = 2$ ) are detected between the two phases. Left (right) spectra correspond to cooling (heating) temperature scans.

the expression of the space-dependent coupling strength. The latter will be derived underneath. In particular, we will compare the case in which the ground state mode and the second-order mode is coupled to the Drude oscillator.

For a 3D-confined mode of a cavity resonator, the coupling strength can be derived from the electric-dipole interaction Hamiltonian (cfr Equation 2.17). The first step is to quantize the electric field of the mode, so that it is normalized to the vacuum ground state energy  $\hbar\omega/2$  when the field is integrated over the cavity volume [105, 206, 207]:

$$\hat{\mathbf{E}}(\mathbf{r}, t) = \mathbf{e}(\mathbf{r}) \sqrt{\frac{\hbar\omega |\mathbf{e}_{\max}|^2}{\epsilon_0 \int d\mathbf{r} \epsilon(\omega) |\mathbf{e}(\mathbf{r})|^2}} \left( \hat{a} e^{-i\omega t} + \hat{a}^\dagger e^{i\omega t} \right). \quad (6.1)$$

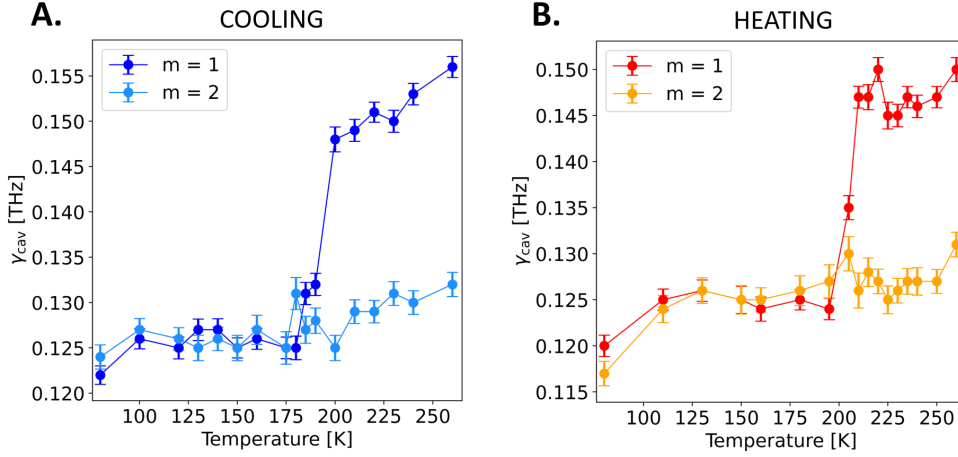


**Figure 6.6: Linewidths of the first and second cavity mode across the metal-to-insulator transition in 1T-TaS<sub>2</sub>.** **A.** Estimated linewidths of the fundamental ( $m = 1$ ) and second order ( $m = 2$ ) cavity mode for the cooling temperature scan. **B.** Temperature dependence of the  $m = 1$  and  $m = 2$  cavity modes measured upon heating the sample. Only the broadening of the fundamental cavity mode ( $m = 1$ ) marks the hysteresis of the metal-to-insulator transition.

In the previous expression  $\mathbf{e}(\mathbf{r})$  is the dimensionless electric field profile of the selected mode, which therefore set the spatial symmetry of the cavity field. The latter is obtained by solving the Maxwell's equations with the cavity boundary conditions. The maximum value of the field is denoted with  $\mathbf{e}_{\max}$ , which we will assume as unity in the following. In Equation 6.1 we denoted with  $\epsilon_g$  the "group" frequency-dependent permittivity of the active medium, defined as  $\epsilon_g(\omega) = \frac{d(\epsilon(\omega)\omega)}{d\omega}$ .

We will model the Drude response of the material as the response of  $N$  dipoles of oscillator strength  $\mu$  driven in phase in response to the modal electric field. Note that we will use the term dipole, even if the Drude-like response of the free carriers has zero frequency. However, free charges can still respond to the cavity electric field and experience damping in the same way as the bound oscillating charges.

The interaction Hamiltonian in the rotating-wave approximation (Tavis-Cummings model, Section 2.2.1) between the  $N$  Drude oscillators and the quantized electric field reads:

$$\hat{H}_{\text{int}} = \sum_{d=1}^N g_c \left( \hat{\sigma}_d^\dagger \hat{a} + \hat{a}^\dagger \hat{\sigma}_d \right), \quad (6.2)$$

where the sum is extended over all the  $N$  dipoles. The spatial dependence of the coupling has been entirely put inside the collective coupling strength  $g_c$  which, recalling the expression of the quantized cavity field (Equation 6.1), reads [105]:

$$g_c = \sqrt{\frac{\hbar\omega}{2\epsilon_0}} \frac{N}{V} \frac{\int d\mathbf{r} |\boldsymbol{\mu}(\mathbf{r}) \cdot \mathbf{e}(\mathbf{r})|^2}{\int d\mathbf{r} \epsilon_g(\omega) |\mathbf{e}(\mathbf{r})|^2}. \quad (6.3)$$

The above expression implies that the coupling can be significantly enhanced by spatially overlapping the dipole positions  $\boldsymbol{\mu}(\mathbf{r})$  to the position of the maximum cavity field  $\mathbf{e}(\mathbf{r})$ . By modelling the cavity employed in the experiment as a co-planar cavity of length  $L$  with an active 1T-TaS<sub>2</sub> layer in the middle of the cavity volume having thickness  $d$  and dielectric constant  $\epsilon(\omega)$ , the coupling strength of Equation 6.3 can be expressed as [105]:

$$g_c = \sqrt{\frac{\hbar\omega N\mu^2}{2\epsilon_0 V} \frac{\int_0^d dz |\mathbf{e}(z)|^2}{\int_{-L/2}^0 dz |\mathbf{e}(z)|^2 + \int_0^d dz \epsilon_g(\omega) |\mathbf{e}(z)|^2 + \int_d^{L/2} dz |\mathbf{e}(z)|^2}}. \quad (6.4)$$

Considering cavity modes under  $s$ -polarized incident field, only the component of the electric field perpendicular to cavity axis,  $\mathbf{e}_x$ , does not vanish. This implies that, supposing zero penetration depth into the mirrors at the THz wavelengths, the adopted cavity confines the light only in the transverse direction.

The electric fields of the ground state ( $m = 1$ ) and of the first excited cavity mode ( $m = 2$ ) can be hence expressed along the cavity axis ( $z$ ) as follows:

$$\begin{aligned} \mathbf{e}^{m=1}(z) &= \cos\left(\frac{\pi z}{L}\right) \hat{x} \\ \mathbf{e}^{m=2}(z) &= \sin\left(\frac{2\pi z}{L}\right) \hat{x} \end{aligned} \quad (6.5)$$

We note that, while the ground state normal mode is maximum at the cavity center ( $z = 0$ ) and even with respect to  $z = 0$ , the first excited mode has a node at the cavity center and displays two symmetric maxima at the  $z = \pm L/4$  positions. Assuming no frequency dependence of the sample's permittivity within the Drude region<sup>1</sup>, the coupling equation (6.4) can be integrated for the ground state ( $m = 1$ ) and for the first excited cavity mode ( $m = 2$ ), leading to:

$$g_c^{m=1}(z_s) = \sqrt{\frac{\hbar\omega N\mu^2}{2\epsilon_0 V} \left[ \frac{d}{L} + \frac{1}{2\pi} \sin\left(2\pi\left(\frac{z_s}{L} + \frac{d}{2L}\right)\right) - \sin\left(2\pi\left(\frac{z_s}{L} - \frac{d}{2L}\right)\right) \right]} \quad (6.6)$$

$$g_c^{m=2}(z_s) = \sqrt{\frac{\hbar\omega N\mu^2}{4\epsilon_0 V} \left[ \frac{2d}{L} + \frac{1}{2\pi} \sin\left(4\pi\left(\frac{z_s}{L} + \frac{d}{2L}\right)\right) - \sin\left(4\pi\left(\frac{z_s}{L} - \frac{d}{2L}\right)\right) \right]} \quad (6.7)$$

In the previous expressions the coupling strength between the Drude oscillators and the cavity modes have been calculated as a function of the sample's position  $z_s$  along the cavity coordinate  $z$ . A map of the coupling strength of the free charges with the first and second order modes along the cavity axis is presented in Figure 6.7. We stress that calculations have been made for the same cavity configuration ( $\omega_c = 0.4$  THz) adopted in the experiments to map the mode-selectivity of the Drude coupling (Figure 6.5).

We highlight that the analytical calculations of the coupling strengths display a consistency with the experimental results presented in Figure 6.5. Indeed, the collective coupling strength exhibits a maximum at the cavity center when the dipoles are coupled to ground state field, while it presents a minimum in the configuration where they are strongly coupled with the second mode. This space-dependent profile of the coupling is mapped onto the mode-dependence of the cavity linewidth measured experimentally. We indeed revealed a line broadening, associated to the coupling between free charges and the cavity field, only when 1T-TaS<sub>2</sub> is coupled to ground state mode. Conversely, no significant change of the cavity line is detected in the case of the coupling with the excited mode.

<sup>1</sup> This assumption is validated by the measurement of the low energy optical conductivity (Figure 6.1A).

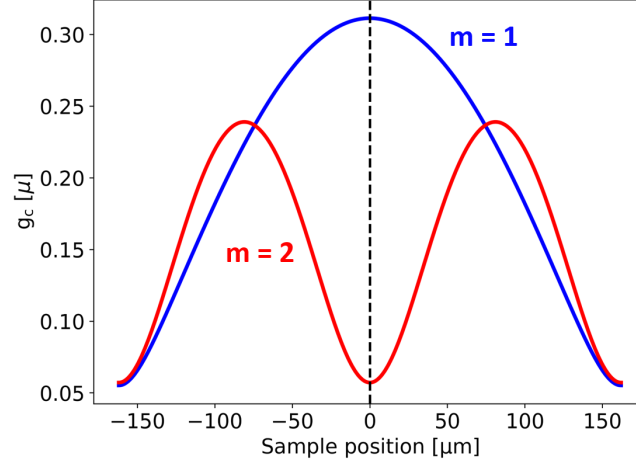


**Figure 6.7: Dependence of the coupling constant of the Drude oscillator on the spatial profile of the cavity modes.** Coupling constant of the Drude oscillator along the cavity coordinate in dipole strength units ( $\mu$ ). Calculations have been made for the ground state ( $m = 1$ ) and for the first excited ( $m = 2$ ) mode of the 0.4 THz cavity adopted in the experiments.

### 6.1.3 TRANSFER-MATRIX SIMULATIONS ACROSS THE PHASE TRANSITION

To further demonstrate that the observed effect is related to the coupling of the cavity field with the free charges responsible of the Drude response, we exploited the Transfer-matrix method to simulate the THz transmission spectra across the charge ordering transition. Transfer-matrix simulations will indeed allow us to model how a change in the Drude oscillator induced by the phase transition is directly mapped onto the THz linear transmission of the coupled cavity. The THz transmission is indeed the observable directly measured in the experiments.

In order to gain insight on both the coupling with the ground state and with the second-order mode, in the simulations we set the cavity frequency at  $\omega_c = 0.4$  THz, as in the experiments. With this choice both the first and second order cavity modes lies within the bandwidth dominated by the free charges response ( $\sim 0.3 - 1.1$  THz).

As in Chapter 4, for the simulations we used the experimentally measured refractive index of gold [96] and then tuned the thin gold layer thickness to match the linewidth of the coupled 0.4 THz cavity at 80 K. An effective thickness of the gold layer  $d_{\text{eff}} = 2.0$  nm was adopted to reproduce the cavity linewidth measured in the C-CDW phase.

To reproduce the coupling of the Drude oscillator with the cavity mode in the two phases of the sample, we modelled the complex optical conductivity  $\tilde{\sigma}(\omega)$  in the insulating and in the metallic state of 1T-TaS<sub>2</sub> according to the Drude-Lorentz model [161, 170, 171]:

$$\tilde{\sigma}(\omega) = \frac{\sigma_0}{1 - i\omega\tau} + i\epsilon_0\omega \left( 1 - \epsilon_\infty - \sum_{j=1}^n S_j \frac{\omega_{0j}^2}{\omega_{0j}^2 - \omega^2 - i\omega\gamma_j} \right). \quad (6.8)$$

The first term of  $\tilde{\sigma}(\omega)$  describes the static Drude conductivity, associated to the response of the free charges driven by the THz field. Within this framework, the response of the conductive charges is therefore modelled by the static conductivity  $\sigma_0$ , which sets the zero-frequency response, and by the scattering time  $\tau$ , which governs the dissipative dynamics of the driven charges. The term  $\epsilon_\infty$  represents the high-frequency response

of the dielectric constant. The last term gives the contribution from the  $j^{\text{th}}$  Lorentzian oscillator, where  $S_j$  is the oscillator strength,  $\omega_{0j}$  the resonance frequency, and  $\gamma_j$  is the linewidth. These Lorentzian terms have been included only in the insulating phase to model the response of the IR-active CDW phonons. We note that the Drude component has been included also in the C-CDW conductivity to model the measured flat response of  $\sigma_1$  at low energy, which is indicative of a Drude-like behaviour [171].

Figure 6.8 presents the complex optical conductivity measured in free space in the metallic ( $T = 280$  K) and in the dielectric phase ( $T = 80$  K) of  $1T\text{-TaS}_2$ , together with the corresponding Drude-Lorentz fits. Both real and imaginary parts of the complex optical conductivity  $\tilde{\sigma}(\omega)$  were fit simultaneously with the REFFIT software, which imposes the Kramers-Kronig relations [208] between the fitted real and imaginary components of  $\tilde{\sigma}(\omega)$ .

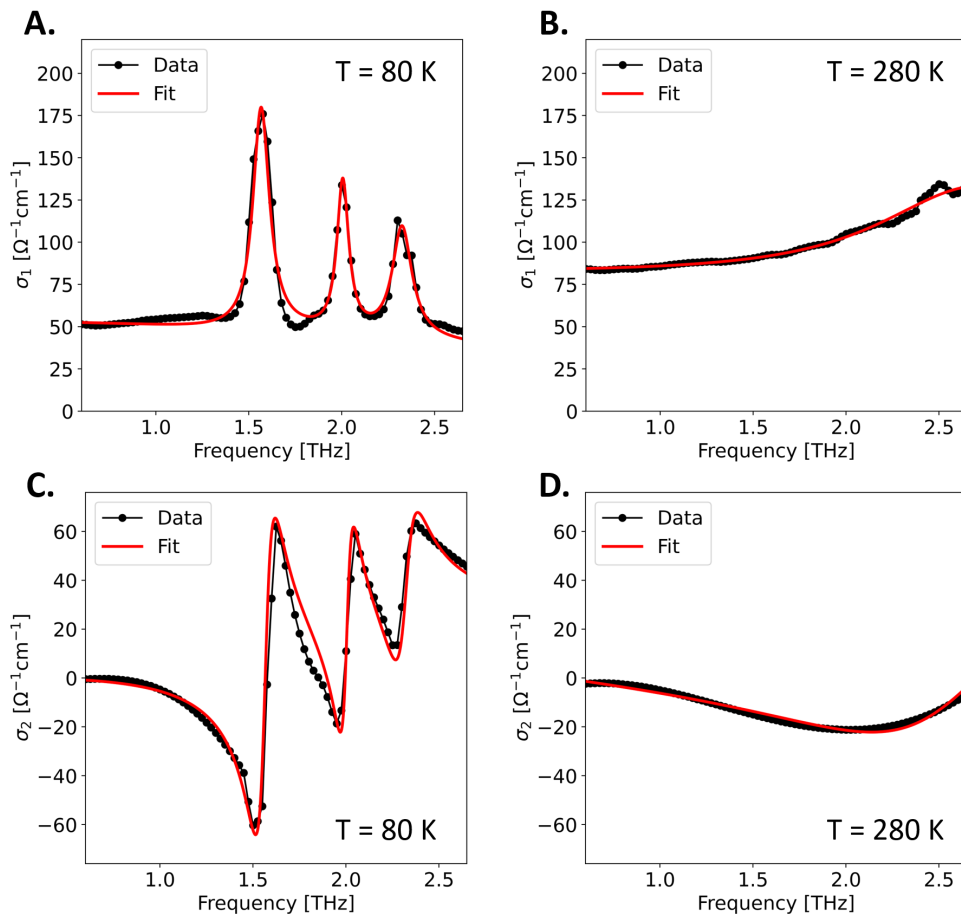


**Figure 6.8: Complex conductivity  $\tilde{\sigma}(\omega)$  of  $1T\text{-TaS}_2$  in the metallic and dielectric phases measured in free space.** **A.** Real part of the optical conductivity ( $\sigma_1$ ) of the insulating C-CDW phase measured at 80 K. **B.** Real part of the optical conductivity ( $\sigma_1$ ) of the metallic NC-CDW phase measured at 280 K. **C.** Imaginary part of the optical conductivity ( $\sigma_2$ ) of the insulating phase at 80 K. **D.** Imaginary part of the optical conductivity ( $\sigma_2$ ) of the metallic phase at 280 K. In the presented plots black dots are the data, while red lines represent the associated fits with the Drude-Lorentz model for a  $15\ \mu\text{m}$   $1T\text{-TaS}_2$  sample in free space.

j	$\omega_{0j}$ [THz]	$\gamma_j$ [THz]	$S_j$
1	1.58	0.110	9.86
2	2.02	0.101	3.05
3	2.35	0.125	2.81

$\epsilon_\infty$	$\sigma_0$ [ $\Omega^{-1} \times \text{cm}^{-1}$ ]	$\tau$ [fs]
3.5	52.8	215

**Table 6.1: Drude-Lorentz fit parameters for bare 1T-TaS<sub>2</sub> in the dielectric phase.** The parameters were obtained by fitting the 80 K complex conductivity (Figures 6.8B, D).

The parameters obtained from the simultaneous fitting procedure are listed in Table 6.1 for the insulating C-CDW phase and in Table 6.2 for the metallic NC phase. We note that in the Drude region, the charge ordering transition is associated with an increase of the static conductivity  $\sigma_0$  passing from the dielectric to the metallic state, together with a slightly increase of the Drude scattering time  $\tau$ . These trends are consistent with the onset of metallicity in the system and in agreement with previous THz reflectivity studies [170].

j	$\omega_{0j}$ [THz]	$\gamma_j$ [THz]	$S_j$
1	2.85	1.47	26.6

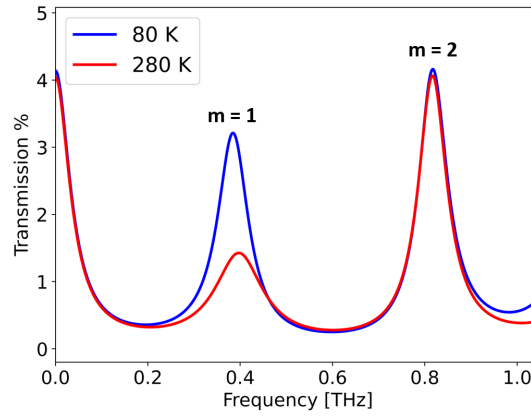
  

$\epsilon_\infty$	$\sigma_0$ [ $\Omega^{-1} \times \text{cm}^{-1}$ ]	$\tau$ [fs]
3.2	85.1	262

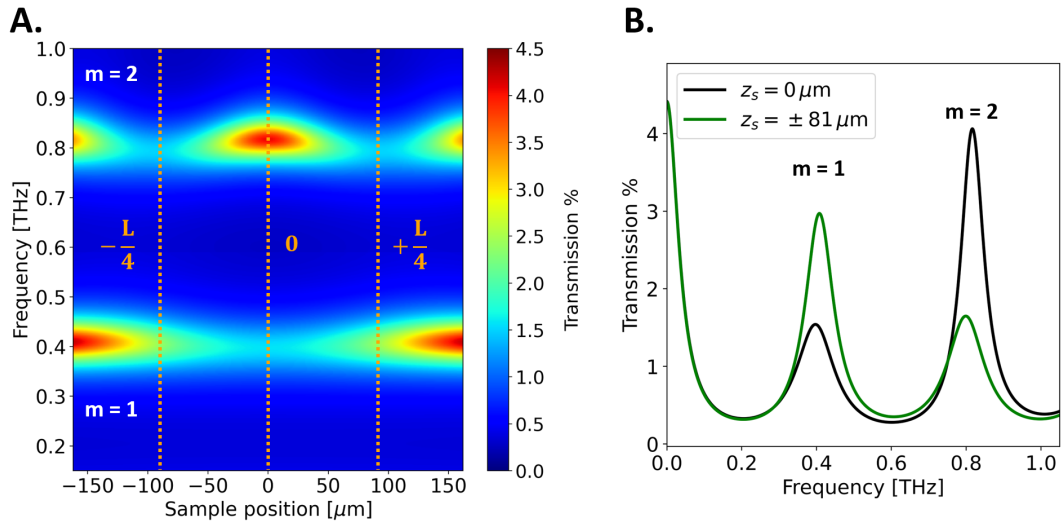
**Table 6.2: Drude-Lorentz fit parameters for bare 1T-TaS<sub>2</sub> in the metallic phase.** The parameters were obtained by fitting the 280 K complex conductivity (Figures 6.8A, C).

Figure 6.9 presents the simulated Transfer-matrix transmission for the 0.4 THz cavity coupled to the Drude excitation of the metallic and dielectric phase. We highlight that the Transfer-matrix simulations display a further consistency with the measured spectra (Figure 6.5) and with the analytical results of the coupled oscillator model (Figure 6.7). Indeed, the simulated THz transmissions show a consistent broadening of the fundamental cavity mode ( $m = 1$ ) in the metallic phase, while no significant difference of the linewidth of the second-order coupled mode ( $m = 2$ ) is detected.

In order to further confirm that the broadening of the cavity mode maps the mode profile of the cavity electric field, and hence it is related to the spatial overlap between the Drude oscillators and the cavity field, we simulated the THz transmission as a function of the sample position (Figure 6.10). We highlight that the simulations have been performed for the sample in the metallic state, i.e. where we expect the coupling



**Figure 6.9: Transfer matrix simulations of Drude oscillator coupling in the metallic and dielectric phase of  $1T\text{-TaS}_2$ .** Simulated transmission spectra of a cavity tuned in the Drude spectral region ( $\omega_c = 0.4$  THz) when the sample is in the insulating state ( $T = 80$  K) and in the metallic state ( $T = 280$  K). A line broadening of the fundamental mode ( $m = 1$ ) related to the coupling with the Drude oscillator is predicted in the NC-CDW phase. Simulations in the two material states were performed starting from the static complex conductivities at 80 K (Table 6.1) and 280 K (Table 6.2) measured on the  $15 \mu\text{m}$   $1T\text{-TaS}_2$  sample.



**Figure 6.10: Simulated distribution of the cavity field in the metallic phase of  $1T\text{-TaS}_2$ .** **A.** Simulated transmission map in  $1T\text{-TaS}_2$  metallic phase as a function of the sample position. The cavity fundamental mode lies in the Drude region and is set at  $\omega_c = 0.4$  THz. **B.** Simulated spectra in the configuration in which the sample is put in the middle of the cavity ( $z_s = 0 \mu\text{m}$ ) and at the  $L/4$  position of the fundamental mode ( $z_s = \pm 81 \mu\text{m}$ ). The line broadening is maximum at the spatial positions corresponding to the maximum cavity field.

with the free carriers, and hence the cavity line broadening, to be maximum. We note that the simulated THz transmission as a function of the sample's position maps the spatial dependence of the coupling constant presented in Figure 6.7. With the Transfer-matrix formalism we indeed obtained the maximum change of the cavity dissipations (i.e. the maximum line broadening) in the positions of the maximum coupling within the cavity volume. These position correspond to the cavity center for the fundamental

mode ( $m = 1$ ) and to the  $\pm L/4$  positions for the second-order mode ( $m = 2$ ), where  $L = 324 \mu\text{m}$  for the employed 0.4 THz cavity.

#### 6.1.4 DEPENDENCE OF THE COUPLING ON THE CAVITY FREQUENCY

In order to experimentally demonstrate that the observed broadening of the cavity mode is related to the coupling with a low energy oscillator (i.e. the Drude oscillator) we mapped the cavity dispersion as a function of the cavity frequency. The rationale of this test is that we expect the coupling of the cavity field with the Drude oscillator to be higher when the cavity frequency is lower, i.e. near to the quasi-static response of the free charges.

The test has been performed in the NC-CDW phase of 1T-TaS<sub>2</sub>. We expect indeed the line broadening of the cavity mode to be maximized in the metallic state (Figures 6.2, 6.3). Moreover, in the non-commensurate phase no polaritonic-like coupling with the CDW phonons can skew the THz transmission of high energy cavities. This enables us to cleanly map the broadening of the single cavity mode as a function of the cavity frequency.

We present in Figure 6.11 the dispersion of the cavity mode in the metallic phase obtained at 280 K together with THz transmission spectra measured at some selected cavity frequencies among the ones employed to map the full dispersion.

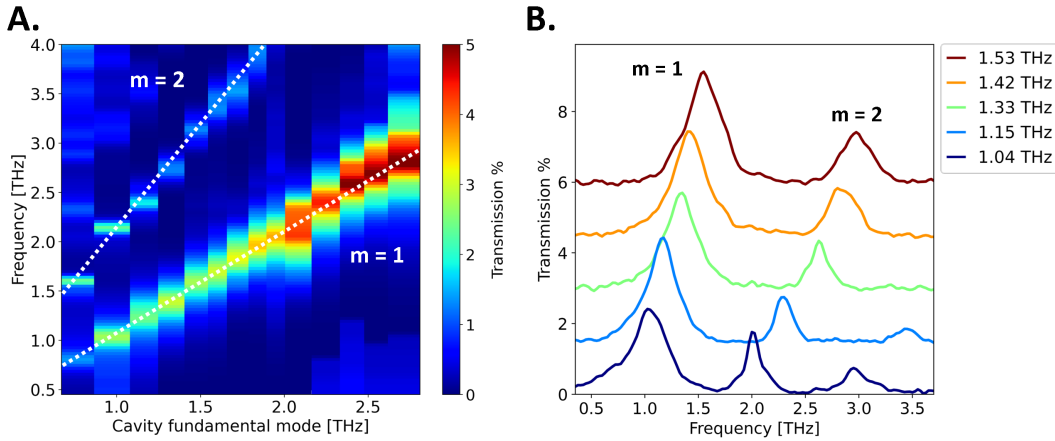


**Figure 6.11: Dispersion of the cavity modes in the NC metallic phase of 1T-TaS<sub>2</sub> measured at 280 K.** **A.** Experimental dispersion of the cavity modes in the NC-CDW phase at 280 K. The white dashed lines mark the ground state ( $m = 1$ ) and the first excited cavity mode ( $m = 2$ ). **B.** Selected cavity transmission spectra measured in the metallic phase at 280 K. The spectra have been vertically shifted for clarity.

In order to quantitative gain insight on the frequency dependence of the cavity line broadening, we estimated the quality factor  $Q_\omega = \frac{\omega_c}{\Delta\omega_c}$  as a function of the cavity fundamental mode  $\omega_c$ . The quality factor is indeed governed by the cavity losses and its value can be used to track the frequency dependence of the line broadening associated to the coupling with the Drude excitation. Note that for frequency-independent optical losses, we expect the quality factor to be constant as a function of the cavity frequency. Therefore, in the studied system (Figure 6.2), deviations from the constant behaviour

has to be linked to a frequency-dependent change of the coupling between the cavity field and the Drude oscillator.

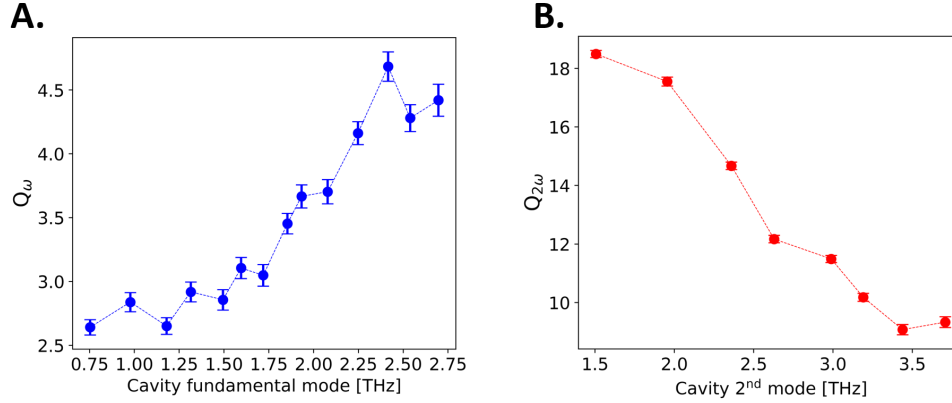


**Figure 6.12: Quality factors of the fundamental and second order cavity modes in the metallic phase of 1T-TaS<sub>2</sub> at 280 K. A.** Measured quality factor of the ground state cavity mode ( $m = 1$ ) at 280 K. **B.** Measured quality factor of the first excited cavity mode ( $m = 2$ ) at 280 K. The quality factors have been calculated from the transmission spectra of Figure 6.11.

The dependence of the quality factor  $Q_\omega$  as a function of the cavity frequency is presented in Figure 6.12A. The linewidths associated to the cavity resonances (together with the relative errors) have been estimated through a Voigt lineshape fitting procedure. We highlight that  $Q_\omega$  is not constant as a function of the cavity frequency and, intriguingly, it decreases at lower frequencies. This evidence implies that the cavity dissipations are enhanced when 1T-TaS<sub>2</sub> is embedded in low frequency cavities.

We note that an opposite behaviour is observed by tracking the frequency dependence of the quality factor of the second-order cavity mode  $Q_{2\omega} = \frac{2\omega_c}{\Delta(2\omega_c)}$ . We justified this opposite trend by noting that at high frequencies the linear absorptive contribution to the dielectric function ( $\sigma_1$ ) increases in the metallic phase, as highlighted in Figure 6.8B. This increased linear absorption can lead to an enhancement of the optical losses of the cavity in the high frequency spectrum, thus justifying the measured trend of  $Q_{2\omega}$ .

We stress that this scenario cannot justify the trend observed for  $Q_\omega$ . Indeed, a mode broadening of the cavity resonance, due to an increased absorption of the NC phase at higher frequency, is not consistent with the narrowing of the fundamental cavity mode measured upon increasing the cavity frequency (Figure 6.12A). We clarify that the evidence that  $Q_{2\omega} > Q_\omega$  within all the employed spectral range is a consequence of the dependence of the quality factor on the mode order (see Section 2.1.1 of Chapter 2 for the full derivation).

The frequency dependence of  $Q_\omega$  justifies therefore the presence of a low energy oscillator associated to the Drude response of the free carriers whose coupling with the cavity field is responsible of the enhanced dissipations of the coupled cavity. The enhancement of the cavity dissipations is greater for lower cavity frequencies (Figure 6.12A) thus validating that the observed effect is related to the quasi-static response of the conductive charges.

## 6.2 MULTIMODE VIBRATIONAL STRONG COUPLING IN THE C-CDW PHASE

In the previous section we have studied the dissipative dynamics of low energy cavities tuned in order to be on resonance with the quasi-static excitation associated to the free carriers. In all the results reported before (Section 6.1) the cavities were tuned within the Drude region and therefore not in resonance with the CDW phonons of the commensurate phase.

In this section we analyse in detail the strong coupling of the multi-phonon structure of the C-CDW phase. Coupling between multiple vibrational resonances and a resonant optical cavity have been already demonstrated in the molecular framework [209–211] where many sharp vibrational transitions can exist within a narrow spectral window. However, no evidences of multi-polariton strong coupling have been reported in condensed-matter complex systems. In these materials phonons can couple with electronic excitations and induce quantum coherent phases like superconductivity, charge density waves, ferroelectricity, or ferromagnetism.

### 6.2.1 MEASUREMENTS

Figure 6.13A reports the THz transmission measured in free space in the C-CDW phase. The THz spectrum marks the presence of three optical phonons ( $\omega_{1,2,3} = 1.58, 2.02, 2.35$  THz) allowed by the CDW symmetry. A representative empty cavity spectrum within the spectral range of the phonons is presented in Figure 6.13B.

We expect the strong coupling between the fundamental cavity mode and the three CDW vibrations to generate  $3 + 1 = 4$  non-degenerate polaritons: an upper and lower polariton (UP, LP), together with two middle polaritonic states (P1, P2), resulting from the photon-mediated hybridization of the CDW phonons. We note that, as in the single phonon case, the hybridization is associated with the formation of  $N - 1$  dark states (DS) at each bare vibrational resonance, where we have supposed to have  $N$  phonons at each frequency in the uncoupled material. The dark states are dipole non-allowed transitions [18, 61] and hence invisible to linear spectroscopy. The scheme of the energy levels scheme resulting from the multi-phonon hybridization of the CDW vibrations is sketched in Figure 6.13.

As in the single mode case (cfr Chapter 4), for strong coupling to occur the coherent energy exchange between the confined electromagnetic field and the CDW modes must dominate over the bare dissipative processes [18, 27, 32, 212]. This implies that strong coupling is achieved when the lifetime of the optical and of the CDW excitations are long enough such that Rabi oscillations can occur. Since the lifetime of an excited state is related to the homogeneous linewidth (FWHM<sup>2</sup>) of the transition, the linewidths of the cavity and of the CDW phonons has to be smaller than  $\Omega_{ij}$  to verify strong coupling, where we have denoted with  $\Omega_{ij}$  the Rabi splitting between two adjacent polaritons ( $i$  and  $j$ ). From the transmission spectrum, we estimated the linewidths of the detected phonons<sup>3</sup> to be  $\gamma_1 = 0.172$  THz,  $\gamma_2 = 0.154$  THz, and  $\gamma_3 = 0.148$  THz (Table 6.3). Moreover, for the employed 15 nm-thick gold layer on the cavity mirrors, we measured a quality factor of the bare cavity  $Q = 7.2$ .

<sup>2</sup> Full Width Half Maximum.

<sup>3</sup> We note a slight deviation from the linewidths estimated with the Drude-Lorentz fit (Table 6.1) This is ascribed to the fact that the Drude-Lorentz fit has been performed on a different observable, the complex optical conductivity, and with a different fitting model, the Drude-Lorentz one.

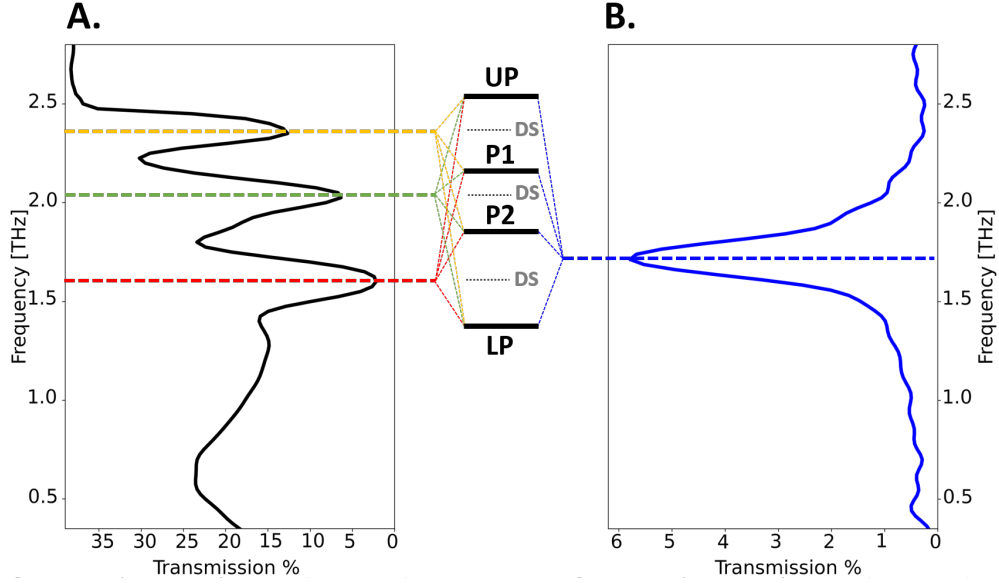


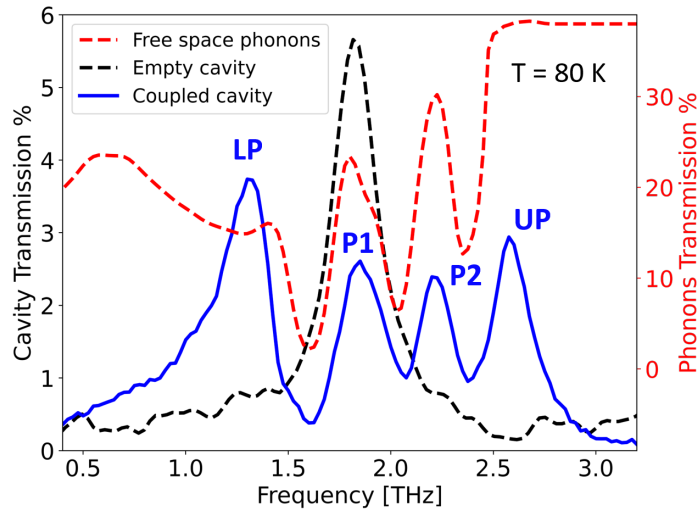
**Figure 6.13: Energy levels scheme of the multi-polariton hybridization of the CDW phonons in 1T-TaS<sub>2</sub>.** **A.** CDW phonon resonances measured in free space at 80 K. **B.** Representative empty cavity spectrum measured at 80 K. The strong coupling between the three phonons and the single cavity mode results in the formation of 4 non-degenerate hybrid states: an upper and a lower polariton (UP, LP) and two middle polaritons (P1, P2). The dark states resulting from the strong coupling are denoted with DS.

$i$	$\gamma_i$ [THz]	$\Omega_{ij}$ [THz]
1	0.172	0.496
2	0.154	0.301
3	0.148	0.310

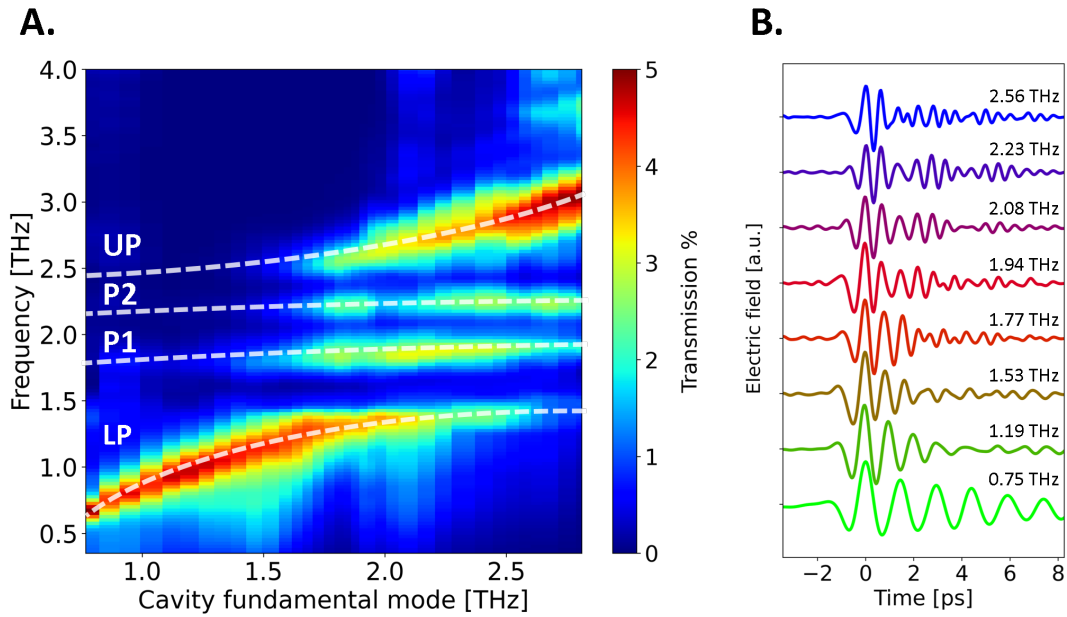
**Table 6.3: Estimation of the bare linewidths of the CDW phonons  $\gamma_i$  and of the polariton splitting  $\Omega_{ij}$ .** The values presented in the table derive from the fit of the THz transmission spectra with a multiple Voigt function.

Figure 6.14 presents a representative transmission spectrum of the measured polariton modes. The spectrum has been obtained in a representative cavity configuration in which the cavity fundamental mode (black dashed line) resonates at the midpoint of two adjacent CDW vibrations (red dashed line). We note that peaks associated to lower (LP), upper (UP), and middle (P1, P2) polariton states are visible in the THz transmission spectrum. Importantly, the splitting between adjacent polaritons  $\Omega_{ij}$  exceeds either the bare phonon linewidths  $\gamma_{1,2,3}$  and the bare cavity linewidth ( $\gamma_{\text{cav}} = 0.25$  THz). This evidence validates the strong coupling regime of the CDW excitations.<sup>4</sup> The comparison between the Rabi splittings and the linewidths of the bare phonons, both obtained from the transmission spectra, is summarized in Table 6.3.

<sup>4</sup> We note that, to confirm the strong coupling regime, the values of the Rabi splitting between adjacent polaritons  $\Omega_{ij}$  have been calculated at a cavity frequency so that the frequency distance between the polariton branches is minimum. For all the four polaritonic modes the strong coupling condition  $\Omega_{ij} > \gamma_i, \gamma_{\text{cav}}$  is valid.



**Figure 6.14: Multi-polariton spectrum measured in the C-CDW phase of 1T-TaS<sub>2</sub>.** Transmission spectrum (blue, left axis) of 1T-TaS<sub>2</sub> at 80 K within a cavity such that the frequency of the optical mode (black dashed spectrum) is at the midpoint of two C-CDW phonons. The upper and lower polariton states (UP, LP), together with the 2 middle polariton modes (P<sub>1</sub>, P<sub>2</sub>) are visible in the transmission spectrum. The spectrum of the uncoupled C-CDW phonon resonances is shown on the right axis in red for reference.



**Figure 6.15: Multi-polariton dispersion in the C-CDW phase of 1T-TaS<sub>2</sub>.** **A.** Experimental dispersion of the four polariton branches measured in the C-CDW phase at 80 K. The lower (LP) and upper (UP) polariton energies strongly disperse with the cavity frequency, while no significant dispersion is measured for the two middle polariton states (P<sub>1</sub>, P<sub>2</sub>). **B.** Measured THz fields exiting the coupled cavity at 80 K for different cavity frequencies across the phonon energies.

To further demonstrate the strong coupling regime within the THz cavity and shed light on the dispersive properties of the multi-polaritons, we tuned the resonance of

the cavity at 80 K and measured, for each cavity length, the THz fields exiting the coupled cavity. In Figure 6.15A we present the THz transmission for each cavity frequency across the phonon resonances and the obtained dispersion of the polariton modes. We highlight two different behaviours of the CDW polaritons as a function of the cavity mode:

- The lower and upper polaritons (LP, UP) strongly disperse with the cavity mode. In particular, their energies, corresponding to their maximum transmission, approach the energy of the bare modes (uncoupled cavity and phonons) in off-resonance conditions. We indeed note the lower (upper) polariton energy to tend to the bare cavity resonance at low (high) frequency and to the lowest (highest) CDW mode at high (low) frequency.
- The energies of the two middle polaritons ( $P_1$ ,  $P_2$ ) do not exhibit a significant dependence on the cavity frequency. Moreover, the frequencies of the middle polariton states lie in a dark region of the vibrational spectra. Indeed, they are located in the midpoints of adjacent phonons, where the CDW excitations are not allowed for the sample in free space.

In order to highlight this different dispersion of the polaritonic modes, we present in Figure 6.16 some selected transmission spectra measured when the cavity frequency is tuned across the energies of the CDW vibrations. The evolution of the single transmission spectra further highlights that while the central frequency of the lower and upper polariton modes strongly shifts upon changing the cavity resonance, no significant frequency shift is observed for the two middle polariton resonances.

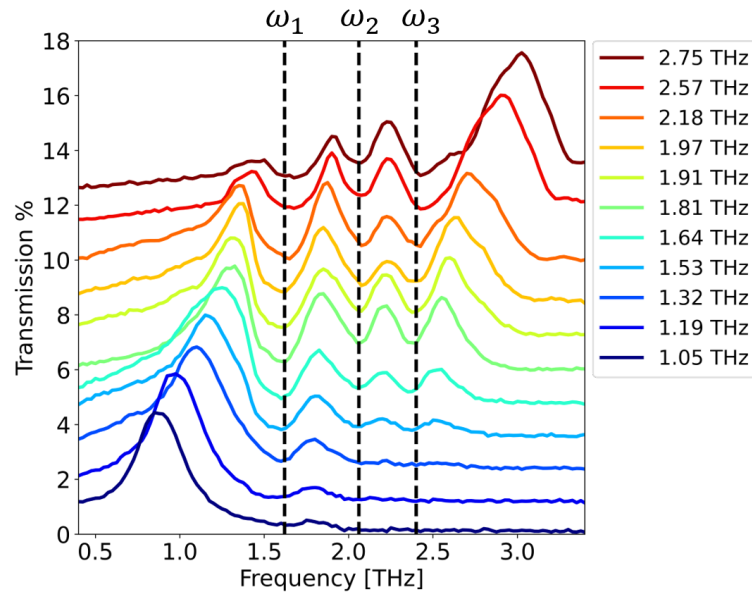


**Figure 6.16: Transmission spectra of the hybridized CDW phonons at 80 K.** Experimental evolution of the cavity transmission spectra at 80 K with cavity fundamental modes (indicated in legend) across the three phonon resonances of the C-CDW phase ( $\omega_1 = 1.58$  THz,  $\omega_2 = 2.02$  THz,  $\omega_3 = 2.35$  THz). The spectra have been vertically shifted for clarity.

The multi-polariton interference is also visible in the THz fields measured at the output of the coupled cavity (Figure 6.15B). At low frequencies, i.e. out of resonance with the CDW modes, the THz fields present indeed a single-decaying oscillatory behaviour characteristic of a single cavity mode. Conversely, when the cavity frequency approaches the spectral region of the CDW vibrations, multiple Rabi oscillations are observed. We note that, due to the multimode nature of the coupling, we do not observe a single beating modulation of the decaying field, as in the single mode coupling measured in CuGeO<sub>3</sub> (Chapter 4). The multiple modulation structure revealed in Figure 6.15B is inherited by the multi-polariton interference. This originates from the fact that, in this case, the cavity photons are at the same time coherently exchanging energy with distinct non-degenerate phonons.

### 6.2.2 MULTI-POLARITON MIXING: THE QUANTUM MODEL

In order to relate the different dispersive properties of the polaritons (Figure 6.15) to quantum superposition effects between the bare CDW vibrations and the cavity field, we resort to the coupled oscillator model in the single photon case (cfr Section 2.2.1). Indeed, the latter gives insight on the cavity/phonon mixing coefficients of each polaritonic wave-functions.

Within the coupled oscillator framework, the full Hamiltonian describing the strong coupling between the CDW excitations and the single cavity mode can be written as:

$$\hat{H} = \hat{H}_{\text{cav}} + \hat{H}_{\text{phon}} + \hat{H}_{\text{int}}. \quad (6.9)$$

The Hamiltonian consists of three contribution. The first term describes the uncoupled cavity oscillator, having tunable fundamental mode  $\omega_c$  and lifetime  $\sim 1/\gamma_{\text{cav}}$ :

$$\hat{H}_{\text{cav}} = \begin{pmatrix} \omega_c - i\gamma_{\text{cav}} & 0 & 0 & 0 \\ 0 & 0 & 0 & 0 \\ 0 & 0 & 0 & 0 \\ 0 & 0 & 0 & 0 \end{pmatrix}. \quad (6.10)$$

The second term represents the three uncoupled CDW vibrations detected in the insulating phase within the employed spectral range:

$$\hat{H}_{\text{phon}} = \begin{pmatrix} 0 & 0 & 0 & 0 \\ 0 & \omega_1 - i\gamma_1 & 0 & 0 \\ 0 & 0 & \omega_2 - i\gamma_2 & 0 \\ 0 & 0 & 0 & \omega_3 - i\gamma_3 \end{pmatrix}. \quad (6.11)$$

The free space frequencies of the CDW phonons are indicated with  $\omega_{1,2,3}$  and their respective linewidths with  $\gamma_{1,2,3}$  (see Table 6.3 for the estimations).

The multimode interaction Hamiltonian under the rotating wave approximation [18, 213] takes the form:

$$\hat{H}_{\text{int}} = \begin{pmatrix} 0 & \frac{\Omega_{12}}{2} & \frac{\Omega_{23}}{2} & \frac{\Omega_{34}}{2} \\ \frac{\Omega_{12}}{2} & 0 & 0 & 0 \\ \frac{\Omega_{23}}{2} & 0 & 0 & 0 \\ \frac{\Omega_{34}}{2} & 0 & 0 & 0 \end{pmatrix}. \quad (6.12)$$

$\Omega_{ij}$  is the Rabi splitting between the  $i$  and the  $j$  polaritons, which quantifies the interaction energy of each CDW mode with the cavity field. We highlight that  $\Omega_{ij}$  corresponds to the minimum energy separation of two adjacent polaritons which occurs when the frequencies of the uncoupled photon and phonon are equal. The estimated Rabi splittings for the three CDW modes observed at 80 K are presented in Table 6.3.

Recalling the Hamiltonian representations of the uncoupled oscillators (Equations 6.10, 6.11) and the expression of the Hamiltonian interaction (Equation 6.12), the full multimode coupled Hamiltonian  $\hat{H}$  has the following form:

$$\hat{H} = \begin{pmatrix} \omega_c - i\gamma_{cav} & \frac{\Omega_{12}}{2} & \frac{\Omega_{23}}{2} & \frac{\Omega_{34}}{2} \\ \frac{\Omega_{12}}{2} & \omega_1 - i\gamma_1 & 0 & 0 \\ \frac{\Omega_{23}}{2} & 0 & \omega_2 - i\gamma_2 & 0 \\ \frac{\Omega_{34}}{2} & 0 & 0 & \omega_3 - i\gamma_3 \end{pmatrix}. \quad (6.13)$$

We note that by experimentally changing the cavity length, the dispersive  $\omega_c$  term of the coupled Hamiltonian can be tuned through the non-dispersive CDW resonances to control their relative coupling. This will produce the anti-crossing multi-polariton branches experimentally observed and reported in Figure 6.15.

Importantly, the coupled Hamiltonian 6.13 allows us to quantify the composition of a given polariton wave-function in terms of a linear combination of the original, uncoupled resonances. Knowing the cavity and phononic fractions of the measured polaritons is indeed crucial to justify the dispersion trends reported in Figure 6.15. Supposing to have within the cavity volume  $N$  excited phonons for each of the three measured CDW modes, each polariton wave-function  $|\psi_{PL}\rangle$  can be expressed on the basis of the uncoupled phonons/cavity modes as follows:

$$|\psi_{PL}\rangle = X_{cav}(\Delta\omega)|0,0,0;1\rangle + X_1(\Delta\omega) \sum_{i=1}^N |e_i,0,0;0\rangle + X_2(\Delta\omega) \sum_{i=1}^N |0,e_i,0;0\rangle + X_3(\Delta\omega) \sum_{i=1}^N |0,0,e_i;0\rangle. \quad (6.14)$$

Here we have indicated with  $|0,0,0;1\rangle$  the purely cavity state, and with  $\sum_{i=1}^N |e_i,0,0;0\rangle$ ,  $\sum_{i=1}^N |0,e_i,0;0\rangle$ ,  $\sum_{i=1}^N |0,0,e_i;0\rangle$  the purely vibrational states in which respectively the first, second, and third CDW phonons are in their excited state  $|e_i\rangle$ . We stress that the wave-function components must satisfy the normalization condition  $|X_{cav}|^2 + \sum_{i=1}^3 |X_i|^2 = 1$  for each cavity frequency  $\omega_c$ .

The mixing coefficients of each polariton wave-function as a function of the cavity frequency  $\omega_c$ , as well as the energies and linewidths of the polariton modes, can be obtained by diagonalizing equation 6.13:

$$\begin{pmatrix} \omega_c - i\gamma_{cav} & \frac{\Omega_{12}}{2} & \frac{\Omega_{23}}{2} & \frac{\Omega_{34}}{2} \\ \frac{\Omega_{12}}{2} & \omega_1 - i\gamma_1 & 0 & 0 \\ \frac{\Omega_{23}}{2} & 0 & \omega_2 - i\gamma_2 & 0 \\ \frac{\Omega_{34}}{2} & 0 & 0 & \omega_3 - i\gamma_3 \end{pmatrix} \begin{pmatrix} X_{cav} \\ X_1 \\ X_2 \\ X_3 \end{pmatrix} = \tilde{E} \begin{pmatrix} X_{cav} \\ X_1 \\ X_2 \\ X_3 \end{pmatrix}. \quad (6.15)$$

In order to validate the accuracy of the model, we firstly exploit it to calculate the dispersion of the polariton energies and compare them with the energies measured experimentally (Figure 6.15A). Using for the interaction energies the estimated Rabi splitting  $\Omega_{ij}$  (Table 6.3), we obtain the polariton dispersion presented in Figure 6.17A. The measured dispersion of the polariton energies is in agreement with the predictions

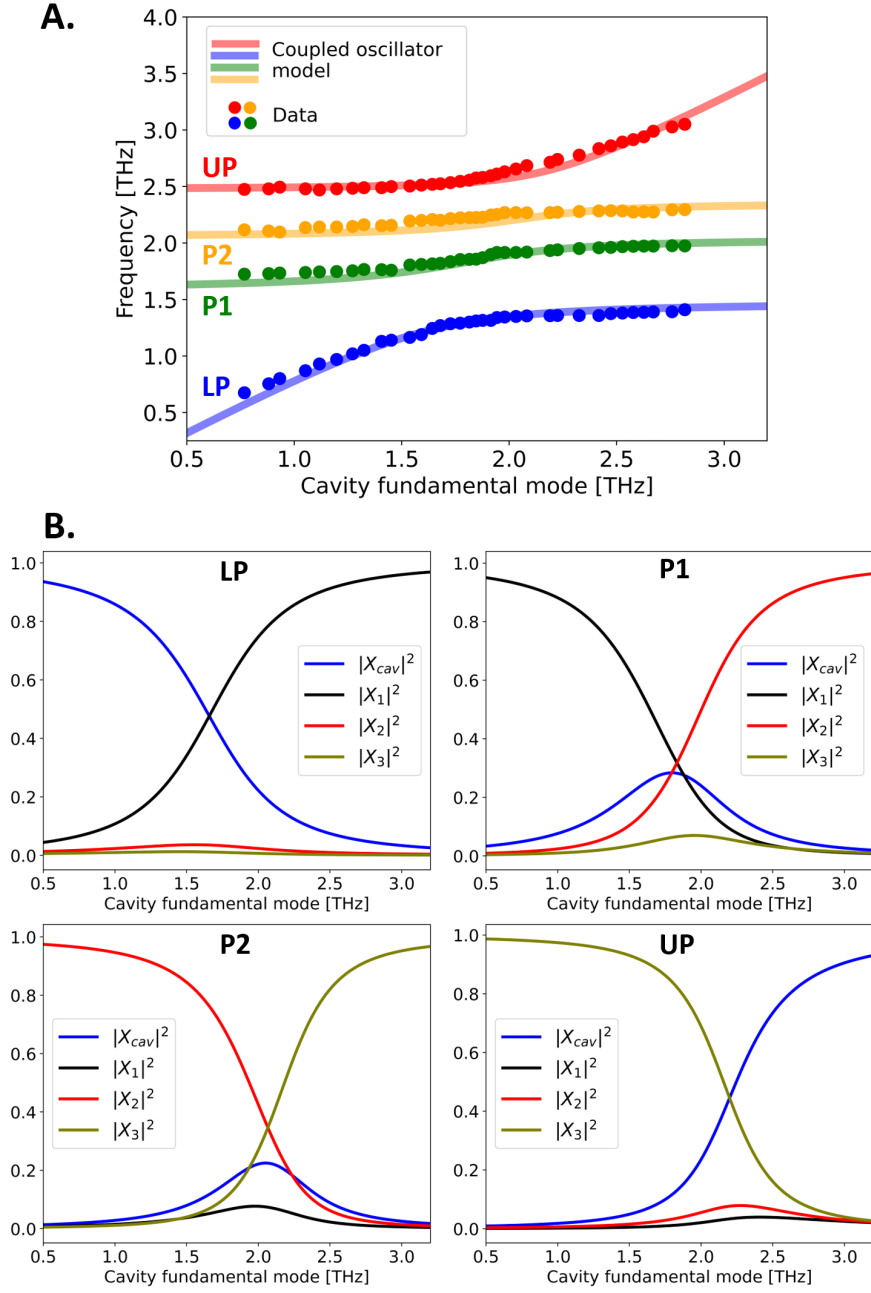


**Figure 6.17: Estimated wave-function components of the polariton states of the C-CDW phase.** **A.** THz vibro-polariton branches for the four hybrid states. The circles correspond to the measured polariton peaks, while the solid curves show the eigen-energies obtained from the coupled oscillator model (Equation 6.15) fitted to the measured data. **B.** Cavity ( $|X_{cav}|^2$ ) and phonon ( $|X_{1,2,3}|^2$ ) fractions of the polariton wave-functions as a function of the cavity frequency. The estimations for the four polaritonic states have been obtained within the coupled oscillator model (Equation 6.15).

of the coupled oscillator model, thus validating the applicability of the model to the experimental setting.

The evolution of the cavity/phonon fractions of the four polaritonic wave-functions upon tuning the cavity fundamental mode is presented in Figure 6.17B. The extracted

coefficients of the wave-functions show that the four polaritons have character from all the three CDW modes as a result of the photon-mediated hybridization. Importantly, we highlight distinct behaviours between the upper (lower) polariton states and the middle polaritons:

- The lower and upper polariton states (UP, LP) exhibit a strong cavity component  $|X_{\text{cav}}|^2$  which significantly depends on the cavity fundamental mode. In particular, the cavity fraction of the lower (upper) polariton tends to 1 at low (high) frequencies, while it tends to 0 at high (low) cavity frequencies. As highlighted by the wave-function coefficients, the anti-crossing behaviour of the lower polariton originates mainly from the coherent mixing of the  $\omega_1$  CDW mode with the cavity field. Conversely, the anti-crossing features of the upper polariton are mainly the result of the mixing between the  $\omega_3$  phonon and the cavity photons. The mixing assignation is further justified by the fact that the cavity fraction  $|X_{\text{cav}}|^2$  of LP crosses the first CDW phonon fraction  $|X_1|^2$  at a detuning  $\omega_c = \omega_1$ . Conversely, the cavity fraction of UP crosses the third CDW phonon fraction  $|X_3|^2$  when the cavity frequency equals  $\omega_3$ .

We note that, for both the upper and lower polaritons, a uniform mixing among all the CDW modes is inhibited by their frequency separation in the free space material.

The significant cavity fraction of the upper and lower polaritons justifies therefore their strongly dispersive properties reported in the transmission spectra of Figure 6.15.

- The middle polariton states (P1, P2) display a substantially lower cavity fraction  $|X_{\text{cav}}|^2$  which justifies their non-dispersive behaviour. The quantum model indicates that the middle polaritons result from the cavity-mediated hybridization of different non-degenerate CDW excitations. In particular, the P1 state results from the coherent mixing of the  $\omega_1$  and the  $\omega_2$  modes, while the P2 state from the hybridization between the  $\omega_2$  and the  $\omega_3$  modes. We stress that both the phonon-phonon hybridizations are mediated by the cavity field.

### 6.2.3 LIFETIMES PROPERTIES OF THE MULTIMODE POLARITONS

We highlight that the different dispersive features of the CDW-polaritons are mapped also onto the evolution of their linewidths, and hence on their lifetimes. As in the single mode case (Chapter 4), we indeed expect the broadening of the polaritons to depend on the detuning of the cavity, given that it results from the contribution of the phonons/cavity linewidths weighted by the relative phonons/cavity fractions [60, 85, 214, 215].

The estimated linewidths of the four polariton modes, defined as the FWHM of the deconvoluted transmission peaks, are presented in Figure 6.18A as a function of the cavity fundamental mode. We highlight that, while the linewidths of the lower and upper polaritons significantly depend on the cavity frequency, the linewidths of the two middle polaritons does not substantially change upon detuning the cavity. This evidence can be linked to the strong contribution that the photon wave-function gives to the LP and UP modes. Indeed, since in our experimental setting the cavity dissipations dominates over the dissipations of the bare CDW resonances, i.e.  $\gamma_{\text{cav}} > \gamma_{1,2,3}$ , we expect the upper (lower) polariton to get broadened (narrowed) when approaching the phonons frequencies.

To relate the linewidth evolution of the polariton states to the quantum superposition of the bare CDW modes with the cavity field, we resort to the coupled oscillator model

(Equation 6.15) and estimate the polaritons linewidths as a function of the cavity detuning. The results of the analytical model are presented in Figure 6.18B. We highlight that, despite an absolute shift due to incoherent dielectric losses within the cavity (cfr Section 4.3.2), the simulated polariton linewidths qualitatively follow the data. This confirms that the strong dependence of the UP and LP lifetimes on the cavity detuning is related to a stronger contribution of the cavity field to their wave-functions. Contrarily, the lifetimes of the middle polaritons (P1, and P2) display a weak dependence on the cavity frequency, consistent the low cavity fraction of their wave-functions.

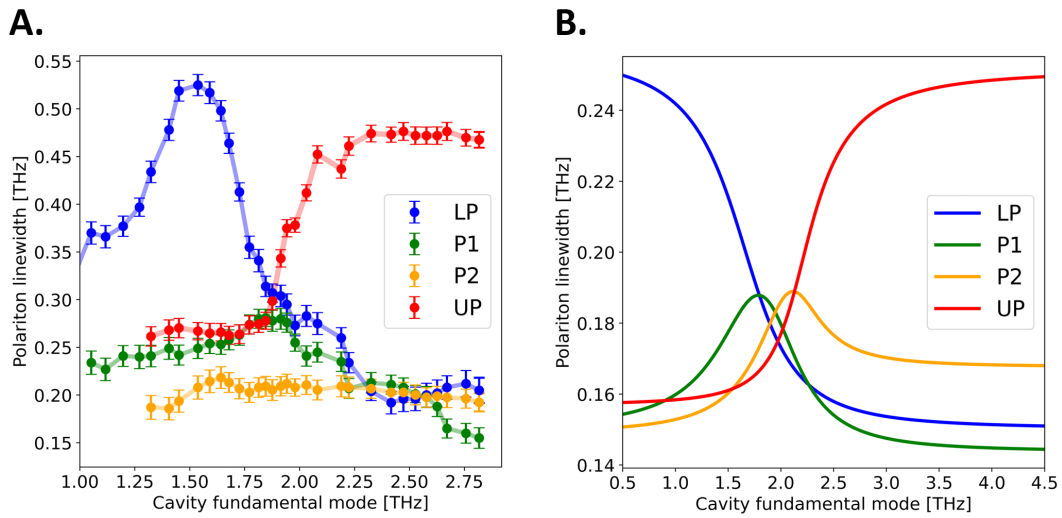


**Figure 6.18: Polariton linewidths in the C-CDW phase as a function of the cavity frequency.** **A.** Measured FWHM of the four polariton modes as a function of the cavity frequency at 80 K. **B.** Calculated linewidths of C-CDW vibro-polaritons from the coupled oscillator model. Only the linewidths of the polaritons having a strong cavity component (LP, and UP) exhibit a strong dependence on the cavity frequency.

## 6.3 TEMPERATURE-DEPENDENT COUPLING REGIMES

In the previous section we have studied in detail the hybridization of the vibrational modes of the C-CDW phase of 1T-TaS<sub>2</sub> and proved that a multimode strong coupling regime can be established at low temperatures. In this section we study how the change in the conductive properties of the free charges across the metal-to-insulator transition affect the response of the strongly coupled CDW phonons.

Figure 6.19 presents the cavity dispersion measured at different temperatures across the charge ordering transition. Dispersions have been obtained by heating the sample-cavity hybrid from the insulating C-CDW phase. The THz transmission measurements highlight the following trends:

- The Rabi splitting between the polariton states closes approaching the phase transition. In particular, the screening of the CDW excitations induced by the free carriers [170, 171] is mapped differently on the polaritonic resonances. Indeed, at temperatures in proximity of  $T_c \sim 215$  K the lower and upper polariton energies are the most affected by the free charge screening. This evidence will be discussed in Section 6.3.1. In the metallic phase, the CDW phonons are then completely screened by the free carriers and no polaritonic features are detected.
- The linewidths of the coupled modes become broader approaching the phase transition, as shown in Figure 6.19. In particular, at the critical temperature we detect the signatures of a weak phonon coupling regime. An increase of the dissipative rates of the coupled cavity is indeed measured when the fundamental mode of the resonator is tuned within the spectral region of the CDW vibrations. This change of the cavity dissipations is not associated with a polaritonic-like structure in the measured transmission spectra, proving that no energy hybridization occurs among the uncoupled resonances. This evidence validates the hypothesis of a weak coupling interaction at  $T_c$  between the CDW excitations and the cavity field [17, 69, 196, 216, 217]. This evidence will be discussed more in detail in Section 6.3.2.

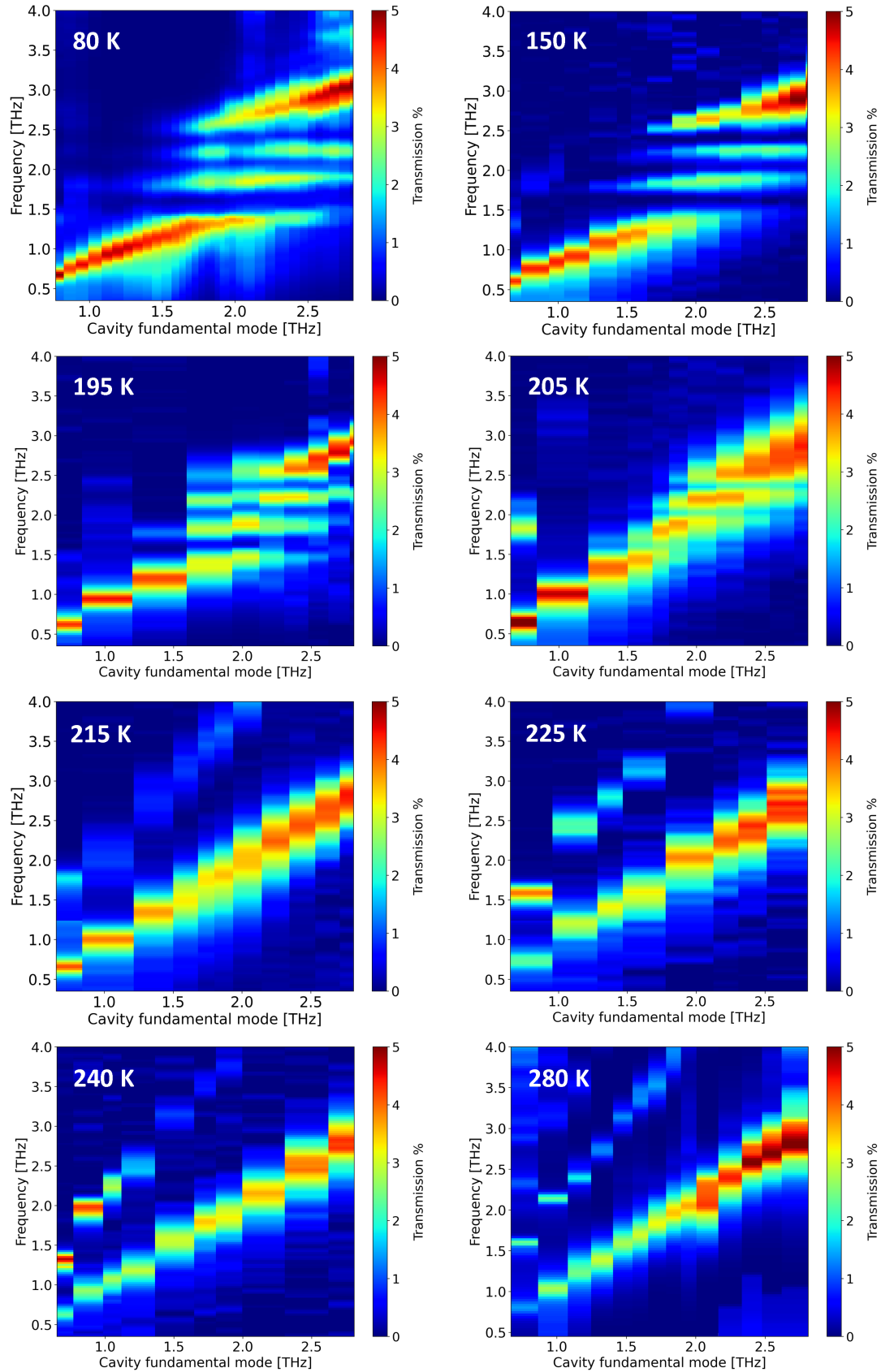


**Figure 6.19: Temperature dependence of the cavity dispersion measured across the metal-to insulator transition of 1T-TaS<sub>2</sub>.** Cavity dispersion measured at different temperatures (indicated inside the plots) across the metal-to-insulator phase transition. The presented transmission maps have been measured upon heating the sample from the insulating C-CDW phase.

## 6.3.1 EVOLUTION OF THE POLARITONS SPLITTING

The temperature dependence of the dispersion maps presented in Figure 6.19 show that the Rabi splitting between the polariton modes observed at low temperature is suppressed across the charge ordering transition. This effect can be rationalized by the screening of the free charges. In order to highlight more clearly this evidence, we present in Figure 6.20A the temperature evolution of the THz spectra at a fixed cavity frequency within the spectral region of the CDW vibrations ( $\sim 1.5 - 2.4$  THz). For this dependence a representative cavity frequency  $\omega_c = 2.1$  THz has been employed. We emphasize that the influence of the free charges screening at the phase transition has a stronger effect on the LP and UP frequencies with respect to the middle polariton ones.

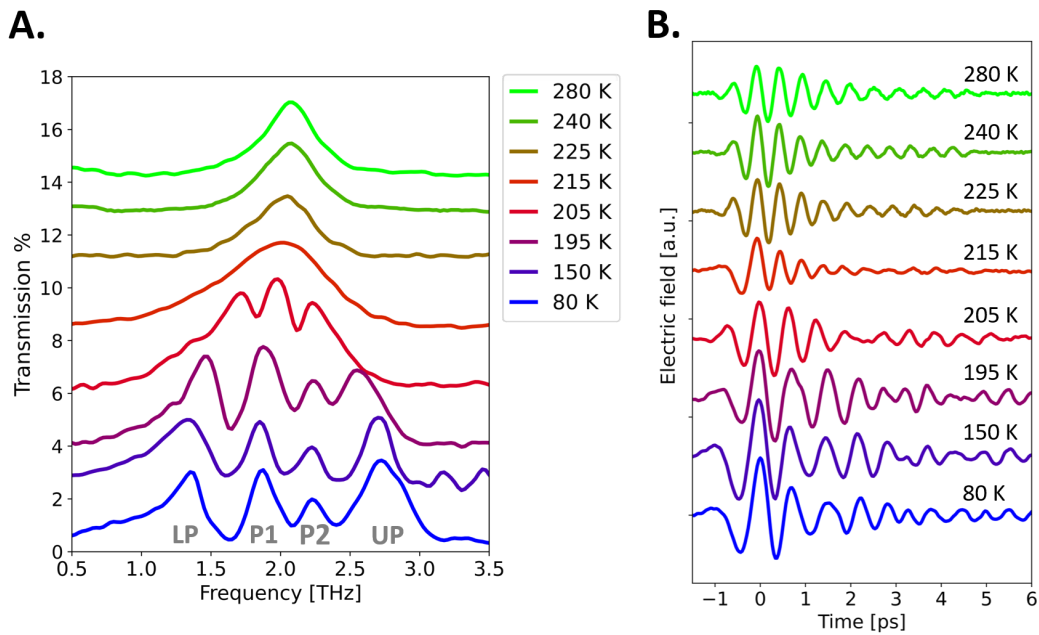


**Figure 6.20: Temperature dependent THz spectra for a fixed cavity frequency within the CDW phonons spectral range.** **A.** Evolution of the THz transmission across the metal-to-insulator transition for a fixed cavity frequency  $\omega_c = 2.1$  THz. The spectra have been vertically shifted for clarity. **B.** Corresponding THz fields exiting the coupled cavity at different temperatures. The THz fields and the corresponding transmission spectra have been measured upon heating the sample from the C-CDW state.

This evidence can be qualitatively rationalized exploiting the results of the coupled oscillators model (Figure 6.17), which show that the lower and upper polariton wavefunctions exhibit a stronger cavity component. In Section 6.1 we have proved that an increase of the Drude-like response in the system, induced by the onset of metallicity, is mapped onto a faster dissipative dynamics of the cavity. We can subsequently relate the stronger shift of the lower and upper polariton frequencies at the phase transition to an increase of the dissipative rates of the cavity component of their hybrid wave-functions. In a simple coupled oscillator model [18, 60, 218] we indeed expect a broadening of the cavity mode, and hence an increased dissipative rate of the cavity photons, to reduce the coupling strength with the targeted excitation and hence the Rabi splitting

(cfr Figure 4.13). Therefore, the strongest reduction of the Rabi splittings associated to the lower and upper polaritons ( $\Omega_{12}$ , and  $\Omega_{34}$ ) can be qualitatively ascribed to an increased coupling of the cavity with the free charges, which results in an enhancement of the optical dissipation rates (Figure 6.2). The closing of the Rabi splitting could hence be more evident on the lower and upper polariton modes, given their stronger cavity fraction.

The screening of the polaritons at the phase transition, related to the coupling with the conductive charges, is also visible in the time-domain THz fields. Figure 6.20B presents the THz fields measured across the metal-to-insulator transition, corresponding to the coupled spectra of 6.20A. We note that the charge screening induces a stretching and a lower modulation depth of the Rabi oscillations<sup>5</sup> near  $T_c \sim 215$  K. The multiple Rabi oscillations evolve in a single decaying oscillations in the metallic state, as a expected from the full screening of the CDW excitations (Figure 5.4).

### 6.3.2 SIGNATURES OF VIBRATIONAL WEAK COUPLING REGIME

In this section we analyse the signatures of phonon weak coupling regime detected at the critical temperature. We present in Figure 6.21A the evolution of the coupled cavity transmission obtained upon tuning the cavity mode across the spectral region of the CDW phonons. Spectra have been obtained at the critical temperature of the charge ordering transition upon heating the sample from the dielectric phase ( $T_c \sim 215$  K). We note that at  $T_c$ , as a consequence of the free charges screening, no polaritonic splitting is revealed across the spectral region of the CDW vibrations.

Nonetheless, we observe a non-monotonic evolution of the linewidth of the coupled cavity. To highlight this non-monotonic trend we present in Figure 6.21B the estimated quality factor of the coupled cavity  $Q = \frac{\omega_c}{\Delta\omega_c}$  as a function of the cavity frequency  $\omega_c$ . The quality factor has been obtained by fitting the cavity transmission peak with a Voigt lineshape. The quality factor is a crucial parameter to justify the establish of a weak coupling regime [217], since it quantifies the dissipative rates within the cavity volume.

We revealed that the quality factor exhibits a minimum when the cavity mode is swept within the spectral region of the CDW vibrations. This implies that in proximity of the critical temperature ( $T \sim 215$  K) the dissipative rates of the coupled cavity are enhanced in resonance with the CDW excitations. This represents a key signature of the phonon weak coupling regime, in analogy with the Purcell effect in the atomic and molecular frameworks [13–16]. We can hence conclude that at  $T_c$  the phonon screening induced by the free charges provokes an increase of the decay rates of the coupled photons when the latter have an energy compared with the CDW excitations. The effect revealed in Figure 6.21B is hence consistent with a strong to weak coupling transition of the CDW vibrations caused by the onset of metallicity in the system.

We highlight that the weak coupling signatures are characteristic of a critical behaviour occurring in proximity of  $T_c$ . Indeed, they are not detected in the high temperature metallic state, where the THz response is dominated by the free carriers.

To highlight that the weak coupling response is peculiar of a critical behaviour, we present in Figure 6.22A the THz transmission of a cavity with fundamental mode on resonance with the CDW modes ( $\omega_c = 2.1$  THz) measured at  $T_c \sim 215$  K and in the 280 K metallic state. We note that the line broadening of the coupled cavity is detected only

<sup>5</sup> We note, as in Section 6.2.1, that, due to the multimode nature of the coupling, in the C-CDW state we do not observe a single beating modulation of the decaying field, as in the single mode coupling. Multiple Rabi oscillations are instead revealed.

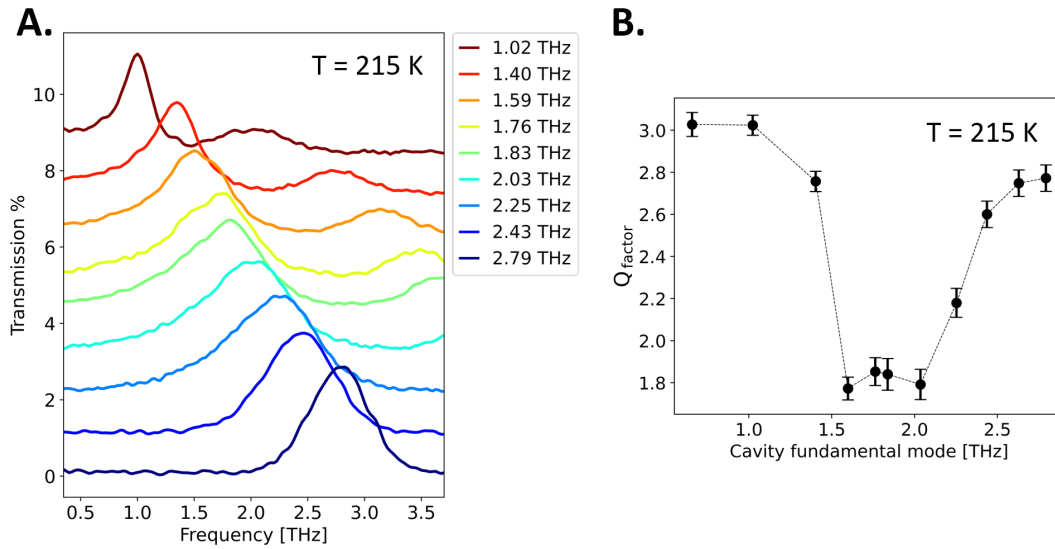


**Figure 6.21: Signatures of weak coupling regime near the critical temperature of the charge ordering transition in 1T-TaS<sub>2</sub>.** **A.** Transmission spectra measured near the heating critical temperature ( $T_c = 215$  K) as a function of the cavity fundamental mode (indicated in the legend). The spectra have been vertically shifted for clarity. **B.** Estimated quality factor in proximity of  $T_c$  as a function of the cavity frequency. A decrease of the quality factor of the coupled cavity is measured across the spectral region of the CDW phonons ( $\sim 1.5 - 2.4$  THz).

at  $T_c$ . On the contrary, a sharper resonance is observed at room temperature. This effect is evident also by looking at the decay times of the time-domain THz fields detected at the output of the coupled cavity (Figure 6.22B). We note that the coherence time of the photons within the cavity volume, and hence the decay time of the oscillating THz field, is reduced at  $T_c$ , while it becomes longer in the high temperature phase of 1T-TaS<sub>2</sub>. The trend of the photon lifetimes is consistent with a speed up of the dissipation rates at  $T_c$ , peculiar of the vibrational weak coupling regime.

Figure 6.22C shows the quality factor of the coupled cavity as a function of the cavity frequency, measured in proximity of  $T_c$  ( $Q_{215\text{K}}$ ) and in the high temperature metallic state ( $Q_{280\text{K}}$ ). We highlight two different trends:

- At low cavity frequencies the quality factor is lower at high temperatures with respect to  $T_c$ , i.e.  $Q_{280\text{K}} < Q_{215\text{K}}$ . This trend is consistent with the coupling with the Drude excitation discussed in Section 6.1), whose effect is to broaden the cavity line (Figure 6.2), and hence reduce the quality factor. We expect indeed the coupling with the Drude-like oscillator to be dominant at lower cavity frequencies (Figure 6.12) and to increase at higher temperatures. The contribution of the free charges to the THz absorption is indeed higher at lower frequencies and increases by raising the temperature [170].
- Within the spectral region of the CDW excitations ( $\sim 1.5 - 2.4$  THz) the cavity linewidth measured at  $T_c$  is dominated by the weak coupling features. Indeed, at 215 K we observe a drop in the quality factor which can be associated to the weak coupling of the CDW vibrations. Conversely, the same trend is not observed at 280 K, where the quality factor is dominated by the coupling with the Drude oscillator. The coupling with the Drude oscillator causes  $Q_{280\text{K}}$  to increase monotonically by sweeping the cavity mode towards higher energies, as discussed in Section 6.1.4.

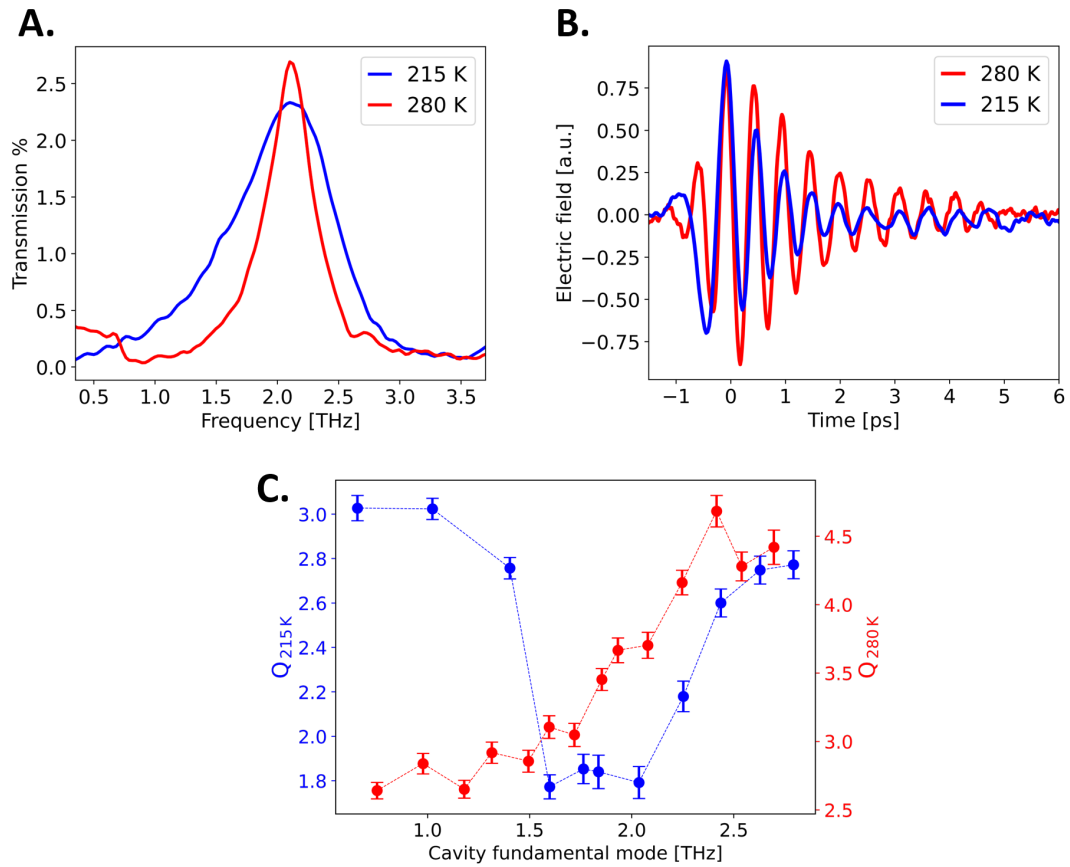


**Figure 6.22: THz linear response of the coupled cavity in proximity of the critical temperature and in the high temperature metallic phase of 1T-TaS<sub>2</sub>.** **A.** Transmission spectra of a cavity with fundamental mode within the spectral region of CDW phonons ( $\omega_c = 2.1$  THz) measured in the high temperature metallic phase (280 K) and in proximity of  $T_c$  (215 K). **B.** Time domain THz fields at the output of the 2.1 THz cavity measured near the heating critical temperature ( $T = 215$  K) and in the NC-CDW phase ( $T = 280$  K). **C.** Measured quality factors at 215 K (blue points) and at 280 K (red points) as a function of the cavity frequency, when the latter is swept through the spectral region of the CDW phonons.

## 6.4 CONCLUSIONS

In conclusion, we have demonstrated how the change in the charge dissipations through the metal-to-insulator transition in 1T-TaS<sub>2</sub> affects the cavity electrodynamics. We revealed that the optical dissipative rates within the cavity can be controlled by coupling the cavity field with the free charges responsible of the Drude excitation. When the cavity is coupled with the quasi-static Drude oscillator we measured a non-constant Q factor across the phase transition, mapping the metallicity in the system.

On the contrary, when the cavity is tuned resonantly with the CDW vibrations of the dielectric phase we detected the THz signatures of a multi-phonon mixing. The Rabi splitting between the hybrid CDW excitations closes across the charge ordering transition as a consequence of the screening of the free charges. In particular, THz signatures of a weak phonon coupling are detected at the critical temperature. Our findings further emphasize how cavity electrodynamics can be affected by the dissipations and in particular how the response of the free charge through a model metal-to-insulator transition affect the cavity properties. Our evidences prove that the free charge screening of bound vibrational excitations can induce a strong to weak coupling transition, opening a new path [187, 219–222] to engineer the energy exchange rates in cavity confined systems.



# ELECTRONIC COUPLING: CHARGE TRANSFER HYBRIDIZATION IN SUPERCONDUCTING YBCO

---

## 7.1 MOTIVATION

The idea of using light-matter hybridization to engineer new material functionalities is emerging as a promising approach in material science. The light confinement in optical cavities has been mostly used over the last decade to manipulate chemical processes, demonstrating the possibility of affecting chemical reactivity [33–35] and charge energy transfer processes [38–41] in a tailored cavity environment.

The effort of using the strong coupling concepts to obtain new material functionalities in superconducting Transition Metal Oxides (TMOs) has been somewhat smaller and by large limited to theoretical proposals. Different works have proposed to use low frequency THz cavities coupled to vibrational or collective electronic excitations to manipulate the superconducting order-parameter phase coherence by coupling to Josephson plasma resonances [43, 46]. Other theoretical works have proposed coupling to excitations at higher energy comparable to on-site Coulomb repulsion and charge transfer excitations, and demonstrated that this could induce a long-range interaction between the electrons and lead to pairing [223–225].

Only recently, the first experimental study of THz cavities strongly coupled to vibrational modes in the organic superconductor  $\text{Rb}_3\text{C}_{60}$  revealed a significant increase of the superconducting transition temperature, interpreted as an enhancement of the electron-phonon coupling in a BCS-like picture [57]. Intriguingly, in the same work [57], strong vibrational coupling has been found instead to reduce the critical temperature in the superconducting cuprate YBCO. This result suggests that, while in BCS-like superconductors the electron pairing is mostly affected by the low energy vibrational modes, in cuprates high energy electronic transitions significantly contribute to the onset of the superconductivity. Hence, an efficient enhancement of the superconducting transition could be attained by direct coupling to the electronic degrees of freedom.

The anomalous high-frequency electrodynamic with respect to the standard BCS scenario is one key feature of unconventional superconductors. While in BCS systems the onset of superconductivity is accompanied by a redistribution of spectral weight only on the energy scale comparable to the superconducting gap [226], ample evidence is found in literature that in cuprates drastic changes also occur on the eV-range [227, 228]. In particular, several optical studies have shown that the charge transfer (CT) transition, i.e., the lowest electronic transition from O-2p orbital to the upper Hubbard band ( $\Delta_{\text{CT}} \sim 2$  eV, Figure 7.1), is mostly affected upon entering the superconducting phase [229–232] and may play a crucial role in the pairing mechanism.

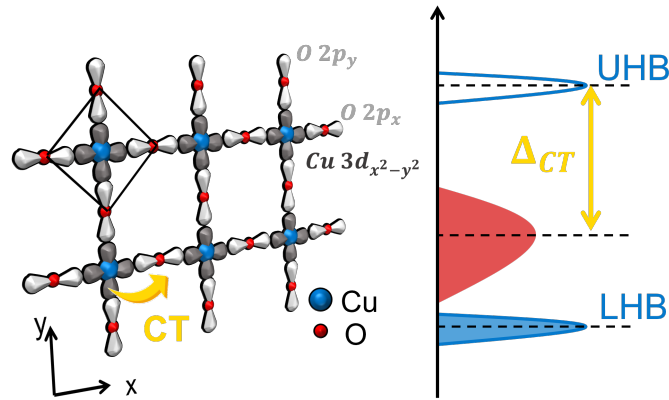


**Figure 7.1: Electronic charge transfer excitation in cuprates.** Sketch of the electronic configuration of a  $\text{CuO}_2$  plane in cuprates. The lowest electronic transition is the charge transfer (CT) transition from the O-2p orbitals to the Upper Hubbard Band (UHB), as highlighted by the yellow arrow.

Here, we explore the possibility of coupling the CT transition in underdoped YBCO to an optical cavity and see how strong electronic coupling may affect the onset of the superconducting response.

## 7.2 DESIGN OF THE YBCO-BASED CAVITY HETEROSTRUCTURES

We experimentally accomplish the electronic strong coupling by realizing YBCO-based heterostructures that sustain modes resonant to the charge transfer excitation. Based on Transfer-matrix simulations, we designed the heterostructure sketched in Figure 7.2A. The cavity consists of a reflecting layer of  $\text{LaNiO}_3$  (LNO) grown on a thick  $\text{LaAlO}_3$  (LAO)  $5 \times 5$  mm substrate. A thin epitaxial YBCO film is placed between two insulating layers of  $\text{CeO}_2$  and laid on LNO. Finally, a semi-reflecting layer of Ag with variable thickness closes the cavity heterostructure. A top layer thickness of 5 nm, 10 nm, and 15 nm has been employed for the present experiments.

The thickness of the top Ag layer ultimately sets the quality factor  $Q$  of the cavity, which gives an indication on how strongly the targeted electronic transition is coupled to the cavity mode. The thicker the semi-reflecting layer, the longer will be the lifetime of the photons trapped in the cavity and so the stronger the coupling to the CT transition is expected to be. This is shown in Figure 7.2B, where we calculate the reflectivity of the cavity for different Ag layer thicknesses, neglecting the absorption term of the YBCO film.

Transfer-matrix simulations show that, even in the cavity with the lowest quality factor, a strong coupling regime can be established due to the high oscillator strength of the CT transition (Figure 7.3). To demonstrate this, we show in Figure 7.3A the absorption of the hybridized charge transfer transition inside the cavity as a function of the thickness of the top silver layer. The Rabi splitting of the charge transfer oscillator increases with higher quality factors of the cavity. Importantly, for all the Ag thicknesses employed in the designed heterostructures (5 nm, 10 nm, and 15 nm) the Rabi splitting is greater than the intrinsic linewidth of the CT oscillator in free space (Figure 7.3B).

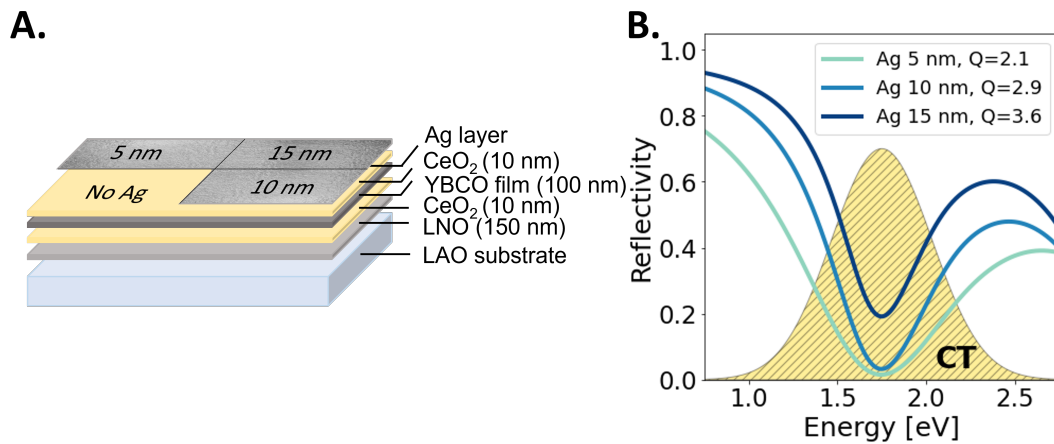


**Figure 7.2: Design of the YBCO-based cavity heterostructure.** **A.** Sketch of the electronic configuration of a  $\text{CuO}_2$  plane in cuprates. The lowest electronic transition is the charge transfer (CT) transition from the O-2p orbitals to the Upper Hubbard Band (UHB), as highlighted by the yellow arrow. **B.** Sketch of the fabricated heterostructure. **C.** Transfer-matrix simulation of the reflectivity of the heterostructure in B. for different thicknesses of the Ag top layer (neglecting the absorption of the YBCO layer). The mode sustained by the cavity is resonant to the CT transition in YBCO [233], denoted by the Lorentz-like shape.

This indicates that a strong coupling regime can be established in all the three cavities analysed in this study.

In order to estimate the quality factors of the designed cavities, we evaluated the FWHM of the reflectivity dip corresponding to the hybridized CT excitation in YBCO after the subtraction of a linear background (Figure 7.4). The estimated quality factors reported in the plot are calculated by dividing the peak energy of the CT oscillator ( $h\nu = 1.78$  eV) by the FWHMs calculated for each cavity configuration.

Proven that a strong coupling of the CT electronic excitation could be established in the designed heterostructures, we carried out a comparative study of the superconducting response in YBCO enclosed in cavities with 5, 10 and 15 nm-thick Ag layer.

In order to avoid artifacts, we deposited different amounts of Ag on different areas of the same heterostructure (Figure 7.5A, Sample A). To study how the cavity environment possibly modifies the onset of superconductivity, we left a portion of the heterostructure free of silver ("No Ag" in Figure 7.5A, Sample A) and used it as a reference. Moreover, we realized a second heterostructure (Sample B in Figure 7.5A), completely identical to Sample A, but without the second  $\text{CeO}_2$  and Ag layers. This YBCO-terminated heterostructure serves as reference for the characterization of the superconducting transition temperature in free space, which has been measured to be approximately 58 K through transport measurements (Figure 7.5B).

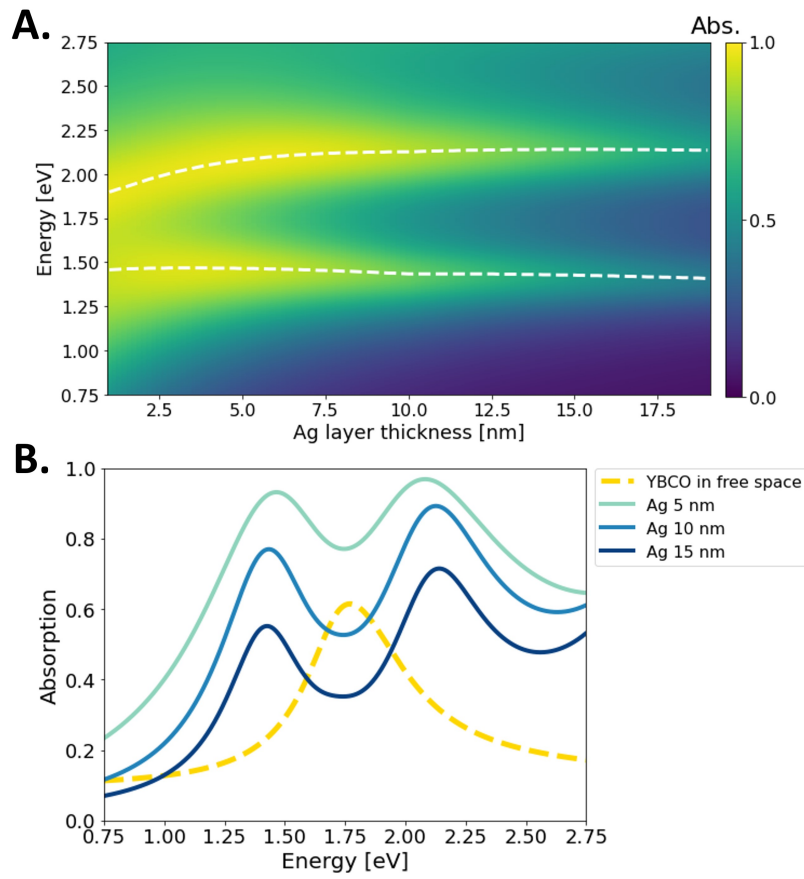


**Figure 7.3: Transfer-matrix simulations of the hybrid YBCO-based cavity.** **A.** Simulated absorption of the hybrid heterostructure cavity as a function of the thickness of the Ag top layer. **B.** Simulated hybridization of the YBCO charge transfer oscillator in the three cavities studied. The CT oscillator absorption in free space of a 100 nm-thick YBCO film on a LAO substrate is shown in yellow dashed line for reference. The dielectric functions of all the layers are taken from the literature [96, 233–236].

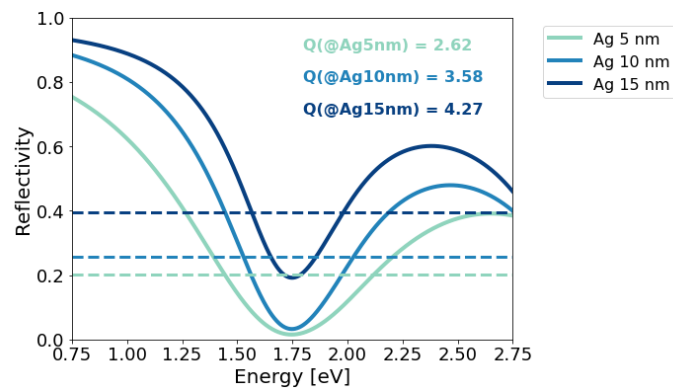


**Figure 7.4: Estimation of the quality factor of the designed heterostructures.** Simulated reflectivity of the three heterostructures fabricated after the subtraction of a linear background. The dashed lines denote the FWHM of the reflectivity dip associated to the resonance of the charge transfer transition in YBCO.

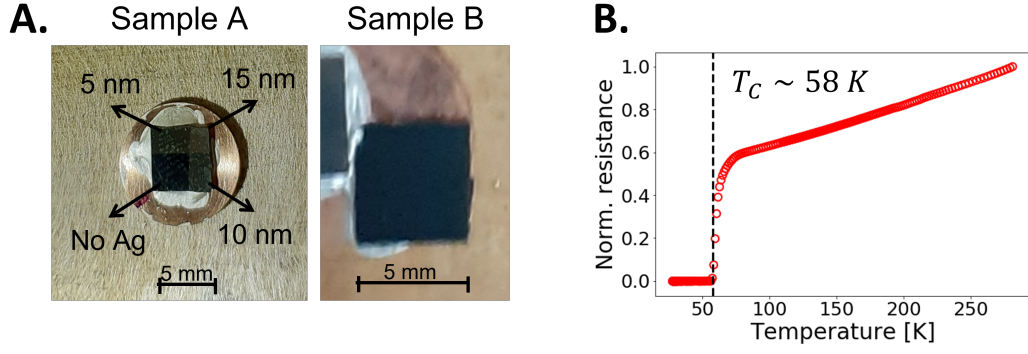


**Figure 7.5: Heterostructures preparation.** **A.** Pictures of the samples. Sample A is the  $\text{CeO}_2/\text{YBCO}/\text{CeO}_2/\text{LNO}/\text{LAO}$  heterostructure on which Ag layers having different thicknesses were deposited (5, 10 and 15 nm thick). We labelled "No Ag" the portion of the heterostructure free of Ag. Sample B is the  $\text{YBCO}/\text{CeO}_2/\text{LNO}/\text{LAO}$  heterostructure. **B.** Transport measurement on Sample B, revealing the onset of superconductivity at  $T_c \sim 58 K$ .

## 7.3 THREE PULSE OPTICAL MEASUREMENTS

### 7.3.1 CHARACTERIZATION OF THE NON-LINEAR RESPONSE OF THE SUPERCONDUCTING PHASE

Due to the presence of the insulating  $\text{CeO}_2$  and Ag layers, transport measurements are not viable in the closed cavities. For this reason we characterize the onset of the superconducting response through time-domain optical spectroscopy.

As the superconducting gap is related to the total number of excitations, the photo-injection of free quasi-particles by means of ultrashort laser pulses results in a time dependent non-linear perturbation of the gap. To reveal the superconducting transition, we leverage on this non-linearity by using a three-pulse scheme.

We drive the sample out-of-equilibrium through the subsequent photo-excitation of a blue pump pulse (P) (3.1 eV) and a mid-infrared push-pulse (p) (75 meV), delayed in time by  $\Delta t$ , and we record the broadband transient reflectivity  $\left(\frac{\Delta R_{pp}}{R_{pp}}\right)$  in the visible range (1.3 - 2.2 eV). Further details on the experimental set-up and on the acquisition system can be found in Section 7.4.1 and in Ref. [237].

By measuring the optical response of the sample when independently photo-excited by the blue pump  $\left(\frac{\Delta R_p}{R_p}\right)$  and the push mid-IR  $\left(\frac{\Delta R_p}{R_p}\right)$  we can single out the non-linear response in the superconducting phase by direct subtraction:

$$\frac{\Delta\Delta R}{R} = \frac{\Delta R_{pp}}{R_{pp}} - \frac{\Delta R_p}{R_p} - \frac{\Delta R_p}{R_p}. \quad (7.1)$$

This approach has proved effective in determining the superconducting temperature in other members of the cuprate family, for example in single-crystals Y-BSCCO for which the critical temperature was known through complementary equilibrium measurements (see Figure 7.11B of Section 7.4.1 of the present chapter).

In the following, we demonstrate how the emergence of a non-linear signal in the YBCO heterostructures is an optical fingerprint of the superconducting phase. Crucially, we will show that the onset temperature for the non-linear optical response coincide

with the discontinuity in the resistivity measurement in the free space YBCO, thus validating the optical technique as a mean to track the superconducting condensate.

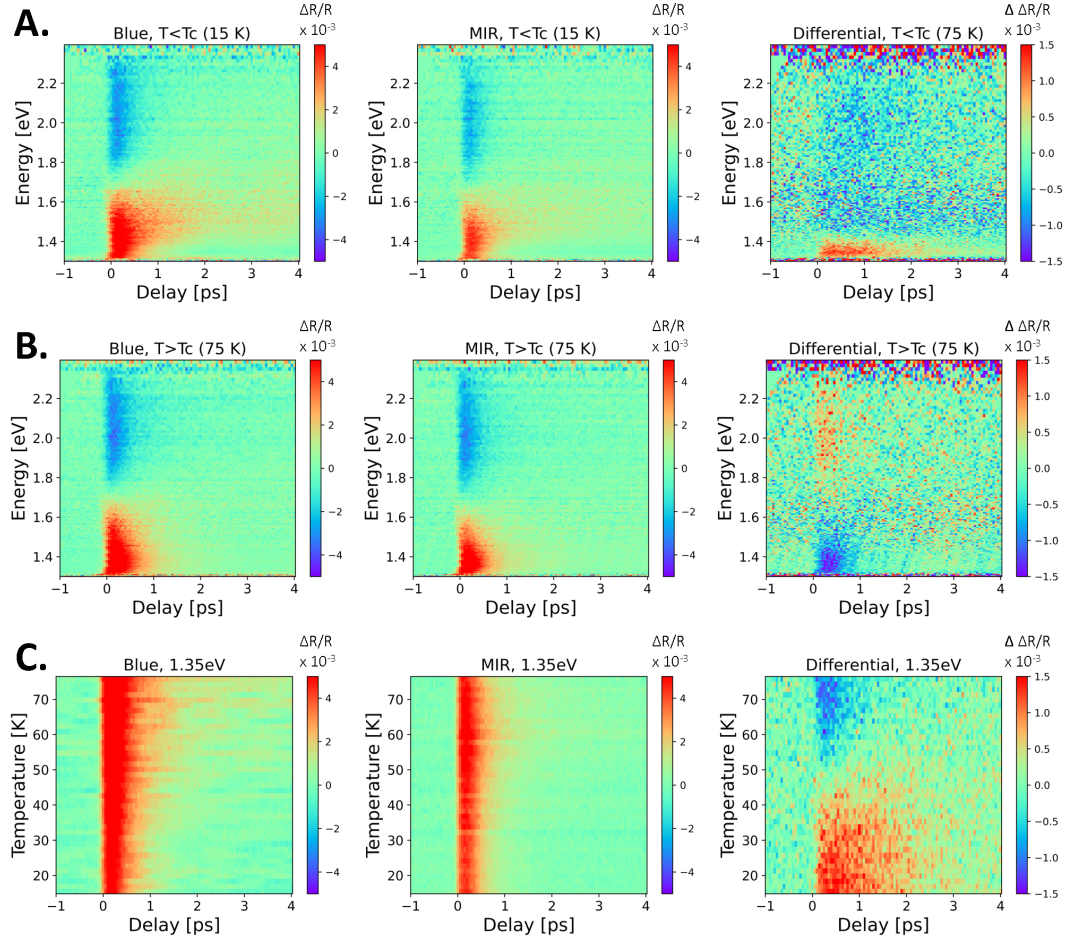


**Figure 7.6: Optical measurements by three-pulse scheme performed on free space YBCO (Sample B).** **A.** Time-resolved maps obtained below the critical temperature ( $T = 15$  K) on Sample B. In the left plot the spectrally resolved reflectivity induced by the single action of the blue pump ( $\frac{\Delta R_P}{R_P}$ ), while in the middle plot the one induced by the action of the push MIR pulse ( $\frac{\Delta R_P}{R_P}$ ). On the right, the spectrally resolved non-linear signal due to the combined pump-push action at  $T < T_c$  at the overlap ( $\Delta t = 0$ ). **B.** Same plots presented in A. above the critical temperature ( $T = 75$  K), marking the change in the non-linear reflectivity (right plot). **C.** Thermal evolution of the 1.35 eV component of the probe obtained exciting the sample with only the pump or push pulses (left and middle maps) and exciting it with the combined pump-push action (right map). The differential non-linear signal  $\frac{\Delta \Delta R}{R}$  marks the superconducting phase transition.

Figures 7.6A, B report the broadband time resolved maps obtained from the three-pulse experiments on free space YBCO (Sample B) above and below the critical temperature estimated from the transport measurements (Figure 7.5B).

Each map represents the transient reflectivity of the broadband probe as a consequence of the single action of blue pump (left map) and of the MIR push (middle

map). The broadband non-linear reflectivity, resulting from the simultaneous action of the pump and push pulses is presented in the right plots of Figures 7.6A, B for the sample above and below  $T_c$ , respectively. We note that the optical features associated to the superconducting condensate are not visible in the transient response due to the photo-excitation of the single pump and push pulses (left and middle plots of Figures 7.6A, B). Conversely, a strong difference above and below  $T_c$  emerges by looking at the non-linear photo-excitation of the superconducting condensate (right plots of Figures 7.6A, B).

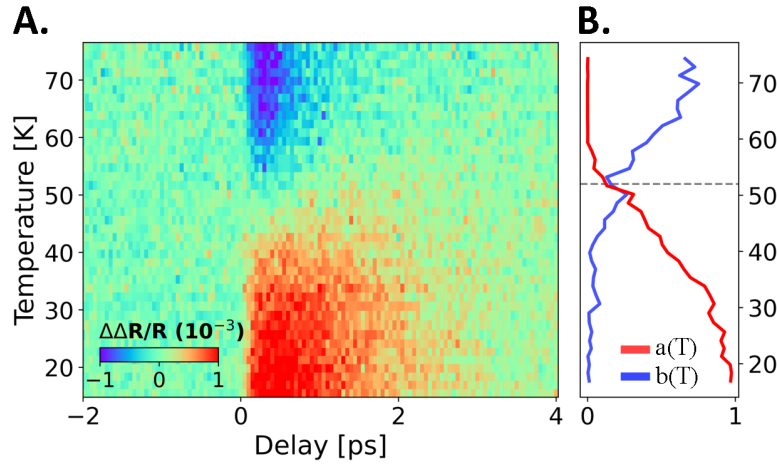


**Figure 7.7: Temperature dependence of the non-linear optical signal for YBCO in free space (Sample B).** **A.** Time and temperature dependent non-linear reflectivity at  $h\nu = 1.35$  eV measured in free space YBCO (Sample B). **B.** Temperature dependence of the fit parameters for the two-dimensional map in A. The parameter  $a(t)$  weights the superconducting contribution to the non-linear signal, while  $b(t)$  the high-temperature one. The crossing temperature has been exploited as a marker of the critical temperature (grey dashed line).

In order to determine the onset of the superconducting phase in the YBCO-based samples we therefore chose a photon energy within the broadband probe for which we expect the non-linear reflectivity to significantly change ( $h\nu = 1.35$  eV) and track its temperature dependence. On the basis of the transport measurement in Figure 7.5B, we focused our investigation in the temperature range from 15 to 75 K. We stress that also the transient reflectivity of this single component does not significantly change in the superconducting phase when the system is excited independently by the pump and the push pulses. Conversely a strong modification of its transient non-linear reflectivity  $\frac{\Delta\Delta R}{R}$  is observed upon entering the superconducting phase (Figure 7.6C, right map).

The reflectivity map of the non-linear 1.35 eV signal  $\frac{\Delta\Delta R}{R}$  measured in the free space YBCO (Sample B) is shown in Figure 7.7A as a function of the sample temperature and of the delay between the simultaneous photo-excitation of the pump and the push, and the arrival of the broadband probe. The differential signal undergoes a clear change in sign from positive to negative when the temperature is increased.

In order to give a qualitative estimate of the crossover temperature we fitted the time-dependent differential signal at a defined temperature  $T$  ( $d(T)$ ) as a linear combination of the lowest and highest temperature pump-probe traces,  $d_{low} = d(T = 15$  K), and  $d_{high} = d(T = 75$  K), respectively, according to the equation:

$$d(T) = a(T)d_{\text{low}} + b(T)d_{\text{high}}. \quad (7.2)$$

The temperature dependence of the fit parameters  $a(T)$  and  $b(T)$  is shown in Figure 7.7B for the free space YBCO sample (Sample B). According to Equation 7.2, we identify the crossing between the two curves as an indication of the superconducting transition, which occurs at  $T_c = 52$  K.

We stress that the observed discontinuity of the temperature-dependent differential signal does not depend on the choice of the photon energy of the probe. Moreover, the robustness of the fitting procedure is validated by the fact that the estimated crossover temperature occurs always at  $T_c = 52$  K for all the probe's spectral components (see the characterizations presented in Section 7.4). We note that the optically-estimated critical temperature in Sample B is lower than the one measured through transport measurements ( $T_c = 58$  K). This discrepancy is explained by considering the local heating of the sample due to the combined pump and the push photo-excitation. This statement is supported by similar measurements reported in Section 7.4, which show that the estimated crossover temperature can be further lowered by increasing the pumping fluences.

### 7.3.2 EFFECT OF THE CAVITY OF THE SUPERCONDUCTING OPTICAL RESPONSE

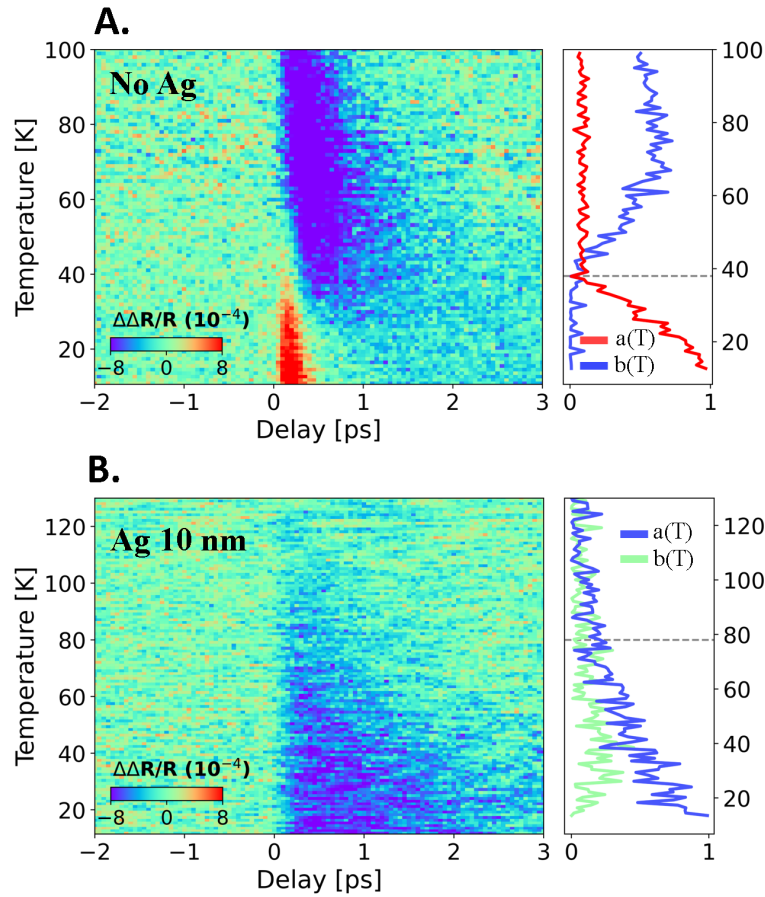
After having established the optical observable which maps the onset of superconductivity in the YBCO-based sample, we present in this section the effect of the presence of the cavity on the superconducting optical response. We conduct this comparative study on Sample A (Figure 7.5), by comparing the optical response of the uncapped portion ("No Ag") with the sample's portions terminated with the Ag layer. In this way a direct comparison between the free space and the cavity-confined response can be conducted and avoid artifacts due to a different deposition process of the underlying YBCO film.

Figure 7.8 presents the differential signal  $\frac{\Delta\Delta R}{R}$  measured in the uncapped YBCO heterostructure ("No Ag") and in the YBCO film enclosed within the cavity with the 10 nm-thick Ag top layer.

In the uncapped sample a non-linear optical response similar to the free space sample (Figure 7.7) is observed. Note that the lower critical temperature determined in the uncapped YBCO sample ( $T_c = 38$  K) with the respect to the free space configuration could be related to a different growing process of the two samples (A and B).

In spite of qualitative differences with respect to the signal measured in the uncapped YBCO heterostructure (Figure 7.8A) that could be ascribed to a modified equilibrium dielectric function in the cavity, the onset of a temperature-dependent non-linear signal is present also in the 10 nm Ag-terminated sample. By performing the same analysis described above (Figure 7.7B), we can identify the critical temperature to be 78 K in this cavity-confined sample, as can be seen by the evolution of the  $a(T)$  and  $b(T)$  parameters presented in Figure 7.8B. This result suggests that the non-linear response that we associate to the superconducting condensate in YBCO can possibly survive at higher temperatures in the cavity-confined material.

We plot in Figure 7.9 the results of the analysis of the three-pulse optical measurements carried out on the uncapped YBCO sample and on the cavity-confined heterostructures, with the estimation of the critical temperature from the non-linear reflectivity. Note that, due to the higher reflectivity of the cavity with the 15 nm-thick Ag layer and to its low penetration depth, optical measurements were not suitable in this sample.



**Figure 7.8: Temperature dependence of the non-linear optical signal in the uncapped YBCO heterostructure and for the YBCO in the cavity confined heterostructure A.** Temperature evolution of the differential signal for the uncapped YBCO ("No Ag" portion of Sample A) and corresponding temperature dependence of the fitting parameters  $a(T)$  and  $b(T)$ . **B.** Non-linear signal measured in the cavity-confined structure ("10 nm Ag" portion of Sample A) as a function of the temperature and respective evolution of the fitting parameters  $a(T)$  and  $b(T)$ . The grey dashed lines in the right boxes mark the estimated critical temperatures. Differential signals in A. and B. have been both extracted, as for the free space sample (Sample B, Figure 7.7), at a probing wavelength  $h\nu = 1.35$  eV.

We highlight that also in the cavity heterostructure capped with 5 nm Ag the signal associated to the superconducting condensate could survive at higher temperatures. For the 5 nm Ag cavity structure we estimate indeed a critical temperature ( $T_c = 70$  K) similar to the 10 nm Ag configuration, and hence greater than the uncapped configuration (Figure 7.9).

Lastly, we note that also the recovery time of the photo-excited quasi-particles of the superconducting state can possibly be affected by the cavity environment. This effect can be seen by comparing the dynamics of the non-linear reflectivity  $\frac{\Delta\Delta R}{R}$  of the superconducting phase measured in the uncapped YBCO ("No Ag", Sample A) with the one measured in the cavity confined heterostructures. These measurements are presented in Figure 7.10, where the non-linear signals measured below  $T_c$  (20 K) in the different heterostructures are compared. We highlight that a longer lifetime of the non-linear signal, which can be associated to a longer lifetime of the photo-excited superconducting

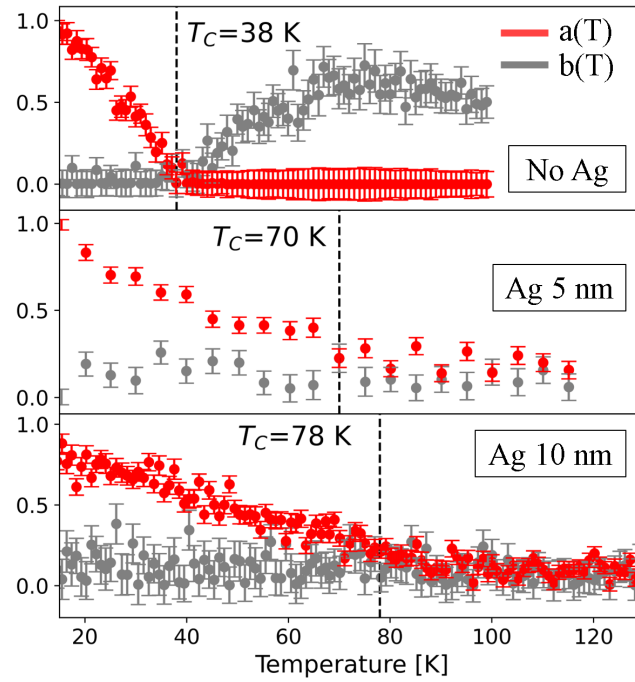


**Figure 7.9: Estimation of the critical temperatures in the uncapped and in the cavity-confined YBCO samples.** Temperature dependence of the fitting parameters  $a(T)$  and  $b(T)$  in the uncapped YBCO ("No Ag", Sample A) and for the cavity confined structures ("Ag 5 nm" and "Ag 10 nm", Sample A). The crossing temperature between  $a(T)$  and  $b(T)$  marks the estimated critical temperature.

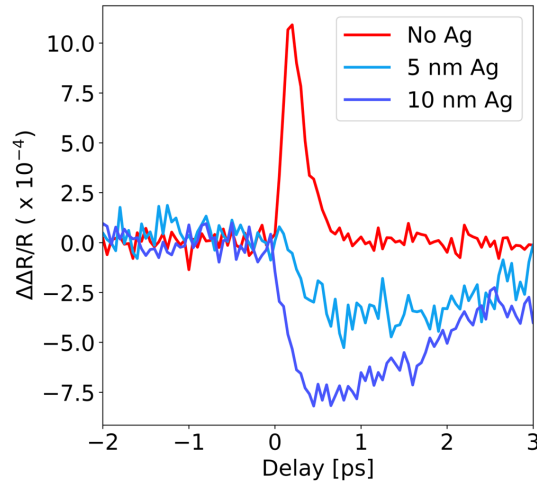


**Figure 7.10: Non-linear signals in the superconducting phase.** Non-linear reflectivity ( $h\nu = 1.35$  eV) measured in the superconducting phase ( $T = 20$  K) of the uncapped YBCO ("No Ag") and of the cavity-confined YBCO ("Ag 10 nm", and "Ag 5 nm"). A longer recovery dynamics of the excited quasi-particles is revealed in the cavity-confined systems.

condensate [108], is measured in the cavity-confined YBCO ("Ag 10 nm", "Ag 5 nm", Sample A).

## 7.4 METHODS

In the previous section we have highlighted the main effects that the cavity confinement may have of the superconducting-like optical response in YBCO. We notice indeed that the optical non-linear response associated to the superconducting condensate can possibly survive at higher temperatures in the cavity-confined material and that the recovery times of the excited quasi-particles may be also affected by the cavity environment.

This section is dedicated to a more extensive description of the optical set-up employed for the time-resolved three pulse experiment and to a detailed validation of the proposed analysis of the optical signals to track the superconducting dynamics.

### 7.4.1 EXPERIMENTAL SET-UP

Figure 7.11A shows a simplified sketch of the optical experiment designed to track the superconducting response of the YBCO heterostructures.

The samples are simultaneously photo-excited by a pump blue pulse ("P",  $h\nu = 3.1$  eV) and a push mid-infrared pulse ("p",  $h\nu = 75$  meV) (Figure 7.11A).

The pump is obtained by Second-Harmonic Generation (SHG) in a  $\beta$ -barium borate (BBO) crystal from the output of a Non-collinear Optical Parametric Amplifier (NOPA, Orpheus-N by Light Conversion), pumped by the Light Conversion Pharos System (1.2 eV, 400  $\mu$ J/pp, 50 kHz). The temporal duration of the pump is measured by Frequency-resolved Optical Gating before SHG to be 18 fs. Cross-correlation between the pump and the probe pulse is used to estimate the temporal duration of the pump at the sample, which is approximatively 50 fs.

The push pulse is generated by Difference Frequency Generation (DFG) in a GaSe crystal by mixing the near-infrared outputs of two OPAs (Orpheus TWIN by Light Conversion), also pumped by the Pharos Laser. The temporal duration of the push is  $\sim 150$  fs, as estimated by push-probe cross-correlation.

The samples are probed by a broadband white-light supercontinuum (1.3-2.2 eV) obtained by Self-Phase Modulation (SPM) in a sapphire crystal, which is pumped by a small fraction ( $\sim 1$   $\mu$ J/pp) of the Pharos output. After SPM, the probe is collimated and the residual component of the generating 1.2 eV-light is filtered out by a short-pass filter (edge at 950 nm). A small portion of the probe beam is routed around the sample and used as a reference. The reference and reflected probe beams are collected by a pair of linear arrays of silicon photodiodes (NMOS, Hamamatsu). The readout is digitalized by a custom-made ADC which allows pulse-by-pulse acquisition up to 50 kHz.

The polarizations of the pump and the push are kept parallel, whereas the probe is cross-polarized. The samples are glued on a copper substrate and mounted in a closed-cycle He-cryostat (by Advanced Research Systems).

Two optical choppers are placed along the optical paths of the pump and the push beams, and made running synchronously at 40 and 20 Hz, respectively. By referencing the blockage of the pump and the push with two photodiodes, we can sort the reflected broadband probe pulses into the following groups:

- $R_{pp}(h\nu, t_{WL}, T)$ : referenced-reflectivity of the sample photo-excited by both the pump and the push.
- $R_p(h\nu, t_{WL}, T)$ : referenced-reflectivity of the sample photo-excited just by the pump.

- $R_p(h\nu, t_{WL}, T)$ : referenced-reflectivity of the sample photo-excited just by the push.
- $R_u(h\nu, t_{WL}, T)$ : referenced-reflectivity of the sample at the equilibrium.

Here  $h\nu$  is the probe energy,  $t_{WL}$  is the temporal delay between the synchronous pump-push photo-excitation and the probe, and  $T$  is the sample's temperature.

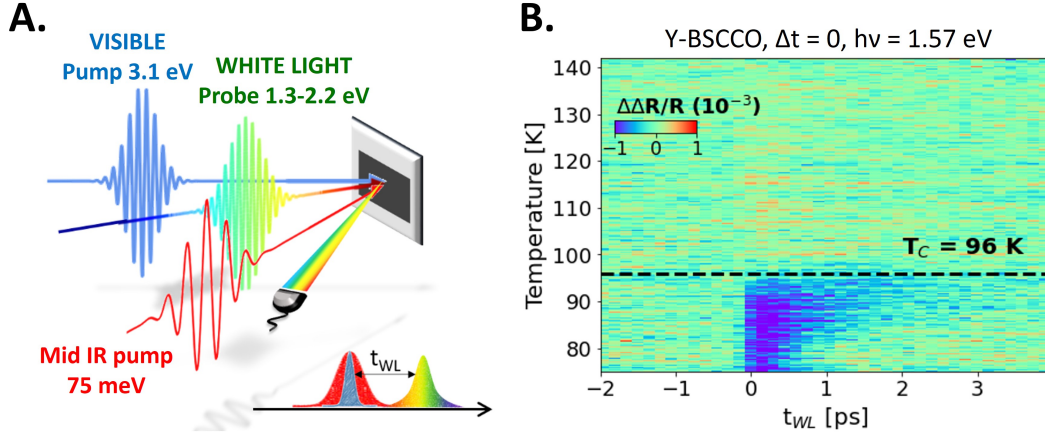


**Figure 7.11: Experimental configuration employed for the time-resolved studies.** **A.** Sketch of the three pulse experiments. The sample is photo-excited by the simultaneous interaction with a blue pump (3.1 eV) and a mid-infrared push (75 meV) pulse. The transient change in reflectivity is measured by a white-light supercontinuum ( $h\nu = 1.3\text{-}2.2$  eV) in a wide temperature range. **B.** Temperature dependence of the differential reflectivity measured on optimally-doped Y-BSCCO [237]. A photon energy  $h\nu = 1.57$  eV has been selected within the broadband probe.

The differential non-linear signal discussed in Section 7.3 has been calculated as:

$$\frac{\Delta\Delta R}{R}(h\nu, t_{WL}, T) = \frac{R_{pp} - R_u}{R_u} - \frac{R_p - R_u}{R_u} - \frac{R_p - R_u}{R_u}, \quad (7.3)$$

where, for the sake of clarity, we have omitted the dependence from  $h\nu, t_{WL}, T$  on the right side of the equation.

To test the suitability of the method to track the superconducting transition in copper oxide compounds, we measured the differential non-linear signal  $\frac{\Delta\Delta R}{R}$  in an optimally-doped Y-BSCCO single-crystal. The sample was grown according to the procedure described in [238] and the superconducting transition was studied by susceptibility measurements ( $T_c = 96$  K). We show in Figure 7.11B the differential reflectivity as function of the temporal delay and the sample temperature upon simultaneous ( $\Delta t = 0$ ) photo-excitation by a pump (1.44 eV) and a push (75 meV) pulse. We plot here the transient response at  $h\nu = 1.57$  eV, but the choice of the spectral component within the probe bandwidth does not affect the result. The superconducting phase is clearly characterized by the presence of a negative differential signal which undergoes an abrupt change upon entering the pseudogap phase. This evidence further validates the choice of the non-linear reflectivity as a probe to track the superconducting onset in the studied heterostructures (Section 7.3).

### 7.4.2 DETAILED ANALYSIS OF THE OPTICAL MEASUREMENTS

As explained in the Section 7.3, we estimated the transition temperature in the heterostructures by performing a linear fit of the time and temperature dependent differential reflectivity, as:

$$d(T) = a(T)d_{\text{low}} + b(T)d_{\text{high}}, \quad (7.4)$$

where  $d(t)$  is the time-dependent signal at temperature  $T$  (one row of the colour map in Figure 7.11B),  $d_{\text{low}}$  and  $d_{\text{high}}$  are the time dependent signals measured at the lowest (15 K) and highest (75 K) temperature, respectively. In this way, the temperature-dependent coefficients  $a(T)$  and  $b(T)$  effectively weight the contributions of the superconducting and the high-temperature response at a given temperature  $T$ . Despite the simplicity of the approach, this procedure qualitatively reproduces the data and captures the onset of the superconducting phase (Figure 7.12).

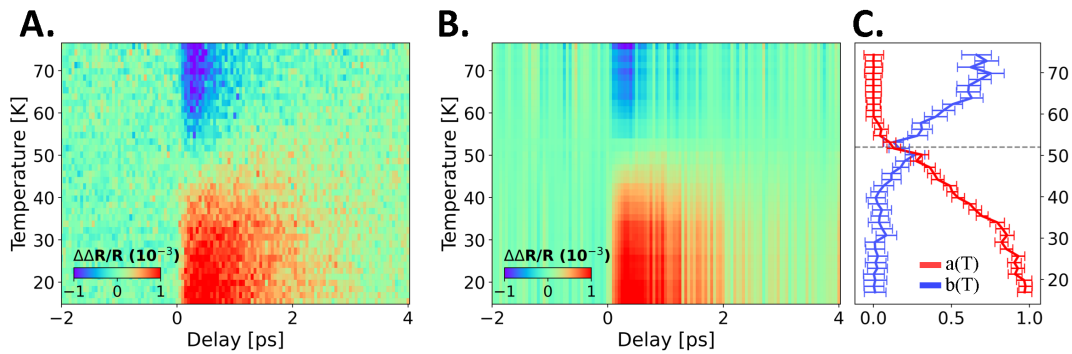


**Figure 7.12: Fitting procedure of the non-linear optical signal.** **A.** Differential reflectivity measured on the YBCO-terminated heterostructure (Sample B) at  $h\nu = 1.35$  eV. **B.** Corresponding fit, according to Equation 7.2. **C.** Temperature-dependence of the fit coefficients  $a(T)$  and  $b(T)$ , whose crossing marks the critical temperature.

We stress that the discontinuity in the temperature-dependent differential signal, which marks the superconducting transition, does not depend on the choice of the spectral component within the white-light broad bandwidth. Figure 7.13 shows the same analysis performed in Figure 7.12C for different probe photon energies. The crossing between the two curves, that is associated to the onset of superconductivity, occurs always at the same critical temperature for probe photon energies ranging from 1.35 eV to 2.2 eV. This proves that the discontinuity in the temperature-dependent differential response is a ubiquitous feature within the visible spectral range and can be considered as a robust indicator of the superconducting transition.

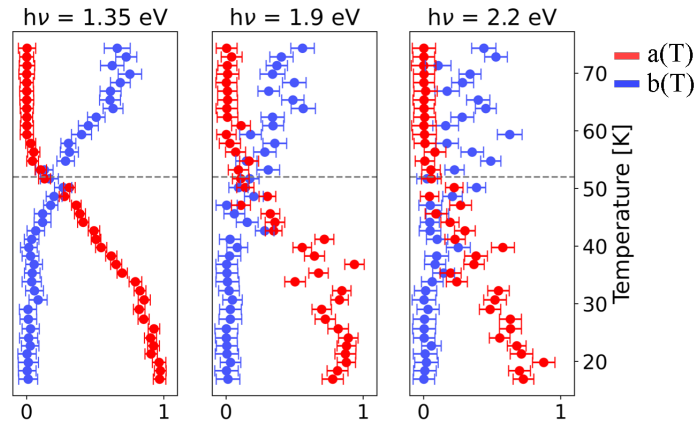


**Figure 7.13: Fitting procedure of the non-linear signal as a function of the wavelength within the white-light probe.** Temperature-dependence of the fit coefficients  $a(T)$  and  $b(T)$ , which weight the superconducting and the high-temperature contributions (respectively) to the optical differential response, in the YBCO-terminated heterostructure (Sample B) at different photon energies within the bandwidth of the white-light probe.

### 7.4.3 FLUENCE-DEPENDENCE OF THE NON-LINEAR SIGNAL

As discussed in Section 7.3, the critical temperature optically estimated in the YBCO-terminated heterostructure (Figure 7.7,  $T_c = 52$  K) is slightly lower than the one revealed through transport measurements (Figure 7.5B). We argue that this discrepancy could be due to the local heating of the sample as an effect of the double photo-excitation.

To check the validity of this claim, we have performed a measurement under similar experimental conditions as the one presented in Figure 7.7 and shown in Figure 7.14A for direct comparison, but with increased fluence of both the pump and the push photo-excitation (Figure 7.14B).

By following the same fitting procedure, it is clear that the crossing between the  $a(T)$  and  $b(T)$  curves is shifted to lower temperatures ( $T_c = 47$  K). This indicates that we operate in a regime in which the non-linear photo-excitation by the pump and the push is not only responsible for a dynamic perturbation of the superconducting condensate, but eventually leads to its slightly quench, resulting in an effective decreased of the superconducting critical temperature.

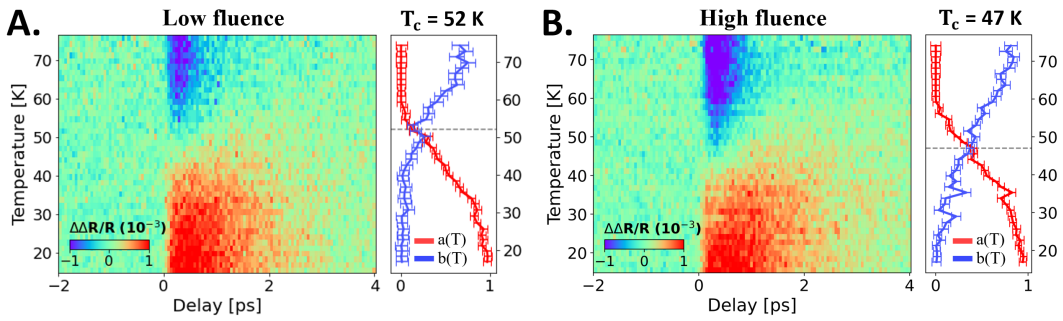


**Figure 7.14:** Comparison between the differential signals measured on the YBCO-terminated heterostructure (Sample B) at low and high fluence excitation. **A.** The pump fluence is set to  $0.15 \text{ mJ/cm}^2$  and the push to  $0.06 \text{ mJ/cm}^2$ . **B.** Both the pump and the push fluences are raised to  $0.18 \text{ mJ/cm}^2$ . On the right side of each color-coded map, the outcome of the fitting procedure is plotted, together with the indication of the estimated critical temperature.

## 7.5 CONCLUSIONS

In these chapter we have explored the possibility of coupling the charge transfer transition in underdoped YBCO to an optical cavity and studied how the cavity environment may affect the superconducting response. Our preliminary measurements, based on the three-pulse pump-probe technique, suggest that the non-linear optical response associated to the superconducting condensate, which is visible up to  $\sim 35 \text{ K}$  in the uncapped material, may survive up to  $\sim 70 \text{ K}$  in the cavity-confined heterostructures. This evidence is associated with a change of the recovery time of the photo-excited quasiparticles in the superconducting phase, which appears longer in the cavity-confined systems.

We stress that the evidences currently in hand cannot be considered conclusive to claim a possible cavity-induced modification of the superconducting transition temperature and further comparative magnetic techniques, like SQUID magnetometry, are needed. SQUID-magnetometry is indeed a well-established technique to characterize the Meissner effect in superconductors.

As a follow up, we present our preliminary SQUID measurements performed at the *IFW* Laboratories in Dresden. We performed measurements cooling down to  $4 \text{ K}$  the heterostructures at different intensities of the magnetic field ( $H_{\text{ext}} = 5, 10, 20, 100, 1000 \text{ Oe}$ ), oriented along both the in-plane and out-of-plane directions of the superconducting Cu-O planes. A determination of the critical temperature can be obtained by recording both the zero-field-cooled (ZFC) and field-cooled-warming (FCW) magnetization curves of each sample. We summarize in Figure 7.15 the preliminary results of the SQUID measurements on all the samples examined at  $H_{\text{ext}} = 20 \text{ Oe}$  parallel to the Cu-O plane.

The Meissner effect is clearly detectable in the bare YBCO-terminated heterostructure (Sample B) and occurs at  $T_c \sim 59 \text{ K}$ . This result agrees with the transport measurement (Figure 7.5B) and the optical measurements (Figure 7.7) and proves the suitability of the SQUID technique for studying the superconducting transition in the heterostructures. However, when additional layers are deposited on the YBCO film, the interpretation of the SQUID measurements becomes more challenging. Due to the small thickness of the YBCO film ( $100 \text{ nm}$ ), the measured magnetic moments are of the order of  $10^{-9} \text{ emu}$ ; moreover, spurious magnetic contributions from the  $\text{CeO}_2$  and  $\text{LaNiO}_3$  layers lead to an artificial splitting of the ZFC and FCW curves at high temperatures, which

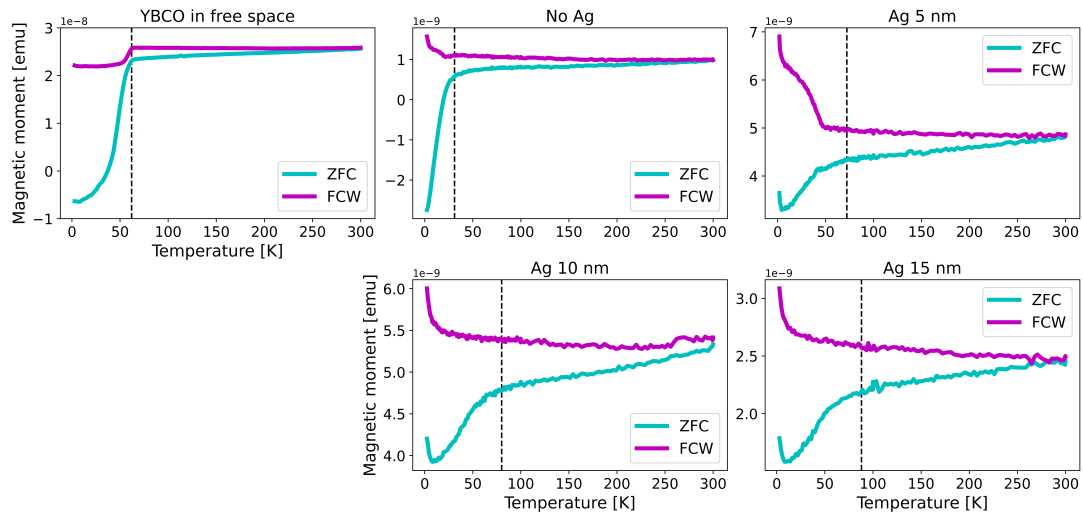


**Figure 7.15: SQUID in-plane measurements in the cavity YBCO-based heterostructures.** Temperature-dependent magnetization in the zero-field-cooled (ZFC) and 20 Oe field-cooled-warming (FCW) configurations for the YBCO in free space (Sample B) and for the cavity heterostructures (Sample A).

hinders the isolation of the superconducting contribution. For these reasons, further complementary techniques, like microwave absorption (MWA), will be needed to isolate the superconducting response in the cavity-confined heterostructures.

These preliminary results will serve therefore as background for future studies where the dependence of the superconducting response within the cavity will be explored also as a function of the YBCO thickness.

## CONCLUSIONS

---

The hybridization between light and matter in the weak and strong coupling regime, which can be obtained by placing materials into optical cavities resonant to phonons or electronic excitations, can determine the onset of macroscopic functionalities which are proper of the "light-matter hybrid" and are different from those of its constituents. The light-matter cavity hybrids can be considered as highly delocalized states where long range interactions in the material can be triggered by the common interaction of all the material's emitters with a single extended cavity mode. For this reason, exploring the weak and strong limit of light-matter interaction within optical cavities is emerging in the last years as a promising tool to control collective properties in quantum materials [11].

In present doctoral thesis we have focused on the experimental possibility of engineering the vacuum electromagnetic field by mean of terahertz and sub-terahertz to control collective properties in correlated materials. To reach this aim, we have developed a unique set-up suitable to study the strong and weak coupling regimes between a tunable optical cavity mode in cryogenic environment and low energy excitations, such as phonons or charge fluctuations. The uniqueness of the built set-up lies in its capability of tuning the cavity resonance at cryogenic temperatures, thus enabling to target different low energy collective modes and study how their coupling with the cavity field may affect the material's macroscopic properties.

We firstly studied the vibrational strong coupling regime in  $\text{CuGeO}_3$  at low temperatures.  $\text{CuGeO}_3$  is a dielectric material exhibiting a strong optical-active phonon within the THz range, and hence an ideal benchmark wherein to test the set-up. The strong coupling of the vibrational excitation led to the formation of phonon-polariton modes which we experimentally observed in the time domain as a normal mode beating and mapped their frequency-dependent avoided crossing features. Moreover, we varied the cavity temperature and proved that the line changes of the bare  $\text{CuGeO}_3$  phonon are mapped in a thermal modification of the linewidth and frequency of the vibro-polariton lines. The thermal modification of the optical phonon line led to an enhanced Rabi splitting at high temperatures, qualitatively consistent with a decrease of the bare phonon lifetime.

Afterwards, we investigated the metal-to-insulator transition in the charge density wave (CDW) material  $1\text{T-TaS}_2$  embedded within THz and sub-THz cavities. We revealed that, while long wavelength cavities favour the metallic phase, the coupling with cavities at higher frequencies results in an effective stabilization of the dielectric CDW phase. Overall, for the employed experimental setting, the effective critical temperature associated to the phase transition could be tune by more than 70 K, overcoming the free space hysteresis and enabling a reversible control of the metal-to-insulator transition. Importantly, we proved the control of the phase transition to be sensitive to the alignment of the THz cavity and hence possibly related to the peculiar cavity electro-dynamics. We rationalized our experimental evidences in a scenario in which the cavity

field is preferentially coupled to one of the two phases of  $1T\text{-TaS}_2$  and can be used to coherently modify the sample's temperature with a Purcell-like mechanism.

We then examined the effect of the coupling of  $1T\text{-TaS}_2$  phases with higher energy cavities (above  $\sim 400$  GHz). We revealed that when the cavity is tuned below the phonon modes of the commensurate CDW phase, and hence in resonance with the continuum Drude, its quality factor is sensitive to the material's phase. Indeed, we measured a lifetime of the cavity photons which decreases going from the insulating to the metallic state. We rationalized this evidence in a framework in which the free charges, responsible of the Drude-like behaviour, couple to the cavity mode and modify its lifetime.

When the cavity is tuned resonantly to the IR-active vibrational modes of the insulating phase we revealed a multiple polariton mixing. The estimated components of the polaritonic wave functions showed that the measured polaritons of the CDW phase have character from all the vibrational resonances as a consequence of the photon-mediated hybridization. In particular, we detected two weakly dispersive middle polariton states resulting from the cavity-mediated mixing of two non-degenerate phonons. Intriguingly, we detected a closing of the Rabi splitting between the hybridized phonons across the metal-to-insulator transition due to the onset of metallicity, reaching the weak-coupling limit near the critical temperature.

Finally, motivated by the strong connection found between the onset of superconductivity in cuprates and the charge transfer (CT) transition, we explored the possibility of coupling the CT excitation in underdoped YBCO to an optical cavity and see how strong electronic coupling may affect the pairing mechanism. Our very preliminary studies, based on the three-pulse pump-probe technique, showed that the optical features associated to the superconducting condensate are modified by the cavity environment and may possibly survive at higher temperatures in the cavity-confined structures.

In conclusion, the presented experiments show how cavity electrodynamics can play a role in the intricate equilibrium physics of different quantum materials, potentially providing a new tool to engineer their cooperative properties.

We note that for the Fabry-Pérot cavities employed in the present thesis the energy and momentum conservation limits the coupling between the cavity modes and collective dispersive excitations to the zone center ( $k = 0$ ). As a future perspective, we will propose to overcome this limitation by introducing on the sample surface periodic metallic nanostructures. In this way the combined action of the tunable cavity mirrors and the nanostructured sample surface will enable the coupling of the cavity mode to specific excitations at arbitrary momentum [239].

# BIBLIOGRAPHY

---

- [1] Alberto de la Torre, Dante M. Kennes, Martin Claassen, Simon Gerber, James W. McIver, and Michael A. Sentef. "Colloquium: Nonthermal pathways to ultrafast control in quantum materials." In: *Rev. Mod. Phys.* 93 (4 2021), p. 041002.
- [2] Ankit S. Disa, Tobia F. Nova, and Andrea Cavalleri. "Engineering crystal structures with light." In: *Nature Physics* 17 (2021), pp. 1087–1092.
- [3] D. Fausti, R. I. Tobey, N. Dean, S. Kaiser, A. Dienst, M. C. Hoffmann, S. Pyon, T. Takayama, H. Takagi, and A. Cavalleri. "Light-Induced Superconductivity in a Stripe-Ordered Cuprate." In: *Science* 331.6014 (2011), pp. 189–191.
- [4] Matteo Mitrano et al. "Possible light-induced superconductivity in  $K_3C_{60}$  at high temperature." In: *Nature* 530 (2016), pp. 461–464.
- [5] L. Stojchevska, I. Vaskivskyi, T. Mertelj, P. Kusar, D. Svetin, S. Brazovskii, and D. Mihailovic. "Ultrafast Switching to a Stable Hidden Quantum State in an Electronic Crystal." In: *Science* 344.6180 (2014), pp. 177–180.
- [6] Matteo Rini, Ra'anan I. Tobey, Nicky Dean, Jiro Itatani, Yasuhide Tomioka, Yoshinori Tokura, Robert W. Schoenlein, and Andrea Cavalleri. "Control of the electronic phase of a manganite by mode-selective vibrational excitation." In: *Nature* 449 (2007), pp. 72–74.
- [7] F. Giusti, A. Marciniak, F. Randi, G. Sparapassi, F. Boschini, H. Eisaki, M. Greven, A. Damascelli, A. Avella, and D. Fausti. "Signatures of Enhanced Superconducting Phase Coherence in Optimally Doped  $Bi_2Sr_2Y_{0.08}Ca_{0.92}Cu_2O_{8+\delta}$  Driven by Midinfrared Pulse Excitations." In: *Phys. Rev. Lett.* 122 (6 2019), p. 067002.
- [8] M. Buzzi et al. "Phase Diagram for Light-Induced Superconductivity in  $\kappa-(ET)_2-X$ ." In: *Phys. Rev. Lett.* 127 (19 2021), p. 197002.
- [9] James W. McIver, B. Schulte, Falk-Ulrich Stein, Takanori Matsuyama, Gregor Jotzu, Guido Meier, and Andrea Cavalleri. "Light-induced anomalous Hall effect in graphene." In: *Nature physics* 16 (2018), pp. 38–41.
- [10] Xian Li, Tian Qiu, Jiahao Zhang, Edoardo Baldini, Jian Lu, Andrew M. Rappe, and Keith A. Nelson. "Terahertz field-induced ferroelectricity in quantum paraelectric  $SrTiO_3$ ." In: *Science* 364 (2018), pp. 1079–1082.
- [11] F. Schlawin, D. M. Kennes, and M. A. Sentef. "Cavity quantum materials." In: *Applied Physics Reviews* 9.1 (Feb. 2022).
- [12] E. M. Purcell, H. C. Torrey, and R. V. Pound. "Resonance Absorption by Nuclear Magnetic Moments in a Solid." In: *Phys. Rev.* 69 (1-2 1946), pp. 37–38.
- [13] P. Goy, J. M. Raimond, M. Gross, and S. Haroche. "Observation of Cavity-Enhanced Single-Atom Spontaneous Emission." In: *Phys. Rev. Lett.* 50 (24 1983), pp. 1903–1906.
- [14] Randall G. Hulet, Eric S. Hilfer, and Daniel Kleppner. "Inhibited Spontaneous Emission by a Rydberg Atom." In: *Phys. Rev. Lett.* 55 (20 1985), pp. 2137–2140.
- [15] M. M. Glazov, E. L. Ivchenko, Alexander N. Poddubny, and G. Khitrova. "Purcell factor in small metallic cavities." In: *Physics of the Solid State* 53 (2011), pp. 1753–1760.

- [16] Dongxing Zhao, Rui E. F. Silva, Clàudia Climent, Johannes Feist, Antonio I. Fernández-Domínguez, and Francisco J. García-Vidal. "Impact of Vibrational Modes in the Plasmonic Purcell Effect of Organic Molecules." In: *ACS Photonics* 7.12 (2020), pp. 3369–3375.
- [17] Anton Frisk Kockum, Adam Miranowicz, Simone De Liberato, Salvatore Savasta, and Franco Nori. "Ultrastrong coupling between light and matter." In: *Nature Reviews Physics* 1 (2018), pp. 19–40.
- [18] Thomas W. Ebbesen. "Hybrid Light–Matter States in a Molecular and Material Science Perspective." In: *Accounts of Chemical Research* 49.11 (2016). PMID: 27779846, pp. 2403–2412.
- [19] M. G. Raizen, R. J. Thompson, R. J. Brecha, H. J. Kimble, and H. J. Carmichael. "Normal-mode splitting and linewidth averaging for two-state atoms in an optical cavity." In: *Phys. Rev. Lett.* 63 (3 1989), pp. 240–243.
- [20] R. J. Thompson, G. Rempe, and H. J. Kimble. "Observation of normal-mode splitting for an atom in an optical cavity." In: *Phys. Rev. Lett.* 68 (8 1992), pp. 1132–1135.
- [21] D. I. Schuster, Lev S. Bishop, I. L. Chuang, D. DeMille, and R. J. Schoelkopf. "Cavity QED in a molecular ion trap." In: *Phys. Rev. A* 83 (1 2011), p. 012311.
- [22] C. Weisbuch, M. Nishioka, A. Ishikawa, and Y. Arakawa. "Observation of the coupled exciton-photon mode splitting in a semiconductor quantum microcavity." In: *Phys. Rev. Lett.* 69 (23 1992), pp. 3314–3317.
- [23] G. Khitrova, Hyatt M. Gibbs, M. Kira, Stephan W. Koch, and Axel Scherer. "Vacuum Rabi splitting in semiconductors." In: *Nature Physics* 2 (2006), pp. 81–90.
- [24] V. M. Agranovich, M. Litinskaia, and D. G. Lidzey. "Cavity polaritons in microcavities containing disordered organic semiconductors." In: *Phys. Rev. B* 67 (8 2003), p. 085311.
- [25] David J. Shelton, Igal Brener, James C. Ginn, Michael B. Sinclair, David W. Peters, Kevin R. Coffey, and Glenn D. Boreman. "Strong coupling between nanoscale metamaterials and phonons." In: *Nano letters* 11 5 (2011), pp. 2104–8.
- [26] Xin Jin et al. "Reshaping the phonon energy landscape of nanocrystals inside a terahertz plasmonic nanocavity." In: *Nature Communications* 9 (2018).
- [27] Ran Damari, Omri Weinberg, Daniel Krotkov, Natalia Demina, Katherine Akulov, Adina Golombek, Tal Schwartz, and Sharly Fleischer. "Strong coupling of collective intermolecular vibrations in organic materials at terahertz frequencies." In: *Nature Communications* 10 (2019).
- [28] Isaac John Luxmoore, Choon How Gan, Peter Qiang Liu, Federico Valmorra, Penglei Li, Jérôme Faist, and Geoffrey R. Nash. "Strong Coupling in the Far-Infrared between Graphene Plasmons and the Surface Optical Phonons of Silicon Dioxide." In: *ACS Photonics* 1.11 (2014), pp. 1151–1155.
- [29] Robrecht M. A. Vergauwe, Jino George, Thibault Chervy, James A. Hutchison, Atef Shalabney, Vladimir Y. Torbeev, and Thomas W. Ebbesen. "Quantum Strong Coupling with Protein Vibrational Modes." In: *The Journal of Physical Chemistry Letters* 7.20 (2016), pp. 4159–4164.
- [30] Jino George, Atef Shalabney, James A. Hutchison, Cyriaque Genet, and Thomas W. Ebbesen. "Liquid-Phase Vibrational Strong Coupling." In: *The Journal of Physical Chemistry Letters* 6.6 (2015). PMID: 26262864, pp. 1027–1031.

- [31] Javier del Pino, Johannes Feist, and Francisco J. García-Vidal. "Quantum theory of collective strong coupling of molecular vibrations with a microcavity mode." In: *New Journal of Physics* 17 (2015).
- [32] Prasahnt Sivarajah, Andreas F. Steinbacher, Blake Dastrup, Jian Lu, Maolin Xiang, Wei Ren, Stanislav Kamba, Shixun Cao, and Keith A. Nelson. "THz-frequency magnon-phonon-polaritons in the collective strong-coupling regime." In: *Journal of Applied Physics* (2019).
- [33] Anoop Thomas et al. "Ground-State Chemical Reactivity under Vibrational Coupling to the Vacuum Electromagnetic Field." In: *Angewandte Chemie International Edition* 55.38 (2016), pp. 11462–11466.
- [34] Stéphane Kéna-Cohen and Joel Yuen-Zhou. "Polariton Chemistry: Action in the Dark." In: *ACS Central Science* 5.3 (2019), pp. 386–388.
- [35] James Andell Hutchison, Tal Schwartz, Cyriaque Genet, Éloïse Devaux, and Thomas W. Ebbesen. "Modifying chemical landscapes by coupling to vacuum fields." In: *Angewandte Chemie* 51 7 (2012), pp. 1592–6.
- [36] Stephen J. DeCamp, Gabriel S Redner, Aparna Baskaran, Michael F. Hagan, and Zvonimir Dogic. "Orientational order of motile defects in active nematics." In: *Nature materials* 14 11 (2015), pp. 1110–5.
- [37] Javier Galego, Francisco J. Garcia-Vidal, and Johannes Feist. "Cavity-Induced Modifications of Molecular Structure in the Strong-Coupling Regime." In: *Phys. Rev. X* 5 (4 2015), p. 041022.
- [38] Gian Paravicini-Bagliani et al. "Magneto-transport controlled by Landau polariton states." In: *Nature Physics* 15 (Feb. 2019).
- [39] Johannes Schachenmayer, Claudiu Genes, Edoardo Tignone, and Guido Pupillo. "Cavity-enhanced transport of excitons." In: *Physical review letters* 114 19 (2014), p. 196403.
- [40] David Hagenmüller, Johannes Schachenmayer, Stefan Schütz, Claudiu Genes, and Guido Pupillo. "Cavity-Enhanced Transport of Charge." In: *Physical review letters* 119 22 (2017), p. 223601.
- [41] Johannes Feist and Francisco J. Garcia-Vidal. "Extraordinary Exciton Conductance Induced by Strong Coupling." In: *Phys. Rev. Lett.* 114 (19 2015), p. 196402.
- [42] Francisco J. Garcia-Vidal, Cristiano Ciuti, and Thomas W. Ebbesen. "Manipulating matter by strong coupling to vacuum fields." In: *Science* 373.6551 (2021), eabd0336.
- [43] Frank Schlawin, Andrea Cavalleri, and Dieter Jaksch. "Cavity-Mediated Electron-Photon Superconductivity." In: *Phys. Rev. Lett.* 122 (13 2019), p. 133602.
- [44] Jonathan B. Curtis, Zachary M. Raines, Andrew A. Allocca, Mohammad Hafezi, and Victor M. Galitski. "Cavity Quantum Eliashberg Enhancement of Superconductivity." In: *Phys. Rev. Lett.* 122 (16 2019), p. 167002.
- [45] Andrew A. Allocca, Zachary M. Raines, Jonathan B. Curtis, and Victor M. Galitski. "Cavity superconductor-polaritons." In: *Phys. Rev. B* 99 (2 2019), p. 020504.
- [46] Y. Laplace, S. Fernandez-Pena, S. Gariglio, J. M. Triscone, and A. Cavalleri. "Proposed cavity Josephson plasmonics with complex-oxide heterostructures." In: *Phys. Rev. B* 93 (7 2016), p. 075152.

- [47] Hongmin Gao, Frank Schlawin, Michele Buzzi, Andrea Cavalleri, and Dieter Jaksch. "Photoinduced Electron Pairing in a Driven Cavity." In: *Phys. Rev. Lett.* 125 (5 2020), p. 053602.
- [48] M. A. Sentef, M. Ruggenthaler, and A. Rubio. "Cavity quantum-electrodynamical polaritonically enhanced electron-phonon coupling and its influence on superconductivity." In: *Science Advances* 4.11 (2018), eaau6969.
- [49] Jiajun Li and Martin Eckstein. "Manipulating Intertwined Orders in Solids with Quantum Light." In: *Phys. Rev. Lett.* 125 (21 2020), p. 217402.
- [50] Simone Latini, Enrico Ronca, Umberto de Giovannini, Hannes Hübener, and Ángel Rubio. "Cavity Control of Excitons in Two-Dimensional Materials." In: *Nano Letters* 19 (2018), pp. 3473–3479.
- [51] Yuto Ashida, Atac Imamoglu, Jérôme Faist, Dieter Jaksch, Andrea Cavalleri, and Eugene Demler. "Quantum Electrodynamical Control of Matter: Cavity-Enhanced Ferroelectric Phase Transition." In: *Phys. Rev. X* 10 (4 2020), p. 041027.
- [52] Simone Latini, Dongbin Shin, Shunsuke A. Sato, Christian Schäfer, Umberto de Giovannini, Hannes Hübener, and Ángel Rubio. "The ferroelectric photo ground state of SrTiO<sub>3</sub>: Cavity materials engineering." In: *Proceedings of the National Academy of Sciences of the United States of America* 118 (2021).
- [53] Katharina Lenk, Jiajun Li, Philipp Werner, and Martin Eckstein. "Dynamical mean-field study of a photon-mediated ferroelectric phase transition." In: *Phys. Rev. B* 106 (24 2022), p. 245124.
- [54] Jonathan B. Curtis, Marios H. Michael, and Eugene Demler. *Local Fluctuations in Cavity Control of Ferroelectricity*. 2023. arXiv: 2301.01884 [cond-mat.mes-hall].
- [55] Ö. O. Soykal and M. E. Flatté. "Strong Field Interactions between a Nanomagnet and a Photonic Cavity." In: *Phys. Rev. Lett.* 104 (7 2010), p. 077202.
- [56] Felice Appugliese, Josefine Enkner, Gian Lorenzo Paravicini-Bagliani, Mattias Beck, Christian Reichl, Werner Wegscheider, Giacomo Scalari, Cristiano Ciuti, and Jérôme Faist. "Breakdown of topological protection by cavity vacuum fields in the integer quantum Hall effect." In: *Science* 375.6584 (2022), pp. 1030–1034.
- [57] Anoop Thomas et al. "Exploring Superconductivity under Strong Coupling with the Vacuum Electromagnetic Field." In: *arXiv: Superconductivity* (2019).
- [58] Anoop Thomas, Éloïse Devaux, Kalaivanan Nagarajan, Guillaume Rogez, Marcus Seidel, Fanny Richard, Cyriaque Genet, Marc Drillon, and Thomas W. Ebbesen. "Large Enhancement of Ferromagnetism under a Collective Strong Coupling of YBCO Nanoparticles." In: *Nano Letters* 21 (2021), pp. 4365–4370.
- [59] Dario Ballarini and Simone De Liberato. "Polaritonics: from microcavities to sub-wavelength confinement." In: *Nanophotonics* 8.4 (2019), pp. 641–654.
- [60] Stanley Pau, Gunnar Björk, Joseph Jacobson, Hui Cao, and Yoshihisa Yamamoto. "Microcavity exciton-polariton splitting in the linear regime." In: *Phys. Rev. B* 51 (20 1995), pp. 14437–14447.
- [61] Courtney Delpo, Bryan Kudisch, Kyu Hyung Park, Saeed Uz Zaman Khan, Francesca Fassioli, Daniele Fausti, Barry P. Rand, and Gregory D. Scholes. "Polariton Transitions in Femtosecond Transient Absorption Studies of Ultrastrong Light-Molecule Coupling." In: *The Journal of Physical Chemistry Letters* 11 (2020), pp. 2667–2674.

- [62] Xinwei Li, Motoaki Bamba, Qi Zhang, Saeed Fallahi, Geoff Gardner, Weilu Gao, Minhan Lou, Katsumasa Yoshioka, M.J. Manfra, and Junichiro Kono. "Vacuum Bloch–Siegert shift in Landau polaritons with ultra-high cooperativity." In: *Nature Photonics* 12 (June 2018).
- [63] Qi Zhang, Minhan Lou, Xinwei Li, John Reno, Wei Pan, John Watson, M.J. Manfra, and Junichiro Kono. "Collective non-perturbative coupling of 2D electrons with high-quality-factor terahertz cavity photons." In: *Nature Physics* 12 (Aug. 2016).
- [64] G. Scalari et al. "Ultrastrong Coupling of the Cyclotron Transition of a 2D Electron Gas to a THz Metamaterial." In: *Science* 335.6074 (2012), pp. 1323–1326.
- [65] R. H. Dicke. "Coherence in Spontaneous Radiation Processes." In: *Phys. Rev.* 93 (1 1954), pp. 99–110.
- [66] Michael Tavis and Frederick W. Cummings. "Exact Solution for an N-Molecule-Radiation-Field Hamiltonian." In: *Phys. Rev.* 170 (2 1968), pp. 379–384.
- [67] Astghik Saharyan, Juan-Rafael Álvarez, Thomas H. Doherty, Axel Kuhn, and Stéphane Guérin. "Light-matter interaction in open cavities with dielectric stacks." In: *Applied Physics Letters* 118.15 (Apr. 2021).
- [68] Kerry J. Vahala. "Optical microcavities." In: *Nature* 424 (2003), pp. 839–846.
- [69] Alexey V. Kavokin, Jeremy J. Baumberg, Guillaume Malpuech, and Fabrice P. Laussy. "243 Weak-coupling microcavities." In: *Microcavities*. Oxford University Press, May 2017. ISBN: 9780198782995.
- [70] P. Forn-Díaz, L. Lamata, E. Rico, J. Kono, and E. Solano. "Ultrastrong coupling regimes of light-matter interaction." In: *Rev. Mod. Phys.* 91 (2 2019), p. 025005.
- [71] S. Haroche and J.M. Raimond. *Exploring the Quantum: Atoms, Cavities, and Photons*. Oxford Graduate Texts. OUP Oxford, 2013.
- [72] I. I. Rabi. "On the Process of Space Quantization." In: *Phys. Rev.* 49 (4 1936), pp. 324–328.
- [73] Shaul Mukamel. "Principles of Nonlinear Optical Spectroscopy." In: *Oxford University Press* 11 (1999).
- [74] Cristiano Ciuti, Gérald Bastard, and Iacopo Carusotto. "Quantum vacuum properties of the intersubband cavity polariton field." In: *Phys. Rev. B* 72 (11 2005), p. 115303.
- [75] Y. Todorov, A. M. Andrews, R. Colombelli, S. De Liberato, C. Ciuti, P. Klang, G. Strasser, and C. Sirtori. "Ultrastrong Light-Matter Coupling Regime with Polariton Dots." In: *Phys. Rev. Lett.* 105 (19 2010), p. 196402.
- [76] B Askenazi, A Vasanelli, A Delteil, Y Todorov, L C Andreani, G Beaudoin, I Sagnes, and C Sirtori. "Ultra-strong light-matter coupling for designer Reststrahlen band." In: *New Journal of Physics* 16.4 (2014), p. 043029.
- [77] Salvatore Gambino et al. "Exploring Light–Matter Interaction Phenomena under Ultrastrong Coupling Regime." In: *ACS Photonics* 1.10 (2014), pp. 1042–1048.
- [78] Carlos Gonzalez-Ballester, Johannes Feist, Eduardo Gonzalo Badía, Esteban Moreno, and Francisco J. Garcia-Vidal. "Uncoupled Dark States Can Inherit Polaritonic Properties." In: *Phys. Rev. Lett.* 117 (15 2016), p. 156402.
- [79] J. J. Hopfield. "Theory of the Contribution of Excitons to the Complex Dielectric Constant of Crystals." In: *Phys. Rev.* 112 (5 1958), pp. 1555–1567.

- [80] Tim Byrnes, Na Young Kim, and Yoshihisa Yamamoto. "Exciton–polariton condensates." In: *Nature Physics* 10 (2014), pp. 803–813.
- [81] Jacek Kasprzak et al. "Bose–Einstein condensation of exciton polaritons." In: *Nature* 443 (2006), pp. 409–414.
- [82] Michiel Wouters, Iacopo Carusotto, and Cristiano Ciuti. "Spatial and spectral shape of inhomogeneous nonequilibrium exciton-polariton condensates." In: *Phys. Rev. B* 77 (11 2008), p. 115340.
- [83] Andrew P. Schlaus, Michael S. Spencer, and X-Y. Zhu. "Light–Matter Interaction and Lasing in Lead Halide Perovskites." In: *Accounts of Chemical Research* 52.10 (2019). PMID: 31571486, pp. 2950–2959.
- [84] Hui Deng, Gregor Weihs, David W. Snoke, Jacqueline Bloch, and Yoshihisa Yamamoto. "Polariton lasing vs. photon lasing in a semiconductor microcavity." In: *Proceedings of the National Academy of Sciences of the United States of America* 100 (2003), pp. 15318–15323.
- [85] Tien-Chang Lu, Ying-Yu Lai, Yu-Pin Lan, Si-Wei Huang, Jun-Rong Chen, Yung-Chi Wu, Wen-Feng Hsieh, and Hui Deng. "Room temperature polariton lasing vs. photon lasing in a ZnO-based hybrid microcavity." In: *Opt. Express* 20.5 (2012), pp. 5530–5537.
- [86] Ying-Yu Lai, Yu Hsun Chou, Yu-Pin Lan, Tien-Chang Lu, Shing chung Wang, and Yoshihisa Yamamoto. "Crossover from polariton lasing to exciton lasing in a strongly coupled ZnO microcavity." In: *Scientific Reports* 6 (2016).
- [87] Maïke Halbhauer, J. Mornhinweg, Viola Zeller, Cristiano Ciuti, Dominique Bougeard, Rupert Huber, and Christoph Lange. "Non-adiabatic stripping of a cavity field from electrons in the deep-strong coupling regime." In: *Nature Photonics* (2020), pp. 1–5.
- [88] Jeremy J. Baumberg, Javier Aizpurua, Maiken H. Mikkelsen, and David R. Smith. "Extreme nanophotonics from ultrathin metallic gaps." In: *Nature Materials* 18 (2019), pp. 668–678.
- [89] Itai Epstein et al. "Far-field excitation of single graphene plasmon cavities with ultracompressed mode volumes." In: *Science* 368.6496 (2020), pp. 1219–1223.
- [90] Andrei Bylinkin et al. "Real-space observation of vibrational strong coupling between propagating phonon polaritons and organic molecules." In: *Nature Photonics* 15 (2020), pp. 197–202.
- [91] M. Born, E. Wolf, and A.B. Bhatia. *Principles of Optics: Electromagnetic Theory of Propagation, Interference and Diffraction of Light*. Cambridge University Press, 2000. ISBN: 9780521784498.
- [92] M. Claudia Tropicovsky, Adrian S. Sabau, Andrew R. Lupini, and Zhenyu Zhang. "Transfer-matrix formalism for the calculation of optical response in multilayer systems: from coherent to incoherent interference." In: *Opt. Express* 18.24 (2010), pp. 24715–24721.
- [93] Atef Shalabney and Ibrahim Abdulhalim. "Electromagnetic fields distribution in multilayer thin film structures and the origin of sensitivity enhancement in surface plasmon resonance sensors." In: *Sensors and Actuators A: Physical* 159.1 (2010), pp. 24–32. ISSN: 0924-4247.
- [94] J. M. Fink et al. "Quantum-To-Classical Transition in Cavity Quantum Electrodynamics." In: *Phys. Rev. Lett.* 105 (16 2010), p. 163601.

- [95] Jacek Kasprzak, Kanchana Sivalertporn, Ferdinand Albert, Schneider, Sven Höfling, M. Kamp, Alfred Forchel, Stephan Reitzenstein, E A Muljarov, and W. Langbein. "Coherence dynamics and quantum-to-classical crossover in an exciton-cavity system in the quantum strong coupling regime." In: *New Journal of Physics* 15 (2013).
- [96] Aleksandar D. Rakić, Aleksandra B. Djurić, Jovan M. Elazar, and M. L. Majewski. "Optical properties of metallic films for vertical-cavity optoelectronic devices." In: *Applied optics* 37 22 (1998), pp. 5271–83.
- [97] Jenő Sólyom. "Optical Properties of Solids." In: *Fundamentals of the Physics of Solids: Volume 2: Electronic Properties*. Ed. by Jenő Sólyom. Berlin, Heidelberg: Springer Berlin Heidelberg, 2009, pp. 411–447. ISBN: 978-3-540-85316-9.
- [98] Raphael F. Ribeiro, Adam D. Dunkelberger, Bo Xiang, Wei Xiong, Blake S. Simpkins, Jeffrey C. Owrutsky, and Joel Yuen-Zhou. "Theory for Nonlinear Spectroscopy of Vibrational Polaritons." In: *The Journal of Physical Chemistry Letters* 9.13 (2018), pp. 3766–3771.
- [99] C. W. Gardiner and M. J. Collett. "Input and output in damped quantum systems: Quantum stochastic differential equations and the master equation." In: *Phys. Rev. A* 31 (6 1985), pp. 3761–3774.
- [100] Cristiano Ciuti and Iacopo Carusotto. "Input-output theory of cavities in the ultrastrong coupling regime: The case of time-independent cavity parameters." In: *Phys. Rev. A* 74 (3 2006), p. 033811.
- [101] S. Portolan, O. Di Stefano, S. Savasta, F. Rossi, and R. Girlanda. "Nonequilibrium Langevin approach to quantum optics in semiconductor microcavities." In: *Phys. Rev. B* 77 (3 2008), p. 035433.
- [102] Hao Li, Andrei Piryatinski, Jonathan Jerke, Ajay Srimath Kandada, Carlos Silva, and Eric Bittner. "Probing dynamical symmetry breaking using quantum-entangled photons." In: *Quantum Science and Technology* 3 (July 2017).
- [103] M. G. Raymer and C. J. McKinstrie. "Quantum input-output theory for optical cavities with arbitrary coupling strength: Application to two-photon wavepacket shaping." In: *Phys. Rev. A* 88 (4 2013), p. 043819.
- [104] Abraham Nitzan. *Chemical Dynamics in Condensed Phases: Relaxation, Transfer and Reactions in Condensed Molecular Systems*. Oxford University Press, Apr. 2006.
- [105] Wonmi Ahn, Igor Vurgaftman, Adam D. Dunkelberger, Jeffrey C. Owrutsky, and Blake S. Simpkins. "Vibrational Strong Coupling Controlled by Spatial Distribution of Molecules within the Optical Cavity." In: *ACS Photonics* 5.1 (2018), pp. 158–166.
- [106] Arnab Bera, Satyabrata Bera, Sk Kalimuddin, Sirshendu Gayen, Mohan Kundu, Biswajit Das, and Mintu Mondal. "Review of recent progress on THz spectroscopy of quantum materials: superconductors, magnetic and topological materials." In: *The European Physical Journal Special Topics* 230 (July 2021).
- [107] Martin Dressel, Natalia Drichko, Boris P. Gorshunov, and Andrei Pimenov. "THz Spectroscopy of Superconductors." In: *IEEE Journal of Selected Topics in Quantum Electronics* 14 (2008), pp. 399–406.
- [108] Claudio Giannetti, Massimo Capone, Daniele Fausti, Michele Fabrizio, Fulvio Parmigiani, and Dragan Mihailovic. "Ultrafast optical spectroscopy of strongly correlated materials and high-temperature superconductors: a non-equilibrium approach." In: *Advances in Physics* 65 (2016), pp. 238–58.

- [109] Akinori Irizawa, Stefano Lupi, and Augusto Marcelli. "Terahertz as a Frontier Area for Science and Technology." In: *Condensed Matter* 6 (June 2021), p. 23.
- [110] James P. Long and Blake S. Simpkins. "Coherent Coupling between a Molecular Vibration and Fabry–Perot Optical Cavity to Give Hybridized States in the Strong Coupling Limit." In: *ACS Photonics* 2 (2015), pp. 130–136.
- [111] Jyoti Lather, Pooja Kapri Bhatt, Anoop Thomas, Thomas W. Ebbesen, and Jino George. "Cavity Catalysis by Cooperative Vibrational Strong Coupling of Reactant and Solvent Molecules†." In: *Angewandte Chemie (International Ed. in English)* 58 (2018), pp. 10635–10638.
- [112] Irene Dolado et al. "Remote near-field spectroscopy of vibrational strong coupling between organic molecules and phononic nanoresonators." In: *Nature Communications* 13 (2022).
- [113] A. J. Taylor, P. K. Benicewicz, and S. M. Young. "Modeling of femtosecond electromagnetic pulses from large-aperture photoconductors." In: *Opt. Lett.* 18.16 (1993), pp. 1340–1342.
- [114] P. R. Smith, David Henry Auston, and Martin C. Nuss. "Subpicosecond photoconducting dipole antennas." In: *IEEE Journal of Quantum Electronics* 24 (1988), pp. 255–260.
- [115] Nir Katzenellenbogen and Daniel R. Grischkowsky. "Efficient generation of 380 fs pulses of THz radiation by ultrafast laser pulse excitation of a biased metal-semiconductor interface." In: *Applied Physics Letters* 58 (1991), pp. 222–224.
- [116] P. Uhd Jepsen, R. H. Jacobsen, and S. R. Keiding. "Generation and detection of terahertz pulses from biased semiconductor antennas." In: *J. Opt. Soc. Am. B* 13.11 (1996), pp. 2424–2436.
- [117] Sergei Lepeshov, Andrei Gorodetsky, Alex Krasnok, E.U. Rafailov, and Pavel Belov. "Enhancement of Terahertz Photoconductive Antennas and Photomixers Operation by Optical Nanoantennas." In: *Laser and Photonics Review* 11 (Jan. 2017), p. 1600199.
- [118] Ian S. Gregory, C. Baker, W. R. Tribe, Ian V. Bradley, Michael J. Evans, Edmund Harold Linfield, A. Giles Davies, and Mohamed Missous. "Optimization of photomixers and antennas for continuous-wave terahertz emission." In: *IEEE Journal of Quantum Electronics* 41 (2005), pp. 717–728.
- [119] André Dreyhaupt, Stephan Winnerl, Thomas Dekorsy, and Manfred Helm. "High-intensity terahertz radiation from a microstructured large-area photoconductor." In: *Applied Physics Letters* 86 (2005), p. 121114.
- [120] Gabor Matthaus, Stefan Nolte, Rico Hohmuth, M. Voitsch, Wolfgang Richter, Boris Pradarutti, Stefan Riehemann, Gunther Notni, and Andreas Tunnermann. "Microlens coupled interdigital photoconductive switch." In: *Applied Physics Letters* 93 (2008), p. 091110.
- [121] Matthias Beck, Hanjo Schafer, Gregor Klatt, Jure Demsar, Stephan Winnerl, Manfred Helm, and Thomas Dekorsy. "Impulsive terahertz radiation with high electric fields from an amplifier-driven large-area photoconductive antenna." In: *Optics express* 18 9 (2010), pp. 9251–7.
- [122] Abhishek Singh, Jiang Li, Alexej Pashkin, Rakesh Rana, Stephan Winnerl, Manfred Helm, and Harald Schneider. "High-field THz pulses from a GaAs photoconductive emitter for non-linear THz studies." In: *Optics express* 29 13 (2021), pp. 19920–19927.

- [123] Q. Wu and Xiang Zhang. "Free-space electro-optic sampling of terahertz beams." In: *Applied Physics Letters* 67 (1995), pp. 3523–3525.
- [124] Ajay Nahata, Aniruddha S. Weling, and Tony F. Heinz. "A wideband coherent terahertz spectroscopy system using optical rectification and electro-optic sampling." In: *Applied Physics Letters* 69 (1996), pp. 2321–2323.
- [125] L.D. Landau, J.S. Bell, M.J. Kearsley, L.P. Pitaevskii, E.M. Lifshitz, and J.B. Sykes. *Electrodynamics of Continuous Media*. COURSE OF THEORETICAL PHYSICS. Elsevier Science, 2013. ISBN: 9781483293752.
- [126] G. Grüner, C. Dahl, K. Dahl, L. Genzel, P. Goy, J.P. Kotthaus, G. Kozlov, M.C. Nuss, J. Orenstein, and A. Volkov. *Millimeter and Submillimeter Wave Spectroscopy of Solids*. Springer Berlin Heidelberg, 1998. ISBN: 9783540628606.
- [127] C.Y. Ho and R.E. Taylor. *Thermal Expansion of Solids*. CINDAS data series on material properties. ASM International, 1998. ISBN: 9781615032150.
- [128] Atef Shalabney, Jino George, James Andell Hutchison, Guido Pupillo, Cyriaque Genet, and Thomas W. Ebbesen. "Coherent coupling of molecular resonators with a microcavity mode." In: *Nature Communications* 6 (2014).
- [129] Blake S. Simpkins, Kenan P. Fears, Walter J. Dressick, Bryan T. Spann, Adam D. Dunkelberger, and Jeffrey C. Owrutsky. "Spanning Strong to Weak Normal Mode Coupling between Vibrational and Fabry–Pérot Cavity Modes through Tuning of Vibrational Absorption Strength." In: *ACS Photonics* 2 (2015), pp. 1460–1467.
- [130] Merav Muallem, Alexander Palatnik, Gilbert Daniel Nessim, and Yaakov Raphael Tischler. "Strong Light-Matter Coupling and Hybridization of Molecular Vibrations in a Low-Loss Infrared Microcavity." In: *The journal of physical chemistry letters* 7 11 (2016), pp. 2002–8.
- [131] Shaelyn R. Casey and Justin R. Sparks. "Vibrational Strong Coupling of Organometallic Complexes." In: *Journal of Physical Chemistry C* 120 (2016), pp. 28138–28143.
- [132] H. Memmi, O. Benson, S. Sadofev, and S. Kalusniak. "Strong Coupling between Surface Plasmon Polaritons and Molecular Vibrations." In: *Phys. Rev. Lett.* 118 (12 2017), p. 126802.
- [133] Adam D. Dunkelberger, Bryan T. Spann, Kenan P. Fears, Blake S. Simpkins, and Jeffrey C. Owrutsky. "Modified relaxation dynamics and coherent energy exchange in coupled vibration-cavity polaritons." In: *Nature Communications* 7 (2016).
- [134] Thibault Chervy, Anoop Thomas, Elias Akiki, Robrecht M. A. Vergauwe, Atef Shalabney, Jino George, Éloïse Devaux, James Andell Hutchison, Cyriaque Genet, and Thomas W. Ebbesen. "Vibro-polaritonic IR emission in the strong coupling regime." In: *ACS Photonics* (2017).
- [135] Javier del Pino, Johannes Feist, and Francisco J. Garc'ia-Vidal. "Signatures of Vibrational Strong Coupling in Raman Scattering." In: *Journal of Physical Chemistry C* 119 (2015), pp. 29132–29137.
- [136] Bo Xiang, Raphael F. Ribeiro, Yingmin Li, Adam D. Dunkelberger, Blake B. Simpkins, Joel Yuen-Zhou, and Wei Xiong. "Manipulating optical nonlinearities of molecular polaritons by delocalization." In: *Science Advances* 5 (2019).
- [137] A. Thomas et al. "Tilting a ground-state reactivity landscape by vibrational strong coupling." In: *Science* 363 (2018), pp. 615–619.

- [138] Masashi Hase. "Spin-Peierls transition in  $\text{CuGeO}_3$ ." In: *Physica B: Condensed Matter* 237-238 (1997). Proceedings of the Yamada Conference XLV, the International Conference on the Physics of Transition Metals, pp. 123–126. ISSN: 0921-4526.
- [139] A. Damascelli, D. van der Marel, G. Dhahlenne, and A. Revcolevschi. "Optical spectroscopy of pure and doped  $\text{CuGeO}_3$ ." In: *Phys. Rev. B* 61 (18 2000), pp. 12063–12074.
- [140] A. Damascelli, D. van der Marel, F. Parmigiani, G. Dhahlenne, and A. Revcolevschi. "Infrared signatures of the spin-Peierls transition in  $\text{CuGeO}_3$ ." In: *Phys. Rev. B* 56 (18 1997), R11373–R11376.
- [141] F. Bondino, M. Zangrando, M. Zacchigna, G. Dhahlenne, A. Revcolevschi, and F. Parmigiani. "Crystal-field and Zhang-Rice-singlet excitations in  $\text{CuGe}_{1-x}\text{Si}_x\text{O}_3$  ( $x=0, 0.05$ , and  $0.1$ ) from temperature-, angle-, and polarization-dependent resonant soft x-ray emission." In: *Phys. Rev. B* 75 (19 2007), p. 195106.
- [142] M. Braden, B. Hennion, W. Reichardt, G. Dhahlenne, and A. Revcolevschi. "Spin-Phonon Coupling in  $\text{CuGeO}_3$ ." In: *Phys. Rev. Lett.* 80 (16 1998), pp. 3634–3637.
- [143] M. Braden, E. Ressouche, B. Büchner, R. Keßler, G. Heger, G. Dhahlenne, and A. Revcolevschi. "Anharmonic structural behavior in  $\text{CuGeO}_3$ ." In: *Phys. Rev. B* 57 (18 1998), pp. 11497–11503.
- [144] Haruhiko Kuroe, Tomoyuki Sekine, Masashi Hase, Yoshitaka Sasago, Kunimitsu Uchinokura, Hironao Kojima, Isao Tanaka, and Yuki Shibuya. "Raman-scattering study of  $\text{CuGeO}_3$  in the spin-Peierls phase." In: *Phys. Rev. B* 50 (22 1994), pp. 16468–16474.
- [145] Z. V. Popović, S. D. Dević, V. N. Popov, G. Dhahlenne, and A. Revcolevschi. "Phonons in  $\text{CuGeO}_3$  studied using polarized far-infrared and Raman-scattering spectroscopies." In: *Phys. Rev. B* 52 (6 1995), pp. 4185–4190.
- [146] Wonmi Ahn and B. S. Simpkins. "Raman Scattering under Strong Vibration-Cavity Coupling." In: *The Journal of Physical Chemistry C* 125.1 (2021), pp. 830–835.
- [147] Parinda Vasa, Wei Wang, Robert Pomraenke, Melanie Lammers, Margherita Maiuri, Cristian Manzoni, Giulio Cerullo, and Christoph Lienau. "Real-time observation of ultrafast Rabi oscillations between excitons and plasmons in metal nanostructures with J-aggregates." In: *Nature Photonics* 7 (2013), pp. 128–132.
- [148] Aaron L Stancik and Eric B. Brauns. "A simple asymmetric lineshape for fitting infrared absorption spectra." In: *Vibrational Spectroscopy* 47 (2008), pp. 66–69.
- [149] Vitaly I. Korepanov and Daria M. Sedlovets. "An asymmetric fitting function for condensed-phase Raman spectroscopy." In: *The Analyst* 143 11 (2018), pp. 2674–2679.
- [150] D. Karaiskaj et al. "Linewidths in a semiconductor microcavity with variable strength of normal-mode coupling." In: *Phys. Rev. B* 59 (21 1999), pp. 13525–13527.
- [151] Vincenzo Savona, Lucio Claudio Andreani, Paolo Schwendimann, and Antonio Quattropani. "Quantum well excitons in semiconductor microcavities : unified treatment of weak and strong coupling regimes." In: *Solid State Communications* 93 (1995), pp. 733–739.

- [152] Nikolett Németh, Donald White, Shinya Kato, Scott Parkins, and Takao Aoki. "Transfer-Matrix Approach to Determining the Linear Response of All-Fiber Networks of Cavity-QED Systems." In: *Phys. Rev. Appl.* 13 (6 2020), p. 064010.
- [153] Antoine Canaguier-Durand, Éloïse Devaux, Jino George, Yantao Pang, James Andell Hutchison, Tal Schwartz, Cyriaque Genet, Nadine Wilhelms, Jean-Marie Lehn, and Thomas W. Ebbesen. "Thermodynamics of molecules strongly coupled to the vacuum field." In: *Angewandte Chemie* 52 40 (2013), pp. 10533–6.
- [154] A. Ganesh Vaidyanathan, William P. Spencer, and Daniel Kleppner. "Inhibited Absorption of Blackbody Radiation." In: *Phys. Rev. Lett.* 47 (22 1981), pp. 1592–1595.
- [155] Andrew Jones, Brian O'Callahan, Honghua Yang, and Markus Raschke. "The thermal near-field: Coherence, spectroscopy, heat-transfer, and optical forces." In: *Progress in Surface Science* 88 (2013), 349–392.
- [156] Alexander Roberts, Manohar Chirumamilla, Kasper Thilising-Hansen, Kjeld Pedersen, and Sergey Bozhevolnyi. "Near-infrared tailored thermal emission from wafer-scale continuous-film resonators." In: *Optics Express* 23 (2015).
- [157] Ivan Celanovic, David Perreault, and John Kassakian. "Resonant-cavity enhanced thermal emission." In: *Physical Review B* 72 (2005).
- [158] Ren-Jye Shiue, Yuanda Gao, Cheng Tan, Cheng Peng, Jiabao Zheng, Konstantin Efetov, Youngduck Kim, James Hone, and Dirk Englund. "Thermal radiation control from hot graphene electrons coupled to a photonic crystal nanocavity." In: *Nature Communications* 10 (Jan. 2019).
- [159] Sajedah Manzeli, Dmitry Ovchinnikov, Diego Pasquier, Oleg Yazyev, and Andras Kis. "2D transition metal dichalcogenides." In: *Nature Reviews Materials* 2 (2017).
- [160] J. A. Wilson, F. J. Di Salvo, and S. Mahajan. "Charge-Density Waves in Metallic, Layered, Transition-Metal Dichalcogenides." In: *Phys. Rev. Lett.* 32 (16 1974), pp. 882–885.
- [161] Arthur H. Thompson, Randall Gamble, and Joseph Revelli. "Transitions between semiconducting and metallic phases in 1T-TaS<sub>2</sub>." In: *Solid State Communications* 9 (1971), pp. 981–985.
- [162] F. Clerc, C. Battaglia, M. Bovet, L. Despont, C. Monney, H. Cercellier, M. G. Garnier, P. Aebi, H. Berger, and L. Forró. "Lattice-distortion-enhanced electron-phonon coupling and Fermi surface nesting in 1T-TaS<sub>2</sub>." In: *Phys. Rev. B* 74 (15 2006), p. 155114.
- [163] Igor Vaskivskiy, Jan Gospodaric, Serguei Brazovskii, Damjan Svetin, Petra Sutar, Evgeny Goresnik, Ian A. Mihailovic, Tomaz Mertelj, and Dragan Mihailovic. "Controlling the metal-to-insulator relaxation of the metastable hidden quantum state in 1T-TaS<sub>2</sub>." In: *Science Advances* 1.6 (2015), e1500168.
- [164] Y Wang, W. L. Yao, Ziming Xin, T. T. Han, Z. G. Wang, L. Chen, C. Cai, Yuan Li, and Y. Zhang. "Band insulator to Mott insulator transition in 1T-TaS<sub>2</sub>." In: *Nature Communications* 11 (2020).
- [165] Balázs Sipoş, Anna Kusmartseva, Ana Akrap, Helmuth Berger, László Forró, and E. Tutis. "From Mott state to superconductivity in 1T-TaS<sub>2</sub>." In: *Nature materials* 7 12 (2008), pp. 960–5.

- [166] Kazuo Nakanishi and Hiroyuki Shiba. "Domain-like Incommensurate Charge-Density-Wave States and the First-Order Incommensurate-Commensurate Transitions in Layered Tantalum Dichalcogenides. I. 1T-Polytype." In: *Journal of the Physical Society of Japan* 43 (1977), pp. 1839–1847.
- [167] Wen Wen, Chunhe Dang, and Liming Xie. "Photoinduced phase transitions in two-dimensional charge-density-wave 1T-TaS<sub>2</sub>." In: *Chinese Physics B* 28 (2019).
- [168] Adam W. Tsen et al. "Structure and control of charge density waves in two-dimensional 1T-TaS<sub>2</sub>." In: *Proceedings of the National Academy of Sciences* 112 (2015), pp. 15054–15059.
- [169] Wen Wang, Dirk Dietzel, and André Schirmeisen. "Lattice Discontinuities of 1T-TaS<sub>2</sub> across First Order Charge Density Wave Phase Transitions." In: *Scientific Reports* 9 (2019).
- [170] Lev Gasparov, Kenneth G. Brown, Anthony Wint, David B. Tanner, Helmuth Berger, Richard Gaal, László Forró, and G.Margaritondo. "Phonon anomaly at the charge ordering transition in 1T-TaS<sub>2</sub>." In: *Physical Review B* 66 (2002), p. 094301.
- [171] Nicky Dean, Jan C. Petersen, Daniele Fausti, Ra'anan I. Tobey, Stefan Kaiser, Lev Gasparov, Helmuth Berger, and Andrea Cavalleri. "Polaronic conductivity in the photoinduced phase of 1T-TaS<sub>2</sub>." In: *Physical review letters* 106 1 (2010), p. 016401.
- [172] W. L. McMillan. "Landau theory of charge-density waves in transition-metal dichalcogenides." In: *Phys. Rev. B* 12 (4 1975), pp. 1187–1196.
- [173] S.-H. Baek, Yeahan Sur, Kee Hoon Kim, Matthias Vojta, and Bernd Büchner. "Interplay of charge density waves, disorder, and superconductivity in 2H-TaSe<sub>2</sub> elucidated by NMR." In: *New Journal of Physics* 24 (2022).
- [174] Damjan Svetin, Igor Vaskivskyi, Petra Sutar, Evgeni Goreshnik, Jan Gospodaric, Tomaz Mertelj, and Dragan Mihailovic. "Transitions between photoinduced macroscopic quantum states in 1T-TaS<sub>2</sub> controlled by substrate strain." In: *Applied Physics Express* 7.10 (2014), p. 103201.
- [175] Yongchang Ma, Yanhui Hou, Cuimin Lu, Lijun Li, and Cedomir Petrovic. "Possible origin of nonlinear conductivity and large dielectric constant in the commensurate charge-density-wave phase of 1T-TaS<sub>2</sub>." In: *Phys. Rev. B* 97 (19 2018), p. 195117.
- [176] Yongchang Ma, Dong Wu, and Zequn Wang. "The evidence of stacking disorder from dielectric response along the c-axis in the commensurate CDW phase in bulk 1T-TaS<sub>2</sub>." In: *Solid State Communications* 316-317 (2020), p. 113946.
- [177] Kazuo Nakanishi and Hiroyuki Shiba. "Domain-Like Incommensurate Charge-Density-Wave States and Collective Modes." In: *Journal of the Physical Society of Japan* 45.4 (1978), pp. 1147–1156.
- [178] G. Grüner. "The dynamics of charge-density waves." In: *Rev. Mod. Phys.* 60 (4 1988), pp. 1129–1181.
- [179] Philipp Pilar, Daniele De Bernardis, and Peter Rabl. "Thermodynamics of ultra-strongly coupled light-matter systems." In: *Quantum* 4 (2020), p. 335.
- [180] K.Lenk, J. Li, P. Werner, and M. Eckstein. *Collective theory for an interacting solid in a single-mode cavity*. 2022. arXiv: [2205.05559](https://arxiv.org/abs/2205.05559) [cond-mat.str-el].
- [181] Michela F. Picardi, Kartika N. Nimje, and Georgia T. Papadakis. "Dynamic modulation of thermal emission-A Tutorial." In: *Journal of Applied Physics* 133.11 (Mar. 2023).

- [182] Jan Ravník, Igor Vaskivskiy, Yaroslav Gerasimenko, Michele Diego, Jaka Vodeb, Viktor Kabanov, and Dragan D. Mihailovic. "Strain-Induced Metastable Topological Networks in Laser-Fabricated TaS<sub>2</sub> Polytype Heterostructures for Nanoscale Devices." In: *ACS Applied Nano Materials* 2.6 (2019), pp. 3743–3751.
- [183] D. R. P. Guy, A. M. Ghorayeb, S. C. Bayliss, and R. H. Friend. "High pressure investigation of the cdw phase diagram of 1T-TaS<sub>2</sub>." In: *Charge Density Waves in Solids*. Ed. by Gyula Hutiray and Jenő Sólyom. Berlin, Heidelberg: Springer Berlin Heidelberg, 1985, pp. 80–83.
- [184] Ryogo Kubo. "Statistical-Mechanical Theory of Irreversible Processes. I. General Theory and Simple Applications to Magnetic and Conduction Problems." In: *Journal of the Physical Society of Japan* 12.6 (1957), pp. 570–586.
- [185] Randy Van Eck, Michiel Klep, and Jos Schijndel. "Surface to Surface Radiation Benchmarks." In: *Comsol Conference Munich 2016*, 2016.
- [186] R. W. Russell, Mark A. Chatelain, James H. Hecht, and John R. Stephens. "Si<sub>3</sub>N<sub>4</sub> emissivity and the unidentified infrared bands." In: *NASA proceedings*, 1989, N-91-14897.
- [187] Felipe Herrera and Frank C. Spano. "Cavity-Controlled Chemistry in Molecular Ensembles." In: *Phys. Rev. Lett.* 116 (23 2016), p. 238301.
- [188] Kochise Bennett, Markus Kowalewski, and Shaul Mukamel. "Novel photochemistry of molecular polaritons in optical cavities." In: *Faraday discussions* 194 (2016), pp. 259–282.
- [189] Johannes Feist, Javier Galego, and Francisco J. Garcia-Vidal. "Polaritonic Chemistry with Organic Molecules." In: *ACS Photonics* 5.1 (2018), pp. 205–216.
- [190] Joel Yuen-Zhou and Vinod M. Menon. "Polariton chemistry: Thinking inside the (photon) box." In: *Proceedings of the National Academy of Sciences* 116 (2019), pp. 5214–5216.
- [191] Daniele De Bernardis, Tuomas Jaako, and Peter Rabl. "Cavity quantum electrodynamics in the nonperturbative regime." In: *Physical Review A* 97 (2017), p. 043820.
- [192] Timothy M. Sweeney, Samuel G. Carter, Allan S. Bracker, Mijin Kim, Chul Soo Kim, Lily Yang, Patrick M. Vora, Peter G. Brereton, Erin R. Cleveland, and Daniel Gammon. "Cavity-stimulated Raman emission from a single quantum dot spin." In: *Nature Photonics* 8 (2014), pp. 442–447.
- [193] Philipp Sulzer, Maximilian Högner, Anneliese Raab, Lukas Fürst, Ernst E. Fill, Daniel Gerz, Christina Hofer, Liudmila Voronina, and Ioachim Pupeza. "Cavity-enhanced field-resolved spectroscopy." In: *Nature Photonics* 16 (2022), pp. 692–697.
- [194] Emanuele Orgiu et al. "Conductivity in organic semiconductors hybridized with the vacuum field." In: *Nature materials* 14 11 (2014), pp. 1123–9.
- [195] David Hagenmuller, Stefan Schutz, Johannes Schachenmayer, Claudiu Genes, and Guido Pupillo. "Cavity-assisted mesoscopic transport of fermions: Coherent and dissipative dynamics." In: *Physical Review B* 97 (2018), p. 205303.
- [196] Yi-Pu Wang and Can-Ming Hu. "Dissipative couplings in cavity magnonics." In: *Journal of Applied Physics* 127.13 (Apr. 2020).
- [197] Andrey Baydin et al. "Magnetically tuned continuous transition from weak to strong coupling in terahertz magnon polaritons." In: *Phys. Rev. Res.* 5 (1 2023), p. L012039.

- [198] Hannes Maier-Flaig, Michael Harder, Stefan Klingler, Zhiyong Qiu, Eiji Saitoh, Mathias Weiler, Stephan Geprags, Rudolf Gross, Sebastian T. B. Goennenwein, and Hans Huebl. "Tunable magnon-photon coupling in a compensating ferrimagnet—from weak to strong coupling." In: *Applied Physics Letters* 110 (2017), p. 132401.
- [199] Tomohiro Fukushima, Soushi Yoshimitsu, and Kei Murakoshi. "Vibrational Coupling of Water from Weak to Ultrastrong Coupling Regime via Cavity Mode Tuning." In: *The Journal of Physical Chemistry C* 125.46 (2021), pp. 25832–25840.
- [200] Damjan Svetin, Igor Vaskivskiy, Serguei Brazovskii, and Dragan Mihailovic. "Three-dimensional resistivity and switching between correlated electronic states in 1T-TaS<sub>2</sub>." In: *Scientific Reports* 7 (2016).
- [201] B. Burk, Ruth Ellen Thomson, John Clarke, and Alex Zettl. "Surface and Bulk Charge Density Wave Structure in 1 T-TaS<sub>2</sub>." In: *Science* 257 (1992), pp. 362–364.
- [202] Maurice S. Skolnick, Tracey Fisher, and D. M. Whittaker. "Strong coupling phenomena in quantum microcavity structures." In: *Semiconductor Science and Technology* 13 (1998), pp. 645–669.
- [203] G. S. Agarwal. "Vacuum-Field Rabi Splittings in Microwave Absorption by Rydberg Atoms in a Cavity." In: *Physical Review Letters* 53 (1984), pp. 1732–1734.
- [204] Vincenzo Savona, Lucio Claudio Andreani, Paolo Schwendimann, and Antonio Quattropani. "Quantum well excitons in semiconductor microcavities : unified treatment of weak and strong coupling regimes." In: *Solid State Communications* 93 (1995), pp. 733–739.
- [205] P. Schouwink, H. v. Berlepsch, L. Dähne, and R. F. Mahrt. "Dependence of Rabi-splitting on the spatial position of the optically active layer in organic microcavities in the strong coupling regime." In: *Chemical Physics* 285.1 (2002), pp. 113–120.
- [206] Marlan O. Scully and M. Suhail Zubairy. *Quantum Optics*. Cambridge University Press, 1997.
- [207] Jelena Vukovic, Andrei Faraon, Ilya Fushman, and Dirk R. Englund. "Cavity QED, Single-Photon Nonlinear Optics and Quantum Information Processing with Quantum Dots in Photonic Crystals." In: *Frontiers in Optics* (2008).
- [208] D. A. Crandles, F. Eftekhari, R. Faust, G. S. Rao, M. Reedyk, and F. S. Razavi. "Kramers-Kronig-constrained variational dielectric fitting and the reflectance of a thin film on a substrate." In: *Appl. Opt.* 47.23 (2008), pp. 4205–4211.
- [209] Jino George, Thibault Chervy, Atef Shalabney, Eloïse Devaux, Hidenfumi Hiura, Cyriaque Genet, and Thomas W. Ebbesen. "Multiple Rabi Splittings under Ultrastrong Vibrational Coupling." In: *Phys. Rev. Lett.* 117 (15 2016), p. 153601.
- [210] Iffat Imran, Giulia E. Nicolai, Nicholas D. Stavinski, and Justin R. Sparks. "Tuning Vibrational Strong Coupling with Co-Resonators." In: *ACS Photonics* 6.10 (2019), pp. 2405–2412.
- [211] Kishan S. Menghrajani, Henry A. Fernández, Geoff R. Nash, and William L. Barnes. "Hybridization of Multiple Vibrational Modes via Strong Coupling Using Confined Light Fields." In: *Advanced Optical Materials* 7 (2019).
- [212] Branko Kolarić, Bjorn Maes, Koen Clays, Thomas Durt, and Yves Caudano. "Strong Light-Matter Coupling as a New Tool for Molecular and Material Engineering: Quantum Approach." In: *Advanced Quantum Technologies* 1 (2018).

- [213] Manuel Hertzog, Mao Wang, Jurgen Mony, and Karl Borjesson. "Strong light-matter interactions: a new direction within chemistry." In: *Chemical Society Reviews* 48 (2019), pp. 937–961.
- [214] Zhicong He, Cheng Xu, Wenhao He, Jinhu He, Yunpeng Zhou, and Fang Li. "Principle and Applications of Multimode Strong Coupling Based on Surface Plasmons." In: *Nanomaterials* 12 (2022).
- [215] Wassie Mersha Takele, Frank Wackenhut, Lukasz Piatkowski, Alfred J. Meixner, and Jacek Waluk. "Multimode Vibrational Strong Coupling of Methyl Salicylate to a Fabry-Pérot Microcavity." In: *The Journal of Physical Chemistry B* 124.27 (2020), pp. 5709–5716.
- [216] Alberto Mercurio, Vincenzo Macrì, Chris Gustin, Stephen Hughes, Salvatore Savasta, and Franco Nori. "Regimes of cavity QED under incoherent excitation: From weak to deep strong coupling." In: *Phys. Rev. Res.* 4 (2 2022), p. 023048.
- [217] Johannes Flick, Michael Ruggenthaler, Heiko Appel, and Ángel Rubio. "Atoms and molecules in cavities, from weak to strong coupling in quantum-electrodynamics (QED) chemistry." In: *Proceedings of the National Academy of Sciences* 114 (2016), pp. 3026–3034.
- [218] S. Rudin and T. L. Reinecke. "Oscillator model for vacuum Rabi splitting in microcavities." In: *Phys. Rev. B* 59 (15 1999), pp. 10227–10233.
- [219] Kyriacos Georgiou, Rahul Jayaprakash, Andreas Othonos, and David G. Lidzey. "Ultralong-Range Polariton-Assisted Energy Transfer in Organic Microcavities." In: *Angewandte Chemie (International Ed. in English)* 60 (2021), pp. 16661–16667.
- [220] Michael Reitz, Francesca Mineo, and Claudiu Genes. "Energy transfer and correlations in cavity-embedded donor-acceptor configurations." In: *Scientific Reports* 8 (2018).
- [221] Tao E. Li and Sharon Hammes-Schiffer. "QM/MM Modeling of Vibrational Polariton Induced Energy Transfer and Chemical Dynamics." In: *Journal of the American Chemical Society* 145.1 (2023), pp. 377–384.
- [222] Mao Wang, Manuel Hertzog, and Karl Borjesson. "Polariton-assisted excitation energy channeling in organic heterojunctions." In: *Nature Communications* 12 (2020).
- [223] Martin Kiffner, Jonathan R. Coulthard, Frank Schlawin, Arzhang Ardavan, and Dieter Jaksch. "Mott polaritons in cavity-coupled quantum materials." In: *New Journal of Physics* 21 (2019).
- [224] Ovidiu Cotlet, Sina Zeytinoglu, Manfred Sigrist, Eugene Demler, and Atac Imamoglu. "Superconductivity and other collective phenomena in a hybrid Bose-Fermi mixture formed by a polariton condensate and an electron system in two dimensions." In: *Phys. Rev. B* 93 (5 2016), p. 054510.
- [225] Fabrice P. Laussy, Alexey V. Kavokin, and Ivan A. Shelykh. "Exciton-Polariton Mediated Superconductivity." In: *Phys. Rev. Lett.* 104 (10 2010), p. 106402.
- [226] M. Tinkham. *Introduction to Superconductivity*. Dover Books on Physics Series. Dover Publications, 2004. ISBN: 9780486134727.
- [227] Alexander V. Boris, N. N. Kovaleva, O. V. Dolgov, Todd Marshall Holden, C. Lin, Bernhard Keimer, and Christian Bernhard. "In-Plane Spectral Weight Shift of Charge Carriers in YBa<sub>2</sub>Cu<sub>3</sub>O<sub>6.9</sub>." In: *Science* 304 (2004), pp. 708–710.

- [228] D. N. Basov and T. Timusk. "Electrodynamics of high-Tc superconductors." In: *Rev. Mod. Phys.* 77 (2 2005), pp. 721–779.
- [229] Claudio Giannetti et al. "Revealing the high-energy electronic excitations underlying the onset of high-temperature superconductivity in cuprates." In: *Nature Communications* 2 (2011).
- [230] Fabio Novelli et al. "Witnessing the formation and relaxation of dressed quasiparticles in a strongly correlated electron system." In: *Nature Communications* 5 (2014).
- [231] Simone Peli et al. "Mottness at finite doping and charge-instabilities in cuprates." In: *Nature physics* 13 (2015), pp. 806–811.
- [232] B. Liu, M. Först, M. Fechner, D. Nicoletti, J. Porras, T. Loew, B. Keimer, and A. Cavalleri. "Pump Frequency Resonances for Light-Induced Incipient Superconductivity in  $\text{YBa}_2\text{Cu}_3\text{O}_{6.5}$ ." In: *Phys. Rev. X* 10 (1 2020), p. 011053.
- [233] S. L. Cooper et al. "Optical studies of the a-, b-, and c-axis charge dynamics in  $\text{YBa}_2\text{Cu}_3\text{O}_{6+x}$ ." In: *Phys. Rev. B* 47 (13 1993), pp. 8233–8248.
- [234] Cayla Nelson, Maria Spies, Lina Abdallah, Stefan Zollner, Yun xu, and Hongmei Luo. "Dielectric function of  $\text{LaAlO}_3$  from 0.8 to 6 eV between 77 and 700 K." In: *Journal of Vacuum Science and Technology A: Vacuum, Surfaces, and Films* 30 (Nov. 2012), pp. 061404–061404.
- [235] J. J. Zhu, Wenwu Li, Y. W. Li, Yu-Hao Shen, Zhigao Hu, and J. H. Chu. "Effects of applied electrical field on electronic structures in  $\text{LaNiO}_3$  conductive metallic oxide film: An optical spectroscopic study." In: *Applied Physics Letters* 97 (2010), p. 211904.
- [236] Silvia Vangelista, R. Piagge, Satu Ek, Tiina Sarnet, Gabriella Ghidini, Christian Martella, and Alessio Lamperti. "Structural, chemical and optical properties of cerium dioxide film prepared by atomic layer deposition on TiN and Si substrates." In: *Thin Solid Films* 636 (2017), pp. 78–84.
- [237] Angela Montanaro et al. "Visible pump–mid infrared pump–broadband probe: Development and characterization of a three-pulse setup for single-shot ultrafast spectroscopy at 50 kHz." In: *Review of Scientific Instruments* 91.7 (July 2020), p. 073106. ISSN: 0034-6748.
- [238] H. Eisaki, N. Kaneko, D. L. Feng, A. Damascelli, P. K. Mang, K. M. Shen, Z.-X. Shen, and M. Greven. "Effect of chemical inhomogeneity in bismuth-based copper oxide superconductors." In: *Phys. Rev. B* 69 (6 2004), p. 064512.
- [239] David Hagenmüller, Johannes Schachenmayer, Cyriaque Genet, Thomas W. Ebbesen, and Guido Pupillo. "Enhancement of the Electron–Phonon Scattering Induced by Intrinsic Surface Plasmon–Phonon Polaritons." In: *ACS Photonics* 6.4 (2019), pp. 1073–1081.

# LIST OF FIGURES

---

Figure 2.1	Linear transmission of a Fabry-Pérot resonator .....	7
Figure 2.2	Cavity transmission as a function of the mirrors reflectivity .....	9
Figure 2.3	Energy diagram of cavity-mediated light-matter strong coupling ..	12
Figure 2.4	Cavity-dependent properties of polariton modes predicted by the coupled oscillator quantum model .....	14
Figure 2.5	Calculated time-dependent emission of a dissipative THz cavity ...	17
Figure 2.6	Weak-to-strong coupling transition as a function of the cavity quality factor .....	18
Figure 2.7	Linewidth enhancement in the weak coupling regime at different coupling strengths .....	18
Figure 2.8	Transmission through a layered structure included in Transfer- matrix simulations .....	20
Figure 2.9	Transfer-matrix calculations of the linear response of a hybrid THz cavity and comparison with the coupled oscillator model .....	24
Figure 2.10	Polariton dispersion simulated with the quantum Input-Output model in the linear regime and comparison with the classical Transfer-matrix method .....	29
Figure 3.1	Tunable cryogenic Terahertz cavity .....	32
Figure 3.2	Measured THz transmission of the silicon nitride membranes within the employed spectral range .....	33
Figure 3.3	Mechanism of THz generation in a photo-conductive antenna .....	35
Figure 3.4	Schematic layout of electro-optical sampling (EOS) .....	37
Figure 3.5	Schematic layout of the Terahertz time-domain spectrometer .....	37
Figure 3.6	Employed THz pulses generated by the photo-conductive antenna	39
Figure 3.7	Extraction of THz optical constants .....	41
Figure 3.8	THz spectroscopy of the empty cavity at 80 K for representative distances $L$ between the cryogenic mirrors .....	42
Figure 3.9	Temperature dependence of the empty cavity properties .....	44
Figure 4.1	Terahertz linear spectroscopy of $\text{CuGeO}_3$ .....	48
Figure 4.2	Normal-mode splitting of $\text{CuGeO}_3$ phonon-polaritons at 80 K .....	50
Figure 4.3	Time-domain THz fields exiting the uncoupled systems and the strongly coupled system .....	51
Figure 4.4	Spectral filtering of the cavity fields .....	51
Figure 4.5	Dependence of the phonon-polariton modes on the strength of the THz field .....	52
Figure 4.6	Dependence of the phonon-polariton states on the cavity frequency	53
Figure 4.7	Fitted polariton spectrum of strongly coupled $\text{CuGeO}_3$ .....	55
Figure 4.8	Estimated wave-function components of the cavity-phonon hy- brid states .....	56
Figure 4.9	Sum of the cavity and phonon fraction of the polaritonic wave- functions .....	56
Figure 4.10	Comparison of the cavity transmission spectra with the Transfer- matrix model .....	58

Figure 4.11	Comparison of the measured vibro-polariton dispersion at 80 K with the Transfer-matrix simulation.....	59
Figure 4.12	Measured upper and lower polariton linewidths as a function of the cavity frequency.....	60
Figure 4.13	Estimated frequency and linewidth of CuGeO <sub>3</sub> vibro-polaritons as a function of the quality factor of the bare cavity.....	61
Figure 4.14	Change in temperature of the bare phonon and of the bare cavity mode.....	62
Figure 4.15	Frequency and time-domain temperature-dependent spectra of CuGeO <sub>3</sub> polariton modes at resonance.....	63
Figure 4.16	Comparison between low and high temperature dispersion of the vibro-polaritons in CuGeO <sub>3</sub> .....	63
Figure 4.17	Temperature dependence of the polariton parameters.....	64
Figure 4.18	Comparison between the measured and the simulated polaritonic spectra at 80 K and 290 K.....	65
Figure 5.1	Mechanisms of cavity control of quantum materials.....	68
Figure 5.2	Crystalline structure of 1T-TaS <sub>2</sub> .....	70
Figure 5.3	THz linear spectroscopy of 1T-TaS <sub>2</sub> metal-to-insulator transition measured in free space.....	71
Figure 5.4	Optical conductivity and THz transmission of 1T-TaS <sub>2</sub> across the metal-to-insulator phase transition.....	73
Figure 5.5	Hysteretic behaviour of the charge ordering transition in THz transmission and optical conductivity $\sigma_1$ .....	73
Figure 5.6	Cavity-driven renormalization of the effective critical temperature of the metal-to-insulator phase transition.....	75
Figure 5.7	Variation of the cavity quality factor as a function of the total misalignment angle of the mirrors.....	76
Figure 5.8	Dependence of the effective critical temperature on the cavity alignment.....	76
Figure 5.9	Dependence of the phase transition on the cavity alignment at fixed temperature.....	78
Figure 5.10	Phase switch irreversibility upon tuning the cavity alignment.....	79
Figure 5.11	Reversible cavity control of the metal-to-insulator transition at fixed temperature (150 K) upon tuning the fundamental mode.....	80
Figure 5.12	Cavity-driven renormalization of the effective critical temperature as a function of the cavity resonance.....	80
Figure 5.13	Temperature hysteretic curves as a function of the cavity frequency.....	81
Figure 5.14	Cavity-driven renormalization of sample's temperature as a function of the cavity resonance.....	82
Figure 5.15	Cavity-driven renormalization of 1T-TaS <sub>2</sub> thermodynamics.....	84
Figure 5.16	THz characterization of the sub-THz empty cavities.....	88
Figure 5.17	Dependence of the metal-to-insulator phase transition on the waiting time.....	89
Figure 5.18	Determination procedure of the effective critical temperature of the metal-to-insulator transition.....	90
Figure 5.19	Free energy model setting.....	92
Figure 5.20	Cavity-induced renormalization of the free energy of the metallic phase.....	94
Figure 5.21	Cavity control of sample dissipations.....	97

Figure 5.22	Cr-Al thermocouple junction sealed within the membranes and in thermal contact with the sample.....	99
Figure 5.23	Finite elements simulation of the membrane's thermal dissipations in free space .....	101
Figure 5.24	Finite elements simulation of membrane's temperature as a function of the relative position of the mirror mounts.....	102
Figure 5.25	Temperature measurements within the cavity.....	104
Figure 5.26	Temperature measurements upon heating and cooling.....	105
Figure 5.27	Temperature of the mirrors in the cryogenic configuration and in the room temperature case.....	106
Figure 5.28	Dependence of the phase transition on the temperature of the cavity mirrors revealed by THz spectroscopy.....	107
Figure 5.29	Dependence of the heating critical temperature on the cavity fundamental frequency for the 290 K and cryogenic mirrors configurations.....	107
Figure 5.30	Finite elements simulation of the membrane's temperature as a function of the cavity fundamental frequency in the cryogenic mirrors configuration .....	108
Figure 5.31	Finite elements simulation of membrane's temperature as a function of the cavity fundamental frequency in the 300 K mirrors configuration .....	109
Figure 5.32	Temperature measurement within the cavity as a function of the mirrors temperature.....	111
Figure 5.33	Temperature measurements within the cavity as a function of the cavity alignment for different mirror temperatures.....	112
Figure 5.34	Variation of the cavity fundamental frequency as a function of the total misalignment angle of the cavity .....	113
Figure 5.35	Finite elements simulation of the membrane's temperature as a function of the cavity alignment .....	114
Figure 5.36	Temperature measurements within the cavity (11.5 GHz) as a function of the cavity alignment .....	115
Figure 5.37	Dependence of the effective phase transition temperature on the cavity geometry (without mirrors).....	116
Figure 5.38	Effect of the shielding of ambient radiation on the sample's temperature .....	116
Figure 5.39	Dependence of the metal-to-insulator transition on the THz probing intensity .....	117
Figure 5.40	Dependence of the membrane temperature on the THz intensity ..	118
Figure 6.1	Selection of the spectral region for the Drude coupling analysis....	121
Figure 6.2	Modification of cavity dissipations in the Drude spectral region of 1T-TaS <sub>2</sub> .....	122
Figure 6.3	Comparison between the cavity linewidth and the Drude-like conductivity across 1T-TaS <sub>2</sub> metal-to-insulator transition .....	123
Figure 6.4	Effect of Drude response on cavity dissipations for different cavity frequencies.....	123
Figure 6.5	Dependence of the coupling with Drude oscillator on the symmetry of the cavity mode.....	125
Figure 6.6	Linewidths of the first and second cavity mode across the metal-to-insulator transition in 1T-TaS <sub>2</sub> .....	126

Figure 6.7	Dependence of the coupling constant of the Drude oscillator on the spatial profile of the cavity modes .....	128
Figure 6.8	Complex conductivity of 1T-TaS <sub>2</sub> in the metallic and dielectric phase measured in free space .....	129
Figure 6.9	Transfer-matrix simulations of Drude oscillator coupling in the metallic and dielectric phase of 1T-TaS <sub>2</sub> .....	131
Figure 6.10	Simulated distribution of the cavity field in the metallic phase of 1T-TaS <sub>2</sub> .....	131
Figure 6.11	Dispersion of the cavity modes in the NC metallic phase of 1T-TaS <sub>2</sub> measured at 280 K .....	132
Figure 6.12	Quality factors of the fundamental and second order cavity modes in the metallic phase of 1T-TaS <sub>2</sub> at 280 K.....	133
Figure 6.13	Energy levels scheme for the multi-polariton hybridization of the CDW phonons in 1T-TaS <sub>2</sub> .....	135
Figure 6.14	Multi-polariton spectrum measured in the C-CDW phase of 1T-TaS <sub>2</sub> .....	136
Figure 6.15	Multi-polariton dispersion in the C-CDW phase of 1T-TaS <sub>2</sub> .....	136
Figure 6.16	Transmission spectra of the hybridized CDW phonons at 80 K .....	137
Figure 6.17	Estimated wave-function components of the polariton states of the C-CDW phase .....	140
Figure 6.18	Polariton linewidths in the C-CDW phase as a function of the cavity frequency .....	142
Figure 6.19	Temperature dependence of the cavity dispersion measured across the metal-to insulator transition of 1T-TaS <sub>2</sub> .....	144
Figure 6.20	Temperature dependent THz spectra for a fixed cavity frequency within the CDW phonons spectral range .....	145
Figure 6.21	Signatures of weak coupling regime near the critical temperature of the charge ordering transition in 1T-TaS <sub>2</sub> .....	147
Figure 6.22	THz linear response of the coupled cavity in proximity of the critical temperature and in the high temperature metallic phase of 1T-TaS <sub>2</sub> .....	148
Figure 7.1	Electronic charge transfer excitation in cuprates .....	152
Figure 7.2	Design of the YBCO-based cavity heterostructure .....	153
Figure 7.3	Transfer-matrix simulations of the hybrid YBCO-based cavity .....	154
Figure 7.4	Estimation of the quality factor of the designed heterostructures...	154
Figure 7.5	Heterostructures preparation .....	155
Figure 7.6	Optical measurements by three-pulse scheme performed on free space YBCO (Sample B) .....	156
Figure 7.7	Temperature dependence of the non-linear optical signal for YBCO in free space (Sample B) .....	157
Figure 7.8	Temperature dependence of the non-linear optical signal in the uncapped YBCO heterostructure and for the YBCO in the cavity confined heterostructure.....	159
Figure 7.9	Estimation of the critical temperatures in the uncapped and in the cavity-confined YBCO samples .....	160
Figure 7.10	Non-linear signals in the superconducting phase.....	160
Figure 7.11	Experimental configuration employed for the time-resolved studies	162
Figure 7.12	Fitting procedure of the non-linear optical signal.....	163
Figure 7.13	Fitting procedure of the non-linear signal as a function of the wavelength within the white-light probe .....	164

Figure 7.14	Comparison between the differential signals measured on the YBCO-terminated heterostructure (Sample B) at low and high fluence excitation .....	165
Figure 7.15	SQUID in-plane measurements in the cavity YBCO-based heterostructures.....	166

## LIST OF TABLES

---

Table 4.1	Lorentz fit parameters for bare $\text{CuGeO}_3$ at 80 K.....	57
Table 4.2	Lorentz fit parameters for bare $\text{CuGeO}_3$ at 290 K .....	64
Table 6.1	Drude-Lorentz fit parameters for bare $1\text{T-TaS}_2$ in the dielectric phase.....	130
Table 6.2	Drude-Lorentz fit parameters for bare $1\text{T-TaS}_2$ in the metallic phase at 280 K.....	130
Table 6.3	Estimation of the bare linewidths of the CDW phonons $\gamma_i$ and of the polariton splittings $\Omega_{ij}$ .....	135



# PUBLICATIONS

---

- **Giacomo Jarc**, S. Y. Mathengattil, F. Giusti, M. Barnaba, S. Dal Zilio, S. Winnerl, A. Singh, A. Montanaro, F. Glerean, E. M. Rigoni, S. Dal Zilio, S. Winnerl, and D. Fausti. *Tunable cryogenic terahertz cavity for strong light-matter coupling in complex materials*. Review of Scientific Instruments, 93, 033102 (2022).
- **Giacomo Jarc**, S. Y. Mathengattil, A. Montanaro, F. Giusti, E. M. Rigoni, F. Fassioli, S. Winnerl, S. Dal Zilio, D. Mihailovic, P. Prelovsek, M. Eckstein, and D. Fausti, *Cavity control of the metal-to-insulator transition in 1T-TaS<sub>2</sub>*. arXiv preprint, arXiv:22010.02346, submitted to Nature (October 2022), paper re-submitted after reviewers comments (May 2023).
- F. Glerean, **Giacomo Jarc**, A. Marciniak, F. Giusti, G. Sparapassi, A. Montanaro, E. M. Rigoni, J. O. Tollerud, and D. Fausti. *Time-resolved multimode heterodyne detection for dissecting coherent states of matter*. Optics letters Vol 45 pp. 3498-3501 (2020).
- A. Montanaro, F. Giusti, M. Zanforgnini, P. Di Pietro, F. Glerean, **Giacomo Jarc**, E. M. Rigoni, S. Y. Mathengattil, D. Varsano, M. Rontani, A. Perucchi, E. Molinari, and D. Fausti. *Anomalous non-equilibrium response in black phosphorus to sub-gap mid-infrared excitation*. Nature Communications 13, 2667 (2022).
- F. Giusti, A. Montanaro, A. Marciniak, F. Randi, F. Boschini, F. Glerean, **Giacomo Jarc**, H. Eisaki, M. Greven, A. Damascelli, A. Avella, and D. Fausti. *Anisotropic time-domain electronic response in cuprates driven by mid-infrared pulses*. Physical Review B 104, 125121 (2021).
- A. Montanaro, F. Giusti, M. Colja, G. Brajnik, A. Marciniak, R. Sergo, D. De Angelis, F. Glerean, **Giacomo Jarc**, G. Sparapassi, S. Carrato, G. Cautero and D. Fausti. *Visible pump-mid infrared pump-broadband probe: Development and characterization of a three pulse set-up for single shot ultrafast spectroscopy at 50 kHz*. Review of scientific instruments 91, 073106 (2020).
- **Giacomo Jarc et al.** *Strong coupling signatures across the metal-to-insulator transition in 1T-TaS<sub>2</sub>*. Article in preparation (May 2023).



# RINGRAZIAMENTI

---

Incredibile ma vero, eccoci qui, alla fine di questa tesi, alla fine di questo percorso tortuoso e faticoso, ma che, guardandomi alle spalle, mi ha insegnato tanto e dal quale mi sento arricchito.

Il mio primo ringraziamento va a Daniele per avermi introdotto in questo magico mondo delle cavità. Ricordo benissimo il suo primo messaggio su Slack: "Non ci sarebbe qualcuno che vuole mettersi a fare due conti sulle cavità? Ne parliamo." La sua capacità di sorprendersi sempre e di spronarmi sono state fondamentali per superare i mille momenti di difficoltà e scoraggiamento attraversati durante questo percorso. Giunto alla fine, è soprattutto grazie a lui se posso sentirmi orgoglioso di tutti i passi avanti fatti in questo progetto partito praticamente da zero, quando sul tavolo ottico c'era solo un laser e un bollitore per provare ad incollare le membrane.

Un grazie immenso va Shahla e alla sua capacità di sopportarmi durante l'infinita quantità di tempo passata assieme in laboratorio. Ricordo i due mesi passati ad intrecciare cavi di rame come delle sarte per fare le trecce criogeniche della cavità per poi scoprire che forse le misure più significative sono quelle senza trecce...Le testimonianze di tutti i nostri sforzi artistici decorano adesso il calendario dell'avvento del gruppo.

Un grandissimo grazie ad Angela, meglio nota come "la Fata Morgana". Grazie infinite per il supporto e per aver fatto la follia di portare in macchina assieme a me un criostato e mezzo laboratorio fino a Colonia. Il ricordo di quel viaggio folle ed infinitamente divertente è vivido sulla mia scrivania in forma di foto incorniciata. Grazie anche ad Hamoon e Omar del laboratorio Raman di Colonia per tutti i momenti divertenti passati assieme. Ah sì a proposito....where is Omar?

Grazie a Francesca (la Fata Madrina), la prima ad introdurmi come ancora come studente triennale nei magici "*Laboratori Fausti*" e alla quale sono grato. La ringrazio anche per il suo tentativo (ahimé vano) di portare il suo ordine nel mio disordinato laboratorio.

Grazie ad Enrico per le conversazioni divertenti e surreali e per avermi fatto istituire il "mercoledì della barzelletta". Un pensiero anche a Filippo, mio relatore della tesi magistrale, ed al suo costante spirito critico. Un grazie anche a Antonio e Michele, studenti che hanno avuto la forza di venire a fare la tesi su questo pazzo mondo delle cavità. Una menzione particolare va al secondo, e alla sua capacità di ricordarci sempre di che colore è il Copper Germanate.

Un grazie immenso a tutte le persone di Elettra, o meglio del "FantaBosco", alle quali ho chiesto mille aiuti e supporti. E soprattutto a tutti quelli a cui ho preso qualcosa in prestito per poi scordarmi puntualmente di restituirlo. In particolare grazie a Rudi e Gabriele del gruppo degli elettronici per i numerosi aiuti e consigli. Grazie a Gianluca per essere riuscito ad esaudire tutte le nostre più strane e complicate richieste con la solita disponibilità. Grazie a Maurizio Barnaba per il tutto il disegno della camera sperimentale. Grazie anche a Federico per i suoi sempre puntuali consigli e per la sua capacità di avere sempre la risposta precisa a qualsiasi domanda. Un ringraziamento anche al professor Parmigiani e al suo sguardo di riguardo che ha sempre avuto verso noi studenti.

Grazie agli amici e coinquilini che mi hanno accompagnato in quest'avventura chiamata dottorato e permesso di trovare il tempo di staccarmi dal mio universo parallelo

dal titolo "Cavity-induced madness". Un ringraziamento speciale va a Denny. Grazie per tutte le avventure passate assieme (testimoniate tra l'altro da 58 tacche su un muro), per la sua capacità di farmi trovare tre highlights alla fine di ogni giornata, anche le più funeste, e per un'infinità di altre cose con cui probabilmente potrei riempire un intero capitolo della tesi.

Grazie poi alla mia famiglia, senza la quale tutto questo non sarebbe stato possibile. Grazie per avermi sempre supportato in questo percorso. Un grande grazie anche a nonni, zii e cugine per quella speciale aria di casa che mi hanno sempre fatto vivere.

Infine, grazie di cuore a te, Valeria. Grazie per i concerti, per quel magico corso di ballo e per l'infinito entusiasmo che hai sempre saputo regalarmi. Per questo, ed un mondo di altre cose, ti voglio bene.

Con affetto e riconoscenza,

**Giacomo**